Multidimensional *In Vivo* NMR

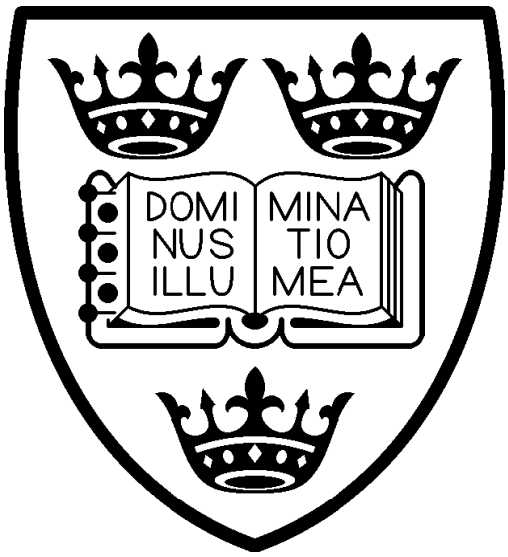

A thesis submitted to the University of Oxford
for the degree of Doctor of Philosophy

John William Richard Welch

St. John's College

MRC Biochemical and Clinical Magnetic Resonance Unit,
Department of Biochemistry, University of Oxford.

Trinity 2001

Contents

Acknowledgements

There are inevitably many people who have helped me during this project. I am extremely grateful to all of them, and apologise to anyone I omit to mention specifically below. Firstly, and most importantly, I would like to thank my supervisors, Drs. Andrew Blamire and Ruth Dixon for their enormous help and patient guidance throughout. I am grateful to Prof. Peter Styles for conceiving the project and the Medical Research Council for funding it.

I am thankful to all those who have shared knowledge with me over various aspects of this work, in particular Dr. Andrew Blamire for *in vivo* spectroscopy and imaging, and Drs. Ruth Dixon, Nicola Sibson and Kishore Bhakoo for what little anatomy and neurochemistry I now know. I should like to thank Ms. Yvonne Anderson for her assistance with the PCA extracts and other bench work, and Drs. Graeme Waddington and John Elder for their support with the computing aspects of this project.

The animal work described herein was performed by Dr. Ruth Dixon, Dr. Nicola Sibson, Dr. Kishore Bhakoo, Ms. Vivienne Austin and Ms. Kerry Broom, with additional support from the staff of the BSU. The vigabatrin treatment was the work of Dr. Kishore Bhakoo; the neutrophil preparations *in vitro* were performed by Dr. Colm Cunningham, whilst the *in vivo* neutrophil induction and histology was done by Dr. Daniel Anthony. Much of this neutrophil project was coordinated by Dr. Nicola Sibson. I am further grateful to those individuals who volunteered to be subjects for the human applications described.

Finally, I would like to thank those whom I have shared office and laboratory space with over the duration, for their company and putting up with me so well. I should like to dedicate this thesis to my wife, Deborah, and our eagerly-awaited baby, as a token of my appreciation for ignoring them both so much over the past few weeks.

Abbreviations

ADC	Analogue to digital converter
ATP	Adenosine triphosphate
COSY	Correlation spectroscopy
DSS	Sodium 2,2-dimethyl-2-silapentane-5-sulphonate
FID	Free-induction decay
GABA	γ-aminobutyric acid
Glx	Glutamate or glutamine
ISIS	Image selected *in vivo* spectroscopy
LPS	Lipopolysaccharide
MRS	Magnetic resonance spectroscopy
NAA	*N*-acetyl aspartate
NADPH	Nicotinamide adenine diphosphate
NMR	Nuclear magnetic resonance
PBS	Phosphate-buffered saline
PCA	Perchloric acid
PCr	Phosphocreatine
PRESS	Point resolved spectroscopy sequence
r.f.	Radio frequency
SAR	Specific absorption rate
S/N	Signal to noise ratio
STEAM	Stimulated echo acquisition mode
t_E	Echo time
t_{IR}	Inversion-recovery time
t_M	Mixing time
TNF-α	Tumour necrosis factor α
TR	Repetition time
TSP	Sodium 3-trimethylsilyl-1-propanoate
VOSY	Volume-selective spectroscopy

Abstract

A proton nuclear magnetic resonance spectrum of the brain *in vivo* contains peaks from every proton-containing molecule in the brain. Sensitivity limitations mean that only those molecules present at concentrations of at least a few millimolar are detectable in a reasonable period of time; this still leaves many important molecules such as amino acids and other small metabolites. Most of their resonance frequencies fall in the region between 1.0 and 4.5 p.p.m.. A typical linewidth *in vivo* is about 0.05 p.p.m., so the number of distinct peaks observable is restricted. The use of two-dimensional NMR techniques such as COSY can spread peaks out into a second dimension enabling otherwise overlapping peaks to be resolved.

This thesis describes the development, testing and application of two such 2D NMR pulse sequences, dubbed ISIS-COSY and ISIS-JRES. They are based on an existing magnetisation localisation sequence and excite detected magnetisation in a manner analogous to the high-resolution sequences COSY and 2D *J*-resolved spectroscopy. A method for quantifying the metabolites visible in an ISIS-COSY spectrum from their cross-peak intensities is described, and results presented from both control rat brains and those of animals treated with vigabatrin, an inhibitor of GABA-transaminase that has the effect of increasing brain γ-amino butyric acid (GABA) levels. Further applications mentioned are in the study of neutrophil-infiltrated rat brain and adaptation of the ISIS-COSY technique for human use.

Chapter 1: Introduction

1.1 In Vivo *Nuclear Magnetic Resonance Spectroscopy*

Over the last thirty years, nuclear magnetic resonance has proved an increasingly useful and popular tool for investigating living tissue and organisms. A vast array of different techniques has yielded information about the anatomy, physiology, biochemistry and metabolism of samples varying from cell populations to human beings. Some of its prevalence may be accorded to its non-invasive and non-destructive nature which facilitates longitudinal time-course studies on a single sample or specimen. NMR is also a diverse field, with many different pulse sequences affording a wealth of information about the sample, and even a variety of nuclei on which to perform experiments.

Most early *in vivo* work focused on ^{31}P NMR[1-3], aimed at detecting the energetic state of cells through measurement of high-energy phosphates such as ATP and phosphocreatine and, through the chemical shift of the inorganic phosphate peak, the pH of the intracellular space. Since then, other nuclei have also been investigated, such as ^{23}Na[4-6] and ^{87}Rb[7, 8] (used as an NMR-observable replacement for ^{39}K, which suffers from an extremely low gyromagnetic ratio) and particularly ^{13}C[9-11] (used generally by introducing isotopically-enriched glucose to observe metabolic pathways as the label is incorporated into various compounds at different rates); however, these are eclipsed by the growing use of ^{1}H as a target for NMR investigation[12-19].

The principal advantages that protons have over other nuclei are their almost universal distribution in bio-molecules and their high (in NMR terms) sensitivity. The former implies that a wide range of molecules contribute signal to an NMR spectrum and are potentially observable; the latter that less time-averaging of the signal will be required to obtain a certain signal/noise level. Some major challenges are posed, though: living tissue invariably contains high levels of water, in which the proton concentration is often four or five orders of magnitude greater than in the other molecules whose investigation is sought. Thus, the water signal potentially swamps the smaller signal from these molecules. Spectral crowding, particularly between 1 and 4 p.p.m., coupled with limited resolution *in vivo* of around 0.05 p.p.m., means that far fewer molecules can be resolved than is potentially the case. In the brain, for

example, while a number of key amino acids and neurotransmitters have signal in the 2–4 p.p.m. range, most routine ^{1}H spectroscopy studies concentrate solely on the singlets from *N*-acetyl aspartate (NAA), creatine / phosphocreatine and choline-containing compounds at 2.0, 3.0 and 3.2 p.p.m. respectively, and also the lactate doublet at 1.3 p.p.m. which becomes elevated in a range of pathological conditions.

1.2 Localised Spectroscopy

Localisation of the signal to a predetermined region of interest is particularly important *in vivo*, either to cut out undesired signals (for example, lipid from the scalp) or to study a particular pathological section of the sample. A variety of techniques have been proposed, from using the sensitivity profile of a small surface coil[20] to chemical-shift imaging approaches[21]. For the purposes of this thesis, only techniques used to produce a 1D spectrum from a cuboidal voxel will be considered.

The main sequences fitting into this category are ISIS[22], PRESS[23] and VOSY[24] or STEAM[25] (the latter two being essentially the same technique; the acronym STEAM will be used throughout this thesis). They are illustrated in Figure 1.1. The mechanism of the ISIS sequence (Figure 1.1a) is described in section 4.1.1.1; it is a difference technique, relying (for localisation in one direction) on the subtraction of a FID in which the voxel region is inverted from one where it is not to isolate the desired signal. This may be extended to full three-dimensional localisation by combining eight FIDs, one with each combination of presence/absence of each 180° inversion pulse (see Figure 1.1b).

The PRESS sequence (Figure 1.1c) is conceptually the simplest of the three: it has three slice-selective pulses arranged to form a double spin-echo. The first 90° pulse excites a slice of magnetisation, a band of which is refocused by the first 180° pulse to form the first spin-echo; the remainder is dephased by the crusher gradients. The second 180° pulse forms a second spin-echo for magnetisation from within the selected voxel, whilst the remainder of the band is dephased. Thus, only signal from within the selected voxel is acquired.

The approach used by STEAM (Figure 1.1d) is slightly different: the three 90° pulses are used to form a stimulated echo. After the first 90° pulse, the slice magnetisation is dephased with a gradient pulse, then a band of this is stored back on

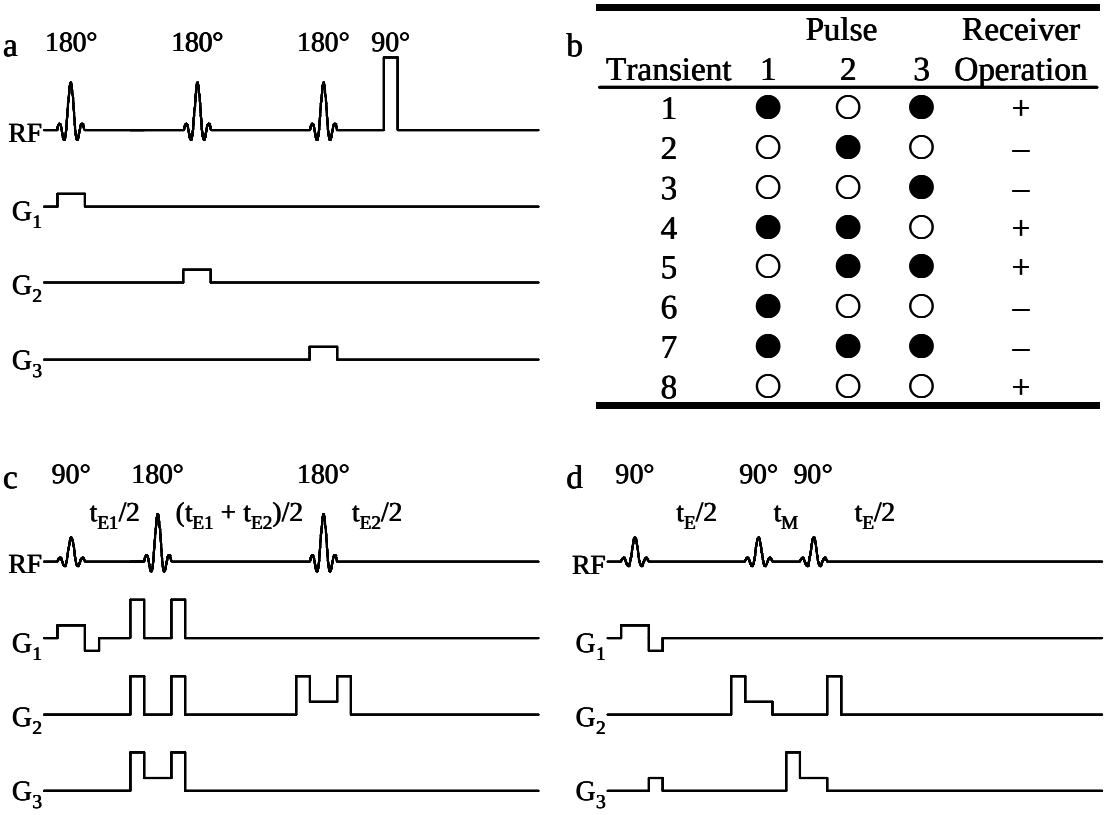

Figure 1.1: Localised one-dimensional spectroscopy pulse sequences. (a) ISIS; (b) Cycle of eight transients for 3D localisation using ISIS (● = pulse present; ○ = pulse absent); (b) PRESS; (c) STEAM.

the *z* axis by a second slice-selective 90° pulse, orthogonal to the first. A period of time (usually called the mixing time t_M) during which no precession occurs (often used for additional water suppression) is followed by the third 90° pulse that brings the magnetisation from the *z* axis back into the *xy* plane. A second gradient pulse then rephases any magnetisation that experienced the first gradient, and dephases the magnetisation from the remainder of the slice. This leaves signal from just the selected voxel; however, 50% of the signal is lost by the combination of spreading the magnetisation around the *xy* plane and the storing of this on the *z* axis.

1.3 Why do 2D NMR In Vivo*?*

As for *in vitro* situations, the use of two-dimensional NMR methods gives considerably greater scope for resolving molecules of interest. The second dimension means that two properties of each proton are used to determine its position in the spectrum. The coincidence of two properties in unrelated molecules is considerably

less likely than of one, so a signal in a certain location in a 2D spectrum is more diagnostic of the presence of a particular molecule than in a 1D spectrum.

A whole raft of approaches from the high-resolution NMR field have potential applicability *in vivo*. Perhaps the simplest, in terms of pulse sequence at least, is COSY[26-28] (correlation spectroscopy). The two properties correlated in a 2D COSY spectrum are the chemical shifts of two protons that are *J*-coupled together. Another relatively straightforward sequence is 2D *J*-resolved spectroscopy[29, 30]. Here, the chemical shift of a proton forms one dimension, whilst its *J*-coupling properties form the second. The mechanism for these two sequences is described in detail later in this introduction. Other techniques such as NOESY[31-33] or TOCSY[34] could be applied, but are not covered in this thesis.

1.4 Spectral Editing

A complementary procedure for observing molecules whose signal is partially or wholly obscured in a simple 1D pulse-and-collect spectrum is provided by spectral editing[35-37]. Several types of experiment fall under this description; a common feature of these is that the final spectrum is obtained from the difference between two acquisitions. In one, a proton resonance is selectively treated (e.g., by presaturation with a long r.f. pulse during the time between acquisitions). The difference between the two shows the effect of the selective treatment on the whole spectrum.

A specific example is provided by the Rothman editing technique[37] for GABA. A 90° excitation pulse is followed by a semi-selective binomial refocusing pulse that forms a spin echo (T_E = 68 ms) with an intensity envelope that is zero at the chosen frequency of 1.91 p.p.m. (the C_3 resonance of GABA). This null inhibits the *J*-modulation of the C_4 resonance at 3.0 p.p.m. arising from the coupling to the C_3 resonance. A DANTE sequence is positioned symmetrically about the refocusing pulse to invert the C_3 resonance and induce *J*-coupling between the two resonances; this causes the outer sidebands of the C_4 triplet to invert at the echo time, chosen to be equal to 1/2*J*. An edited spectrum is obtained as usual from the difference between a spectrum acquired using the DANTE sequence and one obtained without the extra pulses. It shows peaks only from protons coupled to protons around 1.9 p.p.m.; other peaks are largely cancelled by the editing process.

Other recent spectral editing experiments are often based on a double-quantum filter specially tuned to the molecule of interest. The pulses used in the double-quantum filter may be made selective to the region containing the desired peaks, whilst the evolution delays in the filter are set to maximise the formation of double-quantum coherence for the molecule of interest and minimise it for likely contaminating molecules. This can greatly increase the selectivity of the pulse sequence to the detection of that particular molecule.

Editing has some major shortcomings. Firstly, there is the problem associated with other protons resonating close to the selected proton. Any other protons *J*-coupled to these will also appear in the edited spectrum along with those from the molecule of interest. Secondly, the editing experiment has to be repeated for each molecule of interest. Not only does this take longer, but it is necessary to know which molecules are of interest prior to the experiment. This reduces a considerable benefit of NMR, namely that many different molecules are simultaneously observed which permits unexpected effects to be seen as well as those sought.

The relative merits of editing and 2D NMR for observing metabolites in the brain are discussed later (section 6.3).

1.5 Review of Localised 2D NMR

Several sequences have been proposed for localised 2D spectroscopy[38-42], illustrated in Figure 1.2. Two areas of contrast between the sequences may be noted: firstly, some (SLO-COSY[40], STECSY[39], 2D *J*-PRESS[41]) use the same r.f. pulses for localisation as for the 2D excitation, whilst the others (COSY-VSR[42], VOSY-COSY[38]) perform the two functions sequentially in the pulse sequence. Secondly, three of the examples (STECSY, 2D *J*-PRESS, VOSY-COSY) clearly show their relationship to the STEAM[25] or PRESS[23] 1D localised sequences, whilst the other two (SLO-COSY, COSY-VSR) show a stronger relationship to the 2D unlocalised COSY sequence.

One feature shared by all of these sequences, however, is the need to form either spin or stimulated echoes during the localisation period of the sequence. (Note that the SLO-COSY sequence is only localised in two dimensions: if full 3D localisation is sought, a slice-selective 180° pulse is added at the end of the sequence and a spin-

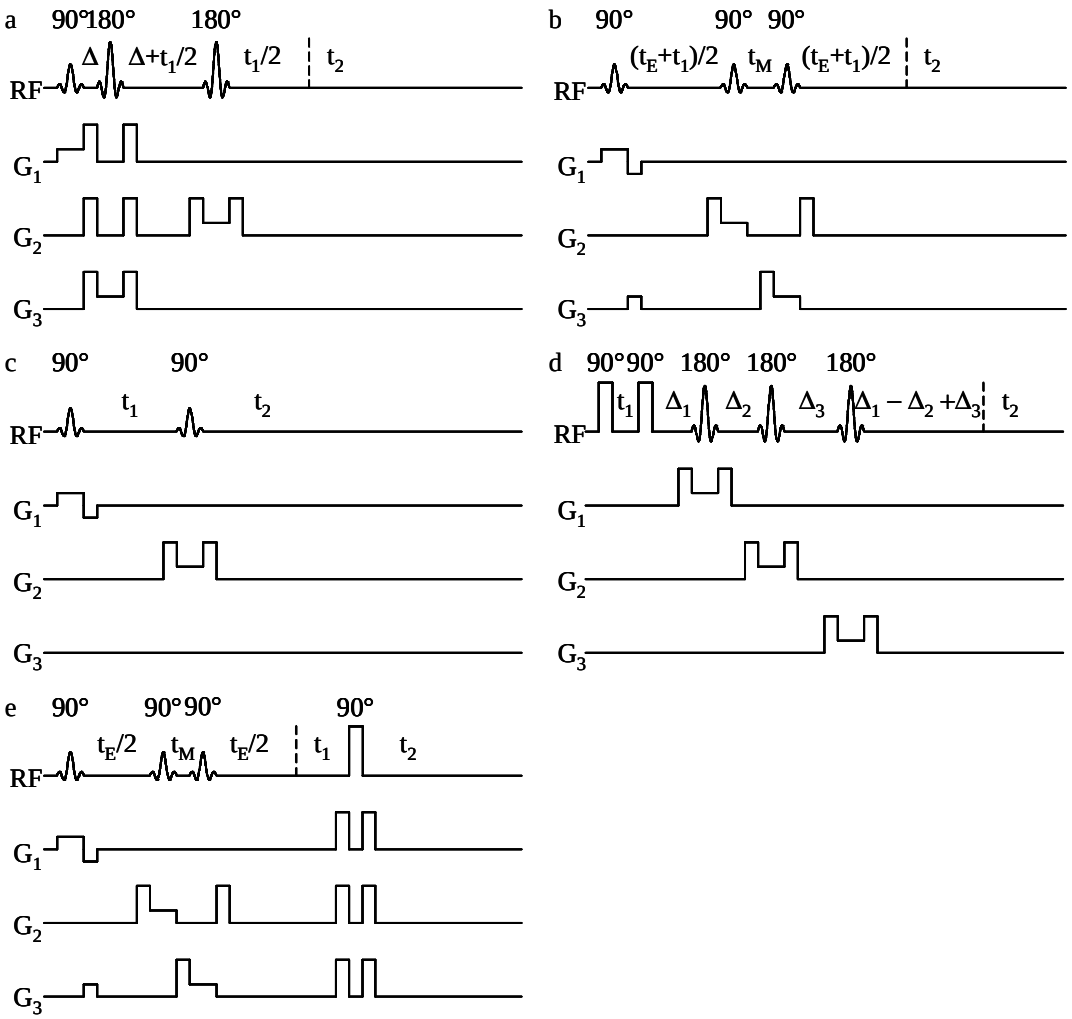

Figure 1.2: Localised two-dimensional spectroscopy sequences: (a) 2D *J*-resolved PRESS; (b) STECSY; (c) SLO-COSY; (d) COSY-VSR; (e) VOSY-COSY.

echo formed.) This suffers from a number of disadvantages. During the period of echo formation (t_E), the magnetisation is in the transverse plane of the rotating frame, where it is subject to transverse (T_2) relaxation. Many molecules in the brain have fairly short T_2 times (for example, the creatine / phosphocreatine peak has a T_2 of 165 ms at 4.7 T[43]), meaning that a significant proportion of the available signal can be wasted during the formation of the echo.

A further problem for molecules containing *J*-coupled spins is that of *J*-modulation during the echo time. Consider the effect of the simple spin-echo pulse sequence

$$90°_x - t_E - 180°_y - t_E - \text{acquire}$$

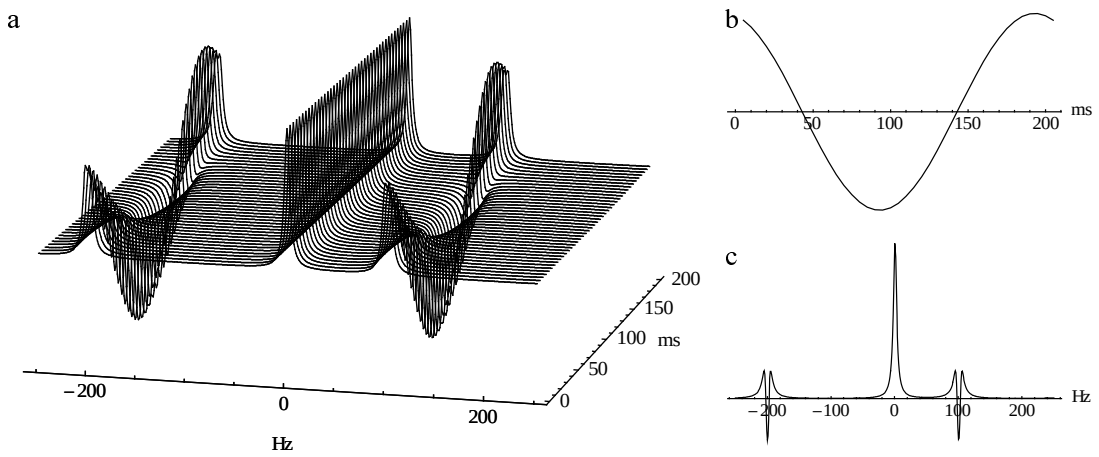

Figure 1.3: (a) Stacked plot showing modulation caused by *J*-coupling during a spin-echo pulse sequence. The spectra were simulated on the program described in section 3.2 using the following parameters: spectral width, 500 Hz; 90° pulse duration, 0.01 μs; spin system, AX and solvent; solvent resonance offset, 0 Hz; AX resonance offsets, 100 & –200 Hz; *J*-coupling constant, 5 Hz; sequence $90°_0$–t_E–$180°_{90}$–t_E–acquire, with t_E incremented from 0 to 200 ms in 5 ms steps. Relaxation is neglected; the lines are broadened to 5 Hz by multiplication of the signal by an exponentially decaying function prior to Fourier transformation. (b) Section through (a) at –206 Hz showing modulation of J-coupled peak intensity. (c) Section through (a) at t_E = 40 ms.

on an AX spin system. At the start of acquisition, the signal may be expressed in product operator notation[44] as

$$\exp\left(\frac{-2t_E}{T_2}\right)\left\{-\left(\mathbf{A}_y+\mathbf{X}_y\right)\cos\left(2\pi J\,t_E\right)+\left(2\mathbf{A}_x\mathbf{X}_z+2\mathbf{A}_z\mathbf{X}_x\right)\sin\left(2\pi J\,t_E\right)\right\} \qquad (1.1)$$

(see section 1.7.2 for a derivation of this, excepting the relaxation term). The second, sine-modulated, term is antiphase and 90° out of phase with the first term (see Figure 1.3c) and so contributes relatively little to the signal observed *in vivo* where linewidths are typically greater than *J*-coupling constants. The first, cosine-modulated, term is the normal doublet observed at the resonance frequency of each nucleus. The modulation of this term by the *J*-coupling means that the intensity observed depends on both the *J*-coupling constant and the echo time. The resulting signal is illustrated by the simulated spectra in Figure 1.3. This shows the effect of a spin-echo pulse sequence with a range of echo times on a sample consisting of an AX pair of nuclei and an isolated non-coupled nucleus. Thus, different molecules with different coupling constants will be observed at different intensities irrespective of the

fact that they may be present at the same concentration. This effect can be minimised by reducing the echo time as far as possible, but cannot be completely eliminated.

One final consideration for sequences using stimulated echoes is their intrinsic loss of 50% of the signal in forming the echo. Particularly for 2D work, where time is inevitably short, the need to acquire four times as many transients to obtain the same signal/noise is a major drawback.

In this thesis, a new approach to *in vivo* 2D NMR is investigated which aims to circumvent such problems by avoiding the need to form echoes for localisation. The method is discussed in section 4.1.1.1.

1.6 COSY Spectroscopy

1.6.1 Sequence

The simplest COSY pulse sequence consists of two 90° pulses separated by an incremented delay t_1. Other variations exist, such as replacing the second pulse with a 45° pulse ("COSY-45", designed to simplify spectra by reducing the amplitude of certain peaks within multiplets) or a series of 90° pulses ("relayed COSY", which can produce cross-peaks between all protons linked in a chain by *J*-coupling), but it is with the simple form that this thesis is concerned. A series of FIDs is acquired with $t_1 = 0, \Delta t_1, 2\Delta t_1, \ldots, (ni-1)\Delta t_1$ where *ni* is the number of t_1 increments to be recorded. These are Fourier transformed twice, once along each FID to form a series of *ni* interferograms, and once perpendicular to this, in the t_1 direction, to form a two-dimensional spectrum.

The apparent simplicity of the process belies a host of complications and subtleties that are beyond the scope of this current work; some of the more elementary concepts involved are mentioned below.

1.6.2 Mechanism

Consider a molecule containing two non-equivalent *J*-coupled protons A and X with resonance offsets Ω_A and Ω_X. Considering initially the effect of the pulses on A, the first pulse results in the magnetisation precessing at frequency Ω_A around the *z*-axis. After a time t_1, there is a second 90° pulse, the effect of which will be discussed

shortly, then a further period of free precession (t_2) during which the NMR signal is recorded. If the second pulse had no effect, the precession frequency would remain the same; after two Fourier transforms, the spectrum would contain a single peak at (Ω_A, Ω_A). This would be rather uninformative: the 1D pulse-and-collect spectrum would simply be reproduced along the diagonal of the 2D spectrum.

Imagine, however, that the magnetisation could somehow be transferred from A to X by this second pulse. Then, during the t_2 period, the magnetisation would precess at frequency Ω_X, giving a peak in the 2D spectrum at (Ω_A, Ω_X). There is then a correlation between the two nuclei: this is what gives rise to the name COSY (correlation spectroscopy).

The mechanism for this transfer is the *J*-coupling between the nuclei. Provided that J_{AX} is sufficiently high (on which more later in this section), an off-diagonal or cross-peak should be observed at (Ω_A, Ω_X) and, because the magnetisation could equally well have started on X and been transferred to A, at (Ω_X, Ω_A) in the COSY spectrum.

A more detailed description of the processes involved in COSY requires the use of product operators[44]. Using the same model as above, and again considering only the A nucleus initially, the effect of the COSY pulse sequence may be described as[45]

$$\mathbf{A_z} \xrightarrow{90_x} -\mathbf{A_y} \tag{1.2}$$

The first 90° pulse converts longitudinal to transverse magnetisation.

$$\xrightarrow{t_1} \begin{matrix} \left(-\mathbf{A_y}\cos\Omega_A\, t_1 + \mathbf{A_x}\sin\Omega_A\, t_1\right)\cos\pi J\, t_1 \\ +\left(2\mathbf{A_x}\mathbf{X_z}\cos\Omega_A\, t_1 + 2\mathbf{A_y}\mathbf{X_z}\sin\Omega_A\, t_1\right)\sin\pi J\, t_1 \end{matrix} \tag{1.3}$$

During the t_1 period, this evolves under the influence of chemical shift and *J*-coupling.

$$\xrightarrow{90_x} \begin{matrix} \left(-\mathbf{A_z}\cos\Omega_A\, t_1 + \mathbf{A_x}\sin\Omega_A\, t_1\right)\cos\pi J\, t_1 \\ +\left(-2\mathbf{A_x}\mathbf{X_y}\cos\Omega_A\, t_1 - 2\mathbf{A_z}\mathbf{X_y}\sin\Omega_A\, t_1\right)\sin\pi J\, t_1 \end{matrix} \tag{1.4}$$

The second 90° pulse converts the magnetisation into a number of terms. Of these, the first ($\mathbf{A_z}$) is zero-quantum magnetisation and the third ($2\mathbf{A_xX_y}$) double-quantum

magnetisation, so neither of these is observable; the second ($\mathbf{A_x}$) corresponds to magnetisation remaining on A throughout, so corresponds to a diagonal peak at (Ω_A, Ω_A), whilst the fourth ($2\mathbf{A_zX_y}$) represents magnetisation transferred from A to X giving a cross-peak at (Ω_A, Ω_X). Of course, if the X nucleus is also included in the starting magnetisation, a diagonal peak at (Ω_X, Ω_X) and a further cross-peak at (Ω_X, Ω_A) would also result.

Examining the observable terms carefully, it can be seen that the cross-peak is antiphase with respect to the *J*-coupling between A and X (implicit by the presence of $\mathbf{A_z}$ in the operator), while the diagonal peak is in phase. Also see that the two types of peak will be 90° out of phase in F_2: the operators are $\mathbf{A_x}$ and $\mathbf{A_zX_y}$, the *x* and *y* implying this phase difference. Exactly the same findings can be shown in the F_1 direction by expanding the trigonometric products[46], i.e.

$$\mathbf{A_x} \sin\Omega_A\, t_1 \cos\pi J\, t_1 = \mathbf{A_x}\, \tfrac{1}{2}\{\sin(\Omega_A + \pi J)t_1 + \sin(\Omega_A - \pi J)t_1\} \qquad (1.5)$$

and

$$-2\mathbf{A_z X_y} \sin\Omega_A\, t_1 \sin\pi J\, t_1 = -2\mathbf{A_z X_y}\, \tfrac{1}{2}\{\cos(\Omega_A - \pi J)t_1 - \cos(\Omega_A + \pi J)t_1\}. \qquad (1.6)$$

The in-phase nature of the diagonal peak (two sine terms are added) and antiphase character of the cross peak (two cosine terms are subtracted) is readily apparent; they are 90° out of phase with each other, evidenced by one term being sine-modulated, the other cosine-modulated.

The effect of these phase differences is that the spectrum cannot be phased such that all the peaks are in phase simultaneously. When the cross-peaks are phased to be absorptive, the diagonal peaks are dispersive. When the sequence is applied *in vivo*, where the diagonal is typically intense compared to the cross-peaks, this gives an undesirably broad band around the diagonal that can obscure nearby peaks.

Relaxation may be included in a simple fashion in the above calculations. If it is assumed that the T_2 is the same for A and X, the evolution of the cross-peak as a function of t_1 and t_2 is given by

$$S_{\mathrm{CP}}(\mathrm{t}_1, \mathrm{t}_2) = \sin \pi J \, \mathrm{t}_1 \sin \pi J \, \mathrm{t}_2 \exp\left\{\frac{-(\mathrm{t}_1 + \mathrm{t}_2)}{T_2}\right\}, \qquad (1.7)$$

modulated by the resonance offset in each direction. The diagonal peak evolution is similar, with the sine terms replaced with the equivalent cosines.

The requirement for a cross-peak to be observable in a COSY spectrum is that $S_{\mathrm{CP}} \gg 0$ at some point (t_1, t_2) during the acquisition period. This may be broken down into two components: (a) $Jt_1 \gg 0$ before the last t_1 increment (where $t_1 = (ni - 1)\Delta t_1$), meaning that significant evolution under the influence of the *J*-coupling during the t_1 period, and (b) $\exp\{-t_1 / T_2\} \gg 0$ at some point where condition (a) is fulfilled, i.e., transverse relaxation does not destroy the magnetisation before it has a chance to evolve. Similar conditions apply to the t_2 direction, but they are not generally limiting as the maximum t_1 is invariably lower than the maximum t_2. In practical terms, under *in vivo* conditions, it would be expected that most 2-bond and 3-bond *J*-couplings (couplings between protons on the same or adjacent carbon atoms) would produce an observable cross-peak (2-bond $^2J_{\mathrm{HH}} \sim 15$ Hz; 3-bond $^3J_{\mathrm{HH}} \sim 7$ Hz), subject to the molecular concentration being sufficient, whereas longer-range couplings would be too weak to see (*J* typically < 2 Hz).

1.6.3 Acquisition

COSY is a very robust technique that produces usable spectra under a range of conditions. The exact calibration of the 90° pulses is not critical; no phase cycle is necessary for spectra to be acquired (but see below).

Whilst the frequency of precession of a signal in the t_1 period is readily apparent in the 2D FIDs, the sign of it is not. There is no way to discriminate between one rotating at frequency $+\Omega$ or one at $-\Omega$. This is akin to a spectrometer that does not use quadrature detection in the directly detected dimension. The effect of this is that all signals appear in the spectrum paired with a duplicate positioned symmetrically about the $F_1 = 0$ axis. There are three ways to approach this problem. The simplistic one is to place the transmitter at one end of the spectrum (say, –1 p.p.m.) and acquire double the spectral width in each dimension. There are then two copies of the spectrum

related by symmetry, but they will not overlap, so one can be disregarded. This is inefficient as three quarters of the 2D spectrum will contain no useful data.

The second method is to ensure that the sense of precession is known relative to the sense in F_2. This may be achieved by phase cycling or gradient-based coherence selection (see discussion in section 1.6.5). For the latter, a pair of strong gradient pulses is positioned symmetrically about the second 90° r.f. pulse. If the sign of the gradients is the same, only those coherences that change precession sense at the 90° pulse remain to be detected (these are known as 'N'-type peaks); if the sign is opposite, only coherences that maintain their sense are not dephased (known as 'P'-type peaks). Either of these may be transformed into a spectrum without the duplicate peaks, but the 'N'-type spectra are usually better[47].

The final approach is to acquire the data in such a way that the phase information is retained. Two techniques are used for this, time-proportional phase incrementation (TPPI)[48] and the hypercomplex method of States *et al.*[49], but both use essentially the same principle. If each t_1 increment is repeated with the phase of the second pulse having had 90° subtracted from it, the second data set thus generated may be treated as the imaginary component of a complex matrix, with the normal acquisition as the real component. These may be treated with a complex Fourier transform to yield a phase-sensitive spectrum.

1.6.4 Artefacts and Suppression

The phase cycle typically used for COSY (applied in addition to any phase-sensitive acquisition for quadrature detection in F_1) consists of alternating the phase of the second 90° COSY pulse (0°, 180°, …) whilst keeping all other phases, including that of the receiver, constant. This cycle is designed to suppress artefacts arising from magnetisation which relaxes back towards equilibrium during the t_1 period. In this case, equilibrium magnetisation is excited by the second 90° pulse only which gives a ridge parallel to the F_2 axis along $F_1 = 0$ ('axial peaks'). As an additional measure, on alternate t_1 increments, 180° is added to the phase of the second pulse. This has no effect if both steps are used; however, if just the first step is used (for instance, to reduce the number of transients required and hence minimise total acquisition time), the ridge is moved to the edges $F_1 = \pm SW_1/2$ where its presence is less objectionable.

This may be combined with quadrature artefact suppression in the F_2 dimension using CYCLOPS if desired, giving a phase cycle up to eight steps long.

An additional class of artefact in a COSY spectrum is t_1 noise. Any random fluctuations in the intensity of each t_1 increment unrelated to evolution during the t_1 period (for example, static magnetic field drift, temperature fluctuations, sample motion, etc.) will appear in the final spectrum as bands of noisy signal parallel to the F_1 axis around intense peaks. *In vivo*, this is particularly noticeable for the water peak as this is typically the most intense peak in the spectrum. A major source of t_1 noise for the water peak would be small fluctuations in the water suppression efficiency.

1.6.5 Gradient-based Coherence Selection

Instead of using phase cycling to remove unwanted coherences, a gradient-based suppression scheme may be employed. Strong $\mathbf{B_0}$ field gradient pulses are included in the pulse sequence with amplitudes and durations such that the dephasing of desired coherences caused by one gradient pulse is refocused by the action of another pulse, whilst for other coherences, the second pulse further dephases the magnetisation and no net signal is recorded.

The dephasing caused by a $\mathbf{B_0}$ gradient pulse is proportional to its amplitude G and duration t, and the coherence level of a particular signal:

$$\Phi \propto pGt, \tag{1.8}$$

where p is the coherence level (single-quantum coherence = ± 1, longitudinal magnetisation = 0, etc.). Thus, as discussed above, a coherence change from $p = +1$ to $p = -1$ at the second 90° pulse in the COSY experiment may be selected using a pair of gradient pulses symmetrically disposed about this pulse, with the same amplitude and duration. The first gradient dephases the signal by an extent $\Phi \propto Gt$; the second by an amount $\Phi' \propto -Gt$, so the signal is rephased. Any longitudinal magnetisation (for instance, magnetisation that relaxes back to the z axis during the t_1 period) is not dephased by the first gradient ($p = 0$); after the 90° r.f. pulse, which transfers it into single-quantum coherence with $p = \pm 1$, the second gradient pulse dephases it and no net signal arising from it is detected.

Gradient-based coherence selection may be used in COSY for the selection of 'P'- and 'N'-type peaks as discussed in section 1.6.3. No gradient-based scheme for suppressing the $F_1 = 0$ artefact, together with phase-sensitive acquisition in the F_1 dimension, is available, however.

There are advantages to both phase cycling and gradient-based methods of coherence selection. A significant benefit accruing from the gradient methods is that they are single-shot, that is, one acquisition is all that is required to obtain the desired signal. By contrast, phase cycling requires multiple acquisitions to be differenced. This can suffer from differencing errors caused by sample motion, a factor that must be considered *in vivo*: if the sample is not in exactly the same location when the two FIDs are acquired, the unwanted coherences will not totally cancel and an artefact will remain in the resultant spectrum. The multiple FIDs required can increase the total acquisition time; however, if they are also required for signal-to-noise considerations, the phase cycle imposes no additional burden.

Non-ideal gradient hardware will produce difficulties with the use of gradient-based coherence selection. In particular, the eddy currents induced in metallic structures within the gradient coils (e.g., the probe) will cause a considerable period after the last gradient pulse (up to the order of milliseconds on a high-field spectrometer, even after pre-emphasis compensation) where the $\mathbf{B_0}$ field is insufficiently stable for the acquisition of a FID.

For no net signal to be recorded after magnetisation from a particular region of the sample has been dephased, the phase spread Φ must be much larger than 2π. The phase spread is proportional to the length of the region; for areas as small as 1 mm (a reasonable figure for rodent brain), strong or long gradient pulses are required. This places stringent demands on the hardware, or can affect the quality of spectra through imperfect dephasing or long delays in the pulse sequence.

1.6.6 Processing

In trying to identify and quantify different molecules in the brain *in vivo*, the cross-peaks are the more useful in the spectrum – the diagonal peaks could just as readily be obtained in a 1D spectrum. Their intensity may be enhanced over that of the diagonal peaks by using a sine bell weighting function on the 2D FIDs prior to

Fourier transformation. Optimum sensitivity is obtained using a matched filter, of the same shape as the evolution described in eq. 1.7. A reasonable approximation is to use a sine bell centred at $t = t_{max}$ in each dimension, where

$$t_{max} = \frac{1}{2J}\cos^{-1}\left\{\frac{1}{\sqrt{1+(\pi J T_2)^2}}\right\} \tag{1.9}$$

is the first maximum of the evolution curve, for an AX spin system. If J is 7 Hz and T_2 is 150 ms, this occurs at 58 ms. This requires that data be collected to at least $t_1 = 116$ ms or truncation artefacts will appear in the spectrum; this would often not be the case in the F_1 dimension. Additionally, the ideally matched filter obviously cannot be achieved for all cross-peaks in the spectrum at once.

These last two considerations imply that less than ideal filtering has to be used. However, good enhancement may still be obtained with any sine bell around the ideal value for the time of its centre point. The values typically used to process *in vivo* spectra in this thesis are 27.5 ms in F_1 and 40 ms in F_2. Different values were used because data was only collected out to $t_1 = 55$ ms to reduce experimental time.

If sine bells are used as weighting functions, the phase-sensitive spectrum possesses unhelpful phase properties, with all peaks alternating rapidly between positive and negative points across their width. (This comes from the properties of a Fourier transform: the amplitude of the first point in the FID defines the total area of the spectrum. With sine bell weighting, this first point is set to zero, so the net area under the spectrum curve is also zero, i.e., positive and negative areas are equal.) This is usually circumvented by presenting the spectra in absolute-value mode, where each point is plotted as the magnitude, rather than the real part, of the complex value.

An optional last step of processing is to symmetrize the spectrum about the $F_1 = F_2$ axis by comparing each point with its symmetry partner and taking either the smaller intensity (the method used here) or the mean of the two. This makes use of the inherent symmetry of the spectrum to remove unwanted noise peaks that do not have an equivalent peak on the other side of the axis. Care must be exercised during this process to ensure that no genuine peaks are lost and that any artefactual peaks that remain are nevertheless disregarded. The latter can quite easily occur, for example,

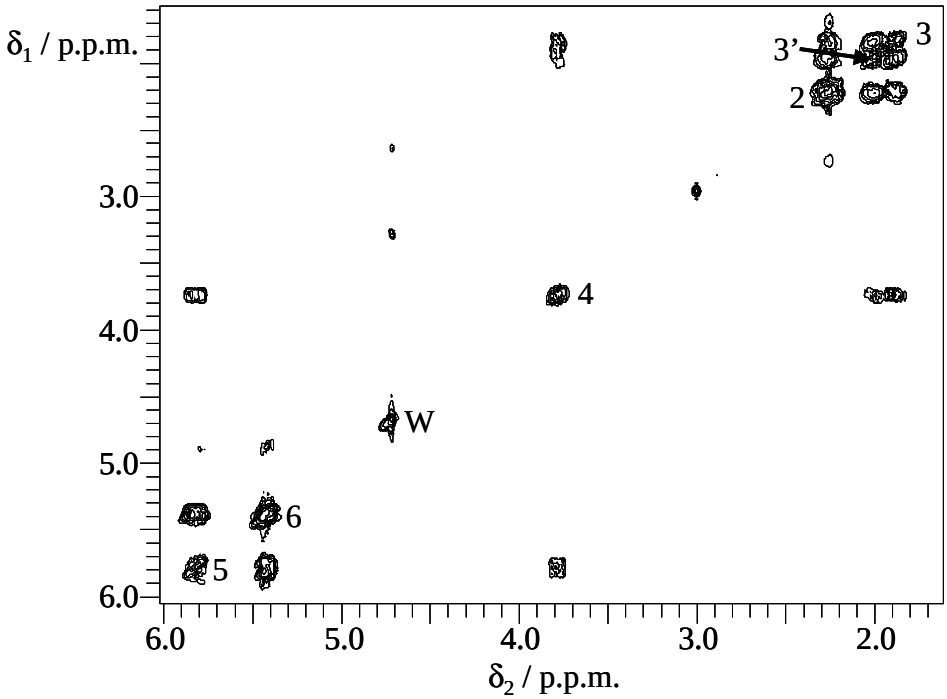

Figure 1.4: High-resolution COSY spectrum of vigabatrin, 4-amino-hex-5-enoic acid, in D_2O at 9.4 T. Protons connected to carbons 2–6 are numbered on their diagonal peaks; W is unsuppressed water. The non-identical protons on carbon 3 are diasteriotopic.

take the situation where two intense diagonal peaks (from water and a concentrated metabolite, say) have long bands of t_1 noise associated with them that pass over the region where a cross-peak between the peaks would appear. The symmetrization procedure would leave the "cross-peaks" whilst removing the remainder of the t_1 noise, which could lead to misinterpretation of the spectrum. The loss of genuine peaks can happen if, for some reason, one of the symmetry-related pair is much weaker than the other. Consider the water-suppressed COSY spectrum of NAA dissolved in water. The NAA has a resonance at 4.4 p.p.m. that is *J*-coupled to two other resonances at 2.7 and 2.5 p.p.m.. If the water suppression (centred at 4.7 p.p.m) also partially saturates this resonance, the cross-peaks at (4.4, 2.7 p.p.m.) and (4.4, 2.5 p.p.m) will disappear, whereas those at (2.7, 4.4 p.p.m) and (2.5, 4.4 p.p.m.) would not. The symmetrization would then remove these cross-peaks also, leading to an unnecessary loss of information in the spectrum.

1.6.7 Spectra

Figure 1.4 shows a typical COSY spectrum of vigabatrin, a small organic molecule containing eight protons visible in this spectrum (for chemical structure, see

section 2.7). It shows the characteristic diagonal of signals along $\delta_1 = \delta_2$ with cross-peaks elsewhere. All of the three-bond *J*-couplings can be seen to have generated cross-peaks, while longer-range ones have not. There is also a two-bond cross-peak visible between the two protons attached to C_3 (labelled 3 and 3'), where the chemical shift difference between the non-identical protons is sufficient to resolve the cross-peak (unlike the protons attached to C_6). Of course, the residual water peak shows no cross-peaks: the small peaks at 2.6, 4.7 p.p.m. and 3.3, 4.7 p.p.m. are artefacts. (Note the absence of corresponding peaks at 4.7, 2.6 p.p.m. and 4.7, 3.3 p.p.m..)

Notice how one can trace along the carbon chain via the cross peaks. For example, starting at the protons attached to C_2, there is a cross-peak with each of the C_3 protons, thence to C_4, and so on. This can be of great worth in elucidating unknown chemical structures. Of more concern to this project, however, is the fact that the cross-peaks can be well separated from the diagonal so, even when the diagonal is crowded such as *in vivo* spectra, there is the potential to identify and quantify these compounds.

1.6.8 Summary

The COSY pulse sequence is a simple sequence that correlates the chemical shifts of two *J*-coupled protons in a two-dimensional spectrum. Particular processing to enhance the intensity of cross-peaks over the diagonal peaks may be applied, but the spectra then must be shown in absolute-value mode. The spectra produced have a diagonal along the $F_1 = F_2$ axis resembling the 1D pulse-and-collect spectrum with cross-peaks away from this indicating correlation between pairs of nuclei. The greater spacing of these cross-peaks means that they afford a greater opportunity for quantifying particular compounds *in vivo*.

1.7 J-Resolved Spectroscopy

1.7.1 Sequence

The 2D *J*-resolved pulse sequence consists of a 90° pulse followed by the t_1 incremented delay, in the centre of which is placed a 180° pulse. This is followed by the t_2 acquisition period. Once again, a series of transients are recorded with successively incremented values of t_1 to generate a 2D dataset. Rather than correlating

chemical shifts of protons *J*-coupled together, this sequence correlates the chemical shift of a proton with its *J*-coupling pattern.

1.7.2 Mechanism

The principle behind this sequence is that of the spin-echo[50, 51]. This refocuses evolution under chemical shift or resonance offset but permits *J*-coupling to continue to evolve, enabling the separation of the two effects in the spectrum. Once more, the effects of the pulse sequence may be explored using product operator calculations for the AX spin system.

Considering first the effects on the A nucleus, the magnetisation evolves through the pulse sequence as follows[52]:

$$\mathbf{A_z} \xrightarrow{90_x} -\mathbf{A_y} \tag{1.10}$$

The first 90° pulse excites transverse magnetisation.

$$\xrightarrow{t_1/2} \begin{aligned} &-\mathbf{A_y}\cos\tfrac{\Omega_A t_1}{2}\cos\tfrac{\pi J t_1}{2} + \mathbf{A_x}\sin\tfrac{\Omega_A t_1}{2}\cos\tfrac{\pi J t_1}{2} \\ &+2\mathbf{A_x X_z}\cos\tfrac{\Omega_A t_1}{2}\sin\tfrac{\pi J t_1}{2} + 2\mathbf{A_y X_z}\sin\tfrac{\Omega_A t_1}{2}\sin\tfrac{\pi J t_1}{2} \end{aligned} \tag{1.11}$$

During the first half of the echo, this evolves under the influences of chemical shift and *J*-coupling.

$$\xrightarrow{180_y} \begin{aligned} &-\mathbf{A_y}\cos\tfrac{\Omega_A t_1}{2}\cos\tfrac{\pi J t_1}{2} - \mathbf{A_x}\sin\tfrac{\Omega_A t_1}{2}\cos\tfrac{\pi J t_1}{2} \\ &+2\mathbf{A_x X_z}\cos\tfrac{\Omega_A t_1}{2}\sin\tfrac{\pi J t_1}{2} - 2\mathbf{A_y X_z}\sin\tfrac{\Omega_A t_1}{2}\sin\tfrac{\pi J t_1}{2} \end{aligned} \tag{1.12}$$

The 180° pulse inverts all magnetisation not along the *y*-axis. Note that the $2\mathbf{A_x X_z}$ term is unaffected as both components of the product operator are inverted; two inversions imply no net effect. For simplicity, the effects of chemical shift and *J*-coupling are considered separately during the next delay (this is possible as their Hamiltonians commute, i.e., $\mathbf{H_J H_{cs}} = \mathbf{H_{cs} H_J}$). Firstly, chemical shifts:

$$\xrightarrow{\Omega_A t_1/2} \begin{aligned} &-\mathbf{A_y}\cos^2\tfrac{\Omega_A t_1}{2}\cos\tfrac{\pi J t_1}{2} + \mathbf{A_x}\cos\tfrac{\Omega_A t_1}{2}\sin\tfrac{\Omega_A t_1}{2}\cos\tfrac{\pi J t_1}{2} \\ &-\mathbf{A_x}\cos\tfrac{\Omega_A t_1}{2}\sin\tfrac{\Omega_A t_1}{2}\cos\tfrac{\pi J t_1}{2} - \mathbf{A_y}\sin^2\tfrac{\Omega_A t_1}{2}\cos\tfrac{\pi J t_1}{2} \\ &+2\mathbf{A_x X_z}\cos^2\tfrac{\Omega_A t_1}{2}\sin\tfrac{\pi J t_1}{2} + 2\mathbf{A_y X_z}\cos\tfrac{\Omega_A t_1}{2}\sin\tfrac{\Omega_A t_1}{2}\sin\tfrac{\pi J t_1}{2} \\ &-2\mathbf{A_y X_z}\cos\tfrac{\Omega_A t_1}{2}\sin\tfrac{\Omega_A t_1}{2}\sin\tfrac{\pi J t_1}{2} + 2\mathbf{A_x X_z}\sin^2\tfrac{\Omega_A t_1}{2}\sin\tfrac{\pi J t_1}{2} \end{aligned} \tag{1.13}$$

The terms in $\mathbf{A_x}$ and $2\mathbf{A_yX_z}$ cancel; the trigonometric relationship $\cos^2\theta + \sin^2\theta = 1$ may be used to cancel the dependence of the remaining terms on chemical shift. The above term is thus equal to

$$-\mathbf{A}_\mathbf{y}\cos\tfrac{\pi J\,t_1}{2} + 2\mathbf{A}_\mathbf{x}\mathbf{X}_\mathbf{z}\sin\tfrac{\pi J\,t_1}{2} \qquad (1.14)$$

Lastly, the effects of *J*-coupling are considered.

$$\xrightarrow{\pi J\,t_1/2} -\mathbf{A}_\mathbf{y}\left(\cos^2\tfrac{\pi J\,t_1}{2} - \sin^2\tfrac{\pi J\,t_1}{2}\right) + 2\mathbf{A}_\mathbf{x}\mathbf{X}_\mathbf{z}\left(\sin\pi J\,t_1\cos\tfrac{\pi J\,t_1}{2} + \cos\pi J\,t_1\sin\pi J\,t_1\right) \qquad (1.15)$$

Using the trigonometric relationships $\cos^2\theta - \sin^2\theta = \cos 2\theta$ and $2\sin\theta\cos\theta = \sin 2\theta$ simplifies the above expression to

$$-\mathbf{A}_\mathbf{y}\cos\pi J\,t_1 + 2\mathbf{A}_\mathbf{x}\mathbf{X}_\mathbf{z}\sin\pi J\,t_1 \qquad (1.16)$$

This final expression represents one doublet in the final spectrum: the first term ($\mathbf{A_y}$) is an in-phase doublet, while the second ($2\mathbf{A_xX_z}$) is an anti-phase doublet. The evolution in the t_1 period is evidently independent of Ω_A whilst depending on *J*, whereas that during t_2 will show the usual dependence on both *J* and Ω_A: the desired separation of *J*-coupling effects has been achieved.

This signal differs from the one in COSY in one fundamental respect. The amplitude of the *J*-resolved signal does not change as a function of t_1; its phase is what varies. This type of modulation is known as *phase modulation* in contrast to the *amplitude modulation* displayed by COSY. The advantage of this is that the sense of precession in t_1 can be determined without recourse to hypercomplex acquisition. The distinct disadvantage is that it is impossible to obtain purely absorptive lineshapes by any phasing procedure; the shape produced is known as a *phase twist*. This really must be displayed in absolute-value mode, and is a very broad line in comparison to a purely absorptive one. The resolution obtained is thus less than optimal.

1.7.3 Acquisition

The acquisition parameters used for *J*-resolved spectroscopy are somewhat different to those used for COSY. The indirect (F_1) dimension is a *J*-coupling domain, so its spectral width need be large enough only to cover the broadest multiplet

anticipated, say 30–50 Hz or so. To digitise this range at reasonable resolution (about 1 Hz would be more than adequate given the line broadening from T_2 relaxation *in vivo*) requires relatively few t_1 increments, perhaps 32. This means that a complete dataset can be acquired in considerably less time than for COSY. As discussed above, the sense of precession in the F_1 direction is inherent in the one set of FIDs, so no hypercomplex acquisition is required.

The linewidths obtained from a *J*-resolved experiment are intrinsically different in the two dimensions. In the F_2 dimension, the linewidth is the same as for a conventional 1D pulse-and-collect experiment, proportional to $1/T_2$*. In the F_1 dimension, however, the 180° pulse refocuses the line broadening caused by $\mathbf{B_0}$ field inhomogeneity, so the linewidth is proportional to $1/T_2$. This results in narrower lines in this dimension, particularly *in vivo*, where local magnetic susceptibility variation often means that $T_2 >> T_2$*.

An imperfect 180° pulse results in artefacts in the *J*-resolved spectrum arising from magnetisation that is not refocused by the pulse. The phase cycle EXORCYCLE[53] was designed to suppress such artefacts. It consists of incrementing the phase of the 180° pulse in 90° steps whilst alternating the phase of the receiver 0°, 180°, …. A multiple of four steps are required for proper suppression of the artefacts. Again, CYCLOPS may be superimposed to suppress quadrature artefacts in F_2 if needed; this would make the cycle sixteen steps long.

1.7.4 Processing

The weighting used on a *J*-resolved dataset is similar to the treatment of a 1D spectrum: there are no cross-peaks to differentially enhance, so an exponential filter (for example, 0.5 Hz in F_1 and 5 Hz in F_2 for *in vivo* data) is adequate. After Fourier transformation in each direction, the spectrum is often sheared by 45°. This ensures that the *J*-coupling multiplets are perpendicular to the chemical shift (F_2) domain. While the F_1 direction contains only *J*-coupling modulation, the F_2 direction contains both chemical shift and *J*-coupling modulation; the shearing transformation (usually called rotation) effectively removes the latter. What remains is a spectrum with the peaks distributed with chemical shift along the F_2 axis and the *J*-coupling multiplets spread symmetrically about this axis.

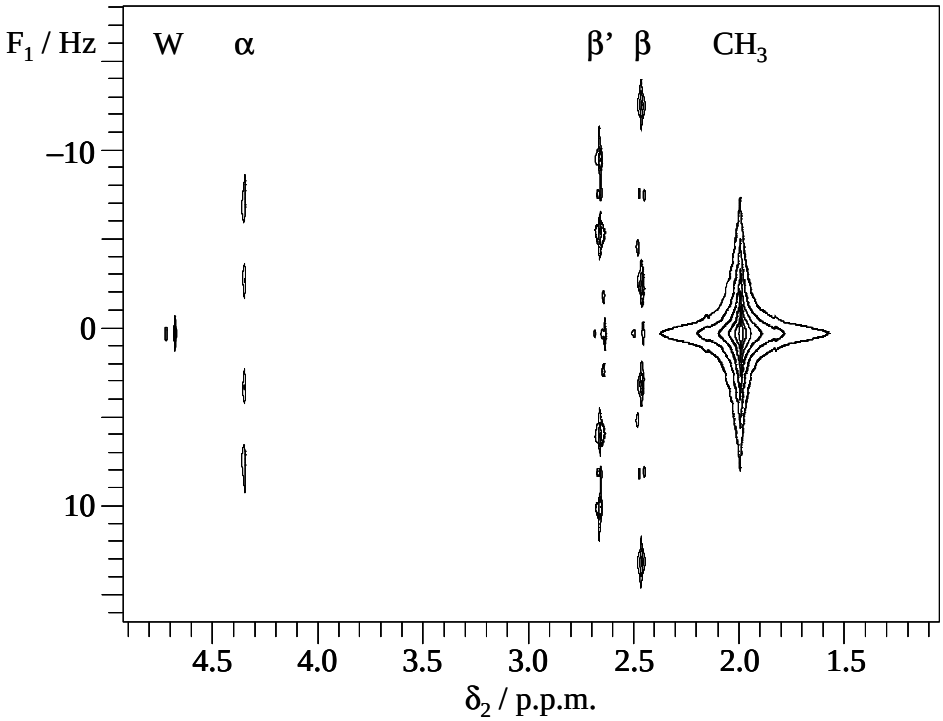

Figure 1.5: High-resolution *J*-resolved spectrum of NAA in D_2O at 9.4 T. Columns are labelled according to the protons originating their signal; W is unsuppressed water.

As a final step in processing, the spectrum may be symmetrized about the F_2 axis. This is more reliable than the equivalent symmetrization used for processing COSY spectra, probably because the peaks being compared are more closely related, being part of the same multiplet rather than a separate peak. Peaks cannot be lost as by the mechanism discussed for COSY. The problems with symmetrizing a *J*-resolved spectrum are from the shearing transformation. This causes relaxation broadening of the peaks to be at 45° to the axes rather than parallel to the F_1 axis. This means that the peaks are not perfectly symmetric and can give some signal loss on symmetrization.

1.7.5 Spectra

A *J*-resolved spectrum of *N*-acetyl aspartate (NAA; see structure in section 2.7) is shown in Figure 1.5. It shows the symmetry about the $F_1 = 0$ axis and the coupling patterns linked with each proton. The acetyl CH_3 peak at $\delta_2 = 2.0$ p.p.m. shows no coupling; each of the other NAA peaks is a doublet of doublets (the other three protons are in the aspartate group and are all *J*-coupled together). This is particularly obvious for the α-proton; the β-protons suffer rather from artefacts. The origin of

these is that the *J*-coupling between the two β-protons is high relative to the difference in their chemical shifts. The complete separation of *J*-coupling and chemical shift onto the two axes relies on the weak coupling approximation, that *J* is much less than the difference in chemical shift (expressed in Hz at the magnetic field used). When this approximation breaks down, extra peaks are observed between the desired ones, as is seen in the above spectrum.

There is nothing in the spectrum to indicate which proton is coupled to which other one, save the magnitude of the coupling constant. This is of marginal concern to potential application *in vivo*, where the concern is with identifying particular molecules from their "signatures" in a spectrum.

1.7.6 Summary

J-resolved spectroscopy is a two-dimensional pulse sequence designed to separate the effects of chemical shift and *J*-coupling onto the two axes of the 2D spectrum. The sequence refocuses chemical shifts during the t_1 period but permits *J*-modulation to remain. Thus, the spectrum contains only *J*-coupling effects on the F_1 axis; the F_2 axis contains both chemical shift and *J*-coupling effects, although the latter may be removed by a shearing transformation. Strong coupling, where it exists, causes a breakdown of the separation and extra peaks may be observed between the expected ones. The off-axis peaks are potentially more separated than peaks in a 1D spectrum, so this sequence may be of use *in vivo* for observing peaks from molecules not otherwise visible.

1.8 Outline

Chapter 2 outlines the methods used in the experiments reported in the remainder of the thesis. It details the spectrometers used and the probes used with them, the samples and their preparation. Further sections describe preparation of animals, extracts and solutions for NMR. The chapter concludes with the means used to assign peaks in spectra to specific groups of protons.

In Chapter 3, the various forms of computer simulation used to support the project are set out. A general discussion of the function of simulation precedes detailed accounts of the three main applications: programs to calculate the effect of arbitrary

pulse sequences on simple spin systems, COSY spectra for complex spin systems and to model the water suppression sequence WET to optimise its parameters. Each has its method and implementation described, and a sample application or results presented.

A description of the development of the novel pulse sequences at the heart of this thesis may be found in Chapter 4. Each sequence is dissected in detail, giving reasons for the choice of each component and the testing undergone, both *in vitro*, to evaluate the components individually and for comparison with existing techniques, and *in vivo*, to demonstrate the usefulness of the sequence in a realistic scenario. There is discussion on optimisation of the sequence parameters and on quantification of the spectra. Two sequences are covered: ISIS-COSY and ISIS-JRES.

Applications are the subject of Chapter 5, three in particular. Firstly, a study of the effect on metabolite concentrations in the rat brain of vigabatrin was undertaken—these are well documented, and this demonstrates the efficacy of ISIS-COSY to measure the *in vivo* concentrations of many metabolites simultaneously within a reasonable timescale. Secondly, an investigation into the possibility of detecting the presence of activated neutrophils in the brain using NMR was carried out. Results are shown from *in vitro* suspensions of activated human neutrophils and also *in vivo* in the treated rat brain. Thirdly, a demonstration of the ISIS-COSY sequence in the normal human brain is shown.

Finally, in Chapter 6, conclusions about the project are drawn: the usefulness of the different sequences developed and how they compare to existing techniques, with a mention of possible future applications.

Appendices are provided giving supplementary information: Appendix A shows high-resolution spectra for fifteen metabolites as a basis for assigning *in vivo* data, while Appendix B displays *post mortem* spectra used in the optimisation of ISIS-COSY and the comparison with VOSY-COSY. Appendix C contains a summary table of the possible assignment of many peaks found in an *in vivo* or extract spectrum, and Appendix D lists correction factors used in the quantification of ISIS-COSY spectra, to convert relative peak volumes into relative metabolite concentrations.

Chapter 2: Methods

2.1 High-field Phantom and In Vivo *NMR*

2.1.1 Spectrometer

The NMR spectrometer used for development of the techniques presented in this thesis, phantom testing and *in vivo* application was a Varian Inova. It was equipped with a 7.0 T vertical-bore magnet (Oxford Instruments) containing actively-shielded gradients combined with an 18-channel shim set (Magnex). The gradients were powered by two twin-channel audio amplifiers (Techron) and capable of providing 24 G/cm with a rise time of 100 μs. The system operates at a proton frequency of 300 MHz.

The spectrometer software was Vnmr version 6.1b. This was used for running the acquisitions, processing and displaying of all experimental data, volume integration and exporting spectra for presentation.

2.1.2 Probes

Two probes were used on this spectrometer, both homebuilt. The first was used for phantom studies, and also for early development using mouse brain (not presented here). It has an Alderman-Grant coil[54] 24 mm in diameter and 27 mm long for transmission and reception of r.f. signals. For *in vivo* work, a blanket heated by passing warm water through it is provided to maintain body temperature. A typical 90° rectangular pulse duration was 70 μs at 20 W power.

Metabolite	Concentration (mM) in solution		
	A	B	C
Creatine			20
Glutamate (sodium salt)		20	20
Glutamine		20	20
Lactate (lithium salt)	1000		20
Taurine			20
DSS		trace	
TSP			trace

Table 2.1: Composition of solutions used in development and testing of pulse sequences. DSS is sodium 2,2-dimethyl-2-silapentane-5-sulphonate; TSP is sodium 3-trimethylsilyl-1-propanoate; both are reference solutions.

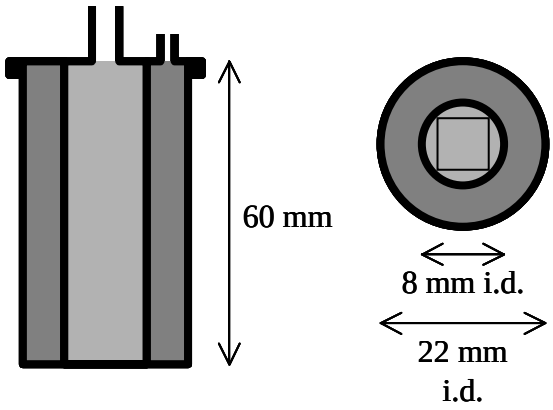

Figure 2.1: Two-compartment glass phantom used for testing localisation properties of pulse sequences. The outer compartment was filled with olive oil, the inner with water. The square box shows the size and position of the voxel selected for localisation.

The second probe was used for rat brain studies. It consisted of an actively-detuned coil pair. For r.f. transmission, an Alderman-Grant coil 34 mm in diameter and 44 mm long was used, whilst for reception, an 18 mm single-turn surface coil was employed, positioned on the top of the head, directly above the brain. This probe also had a similar blanket. A typical 90° rectangular pulse duration for the transmit coil was 160 μs at 20 W power.

2.1.3 Phantom Samples

Several phantom samples were used in the course of the work presented here. Most were dilute solutions of metabolites made up in deionised water and placed in glass tubes 18 mm in diameter and 150 mm long. The composition of three solutions is shown in Table 2.1. The pH of each was measured to be about 7.

For testing the localisation properties of pulse sequences, a glass two-compartment phantom was manufactured, as illustrated in Figure 2.1. The concentric cylinders were filled with oil and water as a crude model of the head.

2.2 High-resolution Solution and Extract NMR

2.2.1 Spectrometer

High-resolution NMR spectra were acquired on another Varian Inova spectrometer. It had a 9.4 T magnet (Oxford Instruments) and a standard 18-channel shim set. It was equipped with conventional accessories, including a temperature

controller and three gradient amplifiers (of which only the *z* was used, to drive the probe gradient coil). It operates at a proton frequency of 400 MHz.

The software was Vnmr version 6.0. This was again used for all aspects of data acquisition and processing.

2.2.2 Probe

The probe used was a Varian-supplied 5 mm inverse probe having an inner ^{1}H coil and an outer broadband coil (not used), with a further ^{2}H lock channel. It is also equipped with a single gradient coil in the *z* direction, and facilities for temperature regulation. A typical 90° rectangular pulse duration was 6 μs at 25 W power. The ability to spin the sample about the *z*-axis was not used.

2.2.3 Samples

Samples were prepared as solutions in D_2O with 1 mM TSP as reference (see sections 2.5 and 2.6). A volume of 0.8 ml was used, placed in a 5 mm thin-walled NMR tube.

2.2.4 Experimental Protocol

All the high-resolution results presented in this thesis followed the same experimental protocol. The sample was inserted pneumatically into the probe and allowed to reach experimental temperature (nominally 30°C; in practice, about 27°C as measured with a mercury-in-glass thermometer suspended in the magnet bore). The probe was tuned and matched and the deuterium lock established. The magnet was shimmed to a TSP linewidth of 0.8–1.4 Hz. The duration of a 90° pulse was found, then a series of inversion-recovery experiments with different inter-pulse delays was used to find the T_1 for the significant components of the sample. These were used to set the repetition time TR for the acquisitions—for the 1D spectrum, a TR of 15 s or 4 times the largest T_1 of interest (all peaks except water and TSP were deemed to be of interest), whichever was larger, was used. For 2D spectra, the TR used was half of this figure.

A 1D spectrum was acquired, with a 5 kHz spectral width centred at 5.0 p.p.m., using 16 transients preceded by 4 ‘dummy’ scans to establish a steady state. (For TR

Parameter	Unit	1-D	COSY		J-resolved
Spectral width	Hz	5k	3k x 3k		3k x 50
Transmitter offset from TSP	p.p.m.	5	3		3
Acquisition time	s	2	2		2
Repetition delay	s	15	7.5		7.5
Minimum multiple of T_1		4	2		2
Number of transients		16	2		4
Steady-state transients		4	4		4
Number of t_1 increments			320		64
Phase-sensitive acquisition			Yes		No
Water suppression		No	Yes		Yes
Total time	min	5	160.5 (2h 40m)		32.5
Line broadening (F2 dimension)	Hz	0	1	-	1
Line broadening (F1 dimension)	Hz		5	-	0.5
Sine bell centre (F2 dimension)	s	-	-	0.1	-
Sine bell centre (F1 dimension)	s		-	0.042	-
Display mode			Phased	Absolute	Absolute
Fourier number (F2 dimension)		32k	16k	2k	16k
Fourier number (F1 dimension)			1k	1k	512

Table 2.2: Summary of parameters used in high-resolution NMR experimental protocol.

~4T_1 the dummy scans are scarcely necessary as the magnetisation will relax virtually back to equilibrium between acquisitions; however, these extra scans will ensure the water peak (where T_1 ~ 15 s) is also in a steady state and thus of reduced intensity.) A 2 s acquisition time was used. For the typical TR of 15 s, this took 5 minutes. The water suppression used for the 2D spectra (a four-pulse WET sequence[55], see section 4.1.1.3; this is used to suppress residual water in the sample) was then optimised by varying the 90° water suppression pulse power to minimise the amplitude of the residual water peak. A 2D COSY spectrum was run with water suppression: 320 t_1 increments, 4 transients per increment (including phase-sensitive acquisition in the F_1 dimension by the hypercomplex method[49]) and 4 steady-state scans. The spectral width was 3 kHz in each dimension, centred at 3.0 p.p.m.. For a TR of 7.5 s, this took 2 hours 40 minutes. Finally, a 2D *J*-resolved spectrum was acquired: 64 t_1 increments, 4 transients per increment (not phase-sensitive) and 4 steady-state scans. The spectral width was 3 kHz in the F_2 dimension and 50 Hz in the F_1 dimension. With a 7.5 s TR, this took 33 minutes. The entire protocol, including set-up and calibration, took around 4 hours to complete.

The data were processed as follows. The 1D FID was zero-filled to 32k points then Fourier transformed with no apodisation. The COSY dataset was processed in

two ways: firstly, with a line broadening of 5 Hz in F_1 and 1 Hz in F_2, and zero filling to 1k x 16k points prior to Fourier transformation in each direction; secondly apodisation with a sine bell centred at (0.042 s, 0.100 s) in (F_1, F_2) and zero filling to 1k x 2k points prior to Fourier transformation in each direction. The former was presented as a phase-sensitive spectrum; the latter as a magnitude spectrum. These two processing methods were used to compare the effects of each on peak intensity: the first has minimal effect whilst the second is designed to enhance cross-peaks over diagonal peaks.

The *J*-resolved dataset was line broadened 0.5 Hz in F_1 and 1 Hz in F_2, zero filled to 512 x 1k points then Fourier transformed in each direction. It was rotated through 45° to ensure that the *J*-resolved multiplets were perpendicular to the F_2 axis, then symmetrized about this axis. It was presented as a magnitude spectrum. The parameters used in the protocol are summarised in Table 2.2.

2.3 Whole-body System

2.3.1 Spectrometer

The spectrometer used for human brain investigations, and phantom studies in preparation for this, was a Bruker Avance. It had a 2.0 T magnet (Oxford Instruments) with a 1 m diameter horizontal bore. The self-shielded gradients (Magnex) were capable of 2.5 G/cm with a 300 μs rise time, driven by MTS amplifiers. The r.f. amplifier had a peak power output of 1 kW.

The software consists of two parts: ParaVision (version 1.0.31), used for imaging, set-up and simple spectroscopy experiments, and X-win-NMR (version 1.0), used for more advanced spectroscopy experiments (such as the 2D experiments presented here) and processing.

2.3.2 R.F. Coil

A homebuilt 16-leg birdcage coil was used for both transmission and reception of the r.f. signal. It has an inner diameter of 25 cm. It is driven in quadrature for optimum efficiency: the amplifier output is split in two, the phase of one signal is shifted by $\pi/2$ and the two signals passed into the birdcage four legs apart. A typical 90° pulse power was 2 dB below maximum power for a 400 μs rectangular pulse, i.e.

800 W. Specific absorption rate (SAR) was monitored at all times by the r.f. "supervision" unit integral to the spectrometer.

2.3.3 Phantom

The phantom used was a glass sphere of 10 cm outer diameter filled with a 50 mM solution of creatine, taurine, *myo*-inositol and lithium lactate.

2.4 Animal Preparation

All experiments involving the use of animals were performed by trained personnel in accordance with Home Office regulations.

The animals used in the experiments presented in this thesis were all adult male Wistar rats, 170–230 g in mass. Anaesthesia was induced with 4% halothane in a 1:1 nitrous oxide: oxygen gas mixture. The rat was positioned in the probe and secured using a bite bar placed between the teeth. The anaesthetic line was taped to end close to the nose. The water blanket was wrapped round the rat's body and taped together and to the probe. The surface coil was secured directly above the centre of the brain. The probe was positioned in the magnet then the halothane turned down to 1–1.5% for maintaining anaesthesia.

If the brain was to be extracted for high-resolution NMR, the animal, whilst still under the anaesthetic, was killed by cervical dislocation and the brain rapidly excised and frozen in liquid nitrogen. It was stored at –80°C prior to extraction.

2.5 Extract Preparation

Perchloric acid (PCA) extracts were prepared from frozen brain tissue as follows. A percussion pestle and mortar were cooled to liquid nitrogen temperatures then used to crush the tissue. This was placed in a cryovial and returned to the liquid nitrogen dewar to cool again. An eppendorf tube was labelled, frozen and weighed, then about 200 mg tissue was added and the tube reweighed to calculate the exact mass used. To this, 1 ml of 6% PCA was added; the tube was vortexed to mix then placed on ice for a few minutes while other samples were prepared. A further 0.6 ml PCA was added, then the tube was centrifuged for five minutes at 4°C. The supernatant was pipetted off and neutralised with potassium hydroxide, forming a precipitate of insoluble

potassium perchlorate. The remaining solution was placed in a round-bottomed flask, which was partially immersed in liquid nitrogen to freeze the sample. The flask was then freeze-dried for several hours to remove the water, then stored at –20°C until needed. For spectroscopy, the powder was made up to a solution with D_2O and the pD adjusted to 7 (measured using an electronic pH meter looking for a pH of 6.4) with drops of dilute NaOD or DCl as necessary.

2.6 Solution Preparation

Solutions for high-resolution NMR were prepared as follows. 0.1 mMol of the compound was dissolved in 1.9 ml D_2O, then 0.1 ml of 20 mM TSP (sodium 3-trimethylsilyl-1-propanoate) added. This was shaken to ensure complete mixing. The pD of the solution was checked and corrected to pD = 7 with drops of dilute NaOD or DCl if necessary. This gives a solution 50 mM in the compound of interest and 1 mM in TSP. 0.8 ml of each solution was placed in a 5 mm thin-walled NMR tube for spectroscopy.

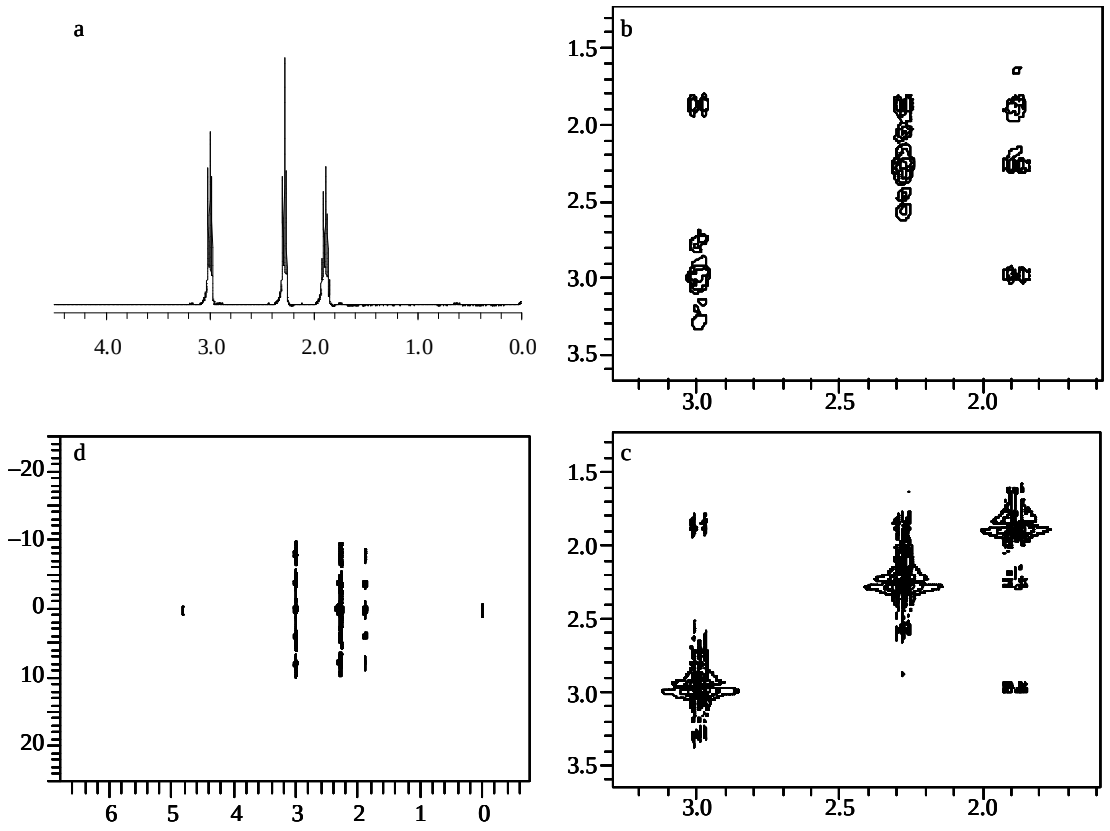

Figure 2.2: High-resolution spectra of GABA. (a) 1D pulse-and-collect spectrum; (b) COSY processed with line broadening; (c) COSY processed with sine bells; (d) *J*-resolved. Acquisition and processing parameters as described in section 2.2.4. The T_1 for the GABA protons was 2.5–3.5 s.

2.7 Spectral Assignment

Peaks were assigned in one- and two-dimensional spectra on the basis of their chemical shifts relative to the added reference compound (the TSP singlet at 0.00 p.p.m.) for *in vitro* spectra; *in vivo* spectra were referenced to the NAA methyl singlet at 2.02 p.p.m. or the creatine singlet at 3.02 p.p.m.. Assignment was from tables of reference data[56, 57] and from high-resolution NMR spectra recorded of individual metabolites. To the latter end, a series of spectra were recorded on a set of solutions (prepared as per section 2.6) of metabolites likely to be observable in ^{1}H NMR of the brain. Each spectrum was acquired and processed identically, according to the protocol set out in section 2.2.4, to provide a good basis for assigning *in vivo* spectra. A typical set of spectra (that for γ-aminobutryric acid, GABA) may be found in Figure 2.2; the complete series is in Appendix A.

The peaks in each of the spectra were assigned as far as possible to individual protons or proton groups and the connectivities and *J*-coupling constants measured. The results of this are presented below.

Molecule		**Protons**	**δ (p.p.m.)**	***J*-coupling constants (Hz)**	
L-Alanine	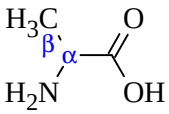	CH	3.76	α-β	7.3
		CH_3	1.47	β-α	7.3
Choline	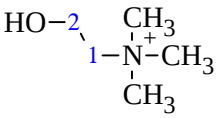	CH_3	3.20	-	
		1-CH_2	4.06	1-2	5.3
		2-CH_2	3.52	2-1	5.3
Creatine	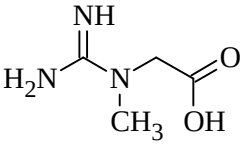	CH_3	3.03	-	
		CH_2	3.92	-	
GABA	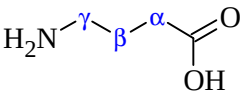	α-CH_2	2.29	α-β	7.7
		β-CH_2	1.89	β-α	7.7
				β-γ	7.7
		γ-CH_2	3.00	γ-β	7.7
D-glucose	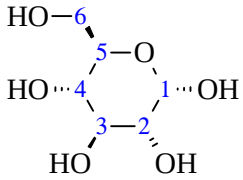	1-CH	5.2	1-2	3.7
		2-CH	3.54		
		3-CH			
		4-CH			
		5-CH	3.2		
		6-CH_2	4.6	6-5	8.0

Molecule		Protons	δ (p.p.m.)	*J*-coupling constants (Hz)	
L-glutamate	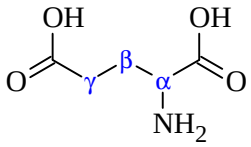	α-CH	3.74	α-β	7.2
		β-CH_2	2.1	β-α	7.2
				β-γ	8.5
		γ-CH_2	2.35	γ-β	8.5
L-glutamine	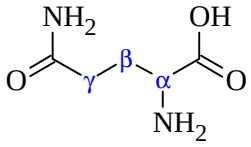	α-CH	3.76	α-β	6.5
		β-CH_2	2.13	β-α	6.5
				β-γ	8
		γ-CH_2	2.44	γ-β	8
***myo*-inositol**	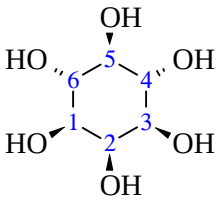	[1,3]-CH	3.52	[1,3]-2	2.8
				[1,3]-[4,6]	9.9
		2-CH	4.04	2-[1,3]	2.3
		[4,6]-CH	3.61	[4,6]-[1,3]	9.7
				[4,6]-5	9.7
		5-CH	3.26	5-[4,6]	9.3
L-Isoleucine		2-CH	3.66	2-3	4.0
		3-CH	1.97	3-2	4.0
				3-4	9.3
				3-4’	4.8
				3-6	7.0
	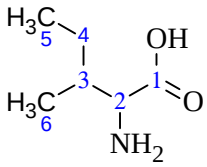	4-CH	1.26	4-3	9.3
				4-4’	13.4
				4-5	7.4
		4’-CH	1.47	4’-3	4.8
				4’-4	13.4
				4’-5	7.6
		5-CH_3	0.93	5-4	7.4
				5-4’	7.6
		6-CH_3	1.01	6-3	7.0
Lactate	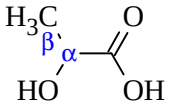	CH	4.10	CH-CH_3	7.5
		CH_3	1.33	CH_3-CH	7.3
L-Leucine	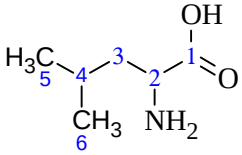	2-CH	3.72	2-3	7.0
		3-CH_2	1.72	3-2	7.0
		4-CH	1.72	4-[5,6]	7.0
		[5,6]-CH_3	0.98	[5,6]-4	7.0
L-Lysine		2-CH	3.74	2-3	6.1
		3-CH_2	1.89	3-2	6.1
				3-4	7.1
	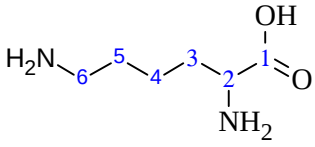	4-CH_2	1.47	4-3	7.1
				4-5	7.5
		5-CH_2	1.72	5-4	7.5
				5-6	7.6
		6-CH_2	3.02	6-5	7.6

Molecule		Protons	δ (p.p.m.)	*J*-coupling constants (Hz)	
L-NAA	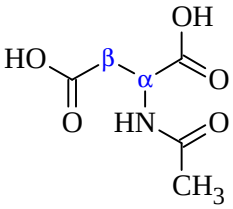	α-CH	4.38	α-β	10.2
				α-β’	4.1
		β-CH	2.48	α-β	10.2
				β-β’	15.8
		β’-CH	2.68	β’-α	4.0
				β’-β	15.7
		CH_3	2.02	-	
Taurine	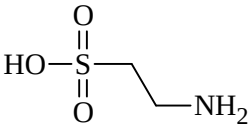	S-CH_2	3.42	CH_2-CH_2	6.7
		N-CH_2	3.25	CH_2-CH_2	6.7
L-Valine	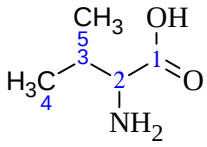	2-CH	3.60	2-3	4.3
		3-CH	2.26	3-2	4.4
				3-4,5	7.0
		4-CH_3	0.98	4-3	7.0
		5-CH_3	1.03	5-3	7.0
Vigabatrin		α-CH	2.23	α-β	7.7
				α-β’	7.3
				α-α’	15.5
		α’-CH	2.28	α’-β	6.5
				α’-β’	8.3
				α’-α	15.5
		β-CH	1.90	β-α	8.3
				β-α’	6.5
				β-β’	13.7
				β-γ	8.8
	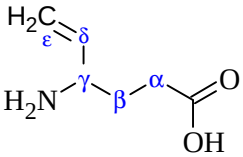	β’-CH	2.01	β’-α	6.5
				β’-α’	8.2
				β’-β	13.7
				β’-γ	5.4
		γ-CH	3.70	γ-β	8.8
				γ-β’	5.4
				γ-δ	8.0
		δ-CH	5.82	δ-γ	8.1
				δ-ε	17.1
				δ-ε’	10.6
		ε-CH	5.41	ε-δ	17.0
				ε-ε’	0.8
		ε’-CH	5.43	ε’-δ	10.6
				ε’-ε	0.8

Table 2.3: Structures, chemical shifts, assignment and *J*-coupling constants for some metabolites observable in ^{1}H NMR of the brain. Vigabatrin is included as it is a drug that was used in a study (see section 5.1).

This table forms the basis for the assignment and eventual quantification of the 2D *in vivo* spectra. An alternative version, sorted by peak frequency, is provided in Appendix C. The two frequencies of a COSY cross-peak can be looked up in the table for a candidate molecule containing two proton groups that resonate at these frequencies that are *J*-coupled together.

Chapter 3: Simulation

3.1 Why Simulate?

Simulation has been used in two principal manners for the work of this thesis: firstly, to calculate NMR spectra and evaluate pulse sequences during development, and secondly, to derive parameters to minimise the residual water signal at the end of a WET water suppression sequence.

There are several advantages to using a simulation program in the development and testing of a pulse sequence. Many non-idealities of experimental testing are circumvented by simulation. Instrumental and sample imperfections are removed, so no time is needed for shimming and calibrating pulse powers, etc. There are no signal/noise ratio difficulties, nor limits on transmitter power or digitiser resolution. The sample properties are precisely known and are completely uniform. No relaxation losses occur during the sequence, so the effects of relaxation may be studied separately from sequence performance.

Simulation does suffer from some drawbacks, however. Very complex cases can take prohibitively long to calculate; it is not possible to model *in vivo* data satisfactorily as the anatomical structure is far too intricate for approximation using cuboids. There is also the potential to simulate spectra that are so ideal that implementation on a real spectrometer would be unrealistic.

The WET water suppression method minimisation is a straightforward calculation in simulation, but would be tedious to optimise experimentally: four independent flip angles (i.e., pulse powers) to systematically vary and find the water signal minimum. This procedure would be prone to experimental error and finding local, rather than global, minima in the function.

3.2 Arbitrary Sequences on Simple Spin Systems

3.2.1 Program

The first program is a general-purpose simulation designed to calculate the effects of an arbitrary pulse sequence on the magnetisation of a simple AX spin system, and to calculate the FID(s) that would be recorded. This can subsequently be transformed

Category	Specification
Spin System	2 *J*-coupled spin I = ½ nuclei and 1 isolated spin I = ½ nucleus
Nuclear Properties	Resonance offset, *J*-coupling constant, relative concentration
Sample Properties	Point sample, or position and dimensions of up to 9 cuboids and relative concentrations of nuclei in each
General Properties	Any spectral width, resonance frequency and gradient strength; up to 1024 complex points per FID, and up to 1024 FIDs for 2D NMR
Pulse Sequence	Up to 32 consecutive events, i.e., pulses, delays, incrementing delays (for 2D NMR), crushers or double-quantum filters
Pulses	Any shape, phase, power, offset, duration, x-, y- and z-gradients. Can be 'presence cycled' for ISIS-type sequences
Relaxation	Not included
Additional Facilities	Display of density matrix after one or all events in pulse sequence; recording any magnetisation component instead of FID ($\mathbf{I}_x + i\mathbf{I}_y$ component)

Table 3.1: Capabilities of the NMR pulse sequence simulation program.

into one or two-dimensional NMR spectra. The main capabilities of the program are summarised in Table 3.1.

The program was written in Fortran 90 and compiled for Solaris 2.6 running on the departmental server (a Sun E450 with two 300 MHz processors and 512 Mb RAM). It is around 2200 lines of code long, with a further 500 lines in library modules. The entire program was written from scratch with the exception of a matrix diagonalisation routine[58]. Development of this simulation program was necessary as the available simulation programs were aimed at generating a pulse-and-collect spectrum from a complex sample, whereas the requirement was for a program to generate spectra for simple spin-systems and arbitrary pulse sequences. No program was known with the capability of simulating spatially diverse samples, magnetic field gradients, shaped pulses and 'presence cycling', all of which are necessary for the development of localised 2D sequences.

3.2.2 Method

The program simulates the free-induction decay of a *J*-coupled AX pair of spin I = ½ nuclei using the results of density matrix theory[59]. This permits the effects of chemical shifts (equivalently, transmitter offsets or $\mathbf{B_0}$ field gradients) and *J*-coupling to be included, but not relaxation.

The state of the spin system at a given time t is given by the wavefunction $\Psi(t)$. This may be expressed as a linear combination of eigenfunctions of the Zeeman Hamiltonian:

$$\Psi(t) = \sum_{i=1}^{4} c_i(t)|i\rangle, \tag{3.1}$$

where c_i is the coefficient of the eigenfunction $|i\rangle$ in the wavefunction. The density matrix $\sigma(t)$, which is a complex 4 x 4 matrix for an AX spin system, is defined as

$$\sigma(t) = \overline{|\Psi(t)\rangle\langle\Psi(t)|} = \sum_{p=1}^{4}\sum_{q=1}^{4} \overline{c_p(t)c_q^*(t)}\,|p\rangle\langle q|, \tag{3.2}$$

where $|\Psi(t)\rangle$ is the wavefunction of the state and $|p\rangle$, $|q\rangle$ are eigenfunctions of the Zeeman Hamiltonian; the overbar denotes an average over the sample. The diagonal elements of this matrix represent the populations of the four energy levels of the AX system, while the off-diagonal elements represent coherent superposition ("coherence") of the states.

The evolution of a density matrix under the influence of effects such as *J*-coupling and radio-frequency irradiation (a pulse) may be found using the *Liouville-von Neumann* equation[59]

$$\frac{\mathrm{d}\sigma(t)}{\mathrm{d}t} = -i[H(t), \sigma(t)], \tag{3.3}$$

which, if the Hamiltonian *H* is time-independent, has solutions given by

$$\sigma(t_+) = \exp\{-iHt\}\sigma(t_-)\exp\{+iHt\}. \tag{3.4}$$

This equation may be used to simulate the effects of a pulse by setting *H* to be the matrix representation of the Hamiltonian for the pulse and *t* equal to the duration of the pulse. This changes the density matrix before the pulse, $\sigma(t_-)$, into that after the pulse, $\sigma(t_+)$. A complex r.f. pulse (e.g., a sinc or sech pulse) is simulated by breaking the shape down into many (e.g., 128) small steps during which the Hamiltonian is approximately constant, and applying the above equation for each step.

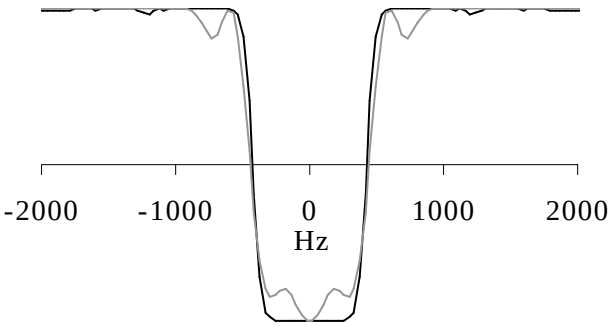

Figure 3.1: Simulation of the inversion profile of a sech (black line) and 5-lobe sinc (grey line) pulse. Simulation parameters: spin system, spin-½; point sample; 90° pulse duration, 100 μs; points per FID, 1; take trace with $\mathbf{I_z}$; arrayed parameter, transmitter offset (128 points, range 5 kHz, output as 2D). The sech pulse duration was 20 ms at 15% maximum power; the sinc pulse 5 ms at 22.5% power. Each line took about 5 s to simulate. This parameter set measures the z-magnetisation at 128 points over the range ± 2500 Hz directly; no processing (line broadening, Fourier transform, etc.) was required to generate the figure.

Calculating the effect of a pulse sequence may be achieved as follows. Firstly, $\sigma(0)$ is set to the equilibrium magnetisation. The effect of each pulse and delay is then successively calculated, using the density matrix resulting from each calculation as the starting point for the next one. Thus, the density matrix at the end of the entire pulse sequence, $\sigma(t_f)$, may be found.

The FID may be derived from this by noting that the point at time t is given by

$$\mathrm{F}(t) = \mathrm{Tr}\{\sigma(t)(\mathbf{A}^+ + \mathbf{X}^+)\}, \tag{3.5}$$

where $\mathrm{Tr}\{\mathbf{x}\}$ denotes the trace of **x**, and $\mathbf{A}^+ + \mathbf{X}^+ = (\mathbf{A}_\mathbf{x} + \mathbf{X}_\mathbf{x}) + i(\mathbf{A}_\mathbf{y} + \mathbf{X}_\mathbf{y})$. The FID is calculated by taking the trace (equation (3.5)) using the density matrix for the start of the FID, $\sigma(t_f)$, then using equation (3.4) to calculate the density matrix some time Δt later using the Hamiltonian for free precession. This is repeated until the desired number of points has been found. The time interval Δt is chosen according to $\Delta t = 1/\mathrm{SW}$, where SW is the spectral width required.

3.2.3 Applications

One of the principal uses of simulation is in independent evaluation of different elements of the sequence. For example, the performance of one particular pulse shape can be compared with that of another for inverting one region of the spectrum: Figure

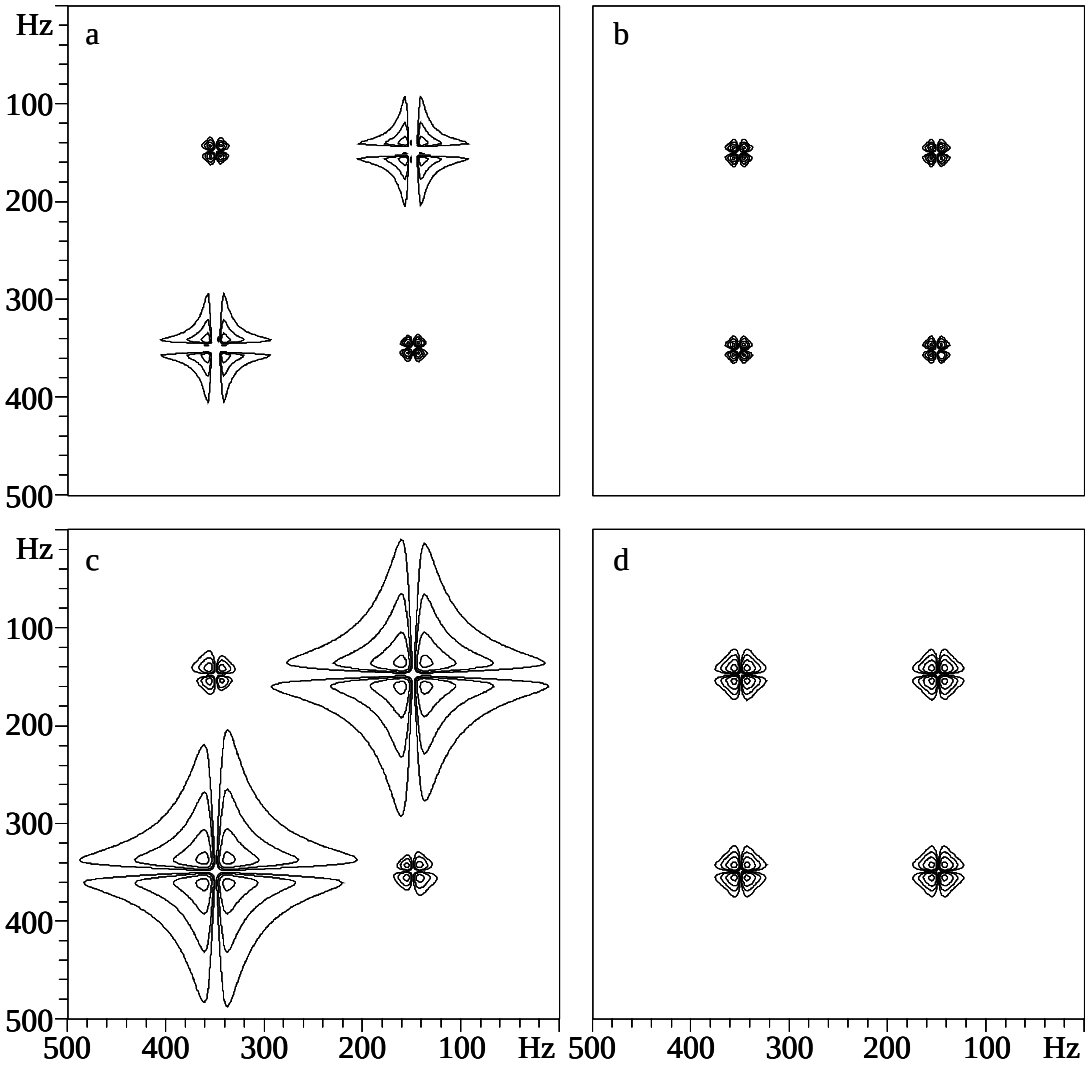

Figure 3.2: Simulation of COSY (a, c) and DQF-COSY (b, d) spectra with two different linewidths. Simulation parameters: AX spin system, resonance offsets 150 and 350 Hz, J_{AX} 10 Hz, spectral width 500 Hz, 128 x 128 complex points, 0.01 μs 90° pulse duration. Processing parameters: 20 Hz (a, b) or 50 Hz (c, d) line broadening, zero-filled to 256 x 256 complex points.

3.1 shows a comparison of the performance of an adiabatic full-passage sech pulse with a 180° sinc pulse for inverting a region of a spectrum. This effect can be seen in isolation from factors that would complicate the situation, such as relaxation. When combined with the ability to examine each element of the density matrix before and after the pulse, this is a powerful technique for carefully evaluating pulse shapes or other elements of a pulse sequence.

The performance of whole sequences can also be tested using this program. For instance, the simulated COSY and double-quantum-filtered (DQF) COSY spectra of an AX spin system at two different linewidths are shown in Figure 3.2. (The

linewidths are applied by multiplying the two-dimensional FIDS by an exponentially decaying function prior to their Fourier transformation.) The example shown here demonstrates the considerably greater linewidth of the dispersive COSY diagonal peaks as compared to the absorptive DQF-COSY diagonal peaks and how, even with a very high linewidth, the DQF-COSY peaks remain well separated. This might influence a decision as to which of the sequences was more appropriate for a given application. Further examples of the use of this simulation program may be found in Figure 1.3 and the section on testing composite pulses (4.2.2).

Simulation has the advantage over theoretical prediction such as product-operator calculations that it can include a wider range of situations, for example strong *J*-coupling, finite length pulses, shaped pulses, and so on. This gives it a greater applicability and means it better approximates the experimental situation. A further benefit is that signal intensity can be measured from the spectrum for comparison between pulse sequences, and with experimental spectra.

3.3 COSY for Complex Spin Systems

Many factors influence the peak intensity observed in a COSY spectrum. The antiphase nature of the cross-peaks makes their magnitude particularly sensitive to linewidth. The sine-bell processing typically used for COSY spectra (see section 1.6.5) means that the T_2 relaxation time and *J*-coupling parameters also have a bearing.

To account for these factors in quantifying compounds from the intensities of their cross-peaks in a COSY spectrum, it is simplest to compare the cross-peak volumes from the sample of interest with either those from spectra recorded on single metabolite phantoms and processed identically or simulated data. To this latter end, a program was needed that was capable of generating COSY datasets for the small molecules responsible for cross-peaks present in experimental spectra. The general-purpose program described in section 3.2 above is not suitable as it is restricted to an AX spin system, whereas the molecules needed are all more complicated than this.

3.3.1 Method

The method of simulation used is fundamentally similar to the general-purpose program. The same density matrix equations are used, adapted for the different spin systems. The calculation is specifically optimised for COSY spectra: for instance, the Hamiltonian for each period of free precession (t_1 and t_2) on each t_1 increment is identical, so this is calculated and diagonalised in advance to save repetition of effort.

The main difference from the other simulation program is the capability to work with spin systems (all spin I = ½) of arbitrary complexity. This requires that the density matrices can be of different size depending on the molecule of interest. In place of the 4 x 4 matrices used for an AX system, *n* x *n* matrices are used, where

$$n = 2^{NumSpins}. \tag{3.6}$$

Thus, for moderate or large spin systems, the density matrices become enormous. The rate-limiting step in the calculations is matrix multiplication, for which the time taken is approximately proportional to n^3, so the simulation rapidly becomes prohibitively slow as the complexity of the spin system increases. The size of the density matrices can be reduced by including magnetic equivalence factoring[60] and separating non-coupled spins into a separate calculation (e.g., the methyl protons in NAA are not coupled to the aspartate protons); however, it was felt that the extra time spent including these in the program would not be repaid in terms of reduction of total simulation time for the molecules of interest, which all have six or fewer protons visible by NMR *in vivo*.

3.3.2 Program

The fact that the program is dedicated to COSY spectra alone greatly simplifies its structure. Only two loops are required—for t_1 and t_2 increments—as there is no allowance for magnetic field gradients, shaped pulses, etc. The major complication in comparison to the program outlined in section 3.2 is the variable-sized density matrices. It was felt that this would be more straightforward to code in *Mathematica*[61] than a conventional programming language, because the facilities for generating and handling arbitrary-sized matrices are considerably more advanced.

```
Iz[k_] := DiagonalMatrix[Table[Sign[Sin[2 Pi (i - 1/2)/2^k]], {i, 1, 2^NumSpins}]] / 2;

Ix[k_] := Table[Which[
    j - i == 2^(k-1), (Sign[Sin[2 Pi (i - 1/2)/2^k]] + 1) / 2,
    i - j == 2^(k-1), (Sign[Sin[2 Pi (j - 1/2)/2^k]] + 1) / 2,
    True, 0], {i, 1, 2^NumSpins}, {j, 1, 2^NumSpins}] / 2

Iy[k_] := I Table[Which[
    j - i == 2^(k-1), (Sign[Sin[2 Pi (i - 1/2)/2^k]] + 1) / 2,
    i - j == 2^(k-1), -(Sign[Sin[2 Pi (j - 1/2)/2^k]] + 1) / 2,
    True, 0], {i, 1, 2^NumSpins}, {j, 1, 2^NumSpins}] / 2
```

Listing 3.1: *Mathematica* functions defining elementary density matrices $\mathbf{I}_x$, $\mathbf{I}_y$ and $\mathbf{I}_z$ for each nucleus *k*.

The first step is the definition of the spin system. This is given by a composite parameter, as in the following example:

```
lactate = {
  "AX3",
  {{"A", 4.1}, {"X", 1.33}},
  {{"AX", 6.9}}
  };
```
(3.7)

The first line gives the spin system (a shorthand form for "AXXX"); the second, the chemical shifts in p.p.m.; the third, the *J*-coupling constants in Hz. The letters "A" and "X" are arbitrary; no distinction is made between strongly coupled ("AB") and weakly coupled ("AX") systems as the simplifications arising from assuming weak coupling are never used. A function is used to convert this parameter into the required *n*-long list of resonance offsets and *n* x *n* array of *J*-coupling constants.

Next, the basic matrices representing $\mathbf{I}_x$, $\mathbf{I}_y$ and $\mathbf{I}_z$ for each nucleus are constructed using the formulae shown in Listing 3.1. Other matrices are built up from these, for example

```
IzIz[k_, l_] := Iz[k] . Iz[l];
```
(3.8)

```
DelayHam := 2 π Sum[Offsets[[k]] Iz[k], {k, 1, NumSpins}] +
  2 π Sum[Sum[Jcon[[k, l]] (IzIz[k, l] + IxIx[k, l] + IyIy[k, l]),
      {l, k + 1, NumSpins}], {k, 1, NumSpins - 1}]

PulseHam := DelayHam + ω Sum[Ix[k], {k, 1, NumSpins}]
```

Listing 3.2: *Mathematica* functions defining Hamiltonians for delays and pulses. **Offsets** and **Jcon** are the arrays prepared from the spin system definition; ω is the $\mathbf{B_1}$ field strength in rad s^{-1}.

and

```
Mz := Sum[Iz[k], {k, NumSpins}];.
```
(3.9)

Two further functions yield the Hamiltonians appropriate for pulses and delays (see Listing 3.2).

The portion of code responsible for simulating the COSY sequence begins by calculating the pulse and delay Hamiltonians, diagonalising them and hence finding the propagator $\mathbf{P} = \mathrm{e}^{-i\mathbf{H}t}$ and its inverse for each, where t is the duration. These are rounded to machine-precision real numbers for speed of later calculations. The magnetization after the first pulse, $\mathbf{P}_{\mathrm{pulse}}{}^{-1}.\mathbf{M_0}.\ \mathbf{P}_{\mathrm{pulse}}$, is found as it is common to each t_1 increment. Finally, a table is constructed that is the 2D FID by, for each row, applying the second pulse then a series of delays, calculating the signal amplitude at each point, exactly as in eq. (3.5) above:

```
trw = N[Mp];
 nσ = ppinv . N[M0] . pp;
 Table[nσt = ppinv . nσ . pp; nσ = dpinv . nσ . dp;
  Table[f = Tr[nσt . trw]; nσt = dpinv . nσt . dp; f, {i2, 1, np}], {i1, 1, np}]]
```
(3.10)

Figure 3.3 (Overleaf): Composite simulated spectrum of nine metabolites found in the mammalian brain. Each was simulated with parameters matching the experimental ones used for *in vivo* spectroscopy: spectrometer frequency, 300 MHz; spectral width, 2 kHz centred at 3.5 p.p.m.; 90° pulse duration, 80 μs; 110 x 160 complex points; 14 x 14 Hz line broadening; sine bell centred at 27.5, 40 ms in t_1, t_2; zero-filled to 256 x 256 points; absolute-value mode.

where **pp** is the pulse propagator, **dp** the delay propagator and **ppinv** and **dpinv** their inverses. (This function was subsequently extended to calculate non-square 2D FIDs for direct comparison with experimental datasets.)

This 2D FID may be exported for external processing, or treated within the *Mathematica* environment. In the latter case, it is multiplied point-by-point with a 2D sine bell or other weighting function, has zeros appended in each dimension to interpolate the spectrum, then Fourier transformed. The resultant spectrum is displayed in one of the built-in formats such as a contour or surface plot.

Further functions were written to integrate the 2D spectrum around each peak with quantification of experimental spectra in mind.

3.3.3 Application

The program was used to produce a reference spectrum for comparison with *in vivo* brain spectra for quantification purposes. The spin system was defined for each metabolite to be included in the model (e.g., lactate as shown in eq. 3.7) and a COSY FID generated using the same parameters as experimental spectra (spectrometer frequency, number of points, spectral width). Each FID was multiplied by an exponentially decaying function in both t_1 and t_2 directions to broaden the lines to typical *in vivo* values (14 Hz), then processed using the same sine bell weighting as used for *in vivo* data. Each spectrum was colour-coded, leading to the composite spectrum shown in Figure 3.3. (N.B. only the $N(CH_3)_3$ moiety of choline was included in the model, not the chain protons.)

The individual spectra were integrated around each peak by summing the intensity of each point that fell within a square of side Δf centred on the peak, where $\Delta f = 0.1$, 0.2 or 0.4 p.p.m.. Three values were used to attempt to include as great a proportion of the intensity in each peak as possible, whilst excluding any from other nearby peaks. For each peak, the intensity thought to be most accurate was chosen (generally that for $\Delta f = 0.2$ p.p.m. unless this was elevated due to another peak within this range, when $\Delta f = 0.1$ p.p.m. was used). This was corrected to proton concentration (assuming the metabolite itself has unit concentration) as follows:

Metabolite	δ_1 (p.p.m.)	δ_2 (p.p.m.)	Correction Factor
Choline	3.19	3.19	0.11
Creatine	3.91	3.91	0.50
NAA	2.02	2.02	0.33
NAA	2.70	2.52	1.91
GABA	2.31	1.91	1.79
GABA	3.02	1.91	1.81
Taurine	3.40	3.20	1.18

Table 3.2: Correction factors for a selection of peaks to correct peak volumes to metabolite concentrations.

$$I_c = \frac{9}{I_{Cho}} I_r, \tag{3.11}$$

where I_c, I_r and I_{cho} are the corrected, raw and raw choline intensities respectively. The choline peak was chosen as a reference for this correction as only one singlet is present in the spectrum, so contamination from other peaks is impossible, and the proton concentration represented in the peak is exactly known as there is no *J*-coupling present.

The desired output from the simulation is a set of correction factors to multiply experimental peak volumes with to correct for *J*-coupling and processing effects to give values that more closely reflect concentrations of metabolites in the brain—only T_1 and T_2 relaxation remain unaccounted for. These correction factors may be obtained by taking the reciprocal of the corrected intensities I_c defined above. A representative sample is listed in Table 3.2; a complete listing may be found in Appendix C.

3.4 WET modelling

The WET water suppression sequence[55] consists of a series of narrow bandwidth r.f. pulses, typically four, to excite the water peak, interspersed with time periods during which crusher gradients are applied to dephase any transverse magnetisation generated by the pulses. It is optimised for a particular sample type (i.e., a particular range of T_1 relaxation times and variations in the $\mathbf{B_1}$ field) by varying the flip angles of the pulses, and optionally the time periods between them, to minimise the residual water signal. Four pulses were used following Ogg *et al.*[55]; there is little practical benefit in using more, as the influence of the first pulse is then negligible in any

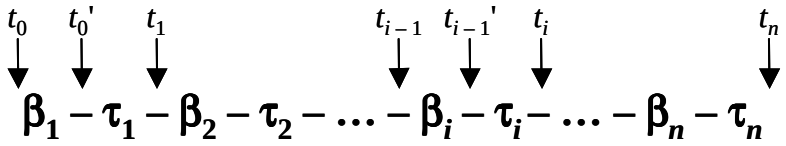

Figure 3.4: Generic WET water suppression pulse sequence.

practical application, whilst using three pulses is marginally inferior in suppression performance to four.

3.4.1 Method

The WET sequence is shown diagrammatically in Figure 3.4. The pulses are represented by the flip angles β_i, and the time periods between them by τ_i. Certain times are labelled above the axis and are referred to below.

The aim of the optimisation procedure is to minimise the residual water *z* magnetisation at $t = t_n$, where the excitation of the FID starts. The calculation assumes the pulses are perfect and of zero duration; this is reasonable provided that τ_i is set to the time between the centre of pulse *i* and pulse *i* + 1. It is further assumed that the crushers are of sufficient strength to completely dephase all transverse magnetisation, implying that the calculation can neglect this entirely.

The calculation proceeds as follows: the initial water magnetisation $M_z(0)$ is set to 1, so all magnetisations are expressed as fractions of this initial magnetisation. The effect of pulse *i* is given by

$$M_z(t_{i-1}) \xrightarrow{\beta_i} M_z(t_{i-1}') = M_z(t_{i-1}) \cos f\beta_i , \tag{3.12}$$

where

$$f = \frac{\left|\mathbf{B_1}\right|}{\left|\mathbf{B_1^{nominal}}\right|}, \tag{3.13}$$

and the effect of delay *i* by

$$M_z(t_{i-1}') \xrightarrow{\tau_i} M_z(t_i) = 1 - \left\{ \left(1 - M_z(t_{i-1}')\right) e^{\frac{-\tau_i}{T_1}} \right\}. \tag{3.14}$$

```
wet[flipfac_, t1_, flips_, taus_] :=
 Module[{i, n, nf, nt, mag},
 nf = Dimensions[flips][[1]];
  nt = Dimensions[taus][[1]];
  n = Min[nt, nf];
  mag = 1;
   Do[
      mag = (1- ( 1 - mag Cos[flips[[i]] flipfac Degree]) Exp[-taus[[i]] / t1]);
   , {i, n}];
 If[nf == nt, mag, -2] (* Return -2 as error is parameter lists are different length *)
 ]
```

Listing 3.3: Function to calculate the residual magnetisation after a WET water suppression pulse sequence.

```
rmswetrange[flr_, t1r_, flips_, taus_] :=
√(Sum[wet[distrib[f, flr], distrib[t, t1r], flips, taus]^2, {f, flr[[3]]}, {t, t1r[[3]]}]
                                  flr[[3]] t1r[[3]])
```

Listing 3.4: Function to average residual magnetisation over a range of T_1 and f.

Appling these two equations sequentially for each pulse and delay yields the final magnetisation $M_z(t_n)$. The calculation is repeated for a range of T_1 relaxation times and $\mathbf{B_1}$ field variations f, and a mean residual magnetisation found. This mean residual is then minimised as a function of the flip angles β_i, and optionally the time periods τ_i. The calculation gives the optimal set of flip angles $\{\beta_i^{best}\}$ for use in the pulse sequence.

3.4.2 Implementation

The algorithm was implemented on *Mathematica*. The flip angles and delays are stored as lists, $\{\beta_1, \beta_2, \ldots, \beta_n\}$ and $\{\tau_1, \tau_2, \ldots, \tau_n\}$. A function was developed to use the above algorithm to calculate the residual magnetisation after the WET sequence defined by these flip angles and delays, shown in Listing 3.3. It accepts four parameters as input: the lists of flip angles and delays, the water T_1 and the ratio of the actual $\mathbf{B_1}$ field to the nominal value (f in eq. 3.13); the return value is the residual magnetisation, or –2 as an error if the two lists are of different length.

A further function (shown in Listing 3.4) is used to calculate the root mean square (r.m.s.) residual over a range of T_1 and f values. The parameters to this are the flip angles and delays as before, and the ranges of T_1 and f over which to calculate the r.m.s. residual. Each of these is described by a three-part list {*min*, *max*, *npoints*}, where *min* and *max* are the smallest and largest values to consider, and *npoints* is the

T_1 range	β_1(°)	β_2(°)	β_3(°)	β_4(°)
2.9 s	94	92	82	146
0.5–3.0 s	88	99	82	161

Table 3.3: The optimal flip angles β_1– β_4 for the four-pulse WET water suppression sequence, to the nearest degree. For minimisation parameters, see text.

number of points in the range to sample. This function is the one that it is desired to minimise to produce the optimum water suppression. The intrinsic function **`FindMinimum`** is used for this purpose, for example

```
FindMinimum[ rmswetrange[ {.9,1.1,9}, {.5,3.,9}, {b1,b2,b3,b4},
        taudelays], {b1,90}, {b2,90}, {b3,90}, {b4,90}]
```
(3.15)

which finds the optimum flip angles b1–b4 (starting the search at 90° for each) for $|\mathbf{B_1}|$ from 90% to 110% of nominal, and T_1 between 0.5 and 3.0 s. Nine sample points are used for each. It is assumed that **`taudelays`** has already been set to the desired list of four delays, e.g., {0.025, 0.025, 0.025, 0.025} for four equal delays of 25 ms. The results are returned in the form {0.00697308, {b1→81.3232, b2→102.809, b3→62.1915, b4→168.057}}. The first number is the minimum of the function; the optimal flip angles b1–b4 (in degrees) follow.

3.4.3 Result

Two situations were modelled using the above functions. The first was designed to correspond to a metabolite solution *in vitro*; the second, rodent brain *in vivo*. The parameters used were as follows: τ_1–τ_4 = 25.1 ms (the sum of the water suppression pulse and crusher used experimentally, see section 4.1.1.3), $|\mathbf{B_1}|$ = 90% to 110% of nominal in 9 steps, T_1 = 2.9 s for the first case (typical of the T_1s measured for metabolite solutions), and 0.5 to 3.0 s in 9 steps for the second (a reasonable range to cover T_1 values *in vivo* at 7 T[43, 62]). The optimal flip angles as calculated for the two sample types are listed in Table 3.3.

These flip angles can be used to calculate the residual magnetisation for any combination of T_1 and f, to show the low sensitivity of the suppression efficiency to these parameters. The results of this simulation are shown graphically in Figure 3.5. Note that over the optimised range (actual flip angle = 81–99°; T_1 = 0.5–3.0 s (*in vivo*)

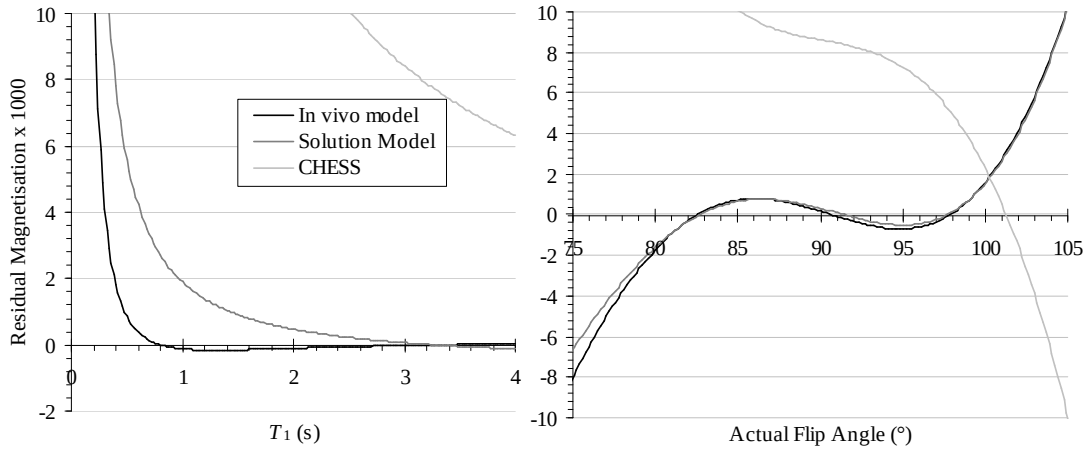

Figure 3.5: Calculated residual *z* magnetisation at the end of a four-pulse WET sequence optimised for *in vivo* (black line) and solution (medium grey line) situations, shown as a function of the water T_1 (left graph) and actual flip angle (right). For comparison, the values for a 3 CHESS pulse suppression sequence are shown in light grey.

or 2.9 s (solution model)), the calculated residual magnetisation is less than 0.1% of the total water magnetisation.

Both WET sequences show superior suppression compared to a 3-pulse CHESS scheme. This may be principally assigned to the higher flip angle of the last pulse. With CHESS, the magnetisation after the last pulse is approximately zero; T_1 relaxation after the last pulse during the crusher gradient causes the recovery of around 1% of the signal (for a T_1 of 2.9 s and an inter-pulse gap of 25.1 ms). In the WET sequences, the magnetisation after the third pulse is nearly zero; T_1 relaxation during the following delay also permits recovery of about 1% of the signal. The fourth pulse largely inverts this to –1%; during the final delay, this relaxes back to around zero. For this range (± 1%), the T_1 relaxation curve is very close to linear, so the residual magnetisation is very small.

Experimental implementation of these WET sequences is, unfortunately, unlikely to produce such good suppression. The performance of the finite-length selective pulses used will be less predictable than the perfect instantaneous pulses used in the model. The crusher gradients will be less than totally effective. As a result of all these, it would not be expected to achieve the 1000:1 suppression factors predicted by this model. The *in vitro* testing is presented in section 4.1.2.3. Human application is discussed in section 5.3.

Chapter 4: Development

The aim of the sequences developed is to overcome some of the spectral crowding issues discussed in the introduction with the use of 2D NMR techniques adapted from existing high-resolution ones. They must allow localisation of the signal and offer good water suppression to ensure maximal information from the molecules of interest. The localisation should avoid the use of spin or stimulated echoes for the reasons set out in section 1.5. Two similar sequences were developed and are discussed in detail below.

4.1 ISIS-COSY

The first sequence is a localised COSY[26-28] sequence. COSY is a simple 2D pulse sequence, but gives spectra that are relatively sparse as the peaks are spread over two chemical shift dimensions. It is relatively robust, having low sensitivity to mis-set pulse flip angles (important *in vivo* where $\mathbf{B_1}$ field inhomogeneities make it impossible to produce a uniform 90° pulse across the whole sample). It is well-characterised, meaning that things such as typical artefacts and methods to suppress them are established. COSY is discussed at length and the mechanism described in section 1.6.

4.1.1 Pulse Sequence

The new sequence, dubbed ISIS-COSY, achieves the three primary functions (water suppression, localisation, COSY excitation) in a modular manner within the pulse program. A fourth module, outer-volume suppression, is also included to improve the efficiency of the localisation. The sequence is shown in Figure 4.1. All pulse durations and bandwidths mentioned below are for the implementation of the sequence on the 7 T spectrometer. Variations for the 2 T whole-body system are discussed in section 5.3.1.

4.1.1.1 Localisation

Localisation of the NMR signal without the need to form echoes is provided by the standard ISIS sequence[22], using three orthogonal slice-selective 180° inversion pulses followed by a non-selective 90° pulse to excite observable magnetisation. Eight transients are recorded, one with each combination of presence/absence of each

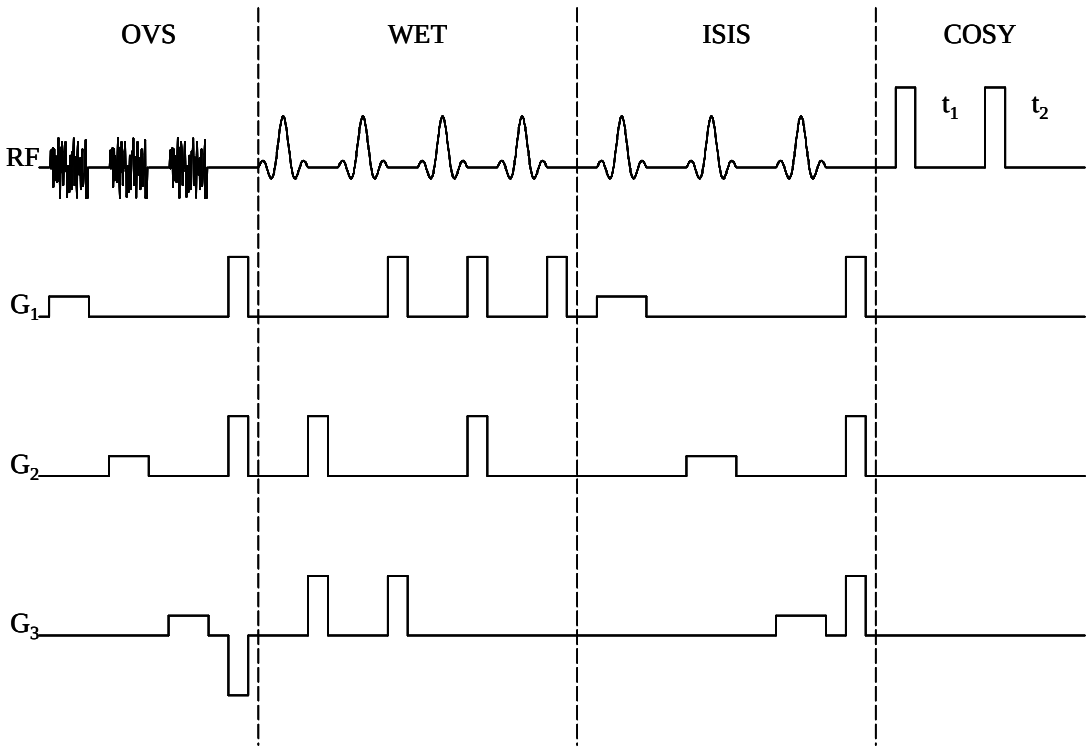

Figure 4.1: The ISIS-COSY pulse sequence. OVS is outer-volume suppression.

180° pulse. These are combined, by modulating the receiver phase, in such a way that the resultant signal arises from within the selected region only. The acquisition order of the transients was chosen to minimise outer-volume contamination[63]. The principal advantage of this sequence is that the magnetisation is maintained on the *z*-axis until the acquisition period, except for brief periods during the pulses. This approach therefore reduces *J*-modulation and T_2 relaxation effects to an absolute minimum, making ISIS the ideal localisation scheme for two-dimensional experiments.

The inversion pulses employed were adiabatic full-passage hyperbolic secant (sech) pulses[64-67], (512 points calculated with $\mu = 5$ and $\beta = 400\ s^{-1}$), selected for good slice profile and insensitivity to variations in the $\mathbf{B_1}$ field. A duration of 4 ms was used, giving an inversion bandwidth of approximately 4 kHz.

4.1.1.2 Outer-Volume Suppression

The localisation in ISIS is reliant on subtracting one transient from another in which the magnetisation from the region of interest has the opposite sign. Where this region is small compared to the remainder of the sample within the coil, this can cause a range of problems, as the recorded signal is the small difference between a number

of large transients. Firstly, any small variation in the amplitude of any transient causes a relatively large change in the calculated signal from the voxel, causing potential contamination problems. Secondly, dynamic range difficulties arise: the signal from the entire sample is large whilst that from the voxel is relatively small; the receiver gain must be sufficiently low to permit digitisation of the whole signal, so relatively little range is available for the voxel signal. For example, if the voxel volume is 1% of the outer volume, only 650 or so levels of a 16-bit (65536-level) receiver can be used for the voxel signal. The problems would clearly be lessened if the intensity of the outer-volume signal were reduced: the subtraction errors would be attenuated and the receiver gain could be increased such that the voxel signal is digitised using more of the available levels.

Outer-volume suppression is therefore included as in the OSIRIS extension to ISIS[68]: this consists of 3 pseudo-random noise pulses[69] in the presence of orthogonal gradients, whose excitation profile is designed to randomise outer-volume magnetisation whilst leaving that within the region of interest unperturbed. Each pulse consists of 512 points, with a total duration of 20 ms and a bandwidth of 26.7 kHz, of which the central 10% is unaffected. The width of this middle window is matched to the inversion width of the ISIS sech pulses by using a lower gradient strength for the noise pulses than the sech pulses.

4.1.1.3 Water Suppression

The proton NMR spectrum of the brain is dominated by the water peak, since the concentration of protons in water (~100 M) is thousands of times greater than in a typical metabolite (~10 mM). In order to observe the metabolites, it is necessary to reduce the water signal to a significantly lower level. Many methods have been proposed to achieve this[55, 70-84], including frequency-selective excitation[55, 79-81] or refocusing[76], selective inversion and a delay[77, 78] and presaturation of the water signal[82-84]. The most useful methods *in vivo*, selected for low power deposition and minimum distortions in the baseline, are WEFT[77, 78], a frequency-selective inversion pulse followed by a delay to permit recovery of the water signal to its null point, and CHESS[80], a selective excitation pulse followed by a crusher gradient, usually repeated three times. The WEFT method requires the same water magnetisation at the start of each iteration of the pulse sequence which in this application, due to the ISIS

T_1 range	β_1(°)	β_2(°)	β_3(°)	β_4(°)
2.9 s	94	92	82	146
0.5–3.0 s	88	99	82	161

Table 4.1: The optimal flip angles β_1– β_4 for the four-pulse WET water suppression sequence, to the nearest degree.

inversion pulses, would require full relaxation between each acquisition. This may be restrictive for *in vivo* applications.

For this reason, the method chosen for water suppression is based on CHESS. It is an improved version, known as WET[55], which allows for T_1 relaxation during the pulse sequence and for inhomogeneity in the $\mathbf{B_1}$ field. This consists of a train of narrow bandwidth r.f. pulses which selectively excite the water peak, interleaved with crusher gradients which dephase the transverse magnetisation generated (see Figure 3.4). For this sequence, four pulses are used. The flip angles of these pulses are numerically optimised for a particular sequence and sample type to provide the best suppression over a range of values of transmitter field ($\mathbf{B_1}$) and water longitudinal relaxation time (T_1) values. The optimisation is discussed at length in section 3.4 and the results for a typical *in vitro* and *in vivo* sample shown, duplicated in Table 4.1 for convenience.

The pulses used were 15 ms five-lobe sinc pulses, giving a bandwidth of 400 Hz. A 10 ms crusher gradient was used. Together with 100 μs gradient rise-time, this gives 25.1 ms between pulses—the figure used as τ_1–τ_4 in the optimisation.

4.1.1.4 Excitation

The final component in the pulse sequence is the excitation of the observed magnetisation. A conventional $90° - t_1 - 90°$ COSY[26-28] sequence was used (for a general discussion of COSY, see section 1.6). This was rendered phase-sensitive in the F_1 dimension using the hypercomplex method. For comparison, 'N'- and 'P'-type gradient-selected COSY sequences[85, 86] were also implemented. The pulses were hard rectangular pulses, about 95 μs in duration for rat brain work, and 80 μs for *in vitro* experiments, in either case optimised to give the maximum signal for each sample.

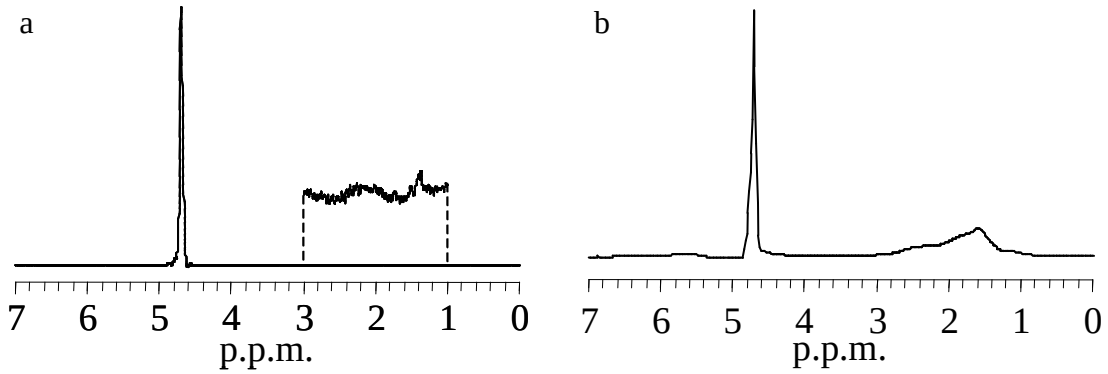

Figure 4.2: Spectra from the two-compartment phantom with water in the inner compartment and olive oil in the outer. (a) ISIS spectrum from a 5 x 5 x 5 mm^3 voxel in the inner compartment. Inset: vertical scale x 100. Note the absence of contamination from outer-volume lipid signals, demonstrating excellent localisation. (b) Same, but acquired with *x*-gradient set to zero, so signal comes from a 5 x 5 mm^2 column along the *x*-axis. Note the large lipid signals at 1-3 p.p.m. and 5-6 p.p.m.. The OVS was not used in either case.

4.1.1.5 Phase Cycle

The phase cycle used is as discussed in section 1.6.4. The *in vivo* acquisitions used 64 transients per t_1 increment, 32 for each half of the hypercomplex dataset, i.e. 4 per ISIS step. This implies that axial peak suppression is included but that only half of the CYCLOPS cycle is present. Quadrature artefacts were not detected on the spectrometers used, so this fact does not present any difficulties.

4.1.2 *In vitro* Testing

4.1.2.1 Localisation

The localisation was evaluated using the two-compartment phantom described in section 2.1.3 and illustrated in Figure 2.1. A 5 x 5 x 5 mm^3 voxel was selected in the centre, as illustrated in the figure, and a spectrum recorded using just the localisation module with a 90° excitation pulse. There is approximately 8500 mm^3 oil in the active region of the coil, all of which is outside the selected voxel. Nevertheless, there is no evidence of contamination of fat in the spectrum, even when multiplied by two orders of magnitude (see Figure 4.2a), demonstrating excellent localisation. For contrast, the gradient amplitude on the *x*-axis was set to zero and another spectrum obtained, now arising from a line along the *x*-axis with a 5 x 5 mm^2 square cross section, which contains about 300 mm^3 oil. This showed considerable contribution from the oil (see

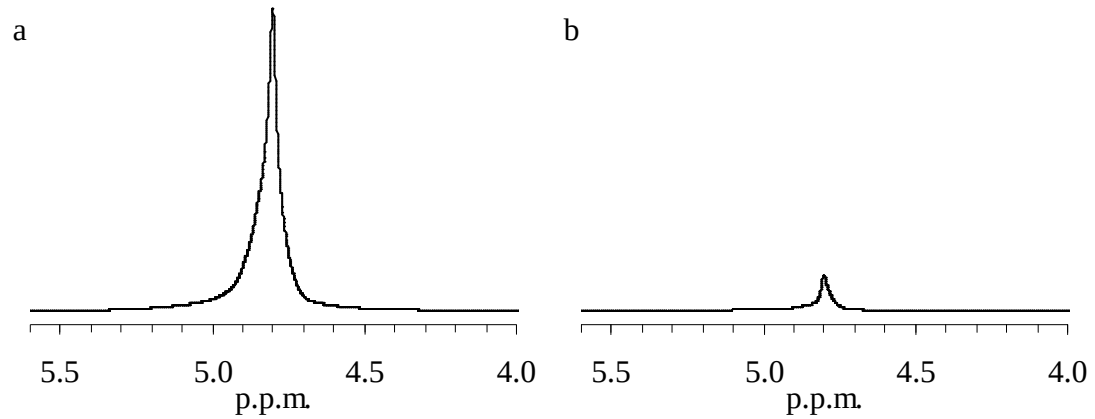

Figure 4.3: The effectiveness of the outer volume suppression module demonstrated by recording two spectra, one with OVS off (a) and one with it on (b); in both cases, the water suppression and the ISIS localisation were off. Voxel: 5 x 5 x 5 mm^3 in centre of tube. Acquisition parameters for each spectrum: 32 transients, 5 kHz spectral width, 15 s repeat time; total time 10 minutes. Processing parameters: 2 Hz line broadening.

Figure 4.2b). Such a signal from a relatively smaller volume of oil merely emphasises the absence of contamination in the first spectrum.

4.1.2.2 Outer-Volume Suppression

The OVS module suppression was tested by recording spectra without the ISIS localisation. A 5 x 5 x 5 mm^3 voxel was selected in the centre of an 18 mm diameter tube of water. With the water suppression also turned off, a spectrum was recorded both with and without outer-volume suppression, and the intensities of the water peak compared. The ratio of the two showed a ten-fold reduction in the outer-volume signal (see Figure 4.3a), thus reducing contamination from outside the selected voxel.

4.1.2.3 Water Suppression

Experimental comparison of WET with three CHESS pulses showed that slightly better suppression was afforded by WET. Perhaps more importantly, the water suppression pulse power needs little or no calibration for each new sample: the power required is a constant fraction of the 90° pulse power measured over the entire sample.

To test the water suppression, ISIS spectra were recorded both with and without water suppression on a phantom containing sodium glutamate and glutamine with DSS as a marker (sample B in Table 2.1). The resulting spectra can be seen in Figure

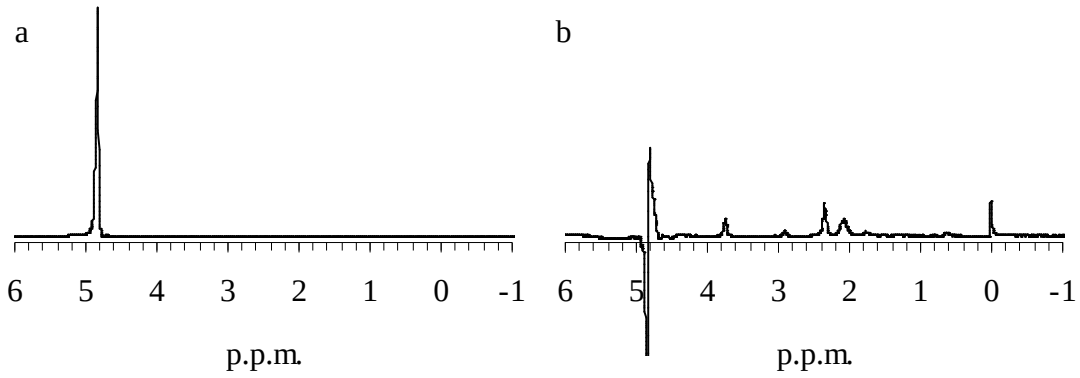

Figure 4.4: The effectiveness of the water suppression demonstrated by recording two spectra, one with WS off (a) and the other with it on (b). Sample: solution B from Table 2.1. Voxel, acquisition and processing parameters as for Figure 4.3. The vertical scale for the water-suppressed spectrum is 300 times that of the other.

4.4. The relative intensities of the water peaks (calculated as the root mean square of the intensity between 5.5 and 4.5 p.p.m.) is approximately 400:1. Such a reduction in the amplitude of the unwanted signal is extremely beneficial: it enables a significantly higher receiver gain to be used, with all the benefits this brings (see discussion in section 4.1.1.2); the problem of metabolite peaks being lost on the 'tails' of the water peak is also largely eliminated.

4.1.2.4 COSY

The COSY module was tested initially without water suppression on a sample of 1 M lithium lactate in water. This test was designed to verify the functioning of the COSY component without the need for fine-tuning of the other modules. The high concentration of the lactate anion means that it can be observed easily even in the presence of unsuppressed water. A typical COSY spectrum acquired from an 8 x 8 x 8 mm^3 voxel placed in the middle of the sample is illustrated in Figure 4.5. This shows the characteristics of a COSY spectrum: along the diagonal $\delta_1 = \delta_2$, the normal one-dimensional spectrum appears (a doublet at 1.33 p.p.m and a quartet at 4.10 p.p.m., see Appendix A), whilst off this diagonal (for example at (δ_1, δ_2 = 4.1, 1.3 p.p.m.) cross-peaks appear correlating *J*-coupled protons (in this case, the α- and β-protons of the lactate anion). The large band of noise along δ_1 = 4.8 p.p.m. is t_1 noise associated with the large water peak. This is caused by fluctuations of the recorded signal between t_1 increments (due to environmental variations, instrumental instabilities, drift in the magnetic field, etc.) that introduce

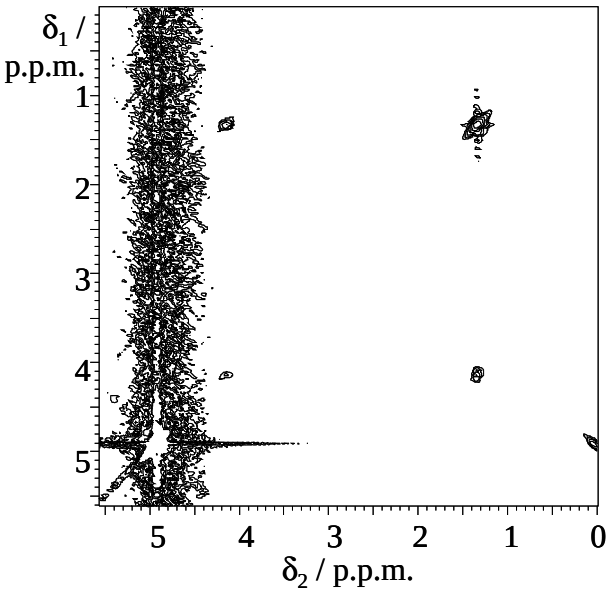

Figure 4.5: Localised COSY spectrum of 1 M lithium lactate in water. Voxel: 8 x 8 x 8 mm^3 in centre of tube. Acquisition parameters: 32 transients, 400 t_1 increments, 3 kHz spectral width in each dimension; total time 7¼ hours. Processing parameters: sine bell centred at 55 ms in each dimension, absolute-value mode.

modulations not intrinsic to the experiment; after Fourier transformation, they are manifest as t_1 noise.

4.1.2.5 Whole Sequence

A further test was performed on a sample containing a mixture of compounds typically observed in ^{1}H NMR spectra of the brain, at concentrations of the order of their occurrence there (solution C in Table 2.1). This test was done to assess the quality of spectra that could be obtained from a phantom broadly similar in concentration to a brain within the time constraints imposed by *in vivo* work, limiting acquisitions to around two or three hours. The spectrum recorded is shown in Figure 4.6. This has an excellent signal/noise (S/N) ratio, with good resolution of the peaks. For example, the S/N for both the lactate cross-peak at 1.3, 4.1 p.p.m. and the taurine cross-peak at 3.2, 3.4 p.p.m. is 320:1.

4.1.3 Animal Testing

After the *in vitro* testing, the next stage of development was evaluation of the pulse sequence in animal brain. This was initially done *post mortem*, then later followed up with *in vivo* experiments in anaesthetised animals.

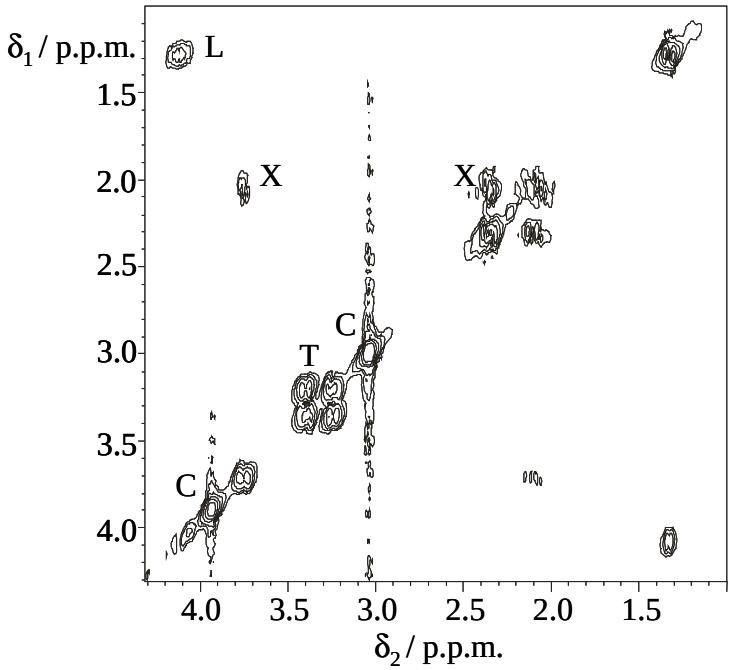

Figure 4.6: ISIS-COSY spectrum of mixed-metabolite phantom to demonstrate the feasibility of *in vivo* application in a reasonable timeframe. Cross-peaks are labelled as follows: L, lactate; X, glutamate/glutamine; T, taurine; C, creatine diagonal peaks. Voxel: 8 x 8 x 8 mm^3 in centre of 18 mm diameter x 150 mm long tube. Acquisition parameters: 16 transients, 128 t_1 increments, 2 kHz spectral width in each dimension, 5 s repetition time; total acquisition time 2 hours 50 minutes. Processing parameters: sine bell centred at t_1, t_2 = 35, 70 ms, absolute-value mode.

4.1.3.1 Post Mortem

The first animal tests of the sequence used mice. Several experiments were performed to gain experience with the sequence and improve acquisition and processing techniques. However, the small size of a mouse brain (typical voxel size restricted to less than about 3 x 6 x 3 mm^3) makes signal/noise a critical issue: in a typical ISIS-COSY spectrum taking around 2 hours, cross-peaks could be observed only from lactate, taurine and *myo*-inositol (see Figure 4.7).

For this reason, further work used the rat. Significantly larger voxels may be placed within the brain (e.g., 6 x 9 x 5 mm^3), so the signal/noise is much better.

A typical experimental protocol for rat brain studies following positioning of the rat in the probe in the magnet consisted of tuning and matching the probe (both volume and surface coils), performing a global shim, measuring the 90° pulse duration and the water resonance frequency. The transmitter offset was adjusted to set the water on resonance and a coronal gradient-echo image acquired (TR 0.2 s, t_E 5 ms,

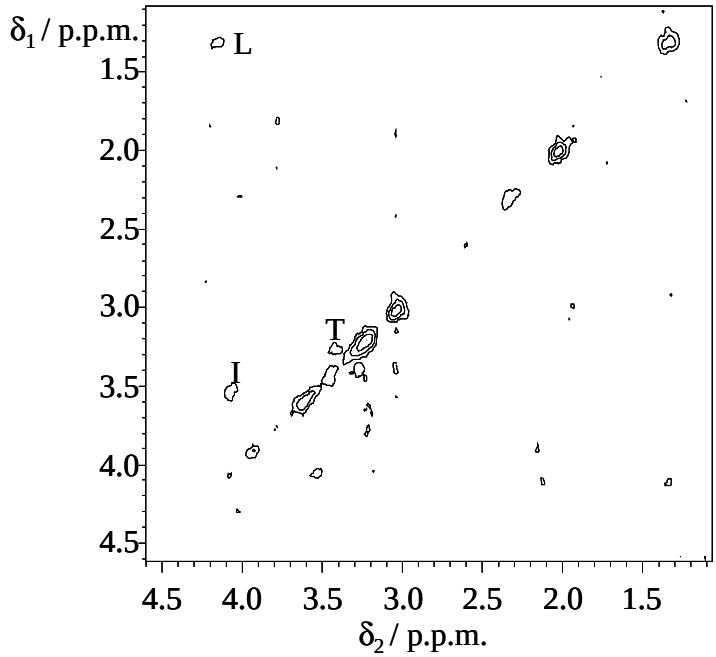

Figure 4.7: ISIS-COSY spectrum of *post mortem* mouse brain. Voxel: 6 x 2.75 x 3 mm^3 in centre of brain. Acquisition parameters: 16 transients per t_1 increment, 256 t_1 increments, 2 s TR, 2 x 2 kHz spectral width; total time, 2¼ hours. Processing parameters: 12 Hz resolution enhancement, 0.07 s sine bell in each dimension; absolute-value mode.

4 x 4 cm field of view, 1 mm slice thickness, 128 x 128 data points, 30 s total acquisition time). This was used to position a sagittal slice along the mid-line for another image (same parameters).

Next, a series of nine coronal slices 1 mm apart were positioned to cover the entire front of the brain and a multislice image set acquired. These were used to position a

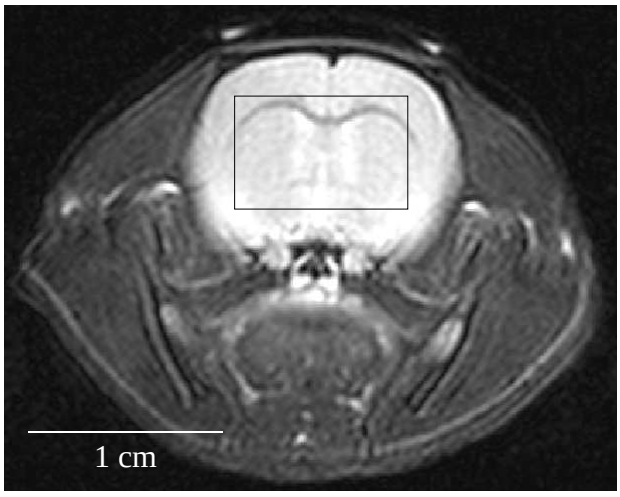

Figure 4.8: Fast spin-echo image of rat brain. Acquisition parameters: see text. Processing parameters: zero-filling to 1024 x 1024 points.

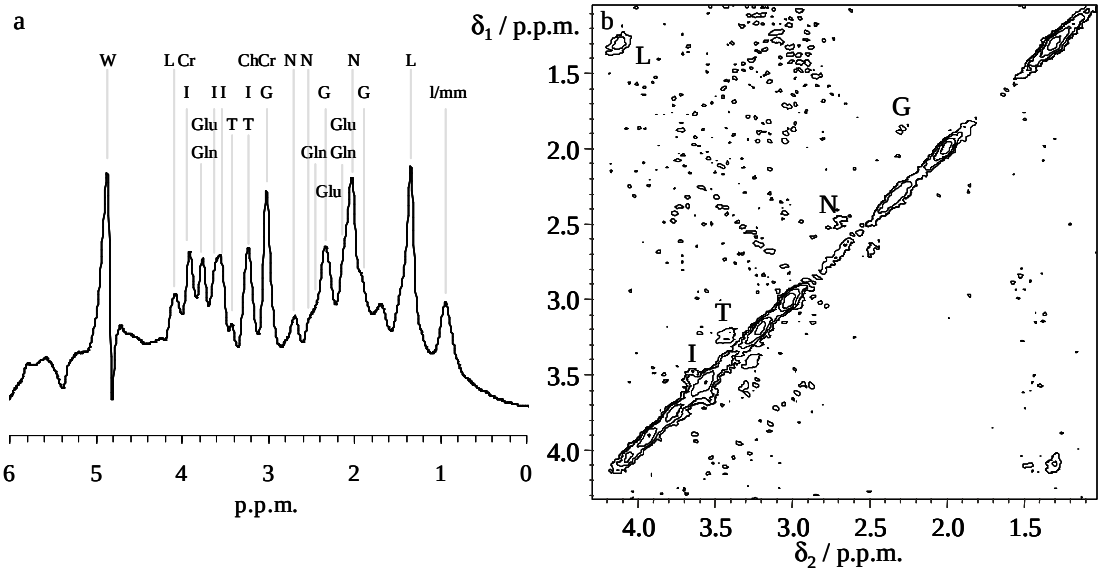

Figure 4.9: Spectra of *post mortem* rat brain. Key: W, unsuppressed water; L, lactate; Cr, creatine + phosphocreatine; Ch, choline; N, NAA; I, *myo*-inositol; G, GABA; l/mm, lipids/macromolecules; Glu, glutamate; Gln, glutamine; T, taurine. (a) ISIS. Acquisition parameters: 450 transients, 2 kHz spectral width, 2 s repetition time; total time, 13 minutes. Processing parameters: Lorentz-to-Gauss transform (10 Hz resolution enhancement, 0.035 s Gaussian weighting). (b) ISIS-COSY. Acquisition parameters: 16 transients, 128 t_1 increments, 1.8 kHz spectral width in each dimension, 3 s repetition time; total time, 1¾ hours. Processing parameters: sine bell centred at t_1, t_2 = 0.035, 0.07 s; absolute-value mode. The band of noise between $\delta_2 \sim 3$ and 4 p.p.m. is t_1 noise (see section 1.6.4) associated with the more intense diagonal peaks.

voxel for spectroscopy and to ensure that the corners of the box did not encounter regions of the head with poor local magnetic field homogeneity (such as near the sinuses) or the skull. For some animals, in order to show more structural detail, a final T_2-weighted coronal image was acquired through the centre of the voxel (fast spin echo, 7 echoes per FID, TR 3 s, t_E 18 ms, 3.5 x 3.5 cm field of view, 2 mm slice thickness, 128 x 126 data points, 2 transients, 108 s total acquisition time). An example of such an image is shown in Figure 4.8.

The voxel was shimmed using single-shot excitation by a STEAM sequence[25] (TR, 2 s; t_E, 40 ms; t_M, 50 ms). The S/N was measured for a one-transient STEAM spectrum (i) using the Alderman-Grant coil for transmit and receive, and (ii) using the surface coil to receive. This was to confirm correct functioning of the surface coil. The linewidths were also compared in the two cases. Typical values were about 1800:1 and 2200:1 for the S/N and about 14 Hz for the linewidths.

The final preparatory stage was the set-up of the ISIS sequence. The 90° pulse duration for the voxel was found. The transmitter frequency for the slice-selective pulses in the OVS and ISIS modules was offset by 500 Hz so that the chemical shift displacement of the voxel is such that the metabolite peaks arise from the best-shimmed region of the brain. Such an offset places peaks around 3.0 p.p.m. in this position. (Since the inversion pulses had a bandwidth of approximately 4 kHz, this offset moves the voxel ⅛ its length in each direction; for a typical 6 x 9 x 5 mm^3 voxel, the displacement will be approximately 0.75, 1.125, 0.625 mm in the three dimensions.) The water suppression was then turned on and the power of the pulses optimised for minimum residual water signal. Lastly, the receiver gain was maximised subject to not overflowing the ADC.

Spectra were then recorded: first, a 1D ISIS then a 2D ISIS-COSY. An example of each, prior to fine-tuning the acquisition parameters for the ISIS-COSY (as described in section 4.1.4), may be found in Figure 4.9. *Post mortem* studies were used for this optimisation of the sequence and for comparison with VOSY-COSY (section 4.1.4).

4.1.3.2 Anaesthetised

The last stage of testing the pulse sequence was application in live, anaesthetised rats. The experimental protocol was the same as for *post mortem* studies, using the parameters determined from them as optimum. Including a 15-minute 1D ISIS spectrum and a two-hour 2D ISIS-COSY acquisition, the entire protocol from administration of anaesthetic to finishing acquisition took about 3½ hours. The experiment was repeated several times to gain an idea of repeatability and to build up a small database of control animals before undertaking studies involving interventional treatment.

A typical pair of spectra from a live rat brain is illustrated in Figure 4.10. Of particular interest is the superior quality of these spectra compared to earlier *post mortem* experiments owing to subsequent optimisation of acquisition parameters.

4.1.4 Optimisation and Comparison with VOSY-COSY

Many experiments were performed to optimise the performance of the ISIS-COSY pulse sequence. A selection of these are described below. Some were carried

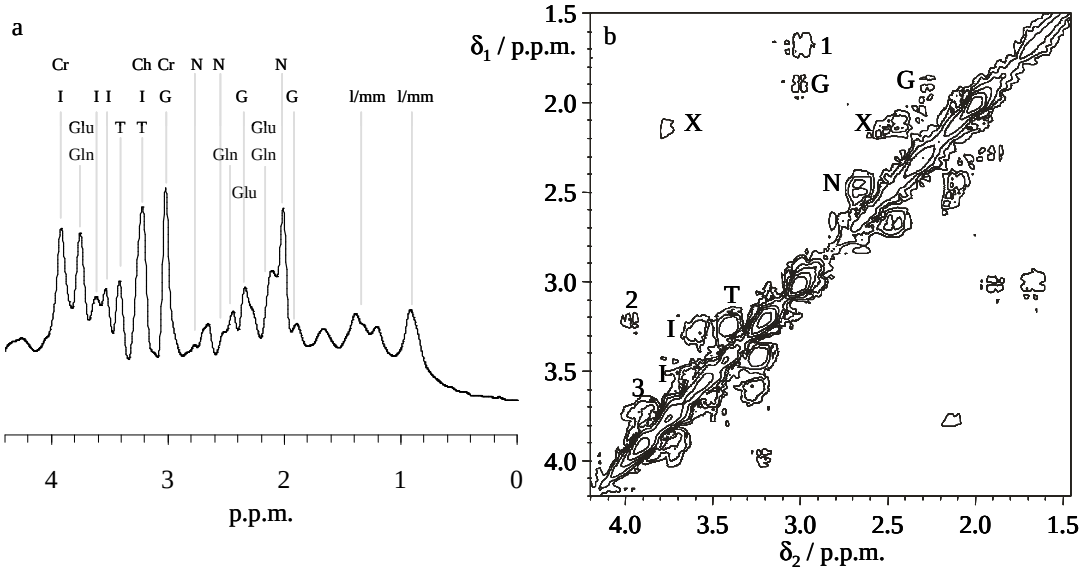

Figure 4.10: Spectra of *in vivo* rat brain. Key: Cr, creatine + phosphocreatine; Ch, choline; N, NAA; I, *myo*-inositol; G, GABA; l/mm, lipids/macromolecules; Glu, glutamate; Gln, glutamine; X, glutamate + glutamine; T, taurine. The peaks marked 1–3 in (b) are of unknown origin, although peak 1 is likely to be from an amino acid such as lysine, either free or in a peptide. Peak 2 shows a position consistent with phosphoethanolamine or histidine, but its identity has not been verified. (a) ISIS. Acquisition parameters: 256 transients, 2 kHz spectral width, 3 s repetition time; total time, 13 minutes. Processing parameters: Lorentz-to-Gauss transform (15 Hz resolution enhancement, 0.03 s Gaussian weighting). (b) ISIS-COSY. Acquisition parameters: 64 transients, 111 t_1 increments, 2 kHz spectral width in each dimension, 1 s repetition time; total time, 2 hours. Processing parameters: sine bell centred at t_1, t_2 = 0.0275, 0.04 s; absolute-value mode, symmetrized.

out in conjunction with comparing ISIS-COSY with VOSY-COSY[38], one of the best of the existing localised 2D NMR techniques discussed in section 1.5.

4.1.4.1 The VOSY-COSY Pulse Sequence

The sequence was adapted from an existing STEAM sequence by the addition of an incremented t_1 delay and a hard 90° pulse immediately prior to acquisition. The VOSY (the same pulse sequence as STEAM) localisation procedure causes difficulties for a phase-sensitive COSY acquisition, so gradient-selected ‘P’ and ‘N’-type COSY were implemented instead. This is because the hard 90° pulse would excite magnetisation from outside the voxel; the crusher gradients used in the gradient-selected variants dephase it before acquisition, but the phase-sensitive variant lacks these. Water suppression in the VOSY-COSY sequence was provided by an inversion-recovery element prior to the first localisation pulse and a single CHESS

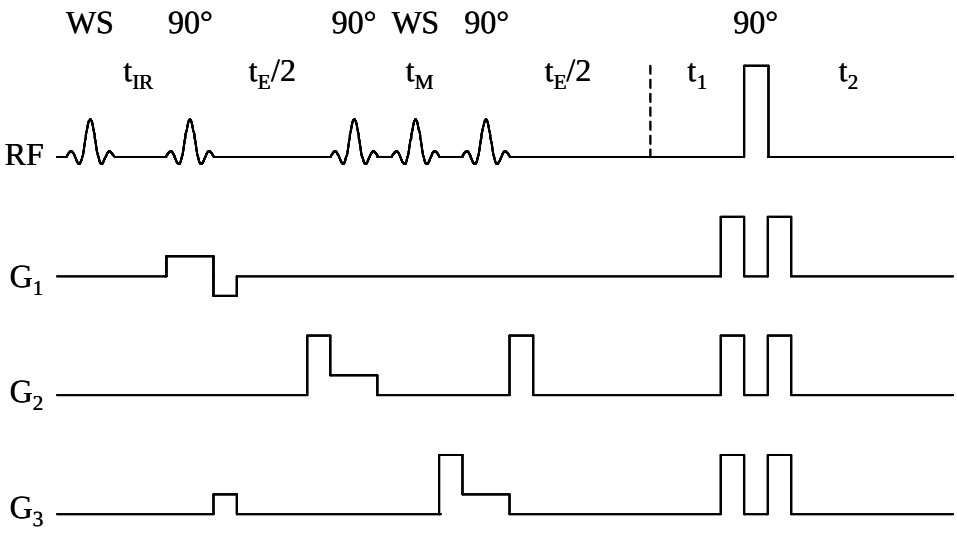

Figure 4.11: The VOSY-COSY pulse sequence. Pulses marked WS are water suppression pulses.

pulse/dephasing gradient in the t_M period of the sequence. A diagram of the sequence may be found in Figure 4.11.

The pulses used for localisation were 2 ms five-lobe sinc pulses with a bandwidth of 3 kHz; the CHESS pulse was a 30 ms sinc pulse (200 Hz bandwidth); the inversion pulse was a 60 ms sech pulse (bandwidth approximately 250 Hz); the hard 90° pulse had a duration of 80 μs. The echo time t_E was 40 ms, whilst t_M had a value of 50 ms. Optimising the water suppression for the VOSY-COSY sequence consisted of finding the best power for the CHESS and inversion pulses and the recovery time. This has to be done separately for each TR used as the optimal recovery time depends strongly on TR.

4.1.4.2 Sequence Order

The ordering of the different modules in the ISIS-COSY pulse sequence may affect the spectra acquired. Unlike most sequences, however, there are several reasonable orderings. The excitation module must clearly go at the end; since the other modules merely alter the *z*-magnetisation of different molecules in the sample, they could in principle go in any order. The main consideration in choosing which of these orders is best is that modules coming late in the pulse sequence will be more effective than those coming early. For example, if the water suppression module is the first module, a considerable period of time will elapse after it before acquisition, permitting recovery of the suppressed water signal: this means that the suppression

efficiency will be lower than if it were the last module before excitation. The most important module apart from excitation is the ISIS localisation: if there is much time between it and the excitation, relaxation of the inverted magnetisation will reduce the efficiency of the localisation. Therefore, this module is placed third in the sequence, immediately prior to excitation.

The ordering of the remaining two modules is less straightforward. To determine which ordering produced better quality spectra, a pair of 1D ISIS spectra were acquired from the glutamate/glutamine/DSS phantom, one with the OVS before the WET module, one the other way round. The resulting spectra were of broadly similar quality, with the one with the OVS first being slightly better. Therefore, the ordering used is that illustrated in Figure 4.1: OVS followed by WET, then ISIS and excitation.

This comparison was undertaken *in vitro*, where the T_1 of the water was 2.7 s and the metabolite protons around 1.5–2 s. This is at the upper limit of the expected T_1s *in vivo*, so the validity of the findings for *in vivo* application must be addressed. If the water T_1 were reduced, this is likely to affect the water suppression in the WET–OVS ordering more severely than the OVS–WET one, reinforcing the above findings. The experiment did not clearly delineate outer-volume contamination anyway, so is difficult to assess the effect of sequence order on this parameter. When a detailed investigation, including measuring outer-volume contamination, of the effect of sequence order on signal contamination in a human volunteer (see section 5.3.3.1), albeit at a different field strength with a somewhat different sample, the findings were in agreement with this OVS–WET ordering.

4.1.4.3 COSY type

A comparison of the spectra generated by the three types of COSY experiment implemented in the ISIS-COSY sequence (phase-sensitive, ‘P’-type and ‘N’-type COSY: see section 4.1.1.4) and the two variants of VOSY-COSY was undertaken. The sample used was the multi-metabolite phantom (phantom C in section 2.1.3); a voxel $8 \times 8 \times 8$ mm^3 was selected in the centre of the tube. After shimming and optimisation of the water suppression in each sequence, five spectra were acquired consecutively from the sample, one with each COSY variant. The parameters used were 16 transients per increment (including phase-sensitive acquisition in F_1 where

Sequence	COSY type	Cross-peak S/N	
		Taurine	Lactate
ISIS-COSY	Phase-sensitive	320	320
	'N'-type	310	380
	'P'-type	120	100
VOSY-COSY	'N'-type	230	230
	'P'-type	130	60

Table 4.2: S/N for cross-peaks in different localised COSY sequences run consecutively on a multi-metabolite phantom. Each experiment took 3 h.

appropriate), 128 t_1 increments, 5 s TR, total time 3 h per spectrum. These were processed using sine bell apodisation and Fourier transformed.

The S/N of two cross-peaks in each spectrum (taurine at (3.2, 3.4) p.p.m. and lactate at (1.3, 4.1) p.p.m.) was measured by extracting rows of the 2D spectrum and comparing the height of the peak with a region containing only noise. The results may be seen in Table 4.2.

Two comparisons within the data prove interesting. Firstly, the S/N for ISIS-COSY is significantly higher than for VOSY-COSY for the 'N'-type COSY, perhaps around 50% higher. This would be expected from the fact that the VOSY localisation procedure discards 50% of the available signal. Secondly, the type of COSY used greatly affects the S/N obtained. 'P'-type COSY is easily the worst performer, so its use cannot be recommended by these data; the comparison between 'N'-type and phase-sensitive COSY is less clear-cut. Despite the slightly increased S/N for the 'N'-type, for the lactate peak at least, the linewidth is apparently greater. On balance, it was felt that the phase-sensitive COSY offered the best quality spectra, so it was this variant that was used for further development work.

The poor performance of 'P'-type COSY is eloquently explained in the paper by Keeler and Neuhaus[47]. There is much inhomogeneous broadening of the peaks *in vivo* arising from local variations in the $\mathbf{B_0}$ field. The intrinsic lineshape of a peak in a gradient-selected COSY spectrum is the phase-twist, which consists of an absorptive and a dispersive Lorentzian component. In a 'P'-type COSY spectrum, the inhomogeneous broadening is parallel to the *negative* lobes of the dispersive component (i.e., perpendicular to the ridge of the phase-twist), so the broadening results in the cancellation of some of the signal from protons resonating at a slightly

different frequency. Contrastingly, in an ‘N’-type spectrum, the broadening is parallel to the *positive* lobes of the dispersive component (i.e., parallel to the ridge of the phase-twist), implying that peaks from protons resonating at a slightly different frequency will reinforce each other. Thus, the peaks in a ‘P’-type spectrum of an inhomogeneous sample will be less intense than in an ‘N’-type spectrum of the same sample.

The phase-sensitive acquisition leads to pure-phase spectra which reinforce in a similar manner to the ‘N’-type COSY peaks.

4.1.4.4 Acquisition Parameters

The final stage of optimisation of the sequence was the acquisition parameters, specifically the repetition time, number of transients per increment and number of t_1 increments. The total acquisition time is the product of these three quantities; assuming it is fixed, increasing one parameter forces another to be reduced. The combination of the three that gives the best S/N *in vivo* for a given total time is sought. This test was combined with an experiment to compare ISIS-COSY with VOSY-COSY in the brain.

Since this is highly dependent on T_1 and other sample properties, the optimisation was performed in *post mortem* rat brain. A voxel was selected and shimmed, then water suppression optimised for ISIS and VOSY localisation for TR of 1, 2 and 3 seconds. A preliminary test was to compare the S/N for a 1D spectrum run for each localisation procedure at each TR. To this end, a series of 1D ISIS and VOSY spectra were run (for each sequence: TR = 1, 2 and 3 s with 900, 450 and 300 transients respectively, 8 steady-state transients; each took about 15 minutes to acquire). These showed the expected S/N difference, that ISIS has twice the S/N of VOSY for a given TR. The S/N for a TR of 1 or 2 s was about 75% greater than that for TR = 3 s for a given pulse sequence.

For the 2D comparison, a target total acquisition time of 2 h was set as being a reasonable time for *in vivo* rat work. Seven consecutive two-hour experiments were run in the same voxel in the same rat to test different combinations of the parameters to see which yielded the best spectra. It was assumed that metabolite concentrations would be reasonably stable over this period of time[137]: following death, there is a

Seq.	TR (s)	ni	nt	sb_2 (ms)	sb_1 (ms)	S/N for peak at F_1, F_2 (p.p.m.)				
						lactate		GABA	taurine	
						1.3, 1.3	1.3, 4.1	1.9, 3.1	3.2, 3.2	3.2, 3.4
IC	3	150	16	35	35	50	12	<5	23	8
	2	222	16	55	55	45	15	5	17	5
				35	35				25	7
	2	111	32	35	27.5	100	20	12	35	12
	1	222	32	55	55	60	20	5	30	12
				35	35	100	23	8	37	15
	1	111	64	70	27.5	116	27	7	45	11
				35	27.5	200	50	13	80	16
VC	3	150	16	35	35	25	21	7	25	8
	1	111	64	35	27.5	50	38	5	40	9

Table 4.3: S/N for five peaks in localised COSY spectra of *post mortem* rat brain. Each of the seven acquisitions took 2 hours. Abbreviations: Seq., sequence (IC, ISIS-COSY; VC, VOSY-COSY); ni, number of t_1 increments; nt, number of transients (including phase-sensitive acquisition in F_1 for the ISIS-COSY experiments); sb_2, time of the centre of the sine bell in the F_2 dimension; sb_1, time of the centre of the sine bell in the F_1 dimension.

short period (a few minutes) over which lactate becomes greatly elevated as a result of anaerobic metabolism; after this, most small metabolite levels (in particular, glutamate, glutamine, lactate, creatine and inositol) are relatively stable for in excess of 24 hours. GABA is seen to rise over the course of a few hours (approximately a factor of two between 3 and 22 hours *post mortem*): this would tend to favour the VOSY-COSY experiments as they were performed as the last two of the seven.

The FIDs were processed using sine-bell apodisation (see table) and Fourier transformed; the resulting spectra are shown in Appendix B. The S/N of three cross-peaks and two diagonal peaks was measured in each spectrum. These results may be found in Table 4.3. The best S/N for all the peaks measured can be seen to be in the ISIS-COSY experiment run with TR = 1 s and 64 transients for each of 111 t_1 increments; the spectrum is shown in Figure 4.12. This combination was therefore used for all *in vivo* experiments. Comparison of this spectrum with that shown in Figure 4.9 shows the considerable improvement that the optimisation process has made to the quality and usefulness of the spectra without increasing the experimental time significantly.

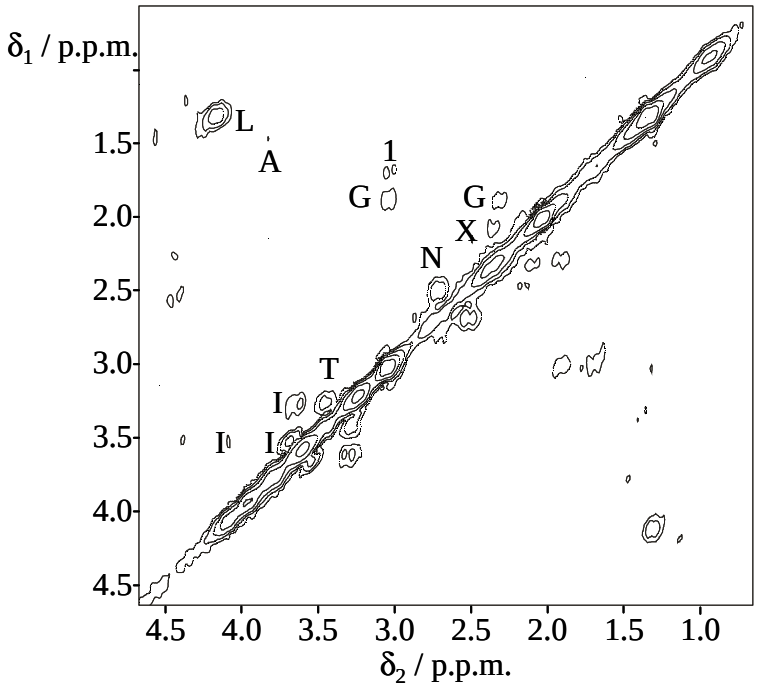

Figure 4.12: ISIS-COSY spectrum of *post mortem* rat brain. Key: L, lactate; N, NAA; I, *myo*-inositol; G, GABA; X, glutamate + glutamine; T, taurine; A, aspartate. The peak marked 1 is of unknown origin, but is likely to be from an amino acid such as lysine, either free or in a peptide. Acquisition parameters: 64 transients, 111 t_1 increments, 2 kHz spectral width in each dimension, 1 s repetition time; total time, 2 hours. Processing parameters: sine bell centred at t_1, t_2 = 0.0275, 0.035 s; absolute-value mode.

4.1.5 Quantification

One of the major benefits of NMR over some other forms of spectroscopy is that the information it provides contains quantitative as well as qualitative data. In a simple 1D ^{1}H NMR spectrum of a solution of a small molecule, the intensity of a particular resonance line is proportional to the concentration of the proton(s) contributing to it. This advantage is retained in conventional 1D spectroscopy *in vivo*, say using the STEAM or PRESS sequences, provided that effects arising from T_1 and T_2 relaxation are corrected for.

Obtaining the absolute concentration of a particular molecule within the sample is the ideal goal of any quantification procedure. This is complicated in NMR by the multitude of influences on the magnitude of the recorded signal, from the tuning of the probe to the effective sample volume in the coil. The solution is usually to measure concentrations relative to some other molecule whose concentration is either known (e.g., an added reference molecule such as TSP) or may be assumed (e.g.,

water in the brain *in vivo*); the assumption is that the complicating influences affect all resonances equally and so do not alter the *relative* intensity of the peaks. This is the approach adopted here.

Once the realm of 2D spectroscopy is entered, matters become more complicated. The intensity of a cross-peak in a typical COSY-type spectrum depends on the *J*-coupling within the molecule, the acquisition parameters (particularly resolution in the F_1 dimension), the processing parameters (if sine-bell apodisation is used) and the relaxation properties, in addition to the concentration. To convert cross-peak intensity to concentration, these various effects must be accounted for. This may be achieved by comparing the experimental spectrum to a reference spectrum either recorded from or simulated for single metabolites, acquired and processed under identical conditions. Once again, the complicating effects should be the same in each spectrum, so taking the ratio of the intensities from each should cancel them.

The program discussed in section 3.3 was designed to simulate reference FIDs for each metabolite of interest that could be processed identically to experimental data to account for *J*-coupling effects, acquisition and processing parameters within the spectrum, leaving just relaxation as a factor unaccounted for in the resulting concentrations. Rather than taking ratios of intensities, a set of correction factors were calculated as described in section 3.2.3—these are the reciprocal of the intensity of each peak in the simulated spectrum, so each intensity measured from the experimental spectrum may be multiplied by the corresponding correction factor to remove the undesirable effects. The correction factors are listed in Appendix C.

The remaining effects are T_1 and T_2 relaxation. The former will reduce the intensity recorded owing to saturation of the signals—a fast repetition rate (short TR) gives insufficient time for complete relaxation between FIDs. Provided that T_1 is known for each metabolite of interest for the conditions in the sample at the magnetic field used, this effect can be calculated and thus removed. It may be estimated by performing the experiment twice, once with a TR long enough that the metabolites may be assumed to be fully relaxed (so T_1 effects are negligible) and once with the TR set to the usual value and comparing the intensities obtained. The T_1 corrections obtained should apply to all similar samples.

Accounting for the T_2 relaxation effects is slightly more difficult. If the appropriate T_2 values are known, the simulation could be extended to include them, at the cost of taking considerably longer to calculate. An approximation assuming negligible relaxation during pulses would be simply to multiply each point in the calculated FIDs by *R*, where

$$R = \exp\left(\frac{-(t_1 + t_2)}{T_2}\right) \tag{4.1}$$

is the effect of T_2 relaxation during the t_1 and t_2 periods of the pulse sequence. The effects of T_2^* relaxation are more complex, as the inhomogeneity broadening is partially refocused by the second COSY 90° pulse. (T_2^* is the apparent relaxation time when the line-broadening effects of an inhomogeneous $\mathbf{B_0}$ field are added to the intrinsic relaxation time T_2.) However, it is difficult to find T_2 for protons that are not well resolved in the 1D spectrum, so exact values for many metabolite protons *in vivo* are elusive.

The quantification in this thesis does not include correction for relaxation effects, but all other factors are included. The metabolite chosen for a concentration reference is creatine: it has an intense diagonal peak in the 2D spectrum, which reduces the error in measuring its intensity, and the concentration of the molecules contributing to the peak (creatine and phosphocreatine) are approximately constant across a range of conditions[57]. The value assigned for the concentration in rat brain was 8.5 mM[87].

Quantification then proceeds as follows. The spectrum (see Figure 4.10b) is integrated around each peak of interest. Each peak volume is multiplied by the corresponding correction factor to account for *J*-coupling, etc., to give a corrected intensity. This is divided by the corrected intensity of the creatine peak and multiplied by 8.5 mM, the assumed concentration of creatine + phosphocreatine, to give a concentration for that metabolite (albeit uncorrected for relaxation). An example of this process is shown in Table 4.4 for a normal rat. The resultant concentrations compare well with published data[87-94].

Metabolite	F_1 (p.p.m.)	F_2 (p.p.m.)	Peak Volume	Correction Factor	Corrected Intensity	Concentration (mM)
NAA	2.5	2.7	22.8	2.00	0.88	7.5
NAA	2.7	2.5	22.5	2.00	0.87	7.4
NAA	2.0	2.0	133.5	0.33	0.85	7.2
GABA	1.9	3.0	3.7	2.00	0.14	1.2
GABA	3.0	1.9	4.8	2.00	0.19	1.6
GABA	1.9	2.3	4.6	1.90	0.17	1.4
GABA	2.3	1.9	4.4	1.90	0.16	1.4
Glx (glu)	2.1	2.4	18.8	5.70	2.08	17.6
Glx (gln)	2.1	2.4	18.8	1.60	0.58	4.9
Glx (glu)	2.4	2.1	19.1	5.70	0.59	17.8
Glx (gln)	2.4	2.1	19.1	1.60	2.10	5.0
Glx (glu)	2.1	3.7	7.0	15.00	2.02	17.2
Glx (gln)	2.1	3.7	7.0	4.70	0.63	5.4
Glx (glu)	3.7	2.1	6.1	15.00	1.79	15.0
Glx (gln)	3.7	2.1	6.1	4.70	0.56	4.7
Taurine	3.2	3.4	22.6	1.20	0.53	4.5
Taurine	3.4	3.2	24.1	1.20	0.56	4.8
Inositol	3.3	3.6	14.3	2.60	0.72	6.1
Inositol	3.6	3.3	12.7	2.60	0.64	5.4
Creatine	3.0	3.0	156.8	0.33	1.00	8.5
Creatine	3.9	3.9	141.1	0.50	1.36	11.6
Choline	3.2	3.2	124.9	0.11	0.27	2.3

Table 4.4: Example of quantification of a spectrum such as that shown in Figure 4.10b. Glx (glu) indicates quantification assuming the glx peak is all glutamate; Glx (gln) indicates quantification assuming it is just glutamine; the actual situation is somewhere between the two, but cannot be determined from this NMR experiment. The peak volume of creatine at 3.9, 3.9 p.p.m. is elevated by contributions from overlapping peaks such as inositol and the diagonal peaks associated with the peaks labelled 2 and 3 in the figure.

4.1.6 Summary

The ISIS-COSY pulse sequence has been shown to fulfil the criteria for which it was designed. It has good localisation and satisfactory water suppression; the resolution of cross-peaks from the diagonal is excellent. Extensive testing has proved that the various elements of the sequence are functioning correctly. The optimisation of the sequence, particularly the acquisition parameters, yielded considerable improvements to *post mortem* data, which were reflected when the technique was applied *in vivo*. Phantom and animal spectra are encouraging, with several metabolites clearly visible in the spectrum from a two-hour acquisition that are not resolved in a normal 1D spectrum. They are superior to spectra obtained in an equivalent manner using VOSY-COSY, a pre-existing technique with similar aims to ISIS-COSY.

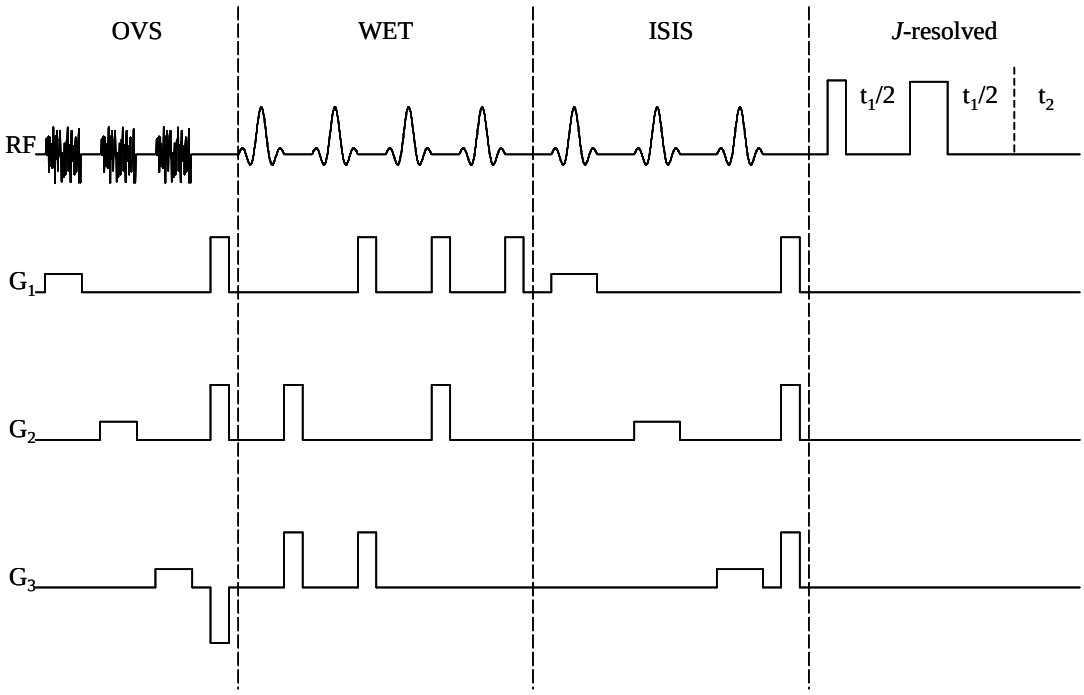

Figure 4.13: Diagram of the ISIS-JRES pulse sequence.

Quantification of the spectra via integration of cross-peaks has proved to be a valuable extension of the process. Whilst the effects of T_1 and T_2 relaxation are not accounted for in this, the results are nonetheless promising. The concentrations obtained in this manner compare favourably with published data obtained using other techniques.

4.2 ISIS-JRES

The second pulse sequence developed is a localised *J*-resolved sequence. This is another simple 2D sequence, but it yields spectra somewhat different to the COSY sequence described above. The second dimension is a *J*-coupling domain, so its spectral width need be only a few tens of Hertz to cover all signals. This means that good (say <1 Hz) resolution can be achieved with relatively few t_1 increments; however, it also implies that separation between peaks will be less, if only because there is less space for them to spread over. The sequence is more sensitive to flip angle variation then COSY, particularly in the 180° pulse, and can suffer from artefacts partly as a result of this; some can be removed by phase cycling (see below), while the sensitivity to $\mathbf{B_1}$ field strength may be reduced by employing a composite

Sequence	Reference	r.f. field range	Offset range (Hz)
180_0	–	± 6%	± 1400
$180_{120}180_{240}180_{120}$	[95]	± 20%	± 800
$180_{104.5}360_{313.4}180_{104.5}180_0$	[96]	± 31%	± 1400

Table 4.5: Constant rotation composite 180° pulses (data adapted from Levitt's review[97]). r.f. field range is variation from nominal r.f. field that keeps net magnetisation after the sequence within 10° of the desired value. Offset range is range of resonance offsets over which the net magnetisation after the sequence is within 10° of the desired value for an r.f. field equivalent to a 100 μs 90° pulse.

180° pulse (also discussed later). A general discussion of 2D *J*-resolved spectroscopy may be found in section 1.7.

4.2.1 Pulse Sequence

Most of the pulse sequence is identical to the ISIS-COSY sequence detailed above. The outer-volume suppression, water suppression and localisation modules remain unchanged; only the excitation of the 2D signal and the associated phase cycle differs. The sequence is illustrated in Figure 4.13.

4.2.1.1 Excitation Module

The excitation module used is the same as a high-resolution *J*-resolved sequence: $90° - t_1/2 - 180° - t_1/2$[29, 30] (see discussion in section 1.7). The pulses used were rectangular pulses, approximately 80 μs (90°) and 160 μs (180°) in duration for use in the rat brain.

4.2.1.2 Phase Cycle

The EXORCYCLE[53] phase cycle was used to suppress artefacts resulting from imperfections in the 180° pulse, as discussed in section 1.7.3. The number of transients per t_1 increment used for *in vivo* acquisitions was sufficient to additionally include the full CYCLOPS quadrature artefact suppression cycle.

4.2.1.3 Composite 180° pulses

An alternative means to reduce the artefact levels is provided by the use of a composite 180° pulse. A composite pulse is a series of contiguous r.f. pulses with different phases and only nominal delays between them. It is designed to mimic the effect of a simple r.f. pulse, but with superior properties in one or more aspects of its

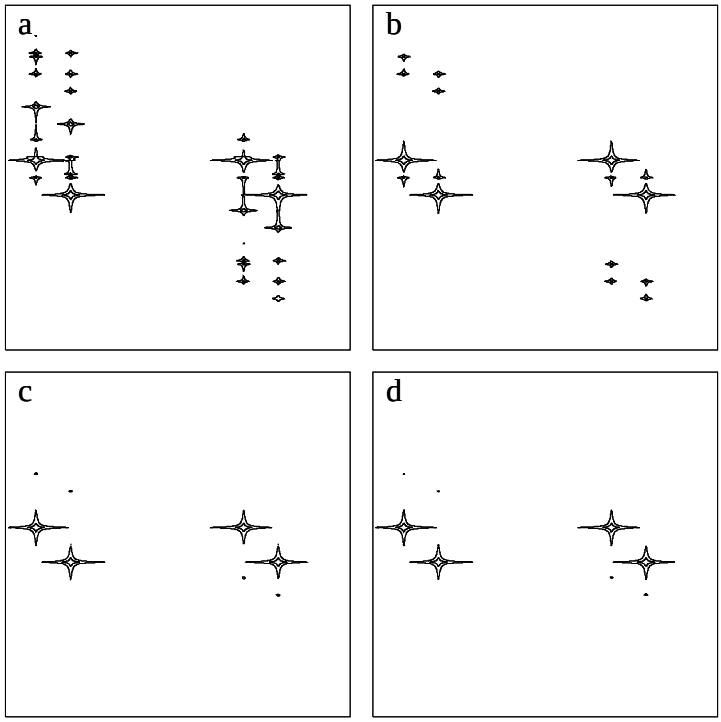

Figure 4.14: Simulated 2D *J*-resolved spectra showing the effectiveness of a composite pulse or the EXORCYCLE phase cycle at reducing artefacts from an imperfect 180° pulse. (a) Spectrum simulated using a simple 180° pulse. (b) Same as (a) but using EXORCYCLE. (c) Spectrum simulated using the composite pulse $180_{120}180_{240}180_{120}$. (d) Spectrum simulated using the composite pulse $180_{104.5}360_{313.4}180_{104.5}180_{0}$. Simulation parameters: spectral width, 500 x 500 Hz; 90° pulse duration, 75% of the nominal 1 μs; AX spin system (chemical shift of A, +120 Hz; chemical shift of X, –180 Hz; *J*-coupling constant, 50 Hz); number of complex points per FID, 256; number of increments, 512. Processing parameters: 4 Hz line broadening in F_1 and 8 Hz in F_2 directions; absolute-value mode.

performance, for example greater bandwidth or reduced sensitivity to variations in the $\mathbf{B_1}$ field strength. It is this latter property that is sought for this application.

Many composite pulses have been designed for various applications[97]. Here, a constant rotation composite 180° pulse is needed, with a greater r.f. field range than a simple 180° pulse. Great insensitivity to resonance offset is relatively unimportant, at least for the high-field applications, as the bandwidth of a typical simple 180° pulse is easily sufficient to excite the entire chemical shift range present in the samples. Two composite pulses stand out for their relative simplicity and improved r.f. field range: their properties are summarised in Table 4.5. It can be seen that some three to five times the variation in the $\mathbf{B_1}$ field strength can be tolerated using the composite pulse sequences than a simple 180° pulse.

180° pulse sequence	180° correct	180° mis-set
180_0	100%	72%
$180_{120}180_{240}180_{120}$	97%	91%
$180_{104.5}360_{313.4}180_{104.5}180_0$	94%	93%

Table 4.6: Relative signal recovery after a spin-echo formed by one of three 180° pulses with the pulse duration either correct or mis-set. This was measured by finding the height of 13 peaks in the 1D spectrum of the multi-metabolite phantom for each of the six sequences and taking the ratio with the corresponding peak height in the first spectrum. The percentages above are the mean of this set of figures.

4.2.2 Simulation Testing

The effectiveness of the composite pulses at reducing artefacts in a 2D *J*-resolved spectrum was evaluated by simulating the effects of the sequence with a simple 180° pulse then a composite one. The duration of the pulses was deliberately mis-set to provide a challenge for the 180° pulse.

As Figure 4.14 shows, the artefacts are greatly reduced in magnitude by the use of a composite 180° pulse in place of a simple 180° pulse. This will increase the size of the signal recovered by the spin-echo and reduce the requirements placed on the phase cycle (which is, of course, just as compatible with a composite 180° pulse as with a simple one).

4.2.3 *In vitro* Testing

Experimental comparison of the performance of the different ways of suppressing artefacts from an imperfect 180° pulse was undertaken on the usual multi-metabolite phantom. An 8 x 8 x 8 mm^3 voxel was selected in the centre of the tube and shimmed. The water suppression was optimised and the 90° and 180° pulse durations carefully calibrated as 68 μs and 135 μs respectively. To exaggerate the effect of poor $\mathbf{B_1}$ homogeneity, the '180°' pulse duration was set to 90 μs (a 120° pulse) for one set of experiments; for the other set it was left at the nominal value.

Firstly, a set of 1D experiments was run, to check the signal recovery from the spin-echo. Each of the three 180° pulses shown in Table 4.5 was used, with the 180° pulse both correct and mis-set. The results are summarised in Table 4.6. They show that using a composite pulse is largely successful in reducing the signal loss otherwise

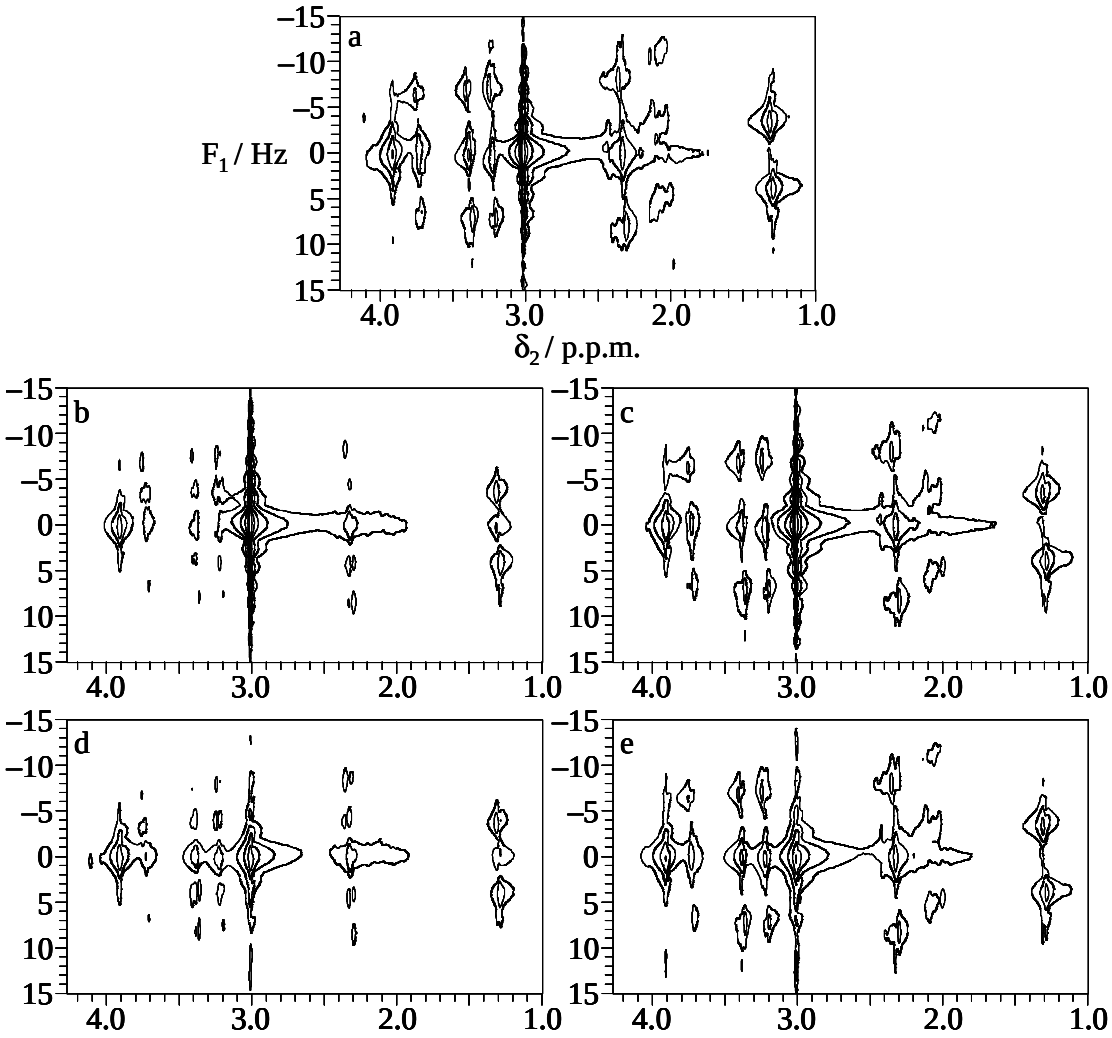

Figure 4.15: 2D *J*-resolved spectra of the multi-metabolite phantom. The 180° pulse duration is set correctly in (a) and to 120° for (b)–(e). (a), (b) and (d) use a simple 180° pulse, whereas (c) and (e) use the $180_{120}180_{240}180_{120}$ composite pulse. The EXORCYCLE phase cycle is used for (d) and (e). The vertical scale is the same for each spectrum. Processing parameters: 1 Hz line broadening in F_1, 2 Hz in F_2, absolute-value mode.

associated with a poor quality (in this experiment, deliberately miscalibrated) 180° pulse.

Secondly, a series of 2D *J*-resolved spectra were acquired, to assess the artefact level and the spectrum quality. The same six scenarios as for the 1D were tested, this time both with and without the EXORCYCLE phase cycle, making twelve experiments in all. A representative set of spectra may be found in Figure 4.15. The top spectrum (a) has the 180° pulse correctly calibrated and shows the expected splitting of the lactate (doublet at δ_2 = 1.3 p.p.m.) and taurine (two triplets at δ_2 = 3.2

and 3.4 p.p.m.) peaks, amongst others. The other four spectra were recorded with a '180°' pulse duration equivalent to a 120° pulse. If no steps are taken to counter the effects of this, spectrum (b) results: note the greatly reduced intensity for the taurine peaks in particular; also, note the artefacts at F_1, δ_2 = 0, 1.3 p.p.m. and between the peaks of the taurine triplets. Using the EXORCYCLE phase cycle improves the quality of the spectrum somewhat (spectrum (d)). This has greater signal intensity in the desired peaks, although the artefacts are still present.

Of the other seven spectra, all those acquired with the 180° pulse correctly calibrated resembled spectrum (a), implying that, *in vitro* at least, the $\mathbf{B_1}$ field is sufficiently uniform that any inhomogeneity has an imperceptible effect on the spectrum. The final two spectra, acquired with the mis-set 180° duration and the $180_{104.5}360_{313.4}180_{104.5}180_0$ composite pulse with and without the EXORCYCLE phase cycle, appear the same as the corresponding spectra for the other composite pulse, (c) and (e).

The use of a composite 180° pulse (spectra (c) and (e)) can be clearly seen to produce the cleanest spectra. There is no discernable artefact between peaks of the multiplets, and the signal intensity is similar to that in spectrum (a). The benefit of EXORCYCLE is marginal in this case: it adds little to the quality of the spectrum, but, if sufficient transients are to be acquired anyway, it might as well be included as a secondary defence to poor calibration or homogeneity of the 180° pulse. The S/N for the lactate cross peak at F_1, δ_2 = 3 Hz, 1.3 p.p.m. in spectrum (c) was 320:1.

4.2.4 Post Mortem Testing and Comparison with JPRESS

Testing of the ISIS-JRES technique in *post mortem* rat brain was accomplished in the same experiments as a comparison of its performance with JPRESS[41], another of the 2D localised NMR sequences discussed in section 1.5. This was chosen for comparison with ISIS-JRES as it gives the same type of spectra and is readily adapted from the established PRESS pulse sequence[23].

4.2.4.1 The JPRESS pulse sequence

The sequence was adapted from a PRESS pulse sequence by making one of the echo periods an incremented one, as shown in Figure 4.16. Water suppression is

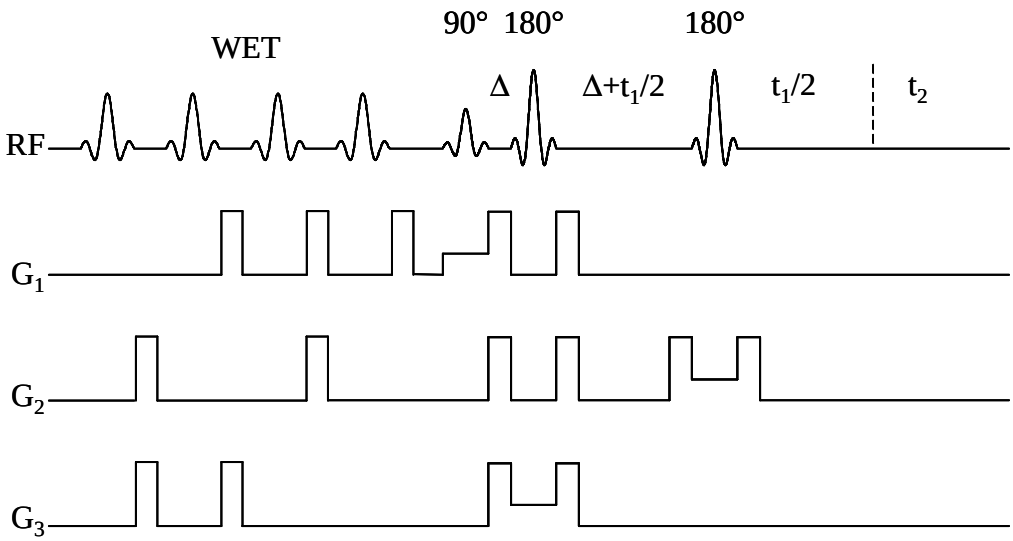

Figure 4.16: Diagram of the JPRESS pulse sequence.

provided with a WET module prior to the first 90° pulse. For the 90° and 180° pulses in the PRESS module, 1 ms five-lobe sinc pulses were used, giving a bandwidth of 6 kHz. The WET pulses were 15 ms five-lobe sinc pulses, giving a bandwidth of 400 Hz. A 10 ms crusher gradient was used, exactly as in the ISIS-JRES sequence.

4.2.4.2 Comparison

The comparison proceeded in the usual manner: a voxel was selected in the brain, shimmed (using STEAM as normal), and the water suppression adjusted for each pulse sequence. A series of 2D spectra were then recorded using the ISIS-JRES and JPRESS sequences with different combinations of TR, number of increments and number of transients per increment. A representative spectrum may be seen in Figure 4.17. The JPRESS spectra appeared similar, but perhaps with slightly less of a broad underlying hump. This would likely be from macromolecules, whose shorter T_2 times results in the signal being largely filtered out during the first t_E period of the JPRESS pulse sequence.

The S/N of the lactate peaks at F_1, $\delta_2 = \pm 3.5$ Hz, 1.3 p.p.m. was measured for each spectrum by extracting rows through the 2D spectra and comparing the height of the lactate peak with the mean height of a region of noise; the figures are found in Table 4.7. They show that the S/N for the ISIS-JRES is consistently greater than that of the JPRESS sequence. The magnitude of this difference is unexpected—the JPRESS sequence does not discard 50% of the signal like a STEAM-based sequence

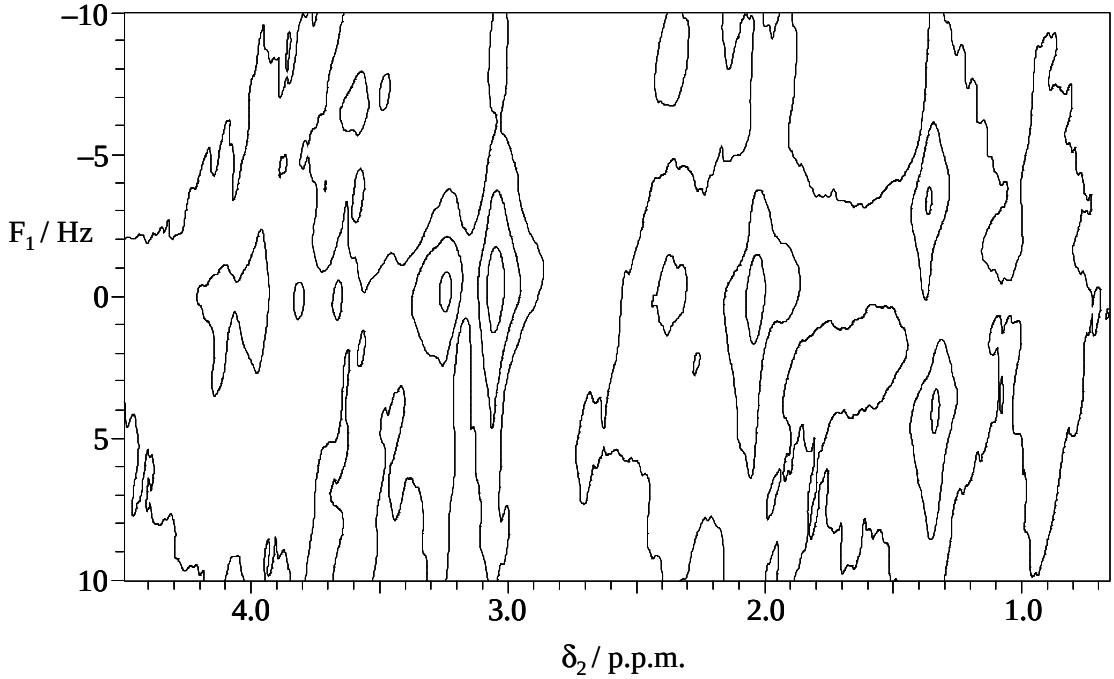

Figure 4.17: ISIS-JRES spectrum of *post mortem* rat brain. Acquisition parameters: 16 t_1 increments, 256 transients per increment, 1.5 s TR, spectral width 5 kHz x 50 Hz. Processing parameters: 0.2 Hz line broadening in F_1, 5 Hz in F_2, rotated 45°, symmetrized, absolute value mode; total acquisition time, 1 h 44 min.

would. Perhaps it is the lipid or macromolecule contribution underlying the lactate peak that is partially responsible. Within each sequence, the pattern of S/N is similar to ISIS-COSY: increasing the number of transients, even at the expense of a shorter TR or fewer t_1 increments, increases the S/N. Thus the spectrum with the best S/N is the one shown in the figure.

Despite the reasonably high S/N values for the lactate peaks, the spectra are largely uninformative. Very few peaks may be distinguished; those that can are

Sequence	TR (s)	ni	nt	Total Acquisition Time	S/N of lactate peaks
ISIS-JRES	3.0	32	64	1 h 44 min	35
	1.5	32	128	1 h 44 min	45
	1.5	16	256	1 h 44 min	55
	1.5	16	128	52 min	45
JPRESS	3.0	32	64	1 h 44 min	20
	1.5	32	128	1 h 44 min	20
	1.5	16	256	1 h 44 min	30
	1.5	16	128	52 min	25

Table 4.7: Comparison of the performance of the ISIS-JRES and JPRESS pulse sequences in *post mortem* rat brain. Abbreviations: ni, number of t_1 increments; nt, number of transients per increment. S/N measured for the lactate peaks at F_1, F_2 = ± 3.5 Hz, 1.3 p.p.m..

extremely broad and would be of very limited use for quantification owing to overlap from neighbouring peaks. In the same length of time, the ISIS-COSY sequence yields a spectrum with well-separated cross-peaks that may be assigned to specific molecules and are suitable for quantification. On this basis, the applications of the development work discussed in this chapter were solely based on the COSY variant, not the *J*-resolved one.

4.2.5 Summary

Replacement of the excitation module of ISIS-COSY with a *J*-resolved sequence gives a different approach to 2D spectroscopy *in vivo*. The spectral width requirements in the F_1 dimension are considerably lower than for the COSY variant, leading to hopes of substantial time savings. The sequence is sensitive to the performance of the 180° pulse, so methods involving phase cycling and composite pulses to reduce this sensitivity to miscalibration of the flip angle and $\mathbf{B_1}$ field inhomogeneities were implemented and tested in simulation and *in vitro*.

A *post mortem* rat brain comparison with JPRESS, a similar technique already published, showed that better S/N for the off-axis peaks was consistently obtained using ISIS-JRES. However, the spectra produced were still very disappointing. Only one pair of off-axis peaks, from lactate, could be assigned; the linewidths were very high and consequently the spectrum is of slight utility for any quantitative analysis. Consequently, the applications developed for 2D MRS *in vivo*, shown in the next chapter, are all based on ISIS-COSY.

Chapter 5: Applications

Three areas of *in vivo* application for the ISIS-COSY pulse sequence were undertaken. The first of these was an investigation into the effect of Vigabatrin, a GABA-transaminase inhibitor, on metabolite concentrations in the rat brain. These have been extensively investigated by other methods, including a 2D NMR study[98] (unlocalised), so this was a validation of the new pulse sequence. Secondly, a study was performed to ascertain whether any markers of neutrophil infiltration into the rat brain could be detected by ISIS-COSY, with potential applications in examining central nervous system inflammation. Finally, the sequence was adapted for use on a whole-body magnet system and some preliminary spectra were recorded from human volunteers.

5.1 Vigabatrin Study

This study was designed to demonstrate the effectiveness of the ISIS-COSY pulse sequence at quantifying metabolite concentrations in the brain and measuring changes in these. A drug that alters the concentrations of some of them in a well-known fashion was sought: vigabatrin provides this.

5.1.1 Vigabatrin

γ-aminobutyric acid, GABA (see Figure 5.1a), is synthesised *in vivo* from glutamate by glutamic acid decarboxylase (GAD, EC 4.1.1.15). The degradation pathway is to succinate semialdehyde, catalysed by GABA-transaminase (4-aminobutyrate-2-ketoglutarate aminotransferase, EC 2.6.1.19). These metabolic pathways are shown in Figure 5.2. GABA is the primary inhibitory neurotransmitter in the mammalian cortex[99, 100] and abnormalities with its metabolism are associated with a range of neurological disorders. For example, some regions of the brain in individuals who suffer from certain forms of epilepsy are deficient in GABA.

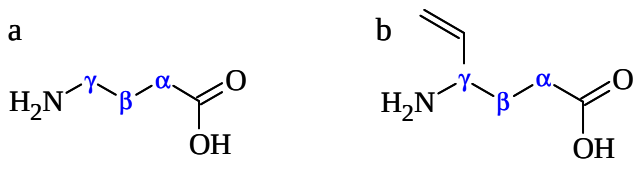

Figure 5.1: The structures of (a) GABA and (b) vigabatrin.

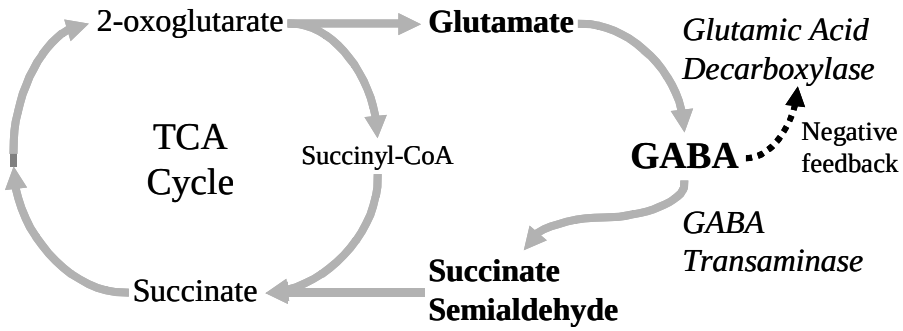

Figure 5.2: GABA metabolism in the mammalian brain. Enzymes responsible for particular transformations are shown in italics. Vigabatrin inhibits the action of GABA transaminase.

Vigabatrin (see Figure 5.1b) is an analogue of GABA that acts as a selective, irreversible inhibitor of GABA-transaminase[101-104]. Administration of a suitable dose leads to an increase in the GABA concentration in the brain. This in turn causes, via a negative feedback loop, a decrease in the rate of GABA synthesis, resulting in an increase in the levels of glutamate also. These effects have lead to the use of vigabatrin as a treatment for epilepsy.

Its employment for controlling GABA levels in the brain and as a therapeutic agent in epilepsy have meant that vigabatrin has been studied extensively, both in humans and in rats. Many different dosing regimes have been used in the rat[103-107]. Some are chronic and others acute; some inject subcutaneously or i.p., some deliver the drug orally. A recent paper[104] shows that significant effects are observed after three days' treatment at 100 mg/kg/day and that these effects are not greatly increased by either lengthening the treatment period to eight days or increasing the dose. Therefore, this protocol was adopted for the current study. These doses are not thought to be neurotoxic.

Magnetic resonance measurement of GABA in the brain is usually achieved with a spectral editing experiment[37, 105, 106, 108-113]. These techniques were discussed in section 1.4. For the detection of GABA, the *J*-coupling from the β-protons at 1.9 p.p.m. is selectively collapsed (e.g., with a long r.f. pulse during a spin-echo[105]) in alternate acquisitions and the γ-protons at 3.0 p.p.m. observed. This combination gives the fewest problems with co-editing of undesired resonances, although care

must be taken over contamination from macromolecules and, in humans, homocarnosine.

5.1.2 Methods

5.1.2.1 Animals

Two groups of male Wistar rats weighing 180–220 g were studied. Group A (n = 6) were gavaged with 20 mg vigabatrin dissolved in 0.5 ml water (100 mg/kg) daily for three days, administered under halothane anaesthesia. The dose was later doubled to 200 mg/kg/day: see results section (5.1.3). Spectroscopy was performed on the fourth day, 24 h after the last drug administration. Group B were untreated control animals (n = 10: 8 from the development phase of the project and 2 specially for this study; animal sizes were similar and spectroscopic procedures identical throughout). Free access to food and water was permitted throughout. All procedures were approved by the Home Office.

5.1.2.2 Spectroscopy

The rats were prepared for spectroscopy as per section 2.4. The spectroscopy protocol used was as described in section 4.1.3. In summary, the protocol involved performing a global shim, acquiring scout images to position the voxel, shimming that voxel, optimising the water suppression and acquiring two spectra, a 1D ISIS (3 s TR, 256 transients, 15 min acquisition time) and a 2D ISIS-COSY (1 s TR, 111 t_1 increments, 64 transients per increment, 2 h acquisition time); the entire protocol including preparation took about 3½ h per animal. Following spectroscopy, the animal, whilst still under anaesthetic, was killed by cervical dislocation and the brain rapidly excised and frozen in liquid nitrogen. Tissue was stored at –80°C prior to extraction for *in vitro* analysis.

The spectra were processed in the usual manner (1D: Lorentz-to-Gauss transform, zero-filling, Fourier transform; 2D: sine-bell apodisation, zero-filling, Fourier transform and presentation in absolute-value mode). Many of the peaks in the ISIS-COSY spectrum were integrated to provide intensities as a basis for quantifying the metabolites represented in the peak. Section 4.1.5 discusses the quantification at length.

Table 5.1: Concentrations of some metabolites in the brains of vigabatrin-treated (1-6, Treated) and control rats (mM), and linewidth (Hz) of the water peak in the localised

Peak	δ_1	δ_2	Control (n = 10)	1†	2†	3	4	5	6	Treated (n = 6)	% Change	Treated (n = 5)	% Change
NAA	2.4	2.7	8.27 ± 0.69	7.73	8.21	8.04	7.22	8.21	10.18	8.26 ± 1.01	-0.1%	7.88 ± 0.42	-4.7%
NAA	2.7	2.5	8.10 ± 0.66	7.51	8.05	7.73	7.15	7.89	9.95	8.05 ± 0.98	-0.7%	7.67 ± 0.35	-5.4%
NAA	2.0	2.0	7.54 ± 0.66	6.90	7.15	7.11	6.70	6.99	8.39	7.21 ± 0.60	-4.5%	6.97 ± 0.18	-7.6%*
Lysine	1.7	3.0	1.19 ± 0.14	1.24	1.12	1.26	1.13	1.16	1.58	1.25 ± 0.17	4.7%	1.18 ± 0.06	-0.9%
Lysine	3.0	1.7	1.21 ± 0.13	1.25	1.14	1.31	1.15	1.15	1.62	1.27 ± 0.18	5.0%	1.20 ± 0.08	-0.8%
GABA	1.9	3.0	1.07 ± 0.17	1.85	1.18	2.44	2.57	2.29	3.92	2.38 ± 0.91	122.1%***	2.07 ± 0.57	93.3%***
GABA	3.0	1.9	1.35 ± 0.20	2.18	1.64	2.92	3.05	3.11	5.16	3.01 ± 1.20	122.5%***	2.58 ± 0.64	90.7%***
GABA	1.9	2.3	1.06 ± 0.23	2.61	1.38	2.56	2.84	2.56	5.84	2.96 ± 1.50	179.0%**	2.39 ± 0.58	124.8%***
GABA	2.2	1.9	1.04 ± 0.23	2.58	1.40	2.61	2.86	2.68	5.80	2.99 ± 1.47	186.8%***	2.43 ± 0.59	132.8%***
Glx (glu)	2.1	2.5	14.75 ± 1.52	19.28	16.02	18.94	17.96	17.93	20.43	18.43 ± 1.50	24.9%***	18.03 ± 1.27	22.2%**
Glx (gln)	2.1	2.5	4.14 ± 0.43	5.41	4.50	5.32	5.04	5.03	5.74	5.17 ± 0.42	24.9%***	5.06 ± 0.36	22.2%**
Glx (glu)	2.5	2.1	15.04 ± 1.46	19.42	16.07	18.83	18.27	18.03	20.61	18.54 ± 1.52	23.2%***	18.12 ± 1.27	20.5%**
Glx (gln)	2.5	2.1	4.22 ± 0.41	5.45	4.51	5.29	5.13	5.06	5.78	5.20 ± 0.43	23.2%***	5.09 ± 0.36	20.5%**
Glx (glu)	2.1	3.8	17.98 ± 3.32	21.30	17.49	23.30	18.31	17.06	35.76	22.21 ± 7.07	23.5%	19.50 ± 2.70	8.4%
Glx (gln)	2.1	3.8	5.05 ± 0.93	5.98	4.91	6.54	5.14	4.79	10.04	6.23 ± 1.98	23.5%	5.47 ± 0.76	8.4%
Glx (glu)	3.7	2.1	17.00 ± 3.25	19.81	16.87	22.96	18.02	16.66	30.91	20.87 ± 5.44	22.8%*	18.86 ± 2.61	11.0%
Glx (gln)	3.7	2.1	4.77 ± 0.91	5.56	4.73	6.45	5.06	4.68	8.68	5.86 ± 1.53	22.8%*	5.30 ± 0.73	11.0%
Taurine	3.2	3.4	3.19 ± 0.50	4.05	3.46	3.66	3.51	3.69	2.96	3.55 ± 0.36	11.4%	3.67 ± 0.23	15.1%*
Taurine	3.4	3.2	3.58 ± 0.49	4.28	3.78	4.04	3.72	4.28	3.53	3.94 ± 0.31	10.0%	4.02 ± 0.27	12.3%*
Inositol	3.2	3.6	5.86 ± 0.48	5.61	5.25	5.72	5.34	5.67	4.76	5.39 ± 0.36	-8.1%*	5.52 ± 0.21	-5.9%
Inositol	3.6	3.2	5.39 ± 0.40	4.97	4.74	5.15	4.74	5.57	4.32	4.92 ± 0.42	-8.8%*	5.04 ± 0.34	-6.6%
Creatine	3.0	3.0	8.50 ± 0.00	8.50	8.50	8.50	8.50	8.50	8.50	8.50 ± 0.00	0.0%	8.50 ± 0.00	0.0%
Creatine	3.9	3.9	9.51 ± 2.86	10.99	8.47	11.24	9.67	9.18	6.76	9.38 ± 1.66	-1.3%	9.91 ± 1.18	4.2%
Choline	3.2	3.2	1.93 ± 0.21	1.98	1.94	1.78	1.79	1.77	1.90	1.86 ± 0.09	-3.5%	1.85 ± 0.10	-4.0%
Water l/w			16.3 ± 2.9	13.9	15.9	16.4	12.7	12.7	14.6	14.4 ± 1.6	-11.9%	14.3 ± 1.7	-12.1%

spectrum (1D ISIS without water suppression). Treated and control columns expressed as mean ± 1 standard deviation. The treated data are analysed twice: once for all 6 animals, and once for just animals 1–5, due to concerns over the results from rat 6. Glx (glu) is quantification of the glx peak assuming it is entirely glutamate; Glx (gln) assumes it is entirely glutamine. The actual situation is between the two, but cannot be distinguished using this experiment. % change is treated vs. control; significance was determined using a two-tailed t-test. The changes for each GABA peak and one pair of the glx peaks were highly significant (*** $P < 0.001$, ** $P < 0.002$). One NAA peak, taurine and *myo*-inositol show a trend towards a difference between treated and control groups, but since the trends are only apparent in one of the two treated analyses in each case, and the significance is low (* $P < 0.1$), these results should be treated with great caution. The peaks assigned to lysine are only a tentative assignment, so the concentration is not corrected for *J*-coupling and processing effects and should be read as if in arbitrary units rather than mM. †Vigabatrin dose 100 mg/kg/day; all other animals 200 mg/kg/day.

5.1.2.3 Extracts

The frozen brains were extracted with perchloric acid (PCA) using the method described in section 2.5. High-resolution NMR was performed on the resultant solutions according to the protocol depicted in section 2.2.4. Selected peaks in the 2D COSY spectrum were integrated to provide a quantitative comparison with the *in vivo* spectroscopic results obtained using ISIS-COSY.

5.1.3 Results

5.1.3.1 *In vivo*

The 1D ISIS and 2D ISIS-COSY spectra (see Figure 5.3) obtained from each rat were similar to those shown in Figure 4.10; in particular, the difference in size of the GABA peaks between controls and treated animals was very similar to the eye. After the first two rats had been studied, there was some doubt about the size of the increase in GABA levels, so the dose for the remaining four was doubled to 40 mg (200 mg/kg) daily to ensure the GABA-transaminase was totally saturated. The 2D spectra were quantified relative to the diagonal creatine peak assuming that this metabolite had a concentration of 8.5 mM. The results for the six treated animals are listed in Table 5.1.

Treated rat number 2 has GABA peaks that fall closer to the range for control animals than for treated ones, albeit at the higher end of the range. This may indicate that it has failed to respond to the treatment for some reason, or that its response was considerably less than the other five rats. This observation was what prompted the

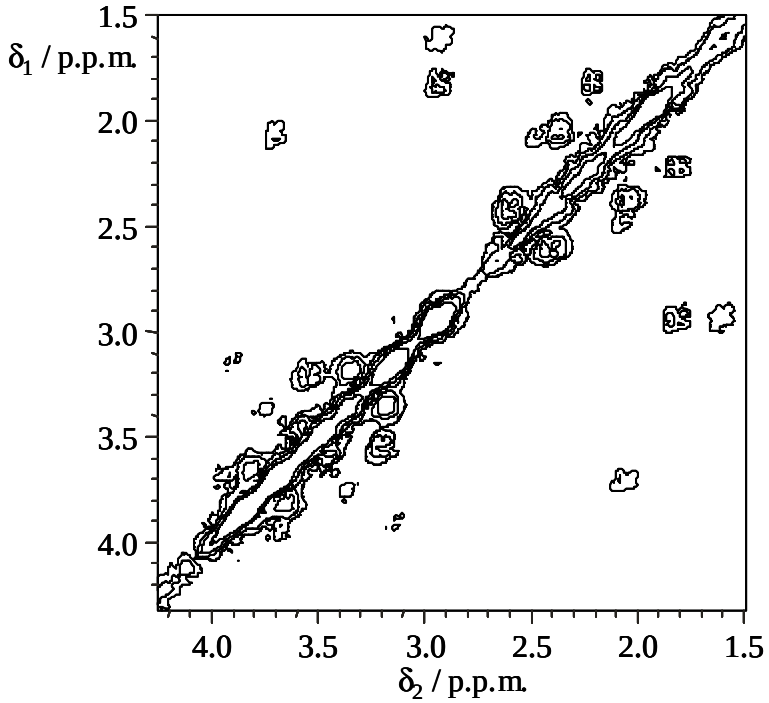

Figure 5.3: ISIS-COSY spectrum of vigabatrin-treated rat brain *in vivo* (rat number 3). Acquisition parameters: 64 transients, 111 t_1 increments, 2 kHz spectral width in each dimension, 1 s repetition time; total time, 2 hours. Processing parameters: sine bell centred at $t_1, t_2 = 0.0275, 0.04$ s; absolute-value mode, symmetrized. Peak identification as for Figure 4.10b.

increased vigabatrin dose for the subsequent four rats. The spectrum from rat 6 has poor S/N relative to the other treated rats; the quantification produced peak integrals all significantly below those from the other spectra. The intensity of the diagonal creatine peak was especially low, so quantifying relative to this is the explanation of the anomalously high concentrations seen for most of the metabolites. Other spectral parameters (for instance, the width of the water peak) fell within the range of the other five rats; the spectra themselves were ostensibly similar, and no reason for the abnormal quantifications could be discerned. Doubt is thus cast on the accuracy of the figures for rat 6, so analysis of the treated spectra was performed both including (n = 6) and excluding (n = 5) the data from this rat. This permits an assessment to be made as to the validity of any differences observed in metabolite concentrations between control and treated rats, and whether they arise solely from the contribution of rat 6; any that do are necessarily to be regarded with caution.

The table also contains, for each metabolite, the mean concentration and its standard deviation for ten control spectra and the percentage difference between the control and treated groups. The significance of each of these differences was tested

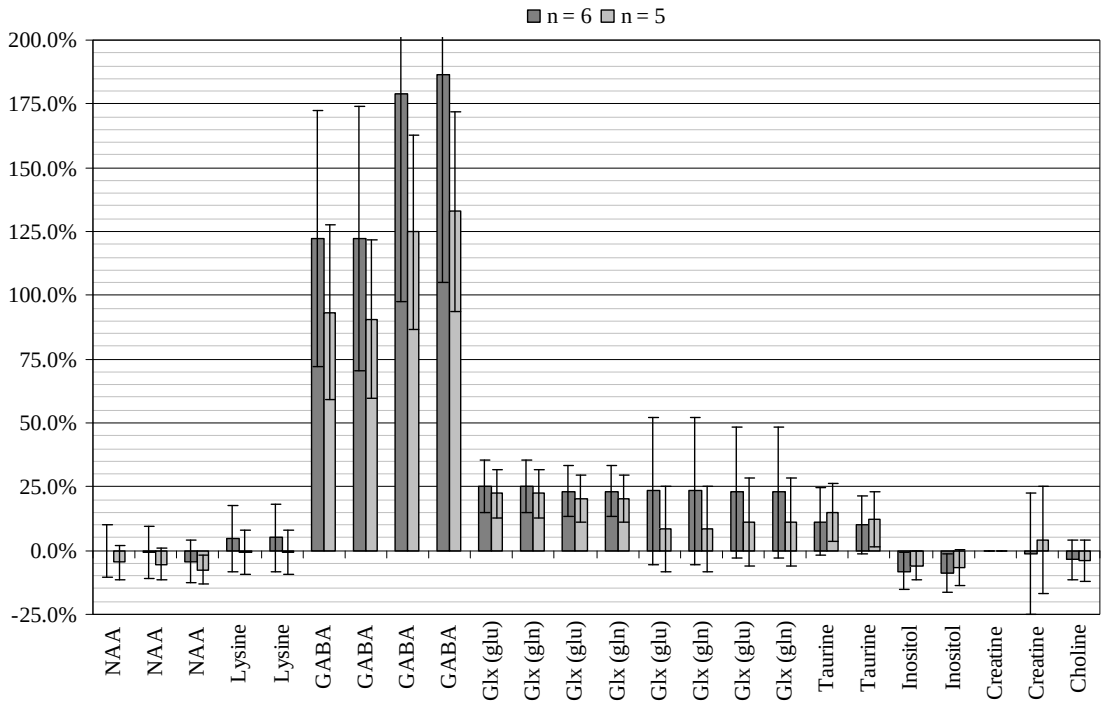

Figure 5.4: Graph of changes in metabolite concentrations in vigabatrin-treated rat brain versus controls as measured by ISIS-COSY. n = 6, all treated rats; n = 5, only rats 1–5. Error bars are ± 1 standard deviation.

using a two-tailed t-test, the results of which are also included in the table. A graphical summary of the changes observed in the treated rats versus the controls is presented in Figure 5.4.

The significant changes ($P < 0.002$) in treated versus control rats are large increases in GABA concentration (up to ~150% increase), with smaller increases (20–25%) in the glutamate / glutamine composite peaks also; these changes are observed in the analysis both with and without rat 6. Such changes are entirely consistent with the inhibition of GABA-transaminase, as explained in the introduction to this section: the rate of GABA breakdown is drastically reduced, leading to a build-up of GABA; a negative feedback loop reduces the rate of its synthesis from glutamate, causing its concentration to increase also. The magnitude of the GABA changes is in accordance with the results of a previous study with a similar dosing regime, where the concentration measurement did not use magnetic resonance[104]. This study did not measure glutamate or glutamine concentrations, but the modest increase reported above seems entirely credible.

Symmetrically related cross-peaks clearly show more similar changes than unrelated cross-peaks. The four GABA peaks are a convenient demonstration of this: in the n = 5 analysis, the first two peaks symmetrically located at (1.9, 3.0 p.p.m.) and (3.0, 1.9 p.p.m.) both show increases of around 90%, whilst the other pair of peaks show increases around 130%. The similarity between symmetric pairs would be entirely expected, however, as the spectra are symmetrized prior to quantification; the minor differences arise from slightly different position and size of the integration boxes. The relatively large difference between the pairs of unrelated cross-peaks for GABA is difficult to explain. Looking at the glx peak n = 5 analysis reveals a similar trend: the pair of peaks including (2.1, 2.5 p.p.m.) show a 20% increase, with the pair including (2.1, 3.8 p.p.m.) having a 10% increase. Here, the origin of the difference is clearer: the latter peaks are much weaker, so there is much greater uncertainty in the measurements, reflected in the standard deviations associated with these peaks being approximately twice as large (particularly apparent in Figure 5.4).

Table 5.1 also shows possible small increases in the taurine concentration and decreases in NAA and *myo*-inositol, although these are much less significant ($P < 0.1$) and only observed in one analysis (either n = 5 or n = 6) in each case. Such low significance, and the reliance on including or excluding one specific rat from the analysis, means that no real importance can be attached to these observations at this stage. Larger numbers of animals to confirm or repudiate the trends would be needed. The mechanism for any changes, if indeed they are genuine, is not known. However, substantiation of any effects in a larger study could prove an interesting and illuminating demonstration of a side effect of vigabatrin, potentially furnishing greater insight into its function in the brain.

5.1.3.2 Extracts

A typical 1D spectrum of a PCA-extracted rat brain (that of treated rat number 6) is shown in Figure 5.5. This shows peaks from a wide range of water-soluble metabolites, plus TSP (added as a reference). Greater resolution is attained in the two-dimensional COSY spectrum (Figure 5.6). These show much similarity with the *in vivo* spectra, albeit with a considerably reduced linewidth (~1 Hz versus ~14 Hz *in vivo*).

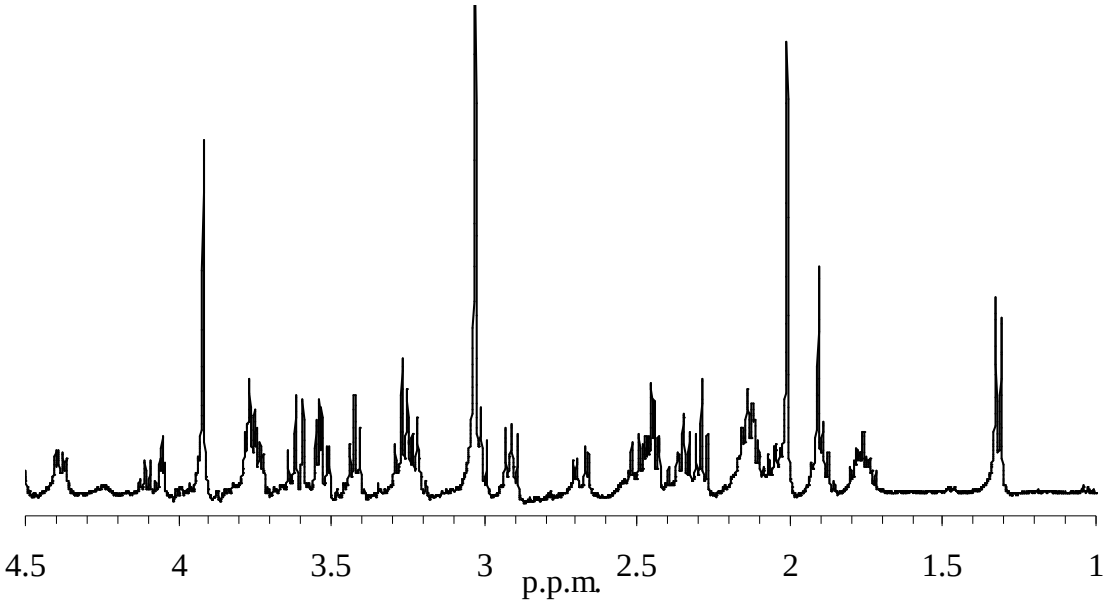

Figure 5.5: 1D spectrum of PCA extract from vigabatrin-treated rat number 6. Acquisition parameters: 15 s TR, 5 kHz spectral width, 16 transients; total time, 5 min. Processing parameters: 0.5 Hz line broadening. Assignment: δ = 1.3 p.p.m., lactate; δ = 1.75, TSP; δ = 1.0, GABA, acetate; δ = 2.0, NAA; δ = 2.05, glutamate; δ = 2.15, glutamate + glutamine; δ = 2.3, GABA; δ = 2.35, glutamate; δ = 2.45, glutamine; δ = 2.5, NAA; δ = 2.65, aspartate; δ = 2.7, NAA; δ = 2.9, TSP; δ = 3.0, creatine; δ = 3.2, choline; δ = 3.25, taurine + *myo*-inositol; δ = 3.4, taurine; δ = 3.5–3.6, *myo*-inositol; δ = 3.75, glutamate + glutamine; δ = 3.9, creatine; δ = 4.05, *myo*-inositol; δ = 4.1, lactate; δ = 4.4, NAA.

The cross-peaks in the COSY extract spectra were integrated to provide quantitative information about the concentration of each metabolite in the extracted solution. Since the correction factors (for definition, see section 4.1.5) have not been calculated for the magnetic field and acquisition parameters used for these spectra, the numbers are in arbitrary units, different for each peak. However, comparisons can be made between spectra as the same conditions were used for each. A summary of the key peaks, most of which were also quantified in the *in vivo* spectra, is presented in Table 5.2. Once again, the data have been processed both for all six animals and for only rats 1–5. Unlike the *in vivo* figures, however, the extract results for rat 6 are very similar to the other five sets, so there is little reason to use the n = 5 results over the n = 6 ones. There were only two control extract spectra done as only the two rats used specially for this study had their brains extracted; the other eight from the development phase were not thus treated.

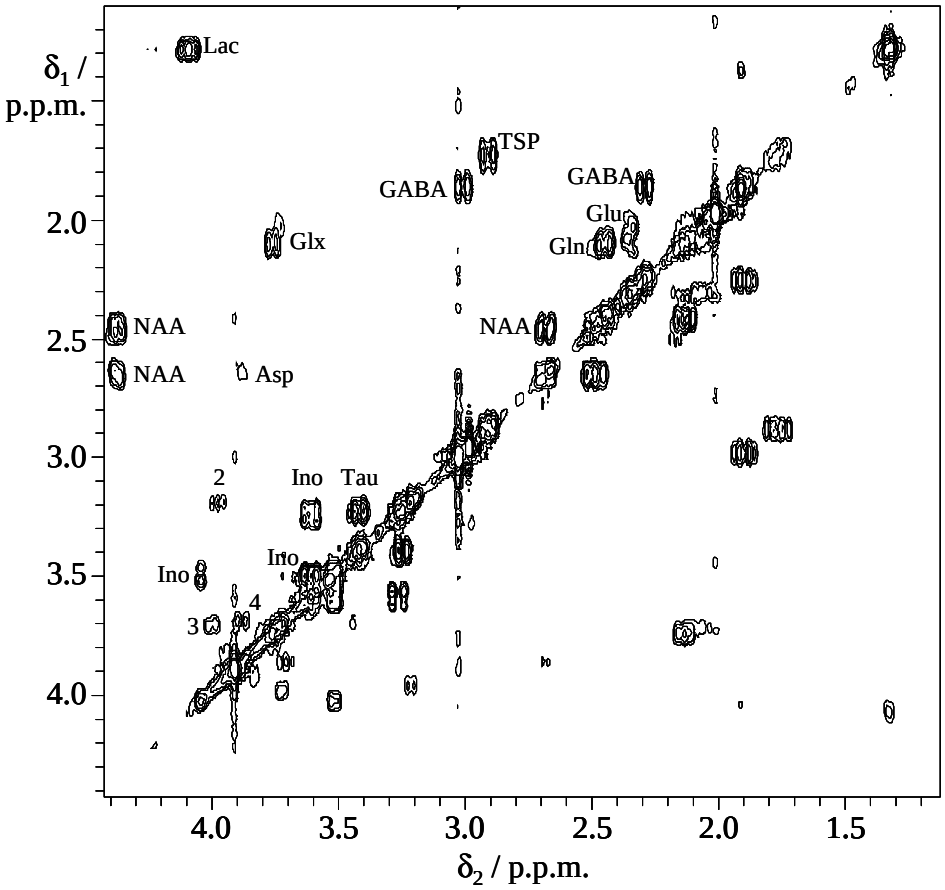

Figure 5.6: 2D COSY spectrum of same sample as Figure 5.5. Cross-peaks are labelled with conventional abbreviations. Peaks 2–4 are from unknown compounds; 2 and 3 also appear in the *in vivo* spectrum (see Figure 4.10). The former has a resonance pattern consistent with phosphoethanolamine or histidine, but the identification has not been verified. Acquisition parameters: 7.5 s TR, 3 x 3 kHz spectral width, 4 transients per increment, 320 t_1 increments; total time, 2 h 40 min. Processing parameters: sine bell centred at t_1, t_2 = 0.042, 0.1 s, absolute-value mode.

The results are somewhat disappointing, in that the standard deviations for the treated spectra are rather greater for many of the peaks than would be desired, and significantly greater than the corresponding ones in the *in vivo* quantification. Several are larger than 10% of the mean intensity for the peak. However, the GABA results do show a considerable increase of around 80% in the treated versus control animals, although this is smaller than the ~150% increase found *in vivo*. Interestingly, the separate measurement of glutamate and glutamine possible in the extract spectra implies a small (not significant) decrease in glutamate but a rise in the glutamine levels ($P < 0.1$) on treatment with vigabatrin. This is counter to what was predicted in the introduction to this section: a rise in glutamate levels would be expected, with any changes in glutamine being relatively smaller.

Table 5.2: Normalised peak intensities (arbitrary units) in high-resolution COSY spectra of PCA extracts of vigabatrin-treated and control rat brains, and TSP

Peak	δ_1 (p.p.m.)	δ_2 (p.p.m.)	Control (n = 2)	1	2	3	4	5	6	Treated (n = 6)	% Change	Treated (n = 5)	% Change
NAA	2.7	2.5	6.98 ± 0.22	6.41	6.82	7.19	7.97	6.45	7.38	7.04 ± 0.60	0.8%	6.97 ± 0.64	-0.2%
NAA	4.4	2.5	0.80 ± 0.32	0.64	0.53	0.43	0.40	0.44	0.41	0.48 ± 0.09	-40.5%**	0.49 ± 0.10	-38.9%*
NAA	2.0	2.0	33.40 ± 2.93	35.30	35.38	35.34	37.06	34.10	33.21	35.06 ± 1.31	5.0%	35.44 ± 1.05	6.1%
GABA	1.9	2.3	1.42 ± 0.23	3.43	1.31	2.42	2.63	2.24	3.31	2.56 ± 0.78	80.3%*	2.40 ± 0.76	69.7%
GABA	3.0	1.9	1.45 ± 0.20	2.93	1.45	2.66	2.79	2.41	3.48	2.62 ± 0.67	80.6%*	2.45 ± 0.59	68.8%*
Glutamate	2.3	2.1	2.80 ± 0.02	3.17	2.34	2.65	2.13	2.43	2.05	2.46 ± 0.41	-12.2%	2.54 ± 0.40	-9.3%
Glutamate	2.3	2.1	4.03 ± 0.29	5.07	3.37	2.84	2.40	3.18	2.27	3.19 ± 1.02	-21.0%	3.37 ± 1.02	-16.4%
Glutamine	2.4	2.1	3.28 ± 0.18	5.77	4.25	4.49	5.68	3.95	5.24	4.90 ± 0.77	49.5%**	4.83 ± 0.84	47.4%*
Glx	3.7	2.1	6.60 ± 0.37	6.72	5.23	5.74	5.78	5.23	5.57	5.71 ± 0.55	-13.5%*	5.74 ± 0.61	-13.0%
Taurine	3.4	3.3	6.82 ± 0.46	9.95	6.46	7.21	7.80	6.22	7.30	7.49 ± 1.34	9.8%	7.53 ± 1.49	10.3%
Taurine	3.4	3.4	7.64 ± 0.65	8.36	8.84	10.40	9.68	8.74	9.22	9.21 ± 0.74	20.5%**	9.20 ± 0.82	20.5%*
Inositol	3.6	3.3	4.50 ± 0.56	6.54	3.75	4.00	4.06	3.22	3.71	4.21 ± 1.18	-6.3%	4.32 ± 1.29	-4.0%
Inositol	3.7	3.6	9.27 ± 1.38	3.53	4.82	0.45	1.50	2.20	0.50	2.17 ± 1.74	-76.6%***	2.50 ± 1.71	-73.0%***
Inositol	4.0	3.5	2.79 ± 0.50	1.59	1.54	1.55	1.96	1.39	1.90	1.66 ± 0.22	-40.6%***	1.61 ± 0.21	-42.3%***
Inositol	3.6	3.6	22.73 ± 3.58	6.44	13.23	3.86	6.55	7.18	4.21	6.91 ± 3.38	-69.6%***	7.45 ± 3.47	-67.2%***
Lactate	1.3	1.3	32.00 ± 0.50	32.01	25.68	24.52	27.53	34.79	19.63	27.36 ± 5.43	-14.5%	28.91 ± 4.35	-9.7%
Lactate	4.1	1.3	1.90 ± 0.52	1.63	0.87	0.95	1.60	1.17	1.02	1.21 ± 0.33	-36.6%*	1.25 ± 0.36	-34.6%*
Aspartate	2.8	2.7	2.11 ± 0.10	1.73	1.68	1.30	1.07	1.38	0.78	1.32 ± 0.36	-37.3%**	1.43 ± 0.27	-32.2%**
Aspartate	3.9	2.7	2.06 ± 0.07	1.08	1.54	1.07	0.80	1.23	0.64	1.06 ± 0.32	-48.6%***	1.14 ± 0.27	-44.5%***
Creatine	3.0	3.0	50.00 ± 0.00	50.00	50.00	50.00	50.00	50.00	50.00	50.00 ± 0.00	0.0%	50.00 ± 0.00	0.0%
Creatine	3.9	3.9	32.60 ± 0.54	31.77	31.86	31.68	32.67	30.94	31.60	31.75 ± 0.56	-2.6%	31.79 ± 0.62	-2.5%
Choline	3.2	3.2	14.78 ± 1.30	10.43	8.15	11.66	9.68	7.79	10.11	9.63 ± 1.45	-34.8%***	9.54 ± 1.60	-35.4%***
TSP l/w			1.1 ± 0.2	0.8	0.9	1.2	0.8	0.8	1.0	0.9 ± 0.2	-12.7%	0.9 ± 0.2	-14.3%

linewidth (Hz). Treated and control columns expressed as mean ± 1 standard deviation. The treated data are analysed twice: once for all 6 animals, and once for just animals 1–5, as for the *in vivo* results. The intensities are normalised to the diagonal creatine peak at 3.0 p.p.m.. %Change is treated versus control; significance was assessed using a two-tailed t-test (* $P < 0.1$; ** $P < 0.05$; *** $P < 0.01$).

One possible reason for the increase in the glx peak being mostly glutamine could be related to the cycling of glutamate and glutamine through different cell populations in the brain. Glutamate is highly active in the synaptic space as an excitatory neurotransmitter, whereas glutamine is relatively inert. This is used by the brain in the glutamate / glutamine cycle: glutamate is released by neurons into the synaptic space as an excitatory neurotransmitter, from where it is taken up by astrocytes and converted back to glutamine. This may be released back into the synaptic space for the neurons to take up again (and convert back to glutamate) without causing unwanted excitation. It could be that any excess glutamate caused by down-regulation of the synthesis of GABA from glutamate is converted by astrocytes to glutamine, which is the molecule observed in the extract data.

The GABA levels observed for rat 2 are again seen to be more similar to the control rats rather than the other treated results. This tallies with the *in vivo* figures, where the rat was also shown not to have responded to vigabatrin treatment to the same extent as the other rats.

The most significant ($P < 0.01$) changes between control and treated extract spectra were seen in the choline, aspartate and some of the *myo*-inositol peaks. The latter is difficult to explain, particularly given the absence of any difference in the other *myo*-inositol peak quantified. The apparent choline changes are also puzzling: there is no evidence for any differences *in vivo*, and no connection with the known action of vigabatrin is apparent. It could be an artefact of the low numbers of control animals used.

5.1.4 Discussion and Conclusions

ISIS-COSY has been successfully demonstrated as capable of measuring changes in the concentration of cerebral metabolites *in vivo*. Specifically, the changes in GABA levels induced by chronic vigabatrin treatment in the rat have been determined and found to be similar to those previously reported[104].

The measurement of GABA concentrations using the ISIS-COSY sequence offers significant benefits over other magnetic resonance methods. One primary advantage is that any changes in other metabolite concentrations are also observed simultaneously, for instance the 25% increase in the intensity of the glx peak, that would have been missed if GABA had been detected using spectral editing. Other possible differences in metabolite levels have been seen, although they are presently of low statistical significance: should further experiments to increase the sample numbers be undertaken and the differences prove to be genuine, mechanisms to explain these side-effects of vigabatrin would have to be formulated, leading potentially to a greater understanding of the system being studied.

The main useful contribution made by the extract data to the study was the discrimination between glutamate and glutamine possible from the greater resolution achieved *in vitro*. This permits speculation about the metabolic pathways affected by treatment with vigabatrin. Some of the extract figures are confusing and show a rather large variability between animals not evident in the *in vivo* spectra. This may be at least partially due to poor extraction technique causing, for example, different amounts of metabolic decay arising from allowing the samples to warm up too much prior to extraction.

However, the aims of the study, to follow changes in metabolite levels *in vivo* using magnetic resonance in animals undergoing vigabatrin treatment, were fulfilled. The capabilities of ISIS-COSY in this respect have been unambiguously demonstrated.

5.2 Neutrophil Study

Inflammation is a major component in many diseases of the brain, from Alzheimer's disease and AIDS-related dementia to Multiple Sclerosis, stroke and trauma resulting from injury[114]. It is a natural constituent of the host's response to these insults, designed to destroy diseased or foreign tissue. Sometimes, however, the inflammatory response is excessive and healthy tissue close to the damaged region is also affected: the so-called "bystander effect". It would be extremely beneficial if the response could be mediated such that the side-effects were curtailed and no healthy tissue was damaged. Such intervention would require the reliable detection of the

inflammatory processes which, in a closed system like the brain, is demanding. Short of taking a biopsy, inflammation is more inferred than detected.

The aim of this study was to identify NMR markers of inflammatory-response cells that could be used to recognise regions of the brain affected by inflammation, with a view to ultimately being able to apply this to human patients as a diagnostic tool. These markers would preferably be not present in more than trace amounts in normal tissue, and ideally not in quiescent inflammatory-response cells either.

5.2.1 Inflammation and Neutrophils

The inflammatory response to an insult to normal tissue function is extremely complex. Early detection of the disruption of normal function is provided by cells already present at the site. They send out chemical signals to cause recruitment of leucocytes, normally circulating in the bloodstream, to deal with the problem. An important class of cells recruited are neutrophils.

Leucocytes (white blood cells) are normally made up of about 30–40% lymphocytes (T and B cells) and 60–70% granulocytes[115]. Of the latter, some 90% are neutrophils. They provide protection from a variety of micro-organisms and are arguably the most important white blood cells in destroying non-viral infections. On receiving appropriate signals, they become activated and emigrate from the blood vessels into the tissues in a process known as chemotaxis. Once at the site, they can engulf the foreign cell (phagocytosis) and destroy it with a range of chemical toxins. These toxins may under some circumstances be released extracellularly—this is part of the reason that inflammation can damage nearby healthy tissue.

An activated neutrophil, as part of the phagocytosis procedure, undergoes a respiratory burst[116]. This is characterised by a marked increase in oxygen consumption by the cell and results in the production of a large number of free radicals. These are mostly oxygen-based radicals such as the superoxide and hydroxyl radicals. Under normal conditions, they are cleared up by enzymes such as superoxide dismutase (SOD), but in an activated neutrophil they are produced in too high a quantity for these endogenous pathways to cope with. The main chemical pathways involved in this processed are summarised in Figure 5.7a[117]. One of the by-products can be seen to be hypochlorous acid, HOCl. This is a reactive oxidant that has

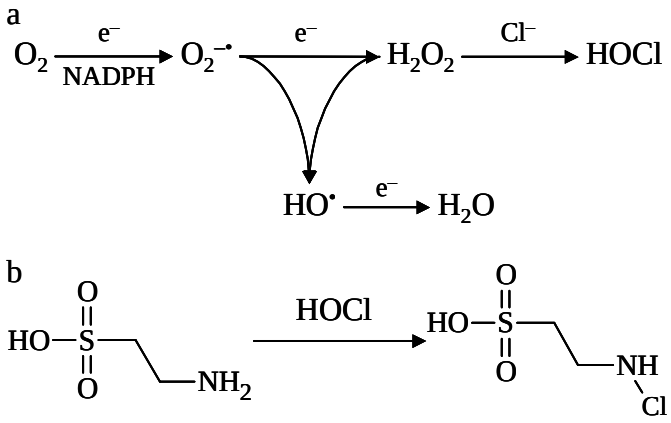

Figure 5.7: (a) The production of reactive oxygen species in a respiratory burst. e^- indicates a reduction step. (b) The production of chlorotaurine from taurine and hypochlorous acid.

microbicidal properties. In a neutrophil, it will often react with taurine (present in relatively high concentration in such cells) to produce chlorotaurine (Figure 5.7b).

This molecule was thought to be a possible marker for activated neutrophils as it is present in only negligible quantities in normal cells. Its structure is similar to taurine, which is readily detected by NMR *in vivo*, particularly by a 2D technique such as ISIS-COSY.

5.2.2 Chlorotaurine Study

A brief study was undertaken to characterise the NMR properties of chlorotaurine to enable its identification in spectra of cells or *in vivo*.

5.2.2.1 Methods

A solution of chlorotaurine was prepared using a modification of a previously reported method[118]. Separate equimolar solutions of taurine and sodium hypochlorite (NaOCl) were prepared in D_2O buffered to pH 7.4 with 0.1 M potassium phosphate. They were mixed and allowed to react at room temperature. The formation of chlorotaurine was monitored by UV absorption: it absorbs maximally at 252 nm, whereas the chlorite solution absorbs maximally at 291 nm. Thus, the disappearance of one peak and appearance of the other can track the extent of the reaction. The final solution was estimated to contain about 3 mM chlorotaurine and 2 mM unreacted taurine.

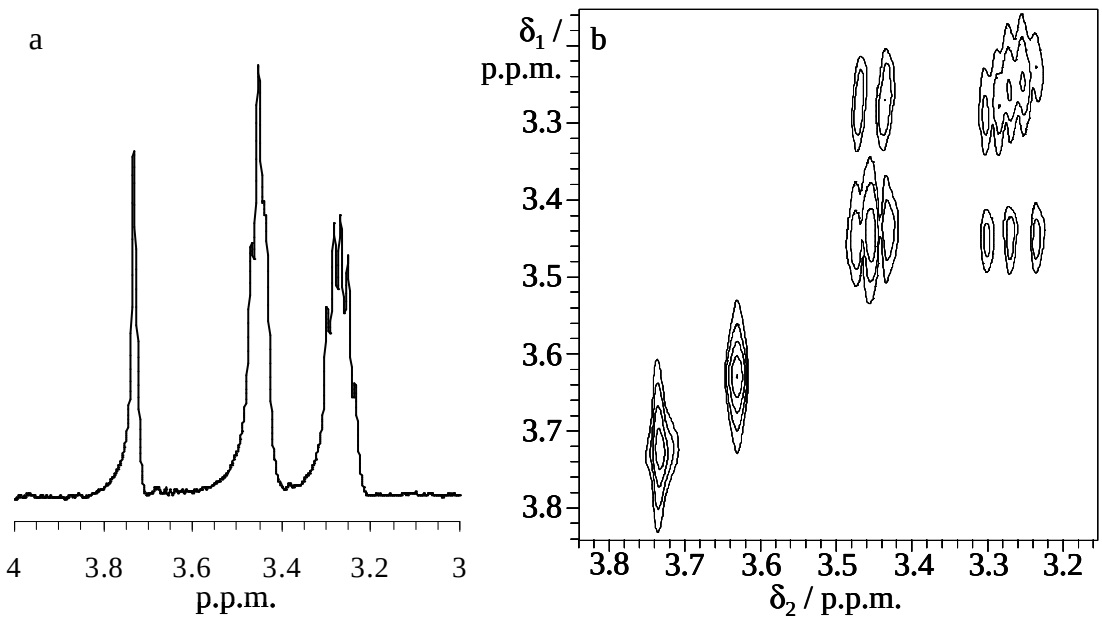

Figure 5.8: Spectra of the chlorotaurine and taurine mixture. (a) 1D. Acquisition parameters: 5 kHz spectral width, 15 s TR, 16 transients; total time, 4 min. Processing parameters: 1 Hz line broadening. (b) 2D COSY. Acquisition parameters: 3 x 3 kHz spectral width, 15 s TR, 4 transients per increment, 600 t_1 increments; total time, 10 h. Processing parameters: sine bell centred at t_1, t_2 = 0.1, 0.2 s, absolute-value mode. The peak at δ_1, δ_2 = 3.63, 3.63 p.p.m. is an origin spike arising from a DC offset in the recorded FID.

^{1}H NMR spectroscopy was performed on the solution. It was placed in a 5 mm NMR tube, equilibrated to a nominal 30°C and shimmed. The T_1 was measured for some of the peaks in the spectrum; for the water, this was greater than 15 s, but for the other peaks, it was less than 4 s. A 1D water-suppressed spectrum was acquired (15 s TR, 16 transients; total time, 4 min), then a 2D phase-sensitive COSY, fully relaxed (15 s TR, 4 transients per increment, 600 t_1 increments; total time, 10 h). Finally, a further 1D spectrum was run to assess whether there had been significant decay of the chlorotaurine during the spectroscopic examination.

5.2.2.2 Results

The one- and two-dimensional spectra may be found in Figure 5.8. The main differences that can be seen from those of pure taurine (see Appendix A) are the additional singlet at 3.75 p.p.m. and the increased multiplicity of the peak at 3.25 p.p.m.. The 2D spectrum is consistent with this peak being two triplets, one from taurine at 3.25 p.p.m. and the other from chlorotaurine at 3.28 p.p.m.. There are naturally no cross-peaks arising from the singlet. The origins of the singlet are

unknown, presumably from a by-product of the reaction or a contaminant. The NH protons will have exchanged with the deuterons in the solvent and so will show in the NMR spectrum as HOD (downfield of the range shown in the figure). Assuming that the singlet does not arise from the chlorotaurine molecule, these *in vitro* spectra imply that, in a cellular suspension or *in vivo*, it is unlikely to be possible to distinguish taurine from its chlorinated derivative. The greater linewidths in such cases make it doubtful that the peaks from taurine and chlorotaurine around 3.25 p.p.m. would be sufficiently well resolved. No significant differences were observed between the 1D spectrum run after the 2D and the one run beforehand.

5.2.3 High-Resolution Study

It is possible to isolate neutrophils from blood for *in vitro* study; they can be activated by the addition of an external compound such as lipopolysaccharide (LPS) or tumour necrosis factor α (TNF-α)[119-121]. This study was designed to observe NMR spectra of neutrophils *in vitro* and compare the quiescent and activated states. It was intended to obtain NMR markers unique to activated neutrophils, perhaps chlorotaurine, for comparison with *in vivo* spectra.

5.2.3.1 Methods

Neutrophils were isolated from human blood by taking 60 ml blood and mixing with 15 ml 15% dextran and leaving for 45 minutes to separate out blood cells. The supernatant containing the cells was removed and layered on top of 15 ml histopaque ficoll gradient, then centrifuged for 30 minutes at 1544 r.p.m. (400 *g*). The supernatant was removed and discarded, then 6 ml D_2O added to the pellet (which contains neutrophils and red blood cells); this was left for 1 minute to lyse the red blood cells.

Phosphate-buffered saline (PBS) was prepared at 3.6% and 0.9% w/v concentration by dissolving 3.6 g or 0.9 g sodium chloride in 100 ml D_2O containing 0.1 mM sodium phosphate (mixture of NaH_2PO_4 and Na_2HPO_4) to buffer the solution to pH = 7.2. After the minute had passed, 1 ml of 3.6% PBS was added to restore the osmotic pressure of the solution to the equivalent of 0.9% saline. A further 1 ml of 0.9% PBS containing 1 mM glucose as an energy source and 40 mg/ml DNA-ase to reduce cell clumping was mixed in. This solution was spun at 1200 r.p.m. for

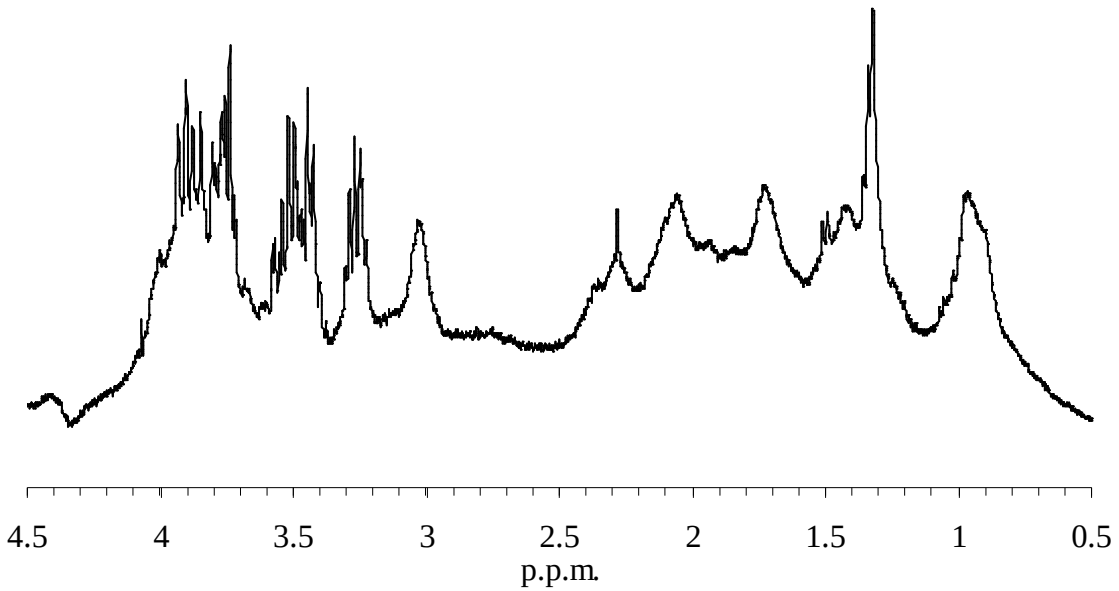

Figure 5.9: 1D spectrum of LPS-activated neutrophils. Acquisition parameters: 2500 Hz spectral width, 4 s TR, 256 transients; total time, 17 min. Processing parameters: 0.5 Hz line broadening.

5 minutes. The supernatant was discarded, leaving a pellet consisting solely of neutrophils.

This pellet was resuspended in 600 µl 0.9% PBS containing1 mM glucose and 40 mg/ml DNA-ase. This suspension was used for the high resolution spectroscopy. On certain occasions, an aliquot was removed, diluted 1:10 with 0.9% PBS and subsequently 1:2 with trypan blue. This permitted cell counting and assessment of cell viability on the basis of trypan blue exclusion.

Conventional water-suppressed 1D and 2D COSY spectra were acquired in the usual manner from a suspension of the cells in D_2O in a 5 mm NMR tube. Some settling of the cells towards the bottom of the tube over the course of the experiments was observed; to check the effects on the spectra were not excessively deleterious, selected experiments had a second 1D spectrum acquired after the 2D had finished for comparison with the one performed first.

5.2.3.2 Results

Cell counting revealed a concentration of 5×10^7 neutrophils/ml in the final suspension (3×10^7 neutrophils in the 600 µl used). The viability determination showed that > 95% of the cells were viable at the start of the NMR protocol.

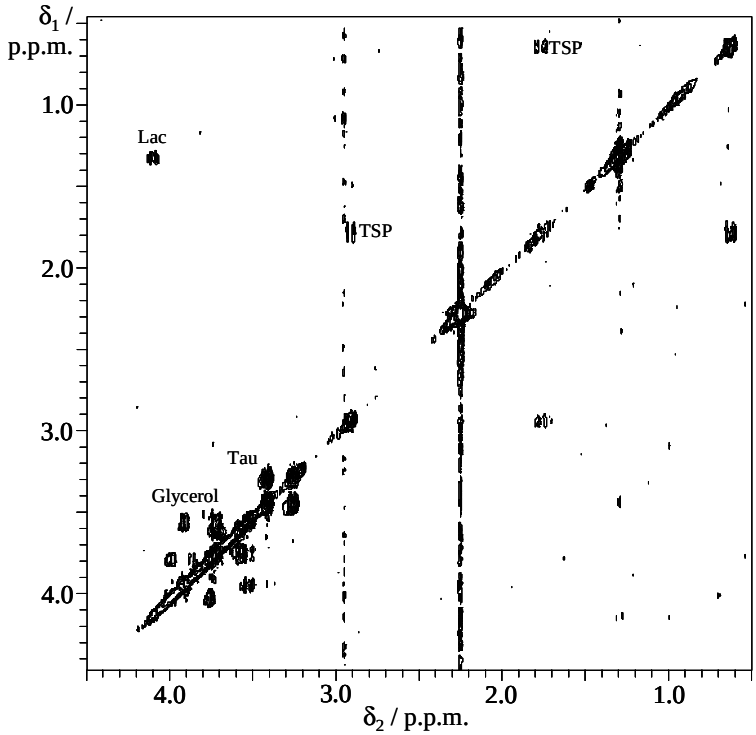

Figure 5.10: COSY spectrum of quiescent neutrophils. Acquisition parameters: 7.5 s TR, 3.0 x 3.0 kHz spectral width, 2 transients per increment, 240 t_1 increments; total time, 2½ h. Processing parameters: sine bell centred at t_1, t_2 = 0.04, 0.1 s, absolute-value mode.

The one-dimensional high-resolution spectrum of the activated neutrophils is shown in Figure 5.9. Several peaks may be distinguished in this spectrum, particularly lactate + lipid at 1.3 p.p.m. (this may very likely be mobile lipid signals[122]), lysine at 1.7 and 3.0 p.p.m. and taurine at 3.2 p.p.m.; other peaks are generally a mixture of several molecules. Nevertheless, no peak attributable to chlorotaurine can be seen: between 3.70 and 3.75 p.p.m., where the unknown singlet appeared in the *in vitro* spectrum, there is merely the edge of several amino acid peaks. The taurine peak at 3.2 p.p.m. consists of more peaks than a triplet, so at least one other molecule is contributing signal to this region; however, this may be attributable to phenylalanine rather than chlorotaurine, as evidenced from the 2D spectrum (see over).

A separate spectrum recorded of a solution of LPS at the concentration used to activate the sample for the above spectrum showed no peaks at all in the 1D spectrum, except for the TSP used as a marker, so a COSY acquisition was not performed on it. This implies that none of the peaks in the activated neutrophil spectra are artefacts coming from the activating solution itself.

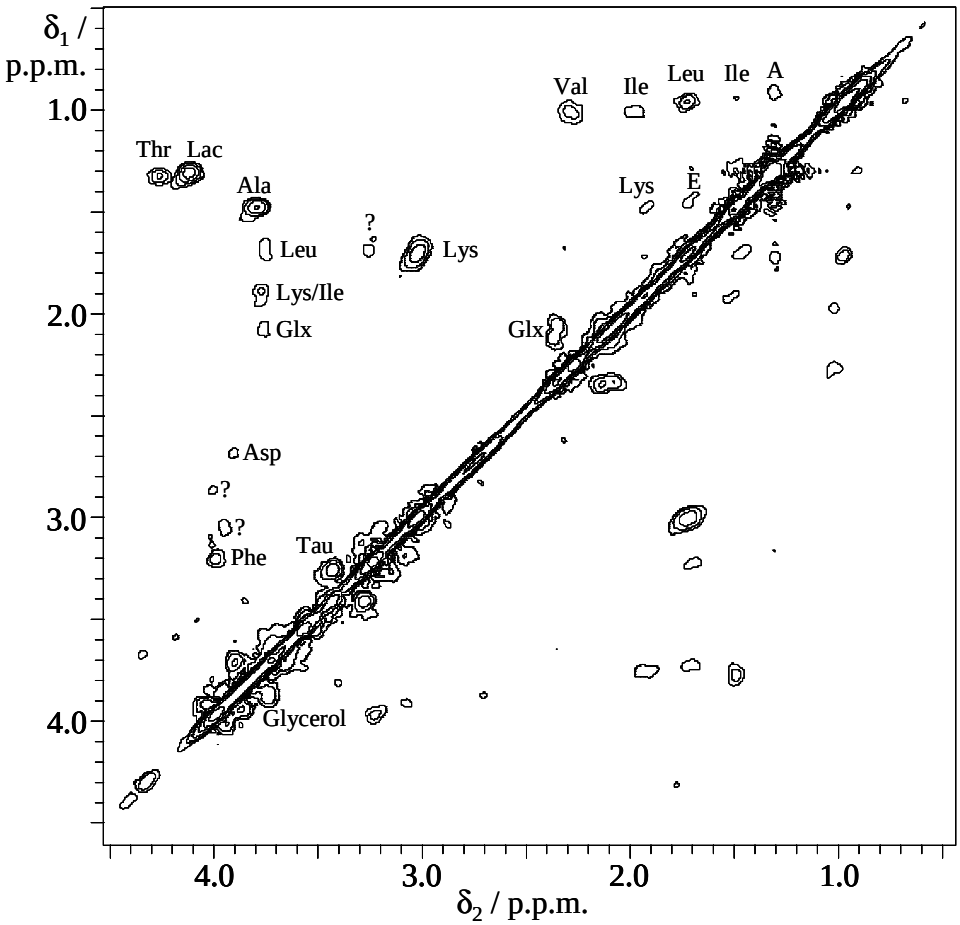

Figure 5.11: COSY spectrum of activated neutrophils. Cross-peaks are labelled with conventional abbreviations. Peaks marked ? are from unknown compounds; those labelled A and E are attributed to lipid signals after May *et al.*[120]. Acquisition parameters: 3 s TR, 2.5 x 2.5 kHz spectral width, 48 transients per increment, 200 t_1 increments; total time, 8 h. Processing parameters: sine bell centred at t_1, t_2 = 0.04, 0.04 s, absolute-value mode.

The COSY spectrum of quiescent neutrophils (Figure 5.10) shows cross-peaks from taurine, lactate and glycerol. Upon activation, the 2D COSY spectrum (Figure 5.11) shows cross-peaks arising from a considerably larger number of molecules, including many common amino acids, lactate and glycerol. There are also two which May *et al.*[120] attribute to lipid signals (labelled A and E both in this figure and the one in their paper).

The most prominent features of this 2D spectrum are the amino acids, particularly lysine at 1.7, 3.0 p.p.m. and alanine at 1.5, 3.8 p.p.m.. There is also a large lactate peak at 1.3, 4.1 p.p.m., although that may be partially due to some cells dying over the course of the experiment. This experiment would suggest that the NMR feature most able to distinguish activated neutrophils from normal brain tissue would be these

Figure 5.12: Image of a 50 μm thick, cresyl violet stained, section of rat brain obtained from a region close to the AD5-IL-1β injection site. The area of intense staining indicates abundant neutrophil presence.

amino acids: lysine is typically present in an ISIS-COSY spectrum of rat brain *in vivo* recorded over two hours or so (see Figure 4.10 for example), but alanine is usually absent due to its lower concentration. The simultaneous appearance of alanine and increase in lysine levels in such a spectrum could be indicative of neutrophil infiltration within the brain.

5.2.4 *In vivo* Study

5.2.4.1 Methods

Neutrophil infiltration was induced in the brain *in vivo* as follows. A male Wistar rat (230 g) was anaesthetised with hypnorm and hypnovel (fentanyl / fluanisone and midazolam, each diluted 1:1 with water); 1.35 ml/kg of both diluted solutions was injected i.p.. An adenoviral vector (AD5-IL-1β) was injected into the left striatum (coordinates from bregma were AP + 1 mm, left 3 mm, depth 4 mm) using a 50 μm-tipped glass pipette. The injection consisted of 10^8 plaque-forming units (PFU) in 1 μl 0.1% BSA in endotoxin-free saline. The AD5-IL-1β adenovirus has previously been shown[123] to result in intense neutrophil influx to the injected striatum and some surrounding cortical areas, as shown in Figure 5.12, a histological section from the brain studied spectroscopically *in vivo*. The recruitment profile over the duration of

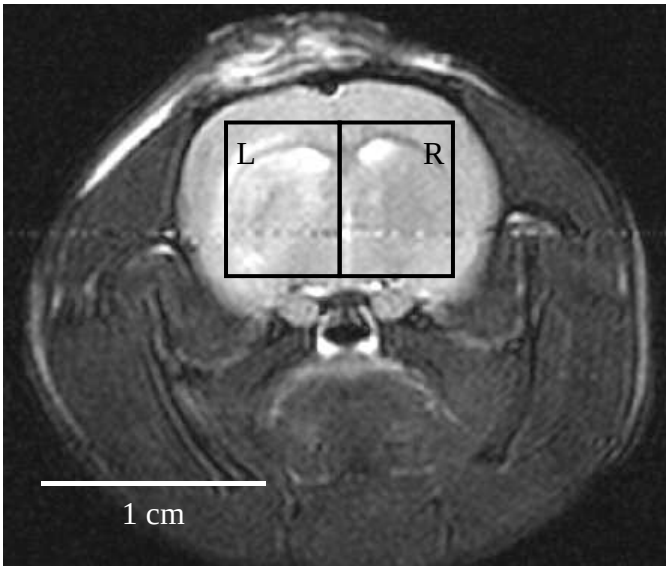

Figure 5.13: Fast spin-echo image of neutrophil-infiltrated rat brain showing the two voxels used for spectroscopy. Acquisition parameters: 7 echoes per FID, TR 3 s, t_E 18 ms, 3.5 x 3.5 cm field of view, 2 mm slice thickness, 128 x 126 data points, 2 transients, 108 s total acquisition time. Processing parameters: zero-filling to 1024 x 1024 points.

the experiment was entirely restricted to neutrophils: no other leukocyte populations were observed in the brains. The rat was allowed to recover and had spectroscopy performed four days later.

Spectroscopy was performed using the usual *in vivo* methods and protocol (see section 4.1.3). Given that neutrophil infiltration was only induced in one half of the brain, the spectroscopy voxel was reduced in size to 6.8 x 5.0 x 5.0 mm^3 and placed only over this half. The contralateral hemisphere was used as an internal control (see image in Figure 5.13 for voxel positioning). This reduction in voxel size by a factor of two naturally reduces the S/N similarly; to observe the familiar range of cross-peaks at comparable S/N requires that data be acquired for four times as long. In principle, appropriate placement of the surface coil specifically over the treated hemisphere should slightly counterbalance this; in practice, any such effects are too small to be significant.

5.2.4.2 Results

A 1D ISIS and 2D ISIS-COSY spectrum was acquired from the voxel in each hemisphere using the standard *in vivo* parameters; the fact that two spectra were acquired increased the total experimental time to around 7¾ hours (this was a non-

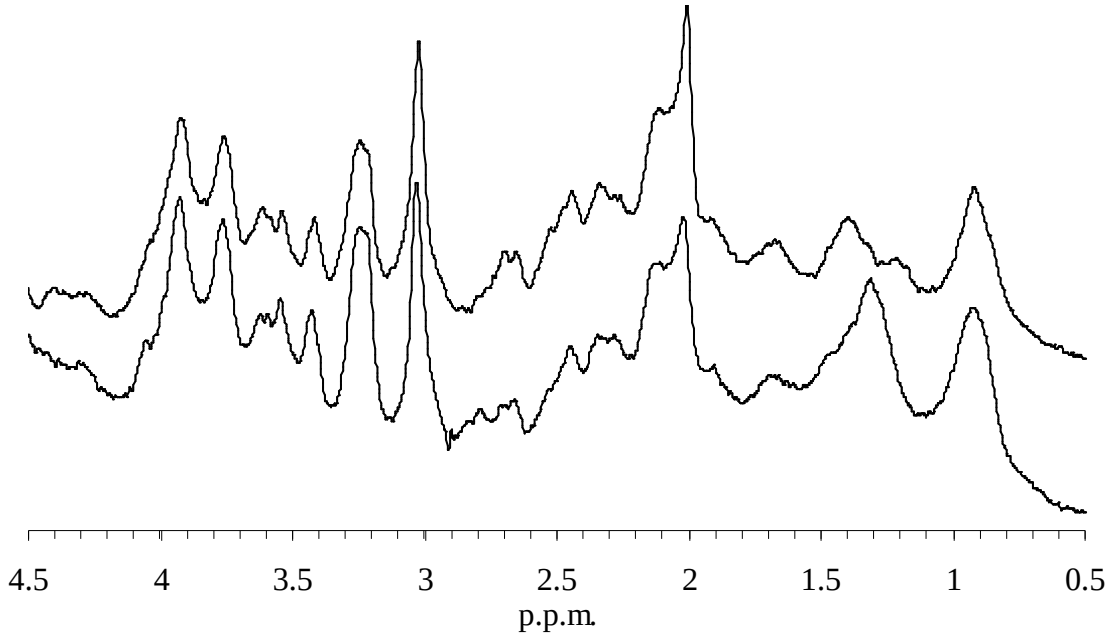

Figure 5.14: One-dimensional spectra from each hemisphere of the brain of a rat treated to induce neutrophil infiltration in the left side. Lower trace: left (treated) side. Upper trace: right (control) side. Acquisition parameters for each spectrum: 5 kHz spectral width, 3 s TR, 256 transients; total time 13 min. Processing parameters: 2 Hz line broadening.

recovery experiment, with the animal being sacrificed whilst still under the anaesthetic and the brain excised for perfusion). The two one-dimensional spectra (Figure 5.14) were similar to each other; the major perceptible difference is a possible greater level of the lipid + lactate signal at 1.3 p.p.m. in the lower (treated) spectrum. There is also some evidence for a decrease in NAA (2.0 p.p.m.) and an increase in choline (3.2 p.p.m.) in the same spectrum.

The two-dimensional spectra (see Figure 5.15) also show a marked similarity in appearance. There are more noise peaks in the spectrum from the left hemisphere, but all remaining peaks exhibit a correspondence between the two spectra. Analysing the spectra quantitatively for each peak, then taking a ratio between the intensities (normalised to the diagonal creatine peak at 3.0 p.p.m.) in the left hemisphere and those in the right gives the figures graphed in Figure 5.16. This shows, for this animal at least, a 30% decrease in the intensity of all three NAA peaks measured and a 48% rise in the choline peak signal in the treated (left) hemisphere versus the control half, with smaller changes in the levels of other metabolites.

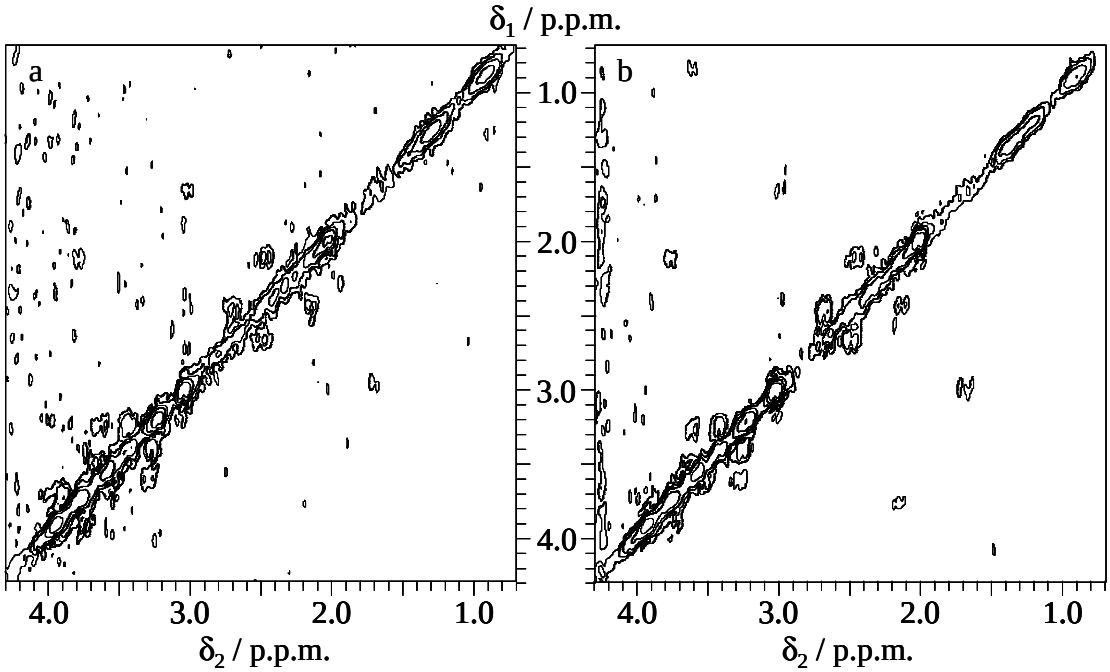

Figure 5.15: 2D spectra from each hemisphere of the brain of a rat treated to induce neutrophil infiltration in the left side. The spectroscopy was performed 4 days after treatment, at approximately peak neutrophil activity. (a) left (treated) side. (b) right (control) side. Acquisition parameters for each spectrum: 2.5 x 2.5 kHz spectral width, 1 s TR, 64 transients per increment, 111 t_1 increments; total time 2 h. Processing parameters: sine bell centred at t_1, t_2 = 0.0275, 0.04 s, absolute value mode.

Alanine could not be detected in the 2D spectrum from either voxel; neither could most of the other amino acids observed in the *in vitro* study of activated neutrophils. The S/N of these spectra from relatively small voxels is insufficient to raise the cross-peaks above the noise level. No evidence for the presence of chlorotaurine can be detected either; this is not surprising given its absence from the spectra in the *in vitro* study.

In this pilot study, the sample size of only one prevents any definite conclusions from being drawn, particularly from the smaller changes observed. Nonetheless, the increases observed in the lysine and taurine signals in particular would be consistent with the spectra observed from activated neutrophils in the preparatory study described above. The two-dimensional quantification is supported by the qualitative observations made from the one-dimensional spectrum about NAA and choline. The increase in lactate levels speculated about there is not backed up by the 2D work: no lactate cross-peak may be seen in either 2D spectrum. However, a cross-peak from

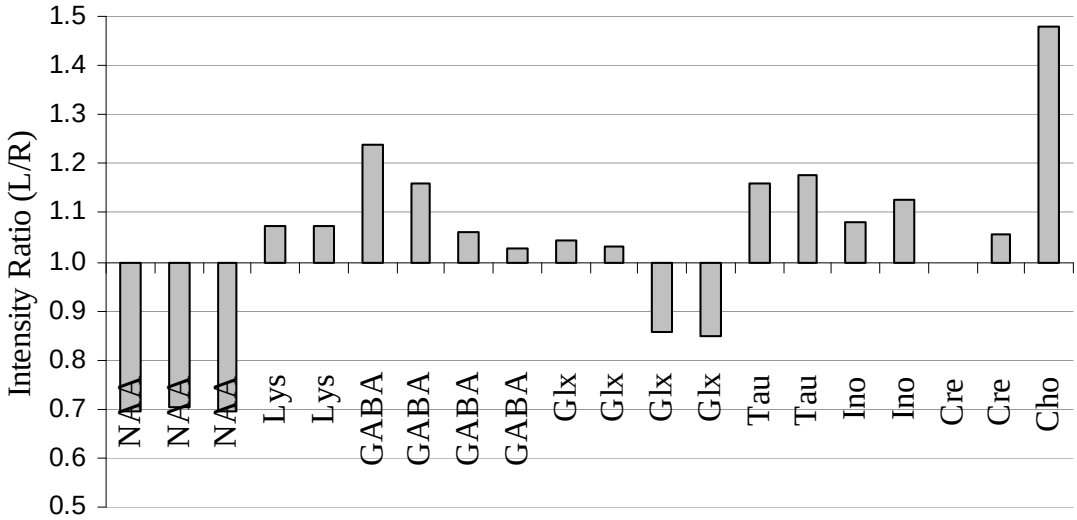

Figure 5.16: Ratio of intensity of each peak in the ISIS-COSY spectra from the two hemispheres of the brain of a rat treated to induce neutrophil infiltration in the left side. Multiple references to the same metabolite correspond to different peaks in the spectrum; the peaks are ordered as for Table 5.1.

lipids (analogous to the one labelled A in Figure 5.11) has been observed in a later repetition of the *in vivo* experiment, recording spectra from the injected hemisphere only, with an increased acquisition time of 7 h. This has been confirmed using chloroform/methanol extractions of the brain[122].

The physiological meaning of the NAA changes is unclear. Two possible reasons for the decrease can be envisaged: firstly, the presence of the neutrophils, which lack NAA, in large numbers has displaced normal brain tissue and hence reduced the NAA signal levels. Perhaps more likely is that the insult that triggered neutrophil recruitment or the neutrophils themselves have damaged the brain cells and caused them to lose their NAA; NAA is often considered to be a marker of healthy neurones[124-126], although it is also present in other brain cell types[127].

The choline peak is made up of contributions from several molecules, principally glycerophosphorylcholine and phosphorylcholine[128]. Phosphatidylcholine also contributes signal, but has a very short T_2 value; free choline is usually a very small proportion of the signal. These molecules, phosphatidylcholine in particular, are associated with cell membranes. Changes in the choline peak levels are often associated with alterations of membrane composition[57]. Activated neutrophils have very active membrane turnover[120] allied with phagocytosis, so the finding of an

increased choline peak signal in the hemisphere containing neutrophils is reasonable, and concurs with the lipid observations discussed earlier.

5.2.5 Conclusions

Inflammation is an important and complex process involved in dealing with challenges to normal tissue function. One of the major cell types involved with the inflammatory response is neutrophils that are recruited from the bloodstream to the site of the inflammation. Detecting them in the brain *in vivo* is extremely problematic, so magnetic resonance markers of activated neutrophils were sought. The first suggestion was chlorotaurine, whose NMR spectral properties were characterised in section 5.2.2. A study of isolated human neutrophils activated *in vitro* failed to show detectable levels of this compound, but did reveal a distinctive pattern of cross-peaks in the COSY spectrum, attributed mainly to various amino acids and some lipids.

Attempts to find *in vivo* markers for neutrophils in the brain produced several results that were consistent with reasonable expectations (increase in taurine, choline and lipids; decrease in NAA; other changes too small to be reliable). However, none of them could be stated as distinctive of neutrophils, a "fingerprint" for them. The S/N in the spectra was insufficient to observe and quantify as many molecules as would be desired. With an improvement on that front, there is a distinct possibility that the continuation of this work will uncover useful markers of inflammation that can be detected by two-dimensional magnetic resonance *in vivo*. Once markers have been identified, it might be more time-efficient to develop a spectral editing sequence to actually detect them rather than using the full 2D acquisition each time.

5.3 Human Application

Adaptation of the pulse sequence to make it applicable to human investigations on a whole-body magnet is vital if the technique is to be used in the future in research on volunteers and patients and ultimately as a diagnostic tool. There are various considerations to take into account in the adaptation from a small-bore high-field system, and these are dealt with first. The next section demonstrates the *in vitro* testing of the modified sequence. This is followed by preliminary spectra obtained from human volunteers.

Ethical approval was obtained from the Central Oxford Research Ethics Committee (COREC) prior to the human experiments, and each subject gave their informed consent.

5.3.1 Pulse Sequence Adaptation

5.3.1.1 Considerations

There are fundamental differences working on a wide-bore 2 T whole-body spectrometer as compared to a 7 T narrow-bore one suited to rodent experiments. The lower field strength means that different spectral widths are required. This is of little consequence in one-dimensional spectra or the directly detected dimension (F_2) of two-dimensional spectra – fewer points are acquired with a greater dwell time between each – but for the indirect dimension (F_1), fewer t_1 increments are required for the same resolution (measured as Hz/point), implying that a reduced experimental time may be obtainable.

The lower magnetic field strength also means that the T_1 times for metabolites will be shorter. This manifests itself in more rapid equilibrium recovery after a pulse, and also in increased losses from relaxation during the pulse sequence. T_2 times are rather less field-dependent; a modest increase is expected at lower field (for example, the creatine + phosphocreatine peak has a T_2 of 165 ms at 4.7 T in rat brain[43], whereas in the human brain at 1.5–2 T, it is 210 ms (average value from 5 papers[129-133])). The linewidth attainable with a good shim from a typical voxel is reduced (in terms of Hertz) at lower field whilst the *J*-coupling is independent of field; this implies that the peaks of a *J*-coupled multiplet are potentially better resolved at 2 T than at 7 T. However, strong coupling effects are more significant then, which can complicate spectra. The greater separation of peaks within a multiplet is particularly useful for cross-peaks in COSY spectra where cancellation between positive and negative components of the multiplet can cause significant reduction of the observed signal.

The r.f. transmit/receive coils used for human brain studies are obviously much larger than those used for small animal work. A larger sample volume is available, which improves the S/N; however, the coils are much less sensitive than smaller ones, rather counteracting the larger sample volumes. Along with the reduced sensitivity, much more power is needed to obtain a 90° pulse: using 800 W power, a 90° pulse is

approximately 400 μs on the whole-body system, whereas 20 W pulse power produces a 160 μs 90° pulse on the high-field system.

In conjunction with this, safety regulations[134, 135] require that the mean rate of energy absorption by the human brain is less than 3 W/kg (to keep local tissue heating to less than 1 °C); a reasonable estimate of adult brain mass is ~ 2 kg, leading to a maximum mean power deposition of ~ 6 W. This becomes a consideration for pulse sequences like ISIS-COSY with moderately rapid repetition rates and high pulse powers (such as those used for adiabatic pulses, e.g. sech pulses). When the final version of the sequence was tested *in vivo*, it was found not to be above about 50% of this maximum permitted mean power level.

Using humans as subjects for study also increases the chances of sample motion, which can result in imperfect cancellation in differencing two transients (as is used in ISIS) and increased t_1 noise, which is largely unavoidable. The total available experimental time is also reduced by considerations of comfort. The target was set at a total examination of less than one hour, to include all imaging, shimming, pulse power calibration, etc.; this limits the time for 2D spectroscopy to about 40 minutes.

Considering all of the above factors, it was felt to be feasible to obtain reasonable two-dimensional ISIS-COSY spectra from the human brain within a sensible period of time.

5.3.1.2 Sequence Order

The order of the modules decided in section 4.1.4.2 as best for the high-field spectrometer needs to be reconsidered for the whole-body system in the light of the considerations discussed above. Each of the modules is substantially longer, resulting mainly from the greater pulse durations employed in this implementation. Combined with the shorter T_1 values at lower field, this results in more longitudinal relaxation during each module. Thus, if the water suppression is performed prior to the outer-volume suppression, there is much greater scope for it to relax away from its optimally suppressed levels during the OVS module and result in less efficient water suppression. Conversely, if the OVS module precedes the water suppression, there is the potential for more contamination of the voxel signal with unwanted outer-volume signals.

a

$$\text{OVS} - \boxed{\beta_1 - \tau - \beta_2 - \tau - \beta_3 - \tau - \beta_4 - \tau -} \quad \downarrow$$

b

$$\boxed{\beta_1 - \tau - \beta_2 - \tau - \beta_3 - \tau + \tau_{extra} - \beta_4 - \tau -} \text{OVS} \quad \downarrow$$

Figure 5.17: WET optimisation for the whole-body system implementation. OVS represents the outer-volume suppression module (140 ms duration); τ is the time between the start of successive WET pulses (45.5 ms); the arrows (↓) indicate the point at which the water magnetisation is desired to be zero. The parameters optimised were the flip angles β_1 - β_4 and (for b) the additional delay τ_{extra}. The results are presented in Table 5.3. (a) OVS – WS ordering; (b) WS – OVS ordering. A box is drawn around the water suppression module in each case.

Whilst calculations may be performed to attempt to approximate the relative importance of these two effects, they are best examined experimentally. The contribution of inner- and outer-volume water to the spectrum was estimated by replacing the standard 1D excitation with a 1D imaging (profile) readout. This enables the positional origin of the signal to be assessed. The results are presented and discussed below (sections 5.3.2.3 (*in vitro*) and 5.3.3.1(*in vivo*)).

5.3.1.3 Pulses

The pulses used for the whole-body implementation of ISIS-COSY were as follows. The inversion pulses used in the ISIS module were adiabatic full-passage sech pulses, as for the high-field implementation. A duration of 10 ms was used, leading to a bandwidth of 1.5 kHz. The outer-volume suppression used 512-point pseudo-random noise pulses, 44 ms long, with a bandwidth also of 7.5 kHz of which the central 20% (1.5 kHz) was unaffected by the pulse. The WET water suppression module used 256-point Gaussian pulses (truncated at the 1% signal level), of 30 ms duration and 80 Hz half-height. The COSY excitation was provided by a pair of 400 μs rectangular pulses.

5.3.1.4 WET Parameters

The WET water suppression was optimised again (see section 3.4) for the different timing involved in this implementation. With 30 ms pulses, 15 ms crusher gradients and 500 μs gradient rise-time, there was a total of 45.5 ms between successive pulses. The T_1 range optimised over was set at 0.2–3 s; the $\mathbf{B_1}$ field variation accounted for remained at ± 10%. Two situations were optimised (see

Case	β_1(°)	β_2(°)	β_3(°)	β_4(°)	τ_{extra}(ms)
OVS–WS	86	100	80	165	0
WS–OVS	90	90	90	175	185

Table 5.3: Optimal parameters for the WET water suppression sequence on the whole-body magnet. Flip angles are given to the nearest degree. The minimisation parameters used were as follows: τ_1, τ_2 = 45.5 ms, τ_3 = 45.5 ms + τ_{extra}, τ_4 = 45.5 ms (first case), 185.5 ms (second case), $|\mathbf{B_1}|$ = 90% to 110% of nominal in 9 steps, T_1 = 0.2 to 3.0 s in 9 steps.

Figure 5.17): firstly, the WS module appearing after the OVS module, so the water magnetisation should be zero immediately after the WET sequence; secondly, WS before OVS, so the zero-crossing should be some 140 ms (the duration of the OVS module) after the end of the WS module. To allow for this second case, an extra delay τ_{extra} was introduced into the WET sequence between the third and fourth pulses whose duration was also included in the optimisation process. The results of this process are shown in Table 5.3.

Note that the two parameter sets are quite different: the first is very similar to the high-field sequence optimal parameters (Table 3.3), while the second resembles an inversion-recovery type sequence. The first three pulses approximately null the magnetisation, which recovers a certain amount during the τ_{extra} delay and is inverted by the fourth pulse. During the OVS module, it then recovers again back towards zero. Provided that T_1 is long compared to the delay times, this procedure can results in almost perfect nulling of the water signal. Here, some of the water T_1 will not be sufficiently long for this, so some residual magnetisation will remain.

5.3.2 *In vitro* Testing

5.3.2.1 Localisation

The localisation of the sequence was tested using a small (5 cm diameter) spherical phantom filled with water. A 5 x 5 x 5 cm^3 voxel was selected encompassing the sample and a 1D ISIS spectrum acquired. This was used as a baseline to compare subsequent spectra with. Six further spectra were recorded, one with the voxel offset just to each side of the phantom in each direction. The spectra were examined for evidence of signal infiltration from the phantom. In none of the six

was more than about 1% of the original signal level observed, so it was concluded that the localisation was functioning adequately.

As a further test of the stability of the sequence, the power of the ISIS inversion pulses was set to zero and a spectrum acquired from the centre of the 10 cm spherical phantom. With no inversion, the eight transients of the ISIS cycle should cancel completely and leave no signal. In practice, less than 1% of the signal remained after the whole cycle, again confirming good performance of the localisation module.

5.3.2.2 Signal level

Confirmation was sought that the sequence was not only excluding outer-volume signals effectively but also including as much as possible of the inner-volume signal and not losing any significant quantity owing to, for example, poor inversion efficiency. A small spherical water phantom was used, placed in the centre of the magnet. Firstly, a 1D pulse-and-collect (unlocalised) spectrum was obtained to define the maximum possible signal recovery from the sample. It was performed using a long TR to ensure the sample was fully relaxed between each of the eight transients acquired. Next, a voxel slightly larger than the phantom was positioned on a scout image. This was used to acquire two spectra (using the same receiver gain as the first spectrum), one using ISIS, the other with STEAM for comparison; these also used eight transients and the same long TR.

The results were exactly as expected. The ISIS sequence attained virtually 100% signal recovery; the STEAM sequence about 50% arising from the loss associated with the use of a stimulated echo in the localisation. This is further substantiation that the ISIS module is functioning correctly.

5.3.2.3 Sequence Order

Two variants of the ISIS pulse sequence were programmed, one with the OVS before the WS module, the other with the order reversed. Each had its excitation module replaced with a 1D profile imaging readout (1000 Hz/cm gradient strength, 256 complex points, 40 kHz spectral width, 6.4 ms acquisition time). Both WET modules were loaded with their optimised parameters (see section 5.3.1.4). A series of profiles was recorded on the 10 cm spherical glass phantom for each sequence with

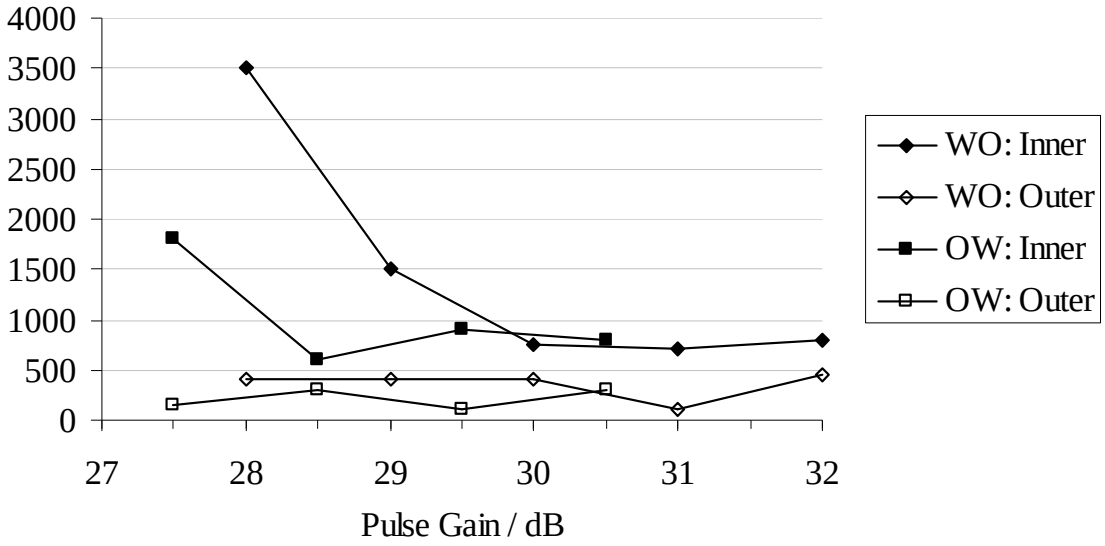

Figure 5.18: Graph showing the maximum residual water magnetisation (arbitrary units) from the inner and outer volume regions after the pulse sequences WS–OVS–ISIS–Profile (WO) and OVS–WS–ISIS–Profile (OW) as a function of the 90° pulse gain.

the power used for the WS module varied around the nominally correct value. The profiles obtained were similar in appearance to those shown in Figure 5.22. The maximum amplitude of the signal inside and outside the voxel was measured and is shown on the graph in Figure 5.18.

This shows that there is little to choose between the two sequence variants in terms of the residual magnetisation at the best 90° pulse power for each. However, the ordering with the OVS before the WS produces more consistently good suppression of the water, especially outside the selected voxel. This is surprising, given the conclusions of section 4.1.4.2, that whichever module comes second is likely to have better performance than the one coming first in the sequence. The graph shows generally reduced outer-volume signal levels from the OVS–WS module order. Since the inner-volume signal is similar for the two arrangements, it seems likely that better performance will be obtained using this order.

These measurements are rather dependent on the T_1 of the sample in question, so the applicability of the results in the brain is uncertain. Nevertheless, the tests were a useful basis for the *in vivo* testing using the same approach, which is discussed later (section 5.3.3.1).

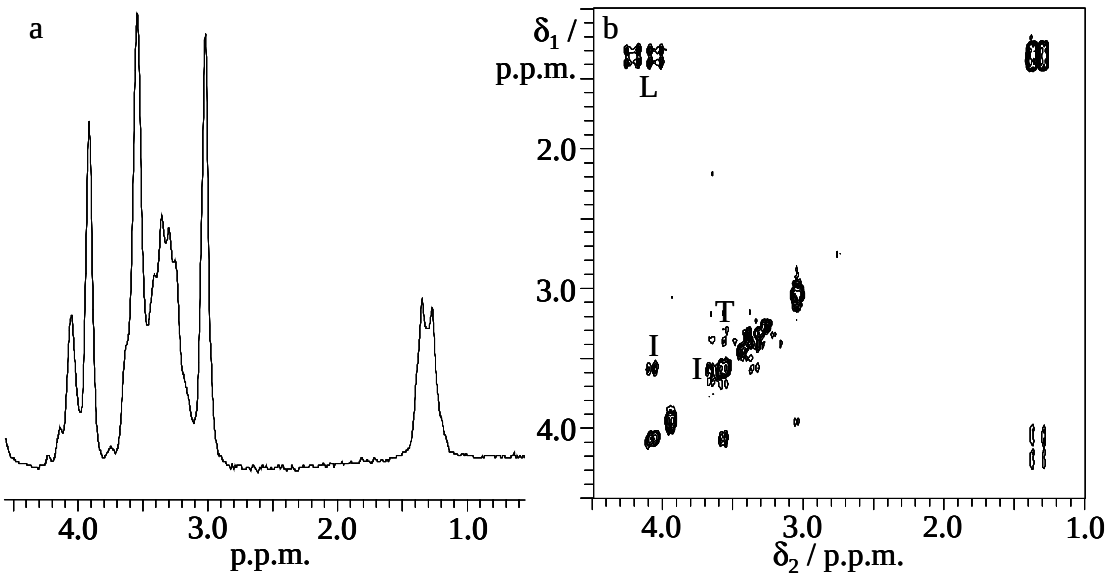

Figure 5.19: Spectra recorded on a 5 x 5 x 5 cm^3 voxel in the mixed metabolite phantom on the whole-body spectrometer. (a) ISIS. Assignment: δ = 1.3 p.p.m., lactate; δ = 3.0, creatine; δ = 3.25, taurine + *myo*-inositol; δ = 3.4, taurine; δ = 3.5–3.6, *myo*-inositol; δ = 3.9, creatine; δ = 4.1, *myo*-inositol + lactate. Acquisition parameters: 500 Hz spectral width, 8 transients, 5 s TR; total time 40 s. Processing parameters: 1 Hz line broadening. (b) ISIS-COSY. Key: L, lactate; T, taurine; I, *myo*-inositol. Acquisition parameters: 500 x 500 Hz spectral width, 16 transients per increment (including phase-sensitive acquisition in F_1), 64 t_1 increments, 2.5 s TR; total time 43 minutes. Processing parameters: sine bell centred at t_1, t_2 = 64, 500 ms; absolute-value mode.

5.3.2.4 Whole Sequence

Evaluation of the whole sequence *in vitro* was undertaken in the usual 10 cm spherical glass phantom containing a 50 mM solution of creatine, taurine, *myo*-inositol and lithium lactate. Once a voxel had been selected from scout images and shimmed using STEAM, the water suppression was optimised. A 1D ISIS spectrum was then recorded, shown in Figure 5.19a. This shows the expected distribution of peaks. Because the *J*-coupling is much larger compared to the separation in peaks and the linewidth at this lower magnetic field strength, the signal from molecules like *myo*-inositol appears much broader than on the 7 T system. This is why the taurine and *myo*-inositol signals appear as a broad peak between 3.2 and 3.6 p.p.m. (with a spike from the *myo*-inositol [1,3] and [4,6] protons, which all resonate at between 3.5 and 3.6 p.p.m.).

An ISIS-COSY spectrum of the same sample is presented in Figure 5.19b. This differs slightly in appearance from how an equivalent spectrum on the 7 T system

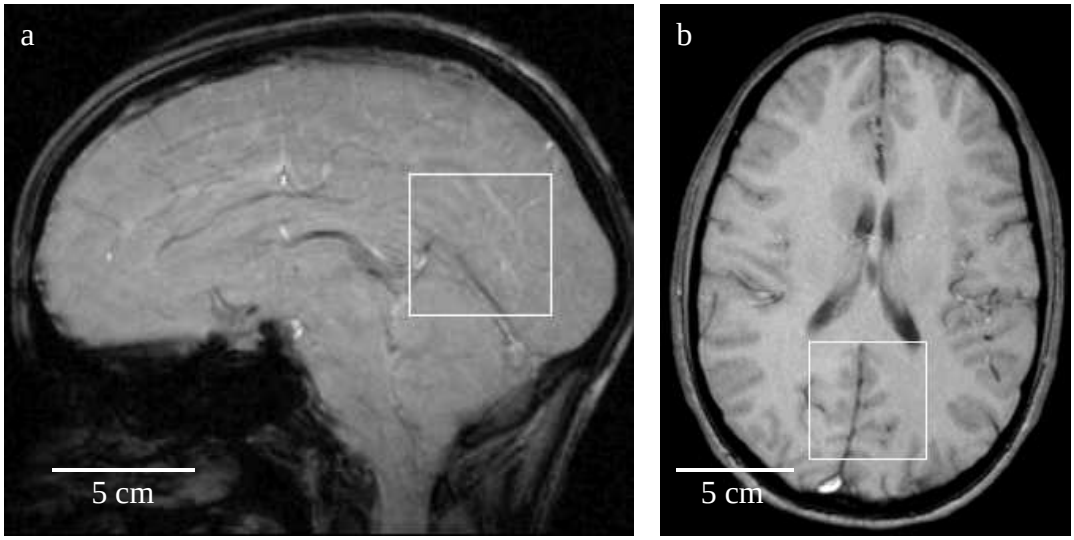

Figure 5.20: Images showing position and size of voxel used for spectroscopy in the human brain. (a) Sagittal gradient-echo scout. Acquisition parameters: 65 ms TR, 10 ms t_E. (b) T_1-weighted gradient-echo axial image, one of five parallel slices. Acquisition parameters: 500 ms TR, 10 ms t_E, 5 mm slice slickness, 2.5 mm inter-slice gap, 80° pulse flip angle, 25.6 cm field of view, 256 x 256 data points.

would look. Particularly noticeable is the resolution of the eight peaks within the lactate cross-peak at (1.3, 4.1 p.p.m.) which would appear as one large peak on the higher-field spectrometer. (This may be readily appreciated by considering that the peaks are separated by J Hz, which is independent of $\mathbf{B_0}$ field strength; the linewidth is approximately proportional to the $\mathbf{B_0}$ field as inhomogeneity of this field is the dominant factor in the linewidth, and the inhomogeneities in the phantoms will be similar. This means that at higher field the peaks are not so well resolved.) All the expected peaks are present, although the taurine cross-peak at (3.2, 3.4 p.p.m.) is weaker than might be hoped, based on the experience of the 7 T phantom spectra. The S/N for the lactate diagonal peak at (1.3, 1.3 p.p.m.) was 450:1, and for the cross-peak at (1.3, 4.1 p.p.m.) was 150:1.

These spectra show considerable promise for *in vivo* application. Their timescale is realistic and quality perfectly acceptable. They also show the different appearance of peaks at this field: multiplets appear much broader, so cross-peaks in the ISIS-COSY spectrum are more spread out; individual components of the peaks are also discernable, and diagonal peaks also show substructure. These last two points mean that a little caution must be exercised when determining cross-peaks in a spectrum: to take a trivial example, there might appear to be a cross-peak at (1.33, 1.34 p.p.m.) in

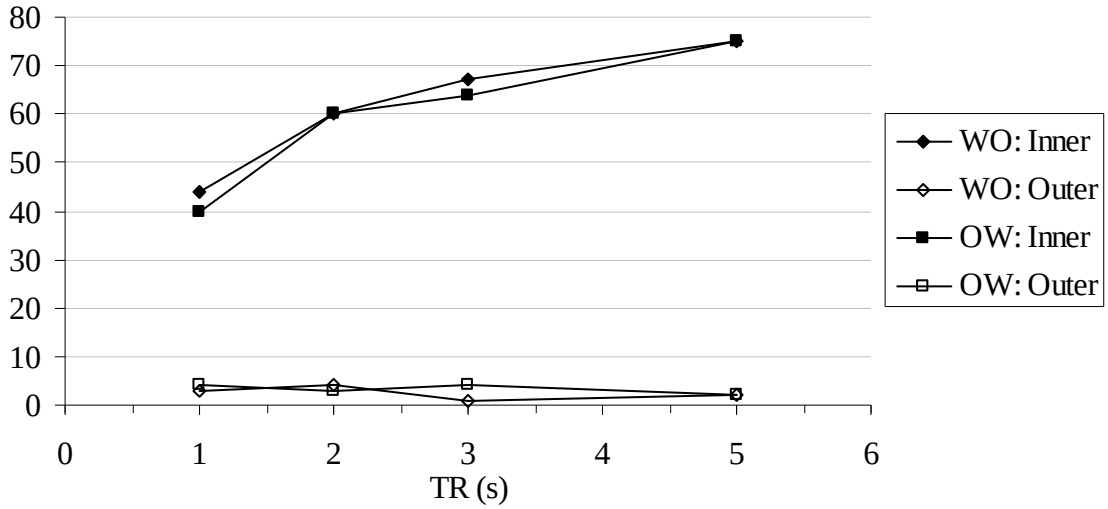

Figure 5.21: Graph showing levels of maximum water signal amplitude *in vivo* (arbitrary units) in the inner- and outer-volume regions as a function of TR and sequence order. Key: WO, WS–OVS order; OW, OVS–WS order.

the above 2D spectrum, whilst in fact this is one of the four sub-peaks within the diagonal peak of lactate.

5.3.3 Human Testing

5.3.3.1 Sequence Order & Repetition Time

An *in vivo* investigation of the sequence order and repetition time (TR) and their effects on the level of contamination on the spectrum by outer-volume signal and water was undertaken. The same two pulse sequences as employed for the *in vitro* testing were used. All profiles were acquired in the brain of a normal volunteer; a 5 x 5 x 5 cm^3 voxel was selected centrally in the occipital lobe from a scout image (see Figure 5.20), the 90° pulse power calibrated and the voxel shimmed using a STEAM sequence to < 7 Hz.

The first part of the study was concerned with the effect of different repetition times on the level of outer-volume contamination. A series of four profiles with TR = 1, 2, 3 and 5.5 s was acquired for each of the two sequences. The water suppression was turned off to increase the outer-volume signal level to facilitate the measurements. Figure 5.21 displays a graph of the levels of maximum water signal amplitude within and outside the voxel. Note that this is the maximum amplitude and does not account for the proportion of the outer-volume containing unwanted signal (e.g., Figure 5.22b has a similar outer-volume amplitude to Figure 5.22a, but much

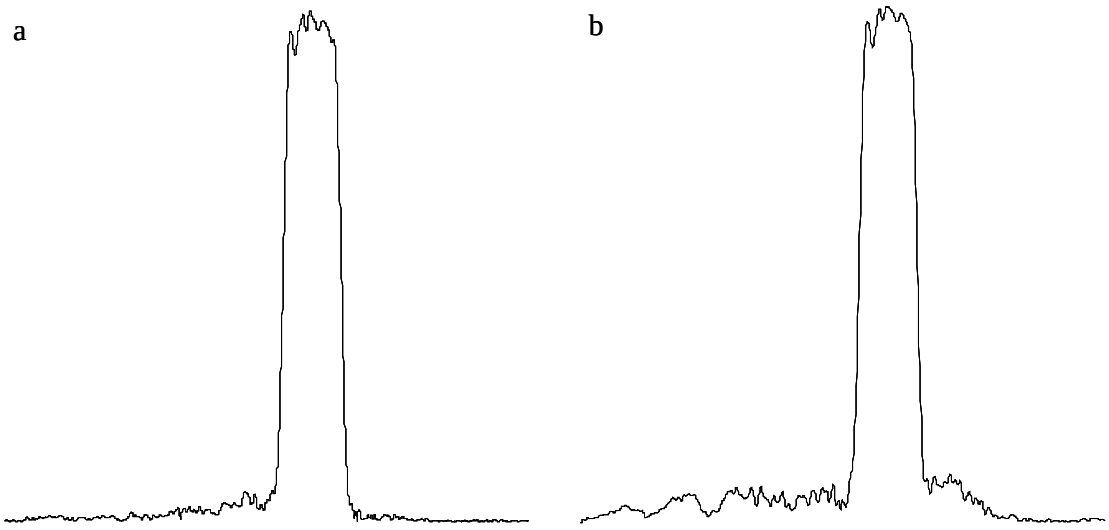

Figure 5.22: Comparison of the efficiency of outer-volume suppression using (a) OVS–WS and (b) WS–OVS sequence ordering *in vivo*. Profiles were acquired with water suppression turned off (pulse powers set to zero). The intense band of signal in each profile arises from within the 5 cm-long voxel; the remainder comes from outside it. Acquisition parameters: 8 transients, 2 s TR. Processing parameters: absolute-value mode. Each profile has the same vertical scale.

more of the outer volume produced this unwanted signal). At TR = 1 s, the best OV suppression was afforded by the WS–OVS ordering; at the longer TR of 2 s, the converse is true (see Figure 5.22; compare the level of outer-volume signal in the two profiles). The best outer-volume suppression overall was provided by a TR of 2 s and the OVS–WS module ordering (Figure 5.22a).

The second portion related to assessment of the water suppression as a function of pulse power and module order. All experiments were carried out at TR = 2 s as this produced the best outer-volume suppression. A profile was acquired, this time with the water suppression on, for a series of WS pulse powers for each module order. A graph showing the approximate levels of outer- and inner-volume water signal is provided in Figure 5.23. It is evident that the best water suppression, especially for inner-volume water, was given by the OVS–WS ordering, as might be expected. Within the voxel, there is about a fivefold decrease in the residual water signal compared to the WS–OVS ordering.

It was concluded that the best parameters to use for acquisition *in vivo* on the whole-body system were a TR of 2 s and the OVS–WS ordering. Notice how the saturation-recovery curve displayed by the upper traces in Figure 5.21 shows that

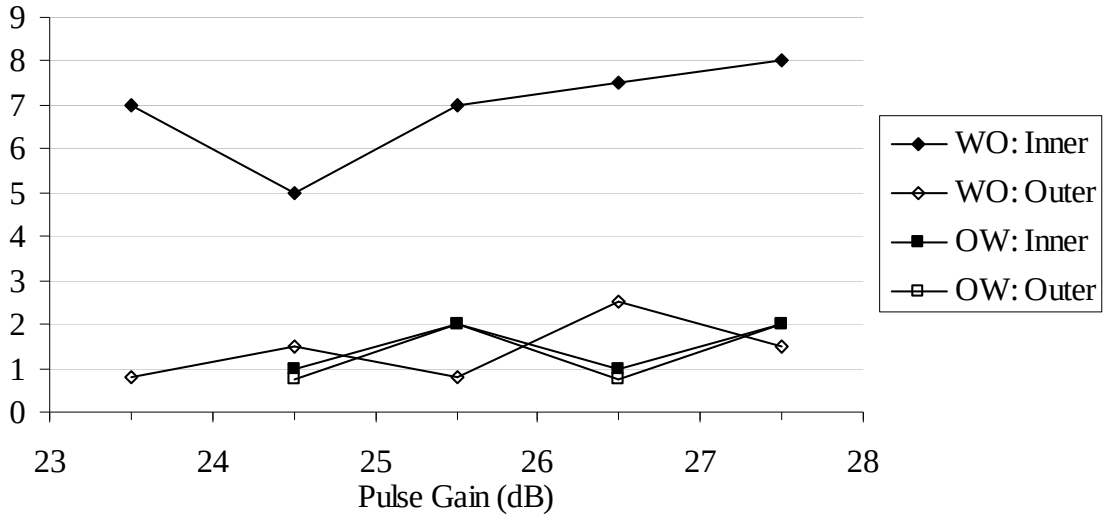

Figure 5.23: Graph of the residual water signal amplitude (arbitrary units, but same scale as used in Figure 5.21) in the inner- and outer-volume regions as a function of gain of the first WET pulse and the sequence order. Key: WO, WS–OVS order; OW, OVS–WS order.

50% more inner-volume signal is achieved by a TR of 2 s rather than 1 s. The best that could be expected from a doubling of the number of transients acquired, made possible by halving the TR, is a 41% improvement (a factor of $\sqrt{2}$) in S/N, so it is not worth the more rapid acquisition, especially as this increases the r.f. power deposition for the subject.

5.3.3.2 Whole Sequence

The whole sequence was tested in volunteers. Initial experimental sessions concentrated on one-dimensional spectra, of which Figure 5.24 shows an example. This shows the full range of peaks that could be expected from normal brain. As is usual for *in vivo* ISIS spectra, there is a lot of underlying broad signal from macromolecules such as proteins, which increases the challenge of quantification to the point where it would be extremely unreliable from this 1D spectrum. There are just too many overlapping peaks to permit reliable assignment of concentrations to particular molecules.

It is for this reason that the 2D ISIS-COSY sequence was designed. Its greater resolving power should be able to distinguish cross-peaks from many of the molecules identified in the 1D spectrum above. Unfortunately, no 2D spectrum of good quality has yet been recorded from the human brain using ISIS-COSY. An example spectrum is provided in Figure 5.25. Substantial lipid contamination is evident in this spectrum,

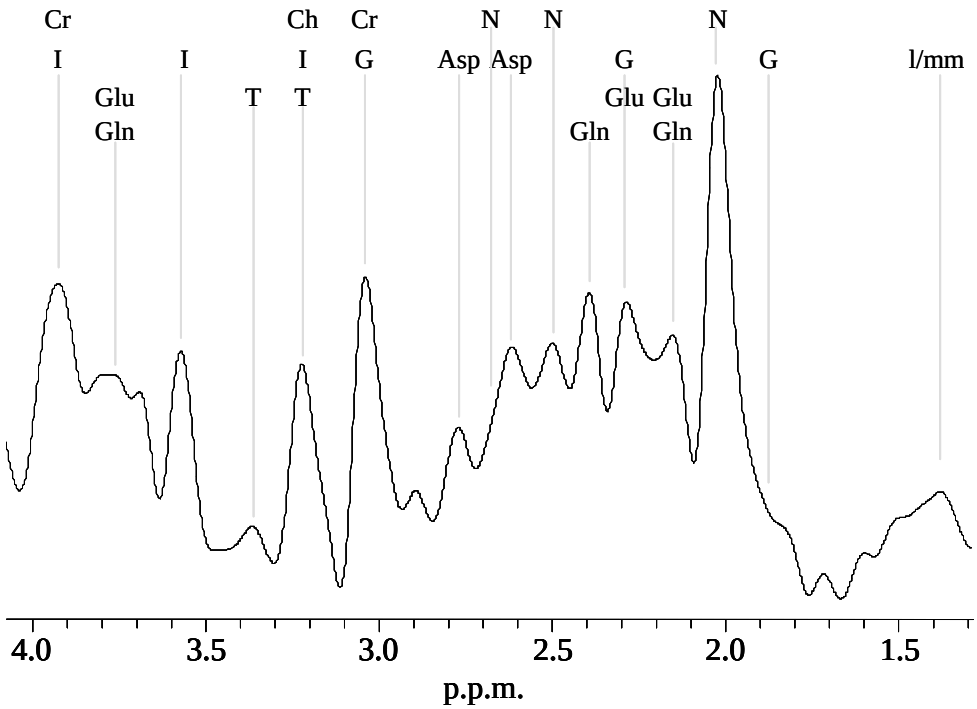

Figure 5.24: ISIS spectrum of a 5 x 5 x 5 cm^3 voxel in human brain. Key: Cr, creatine + phosphocreatine; Ch, choline; N, NAA; I, *myo*-inositol; G, GABA; Asp, aspartate; l/mm, lipids/macromolecules; Glu, glutamate; Gln, glutamine; T, taurine. Acquisition parameters: 64 transients, 3 s TR; total time, 3½ minutes. Processing parameters: Lorentz-to-gauss transform (10 Hz resolution enhancement, 0.15 s Gaussian weighting).

and no cross-peaks can be discerned. Given the reasonable S/N of the *myo*-inositol peak on the diagonal, and the *in vitro* phantom data previously discussed, some evidence of cross-peaks might be expected, but no combination of processing parameters could be found to show them. Improving the S/N sufficiently to make the spectra useful in the human brain will require some combination of hardware (e.g., a surface coil, preferably quadrature, to receive; a stronger $\mathbf{B_0}$ field would also contribute.) and acquisition (e.g., larger voxel, increased experimental time) measures.

In the human application of ISIS-COSY, many technical challenges have been raised and subsequently surmounted, but a good spectrum has remained elusive thus far. However, demonstration that the technique works well in the rat brain (section 4.1) indicates that the problem is likely to be one of implementation rather than fundamental to the sequence.

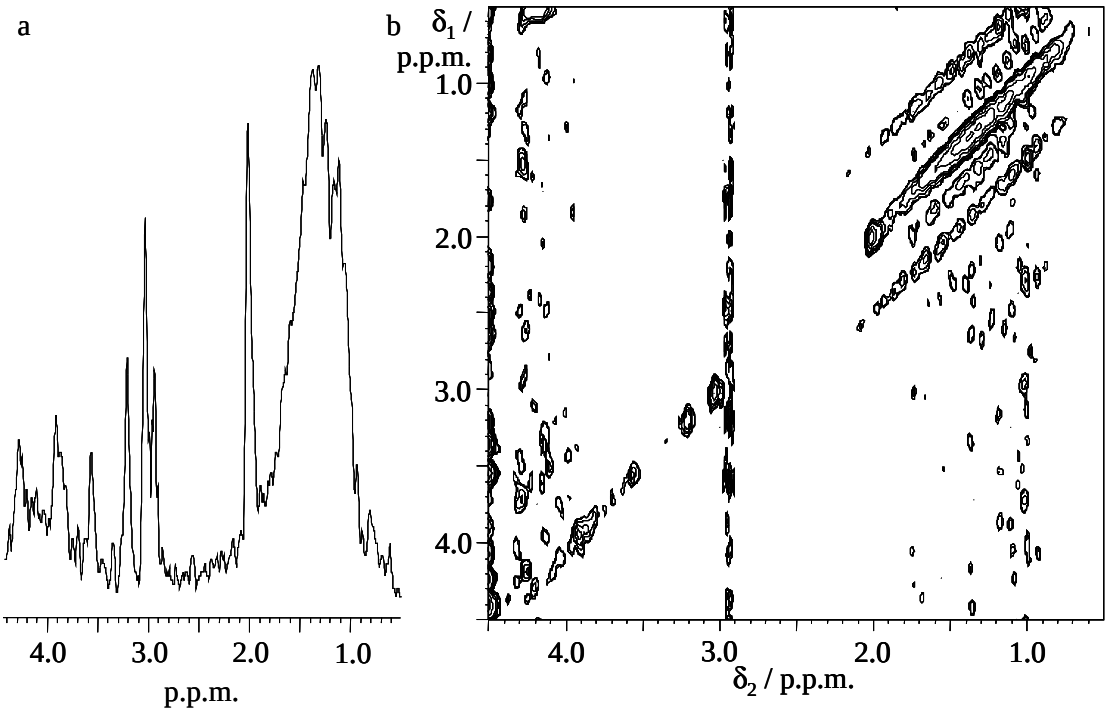

Figure 5.25: ISIS-COSY spectrum of human brain. (a) Projection onto the δ_2 axis; (b) 2D spectrum. Acquisition parameters: 500 x 500 Hz spectral width, 2 s TR, 16 transients for each of 64 t_1 increments; total acquisition time 42 min. Processing parameters: sine bell centred at t_1, t_2 = 64, 250 ms. Assignment of diagonal peaks and projection: δ = 1.0-1.7 p.p.m., lipid; δ = 2.0, NAA; δ = 3.0, creatine + phosphocreatine; δ = 3.2, choline; δ = 3.6, *myo*-inositol; δ = 3.9, creatine + phosphocreatine. The line along δ_2 = 2.95 p.p.m. appears as a result of the failure of the automatic d.c. offset correction software.

5.3.4 Conclusions

The ISIS-COSY pulse sequence has been adapted for application in the human brain on a whole-body spectrometer. Testing of the various modules making up the sequence yielded excellent results and showed that the best ordering of the modules is the same as for the high-field system, OVS–WS–ISIS–COSY. The whole sequence has been shown to produce good spectra *in vitro*, both 1D ISIS and 2D ISIS-COSY. The use of the sequence *in vivo* has demonstrated very good 1D spectra, but a good 2D spectrum has hitherto not been acquired.

The ultimate goal of this particular application has yet to be achieved. Nevertheless, the foundations are now in place for the human application of ISIS-COSY and all the potential benefits of this.

Chapter 6: Conclusions

6.1 ISIS-COSY

The development and testing of the ISIS-COSY pulse sequence was discussed at length in section 4.1. The sequence has been shown to produce useful spectra within a timescale viable for *in vivo* studies. Quantitative analysis of the spectra has also been demonstrated to give concentrations of cerebral metabolites in good agreement with published data. Further validation was provided in the application (described in section 5.1) to measure changes in metabolic concentrations as a result of chronic treatment with vigabatrin: highly significant increases in GABA and the glutamate + glutamine peak were observed, as expected, with possible changes in NAA and taurine additionally.

Comparison of the technique with VOSY-COSY showed that better S/N was consistently obtained using ISIS-COSY. This was to be expected given that the stimulated echo in VOSY discards 50% of the available signal.

The fundamental drawback of the technique is the S/N available in the spectra. Were this higher, the acquisition time could be accordingly reduced, or the range of metabolites observable increased correspondingly. To some extent, improvements in the hardware such as probe and coil design (e.g., a quadrature surface coil to receive) will help. Narrower linewidths may result from implementation of an automated gradient-based shimming routine, which would improve sensitivity also. One of the disadvantages of COSY spectra is the antiphase nature of the cross-peaks: the linewidths *in vivo* at 7 T (~12 Hz) are greater than typical *J*-coupling constants, so some signal is lost to cancellation within each multiplet.

It may be that an alternative excitation sequence such as SUPER-COSY[136] or indeed, subject to power constraints, TOCSY[34], that yield in-phase cross-peaks would prove to be more sensitive for excitation. However, the spin-echo delays in SUPER-COSY (a total of 4Δ, where $\Delta = 0.3/J \approx 40$ ms for $J \approx 7$ Hz) might lose much signal from T_2 decay. NOESY would be extremely problematic *in vivo*: the combination of motion (both microscopic and macroscopic) during the T_M period, dominating solvent NOEs from the water and a cross-peak S/N per unit time typically much lower than that obtained from COSY would be a severe challenge. Separation of molecules

according to their diffusion properties (e.g., DOSY) offers slightly better potential; however, most molecules that are present in appreciable quantities in the brain are similarly small, so would possess comparable diffusion coefficients. Molecules such as proteins that would diffuse at very different rates are present in low concentrations, so would be problematic to detect in a reasonable period. There is again the trouble of motion during the diffusion periods, particularly as the sequences are intentionally sensitive to motion in order to detect diffusion. Needless to say, however, any of these excitation sequences would be compatible with the OVS–WET–ISIS magnetisation preparation sequence.

The major conclusion of this section of the research is that ISIS-COSY gives useful spectra from the rat brain containing cross-peaks from several molecules not readily resolved in a one-dimensional spectrum within a quite reasonable period of time. These peaks may be quantified to give concentrations of the metabolites.

6.2 ISIS-JRES

One alternative excitation sequence investigated at length (see section 4.2) was 2D *J*-resolved spectroscopy. This produces spectra that have a much lower spectral width requirement in F_1, so fewer t_1 increments are required for good resolution in that dimension. They suffer from reduced spread of the peaks, making the assignment of a peak at a particular position in the spectrum more ambiguous. In the rat brain, the spectra are very broad to the extent that no off-axis peaks could be discerned except lactate. The S/N was reasonable, slightly greater then JPRESS in identical conditions, but the resolving power was poor.

The off-axis peaks in a *J*-resolved spectrum are disadvantaged by the fact that the magnetisation for each proton is spread throughout the multiplet, which in *J*-resolved spectroscopy can occupy a significant proportion of the spectral width in F_1. If strong coupling is a factor, as it is for several metabolites at 2 T, this will further distribute the magnetisation around still more peaks.

An intrinsic problem with separating peaks on the basis of their *J*-coupling in the brain is that many, if not most, *J*-coupling constants for the molecules of interest fall in the range 6–8 Hz. This is not surprising – the *J*-coupling between adjacent CH_2

groups in freely rotating carbon chains is about 7 Hz – but it reduces the likely separation of peaks in the *J*-resolved spectrum.

Two-dimensional *J*-resolved spectroscopy did not prove to be informative as a sequence for resolving metabolite peaks in the brain, but it was a constructive exercise, demonstrating the flexibility of the OVS–WET–ISIS magnetisation preparation sequence and giving the chance to verify techniques such as the use of composite pulses in the brain.

6.3 Comparisons

The use of ISIS rather than STEAM or PRESS for localising the NMR signal to the region of interest within the sample has several advantages. Principally, there are no spin- or stimulated-echoes required, so there is no signal loss from T_2 relaxation or *J*-modulation effects (see discussion in section 1.5). STEAM also suffers from a 50% signal loss from the stimulated echo. Another advantage that ISIS has over PRESS is that the adiabatic sech pulses available to ISIS as 180° inversion pulses have a good slice profile with sharp edges, whereas the sinc pulses typically used for the 180° refocusing pulses in PRESS perform relatively poorly (see simulation in Figure 3.1). This can make a PRESS voxel relatively poorly defined, and also wastes some of the signal available from within the voxel.

The principal disadvantage that ISIS suffers over STEAM and PRESS is the fact that it is a difference technique, relying on eight transients to locate the signal from the region of interest. The dynamic range problem was addressed in section 4.1.1.2; further difficulties are caused by motional artefacts (arising from incomplete cancellation of outer-volume signal). It is also inconvenient that a different pulse sequence must be used for shimming, although the advent of automated shimming procedures will reduce this issue. ISIS needs more careful preparation than STEAM or PRESS, but can produce spectra with peak intensities more faithful to the concentrations of molecules within the brain. The absence of T_2 filtering increases crowding in the 1D spectrum with all the additional peaks, but is a significant asset to a 2D sequence capable of resolving these extra peaks.

There are numerous issues surrounding the use of COSY versus *J*-resolved excitation sequences, many of which have been discussed earlier in this thesis. The

separation of peaks is generally greater in a COSY spectrum; the spectral width, number of t_1 increments required and total acquisition time can be much less for *J*-resolved. Some of the resolution difficulties for the latter arise from the clustering of *J*-coupling constants of most metabolites around 7 Hz, reducing the spread of peaks in the F_1 dimension. The *J*-resolved spectra are also more prone to artefacts from mis-calibrated pulses, which can be ameliorated by the use of phase cycling or composite pulses, and strong coupling, which is intrinsic to the spectrum and cannot be removed. The final analysis has to be of spectra from the brain, and their ability to resolve peaks from different molecules. In this respect, the COSY spectra were vastly superior to the *J*-resolved spectra.

Spectral editing, introduced in section 1.4, is an alternative means to observe peaks from overlapping peaks in a crowded 1D spectrum. The principle is that the intensity of one peak from a particular molecule may be altered with a selective r.f. pulse directed at a different peak in the same molecule that is coupled to the first. If two spectra are acquired, one with this perturbation off and another with it on, and the difference calculated, most of the spectrum is cancelled, leaving the edited peaks behind.

As mentioned in the introduction, there are two main shortcomings with this approach. The first is the difficulty in finding a suitably isolated peak to use for the selective pulse: if any other peaks share the resonance frequency, the protons they are coupled to will co-edit with those in the desired molecule, which complicates the procedure. The second downside is the need to know which molecule is of interest before performing the experiment. This removes one of the benefits of NMR, that molecules that are not necessarily of interest are quantified as well as those being sought: unexpected changes are observed along with any anticipated ones. Two-dimensional NMR such as ISIS-COSY retains this positive aspect. For example, in the vigabatrin study (section 5.1), if the NMR experiment used had been a GABA editing sequence, the changes in the glutamate + glutamine peak would have been overlooked, as would possible alterations in other metabolites such as NAA and taurine.

Spectral editing requires much less acquisition time than 2D NMR, which is an advantage, particularly *in vivo*. On balance, it is probably preferable to use spectral

editing to monitor one or two metabolites for which editing is possible, and to use a 2D sequence to observe a greater number, or when the exact nature of the anticipated metabolite changes in a particular application is unknown.

Two-dimensional localised spectroscopy, and ISIS-COSY in particular, has a wide range of potential uses and applications *in vivo*. It has the ability to follow the concentrations of many important cerebral metabolites such as amino acids non-invasively, permitting serial studies on individual animals. This could reduce the numbers of animals needed for measuring the effects of certain interventions and decrease biological variability between samples by allowing the same subject to be studied repeatedly. Improvements in S/N (e.g., from better r.f. coils, shimming, acquisition methods, data handling, etc.) can only increase the usefulness of ISIS-COSY and the range of situations where it provides valuable information about the metabolic state of the brain *in vivo*.

Such spectroscopic methods would be extremely beneficial in the study of many multifaceted disorders, particularly those affecting the central nervous system, such as Huntington's, Alzheimer's and Parkinson's diseases. The genetic factors in many of these are becoming increasingly understood; the ability to follow biochemical changes to the brain *in vivo* in a non-invasive manner would complement this admirably. The changes are likely to affect many metabolites, so a universal approach like 2D NMR has much to offer.

6.4 Summary

Two novel pulse sequences for localised two-dimensional spectroscopy *in vivo* have been developed, tested and applied in the brain. Of these, ISIS-COSY is considerably more promising than ISIS-JRES. It has proved capable of resolving peaks in the 2D spectrum from several metabolites in the rat brain not separately observable in the 1D localised pulse-and-collect spectrum, within a timescale reasonable for *in vivo* investigations. These spectra are also suitable for quantitative analysis.

The technique may be applied to a wide variety of situations, two of which were developed in this thesis. Quantitative changes in brain GABA levels, and other metabolites, were observed in the rat brain upon chronic treatment with vigabatrin. A

study on neutrophil infiltration into the brain showed some interesting changes comparing the metabolic profile of neutrophils *in vitro* with the normal brain; the *in vivo* results, due to a lower S/N, showed fewer differences from the control, but some interesting observations were nonetheless made. This is an ongoing application, and future experiments should hopefully be able to demonstrate NMR markers for neutrophil infiltration *in vivo*.

Future applications could include studies of many different brain disorders, from dementia to cancer, in both animal models and human subjects. It is hoped that ISIS-COSY will become a valuable weapon in the armoury of the *in vivo* NMR spectroscopist.

Appendix A: High-Resolution Metabolite Spectra

The high resolution ^{1}H NMR spectra of fifteen molecules thought to be potentially observable in the brain *in vivo* are shown below, together with Vigabatrin, the drug used in the study in Chapter 5:. For each molecule, four spectra are shown (as per section 2.2.4), labelled a-d clockwise from the top left: (a) 1D; (b) COSY, sine-bell weighting, absolute-value mode; (c) COSY, exponential weighting, phase-sensitive mode; (d) *J*-resolved, exponential weighting, rotated and symmetrized, absolute-value mode.

Alanine

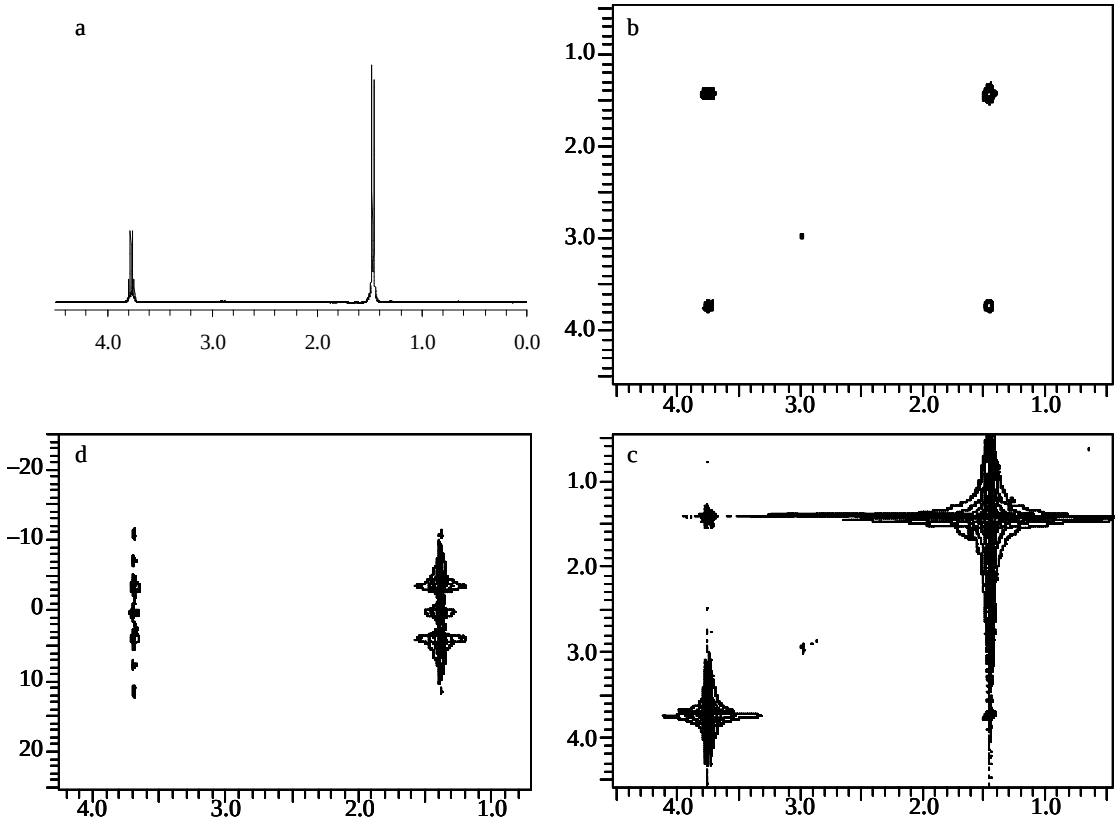

Choline

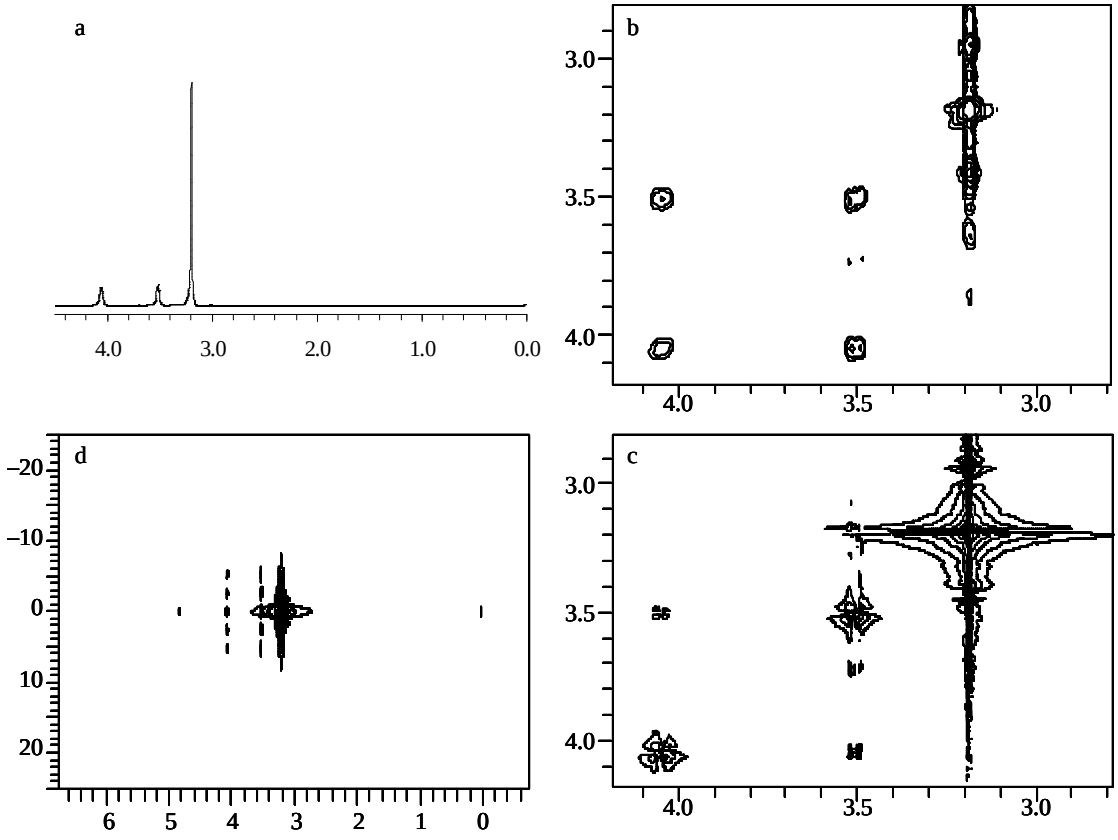

Creatine

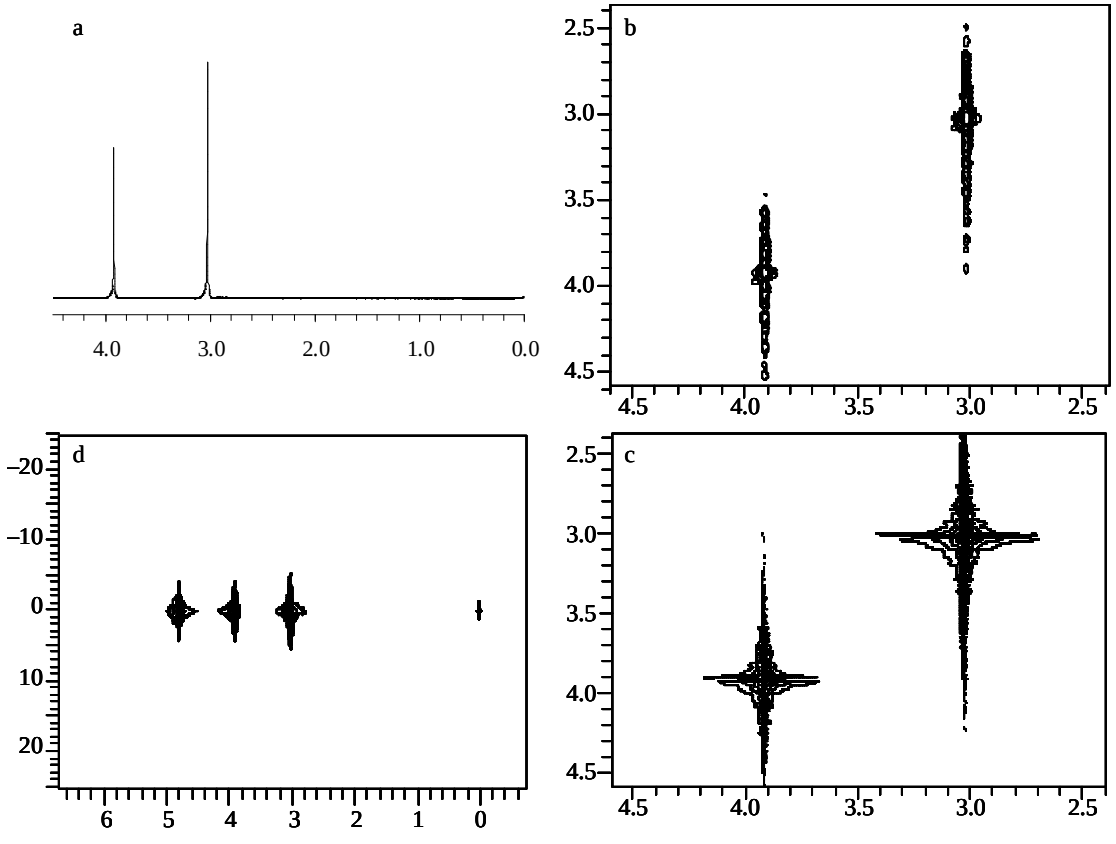

GABA

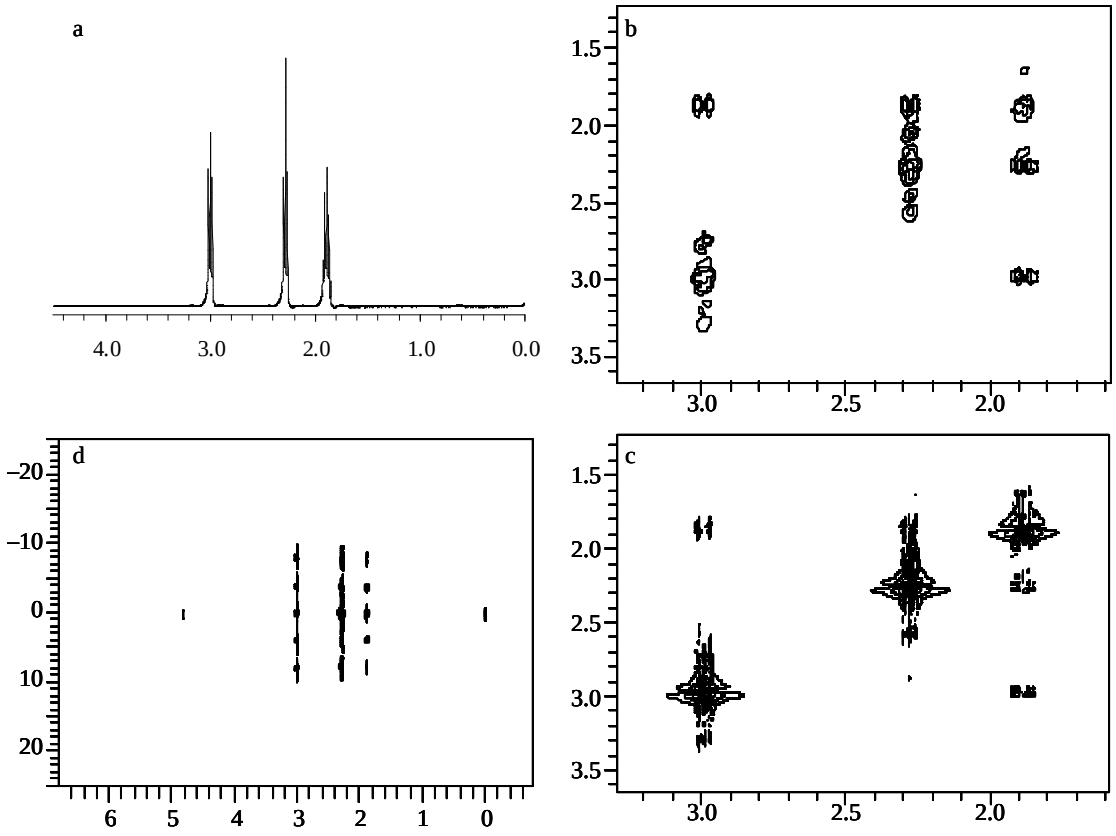

Glucose

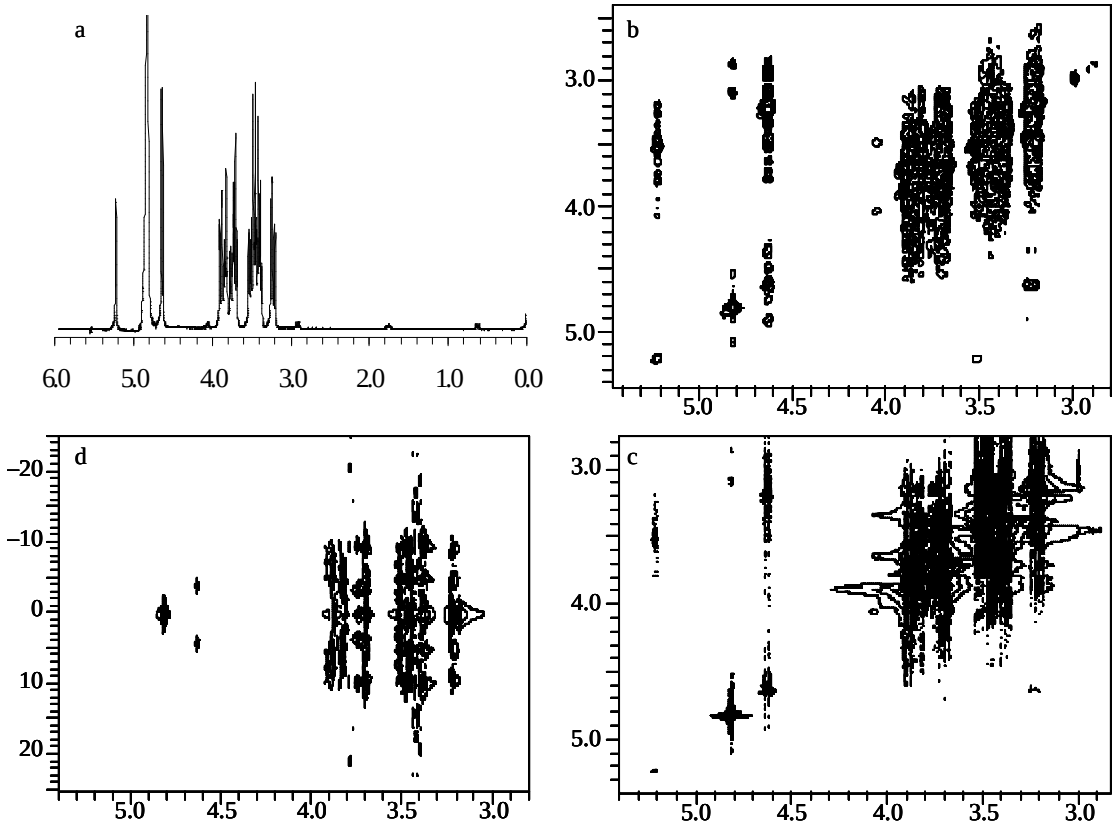

Glutamate

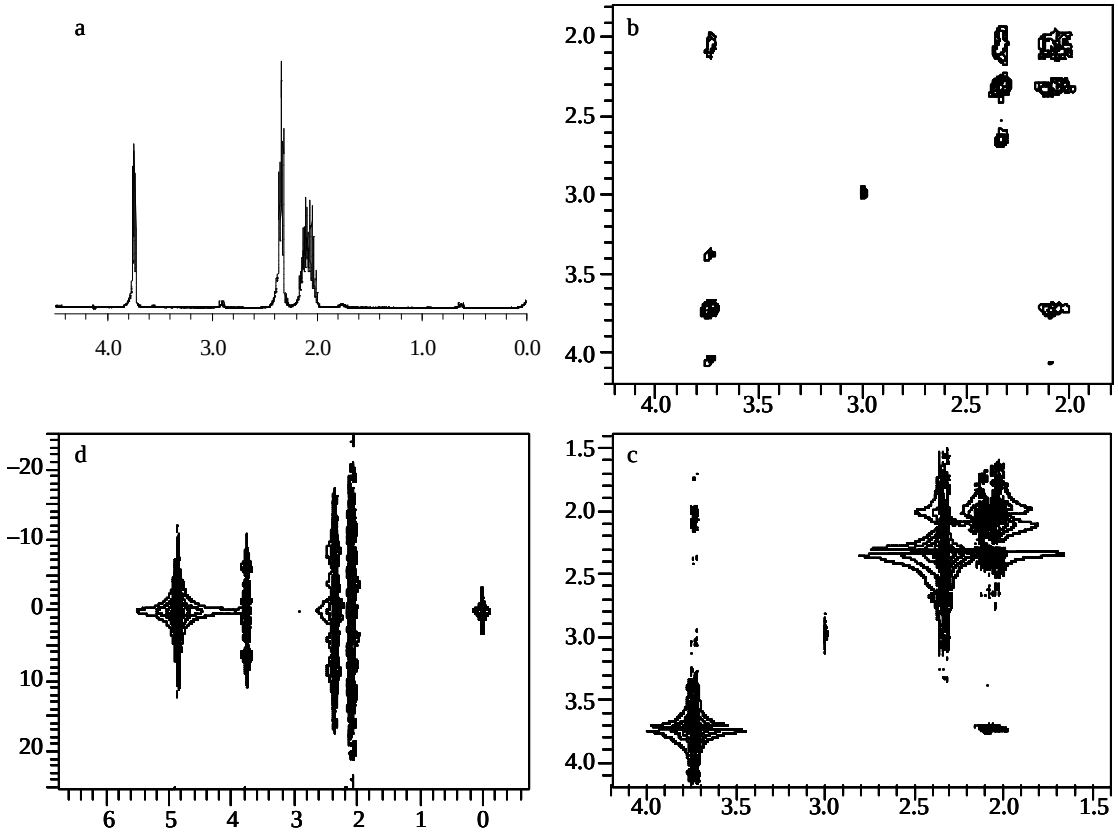

Glutamine

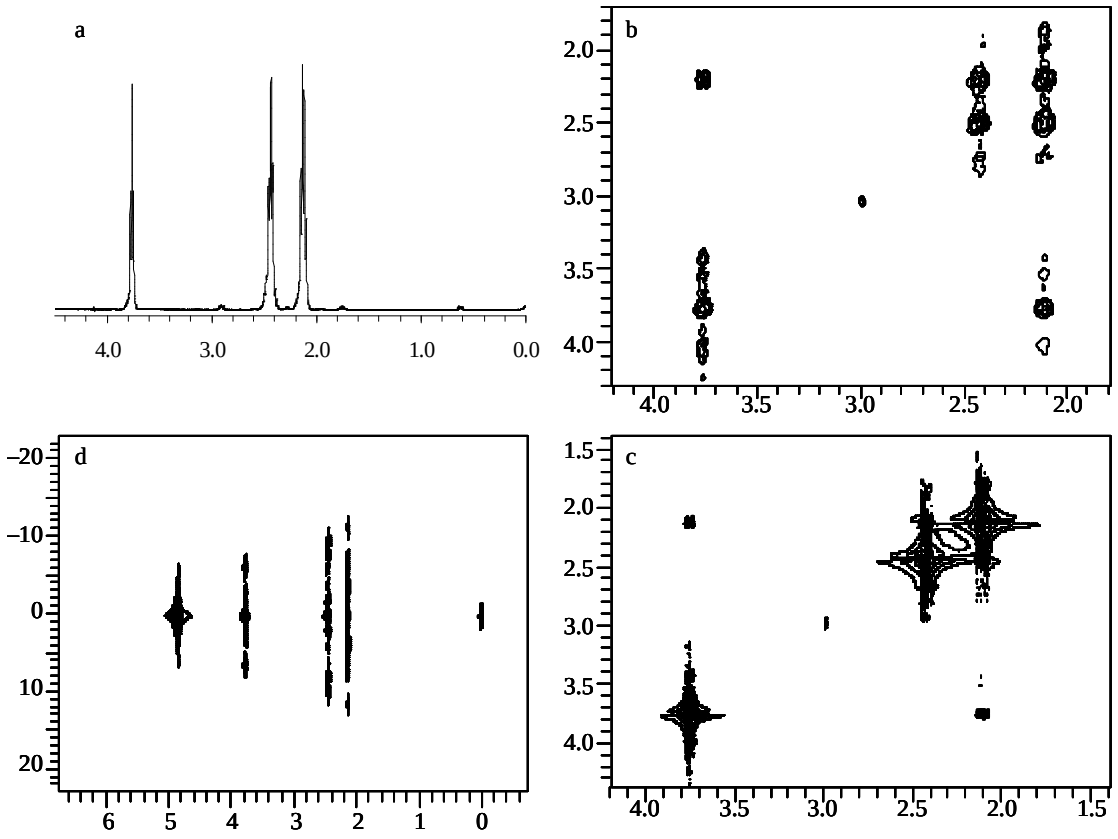

myo-Inositol

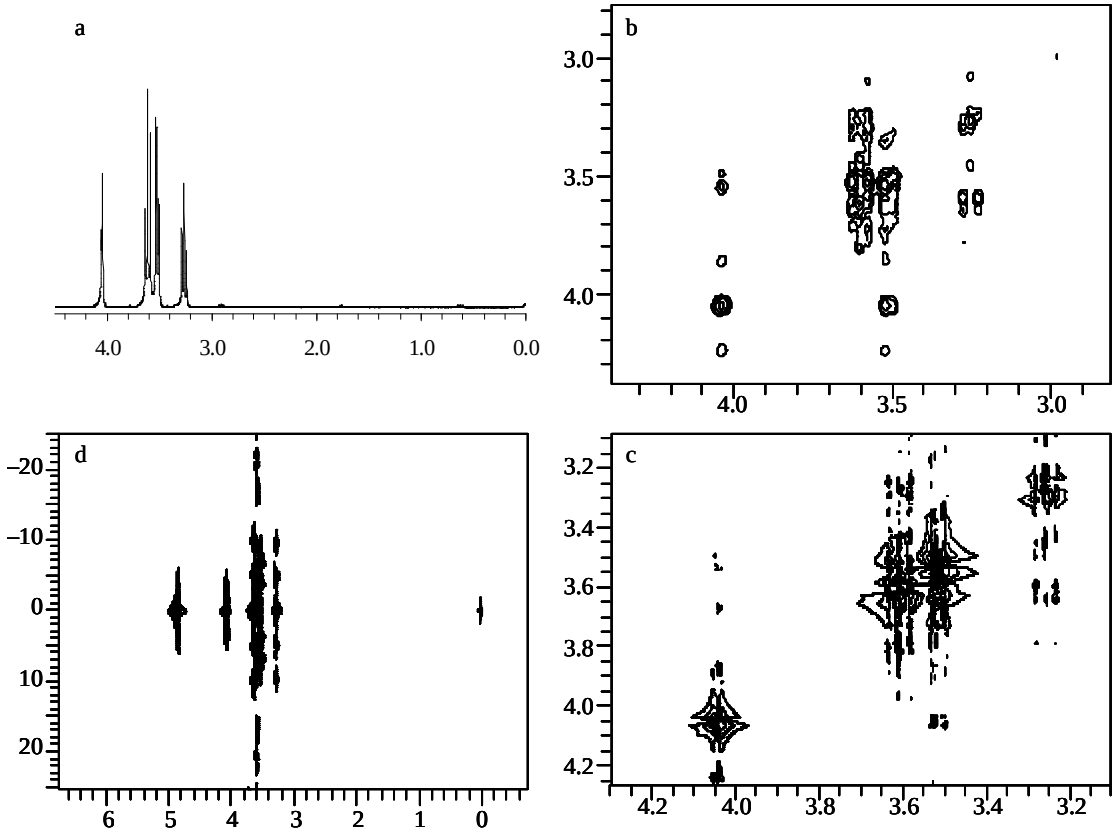

Isoleucine

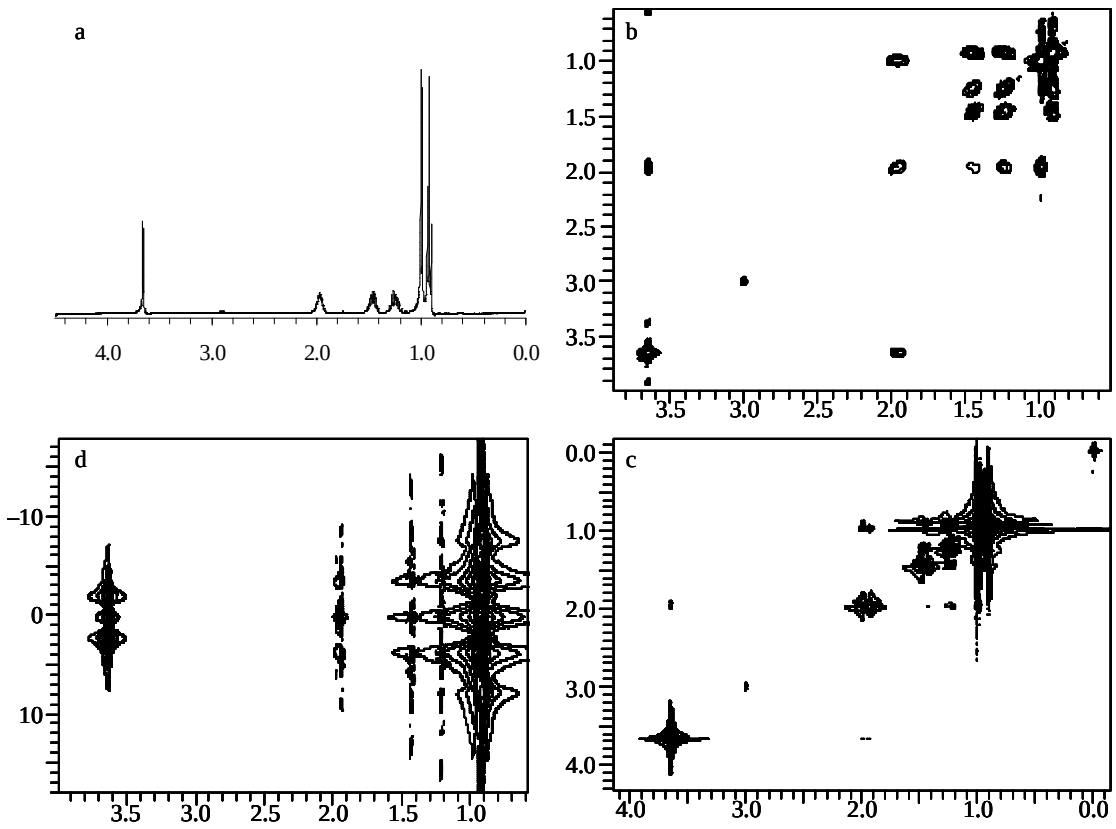

Lactate

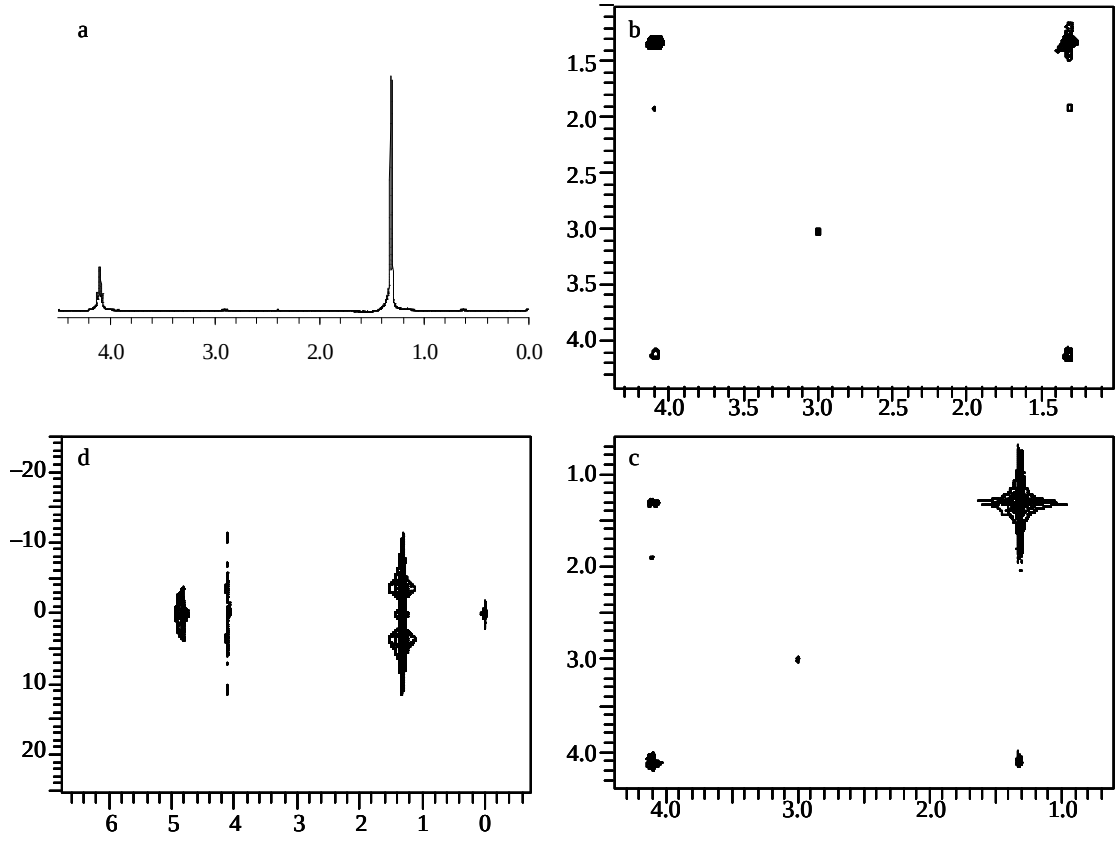

Leucine

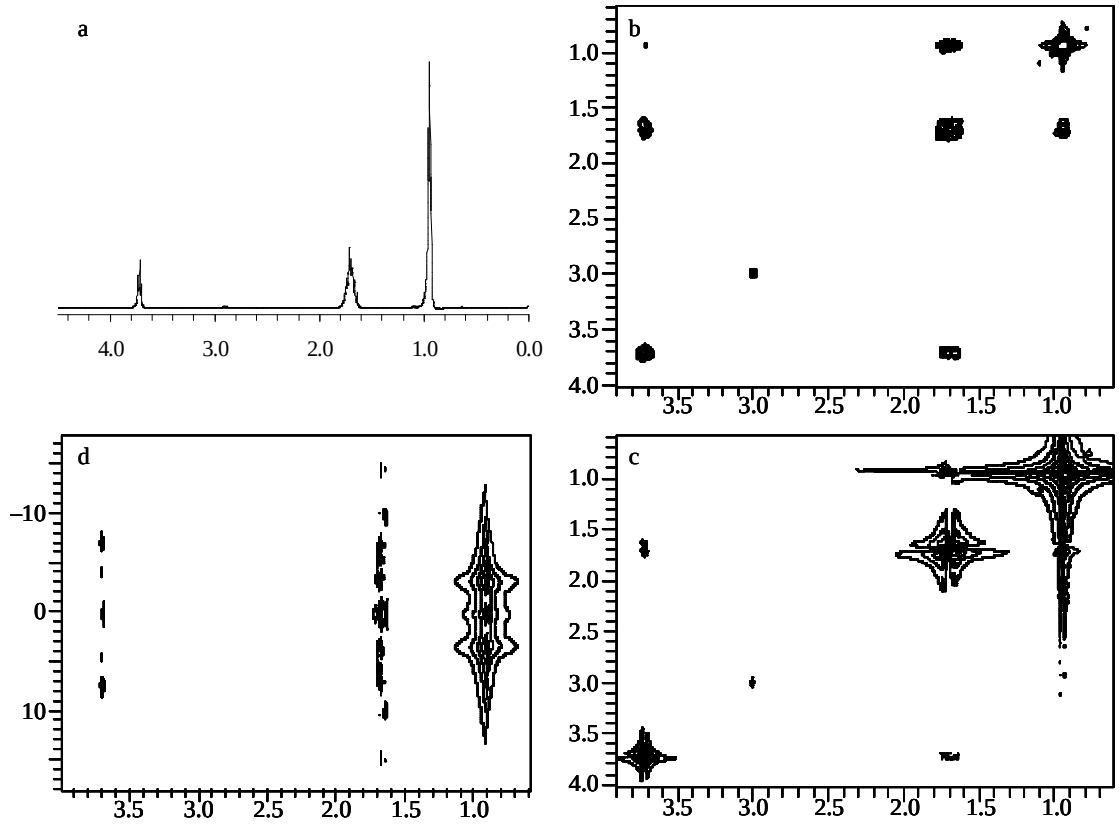

Lysine

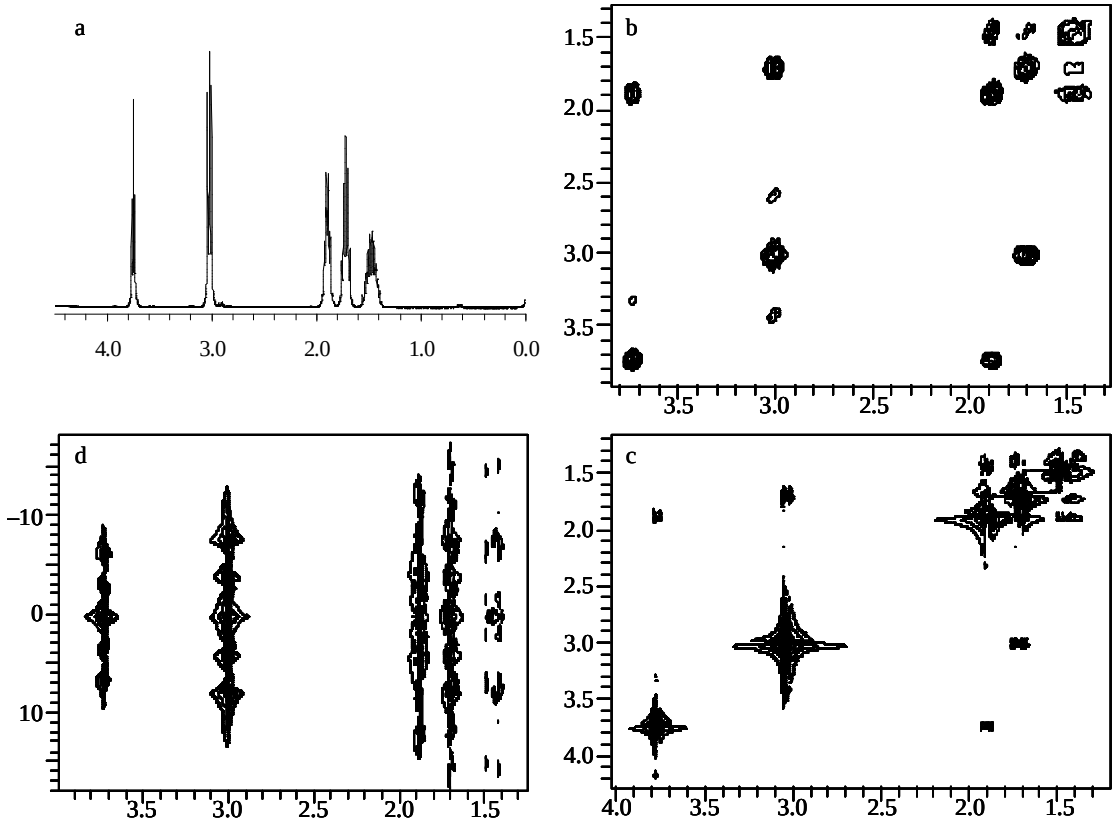
a
4.0
3.0
2.0
1.0
0.0
b
1.5
2.0
2.5
3.0
3.5
3.5
3.0
2.5
2.0
1.5
d
–10
0
10
3.5
3.0
2.5
2.0
1.5
c
1.5
2.0
2.5
3.0
3.5
4.0
4.0
3.5
3.0
2.5
2.0
1.5

NAA

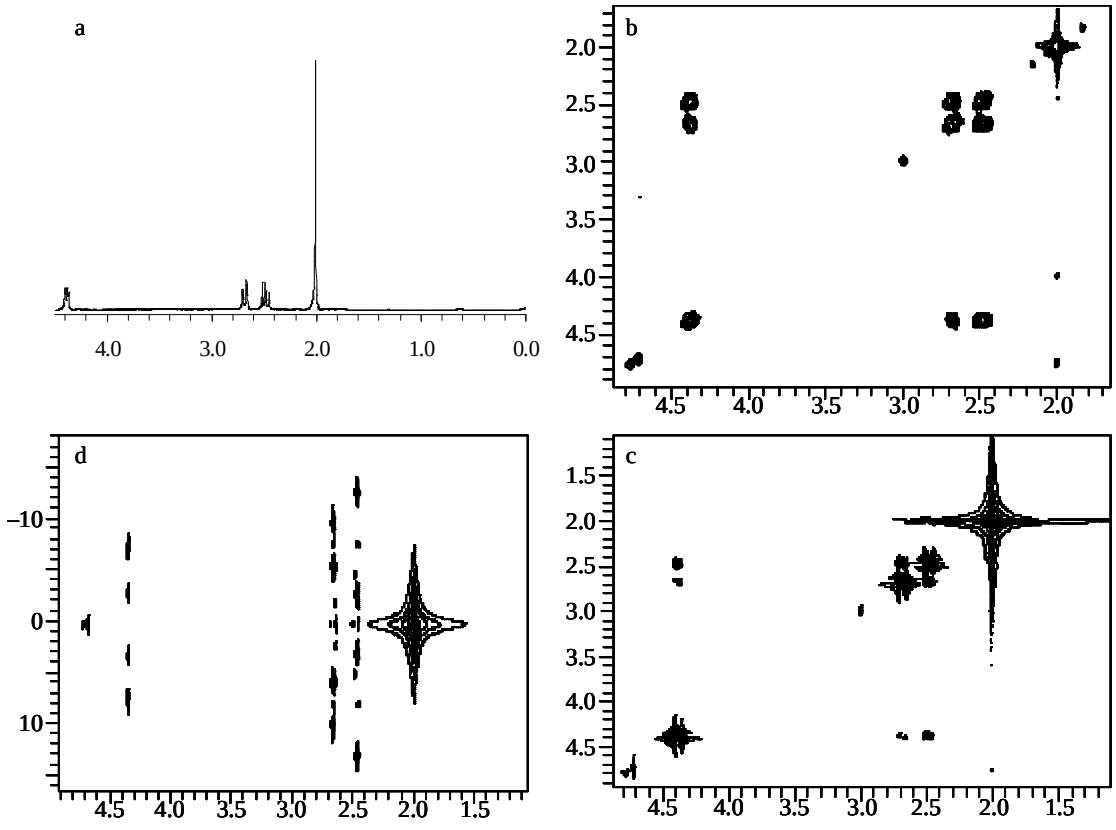
a
4.0
3.0
2.0
1.0
0.0
b
2.0
2.5
3.0
3.5
4.0
4.5
4.5
4.0
3.5
3.0
2.5
2.0
d
–10
0
10
4.5
4.0
3.5
3.0
2.5
2.0
1.5
c
1.5
2.0
2.5
3.0
3.5
4.0
4.5
4.5
4.0
3.5
3.0
2.5
2.0
1.5

Taurine

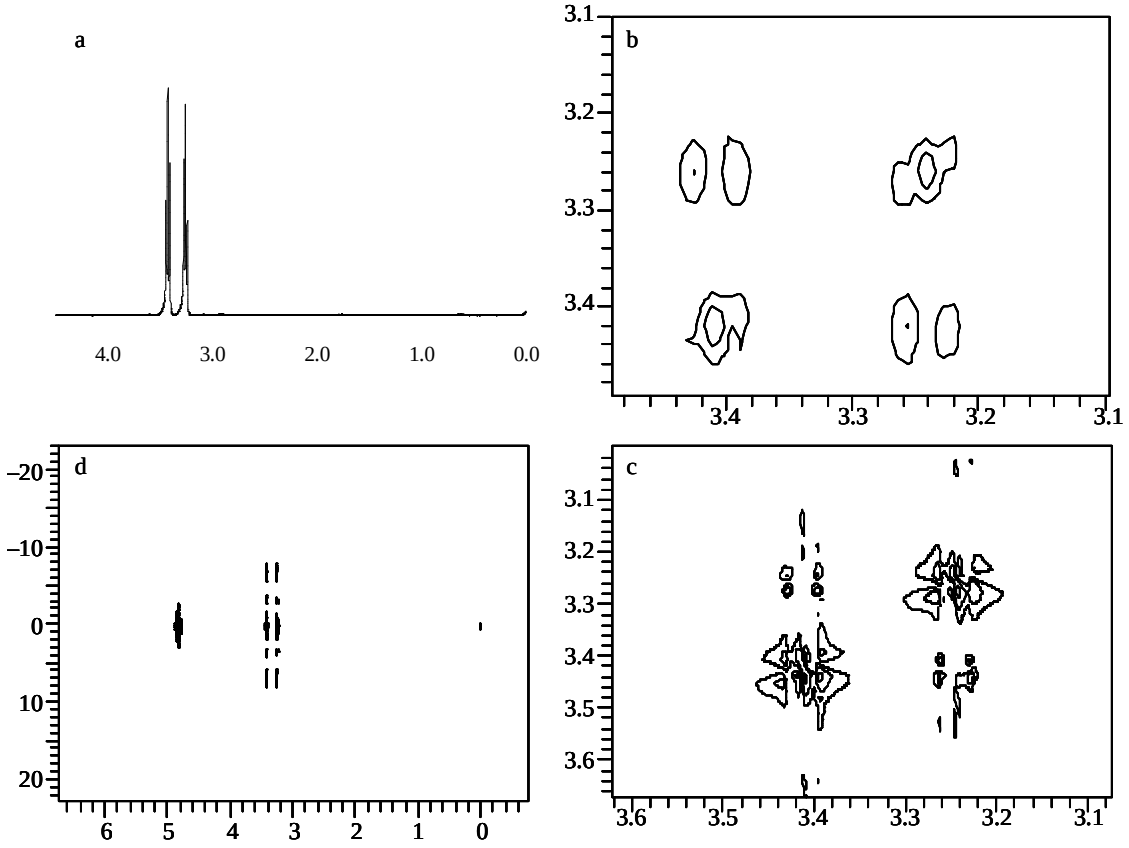

Valine

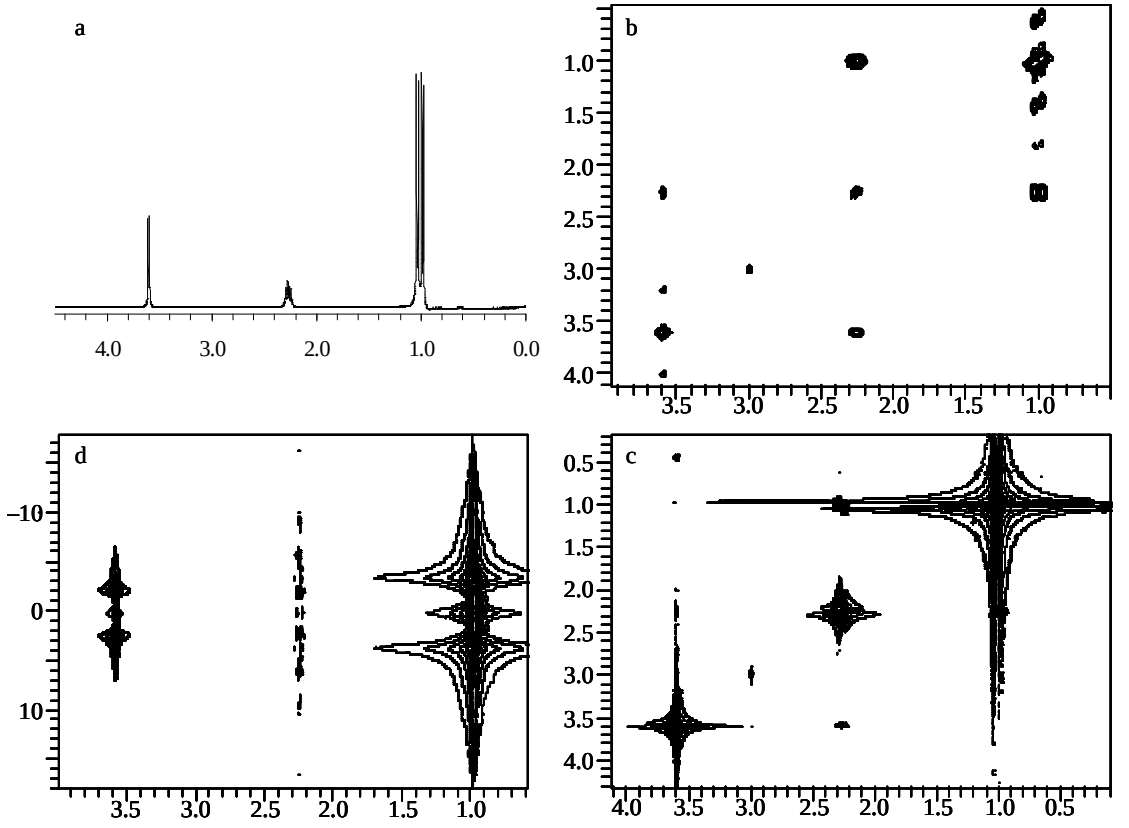

Vigabatrin

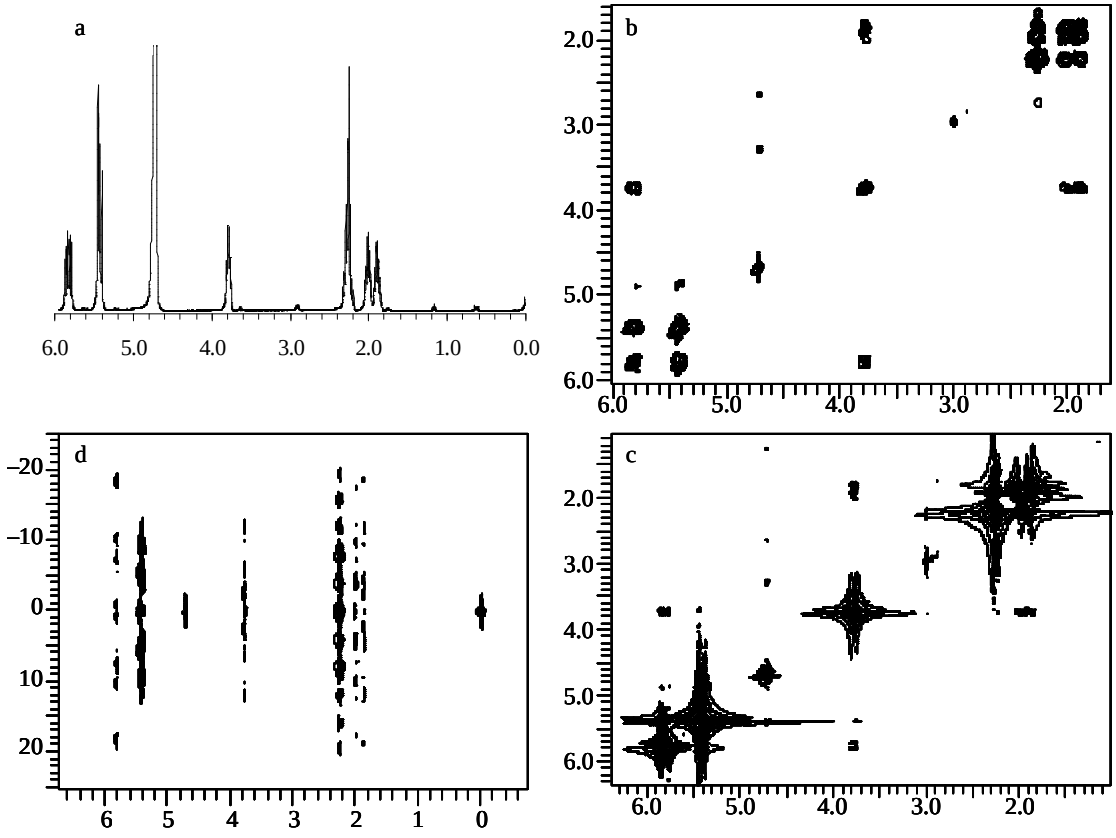
a
6.0
5.0
4.0
3.0
2.0
1.0
0.0
b
2.0
3.0
4.0
5.0
6.0
6.0
5.0
4.0
3.0
2.0
d
–20
–10
0
10
20
6
5
4
3
2
1
0
c
2.0
3.0
4.0
5.0
6.0
6.0
5.0
4.0
3.0
2.0

Appendix B: Post Mortem Spectra for Comparison of ISIS-COSY Acquisition Parameters

The following spectra were recorded on *post mortem* rat brain to compare the effect of different acquisition parameters on the ISIS-COSY pulse sequence and to compare it with VOSY-COSY (see section 4.1.4.4). Each spectrum took 2 h to acquire, with a 2.0 x 2.0 kHz spectral width, and is displayed in absolute-value mode. Other parameters are shown below:

Spectrum	Sequence	TR / s	ni	nt	sb_1 / ms	sb_2 / ms	Contour
A	IC	3	150	16	35	35	2
B	IC	2	222	16	35	35	2
C	IC	2	111	32	27.5	35	2
D	IC	1	222	32	35	35	2
E	IC	1	111	64	27.5	35	1
F	VC	3	150	16	35	35	4
G	VC	1	111	64	27.5	35	2

Key: IC, ISIS-COSY; VC, VOSY-COSY; ni, number of t_1 increments; nt, number of transients; sb_1, sb_2, sine bell in the F_1, F_2 dimension; contour, relative amplitude of lowest contour (arbitrary units).

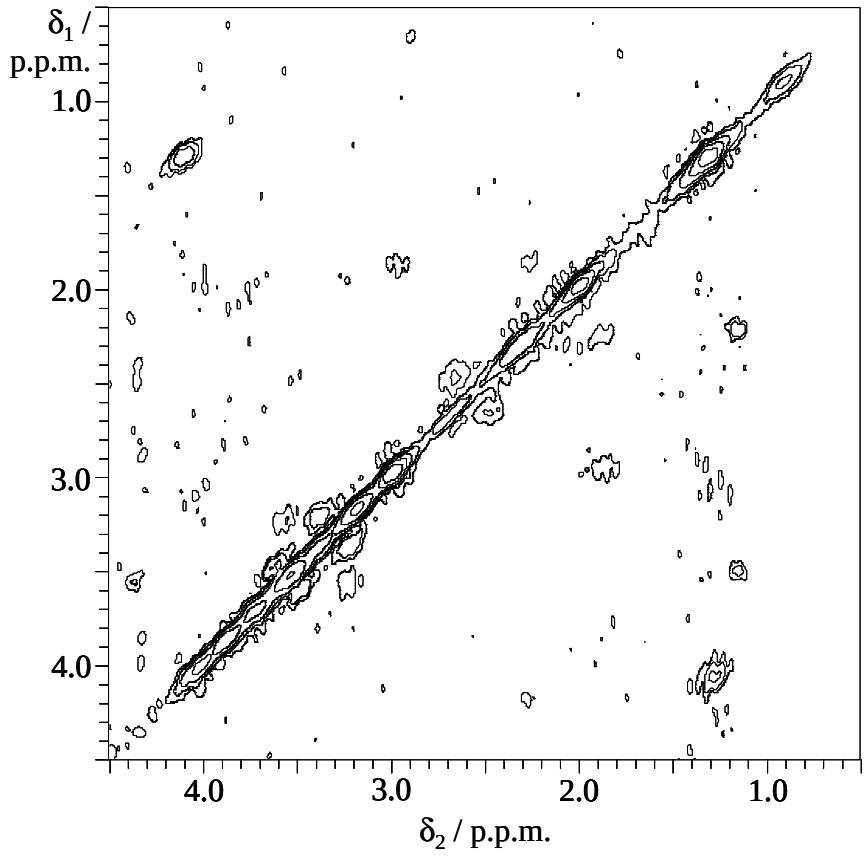

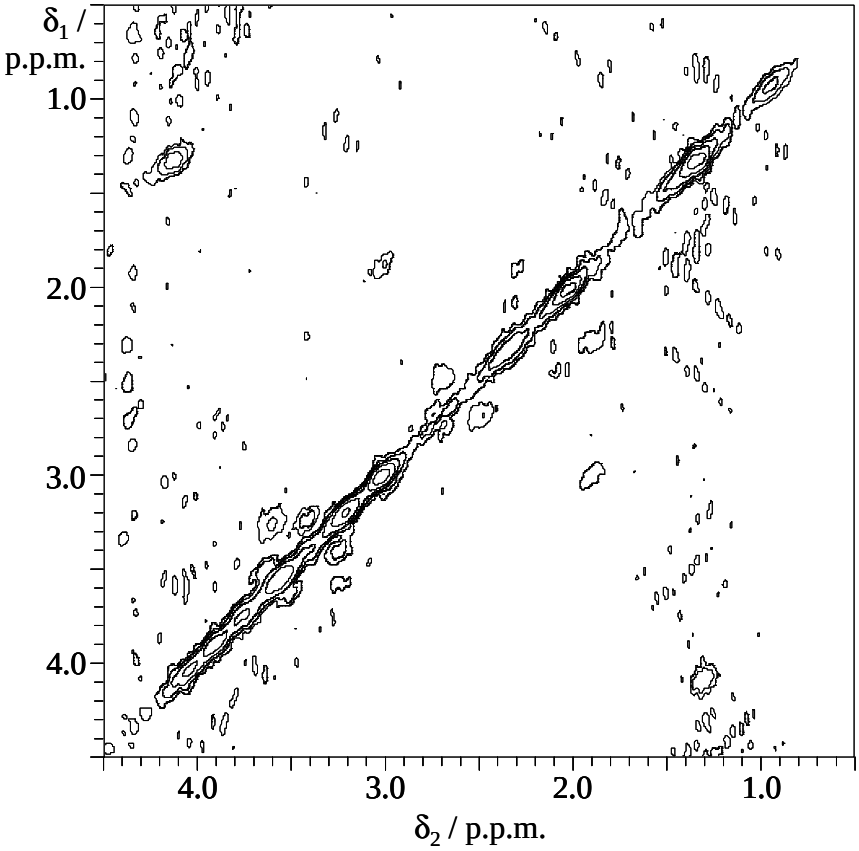
δ1 / p.p.m.
1.0
2.0
3.0
4.0
4.0
3.0
2.0
1.0
δ2 / p.p.m.

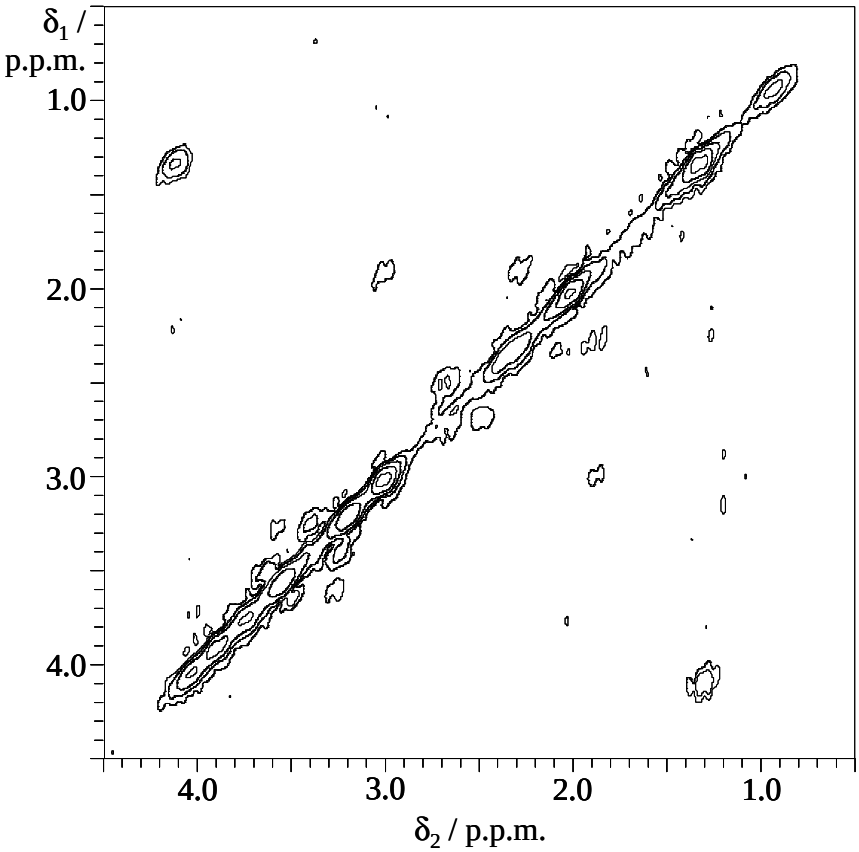
δ1 / p.p.m.
1.0
2.0
3.0
4.0
4.0
3.0
2.0
1.0
δ2 / p.p.m.

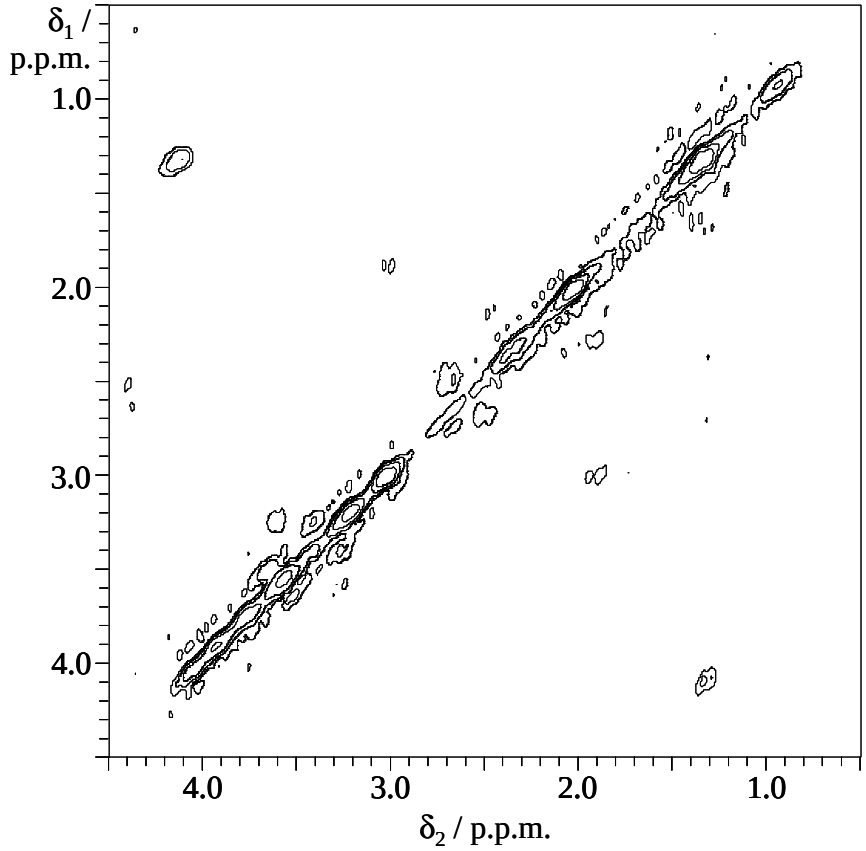
δ1 /
p.p.m.
1.0
2.0
3.0
4.0
4.0
3.0
2.0
1.0
δ2 / p.p.m.

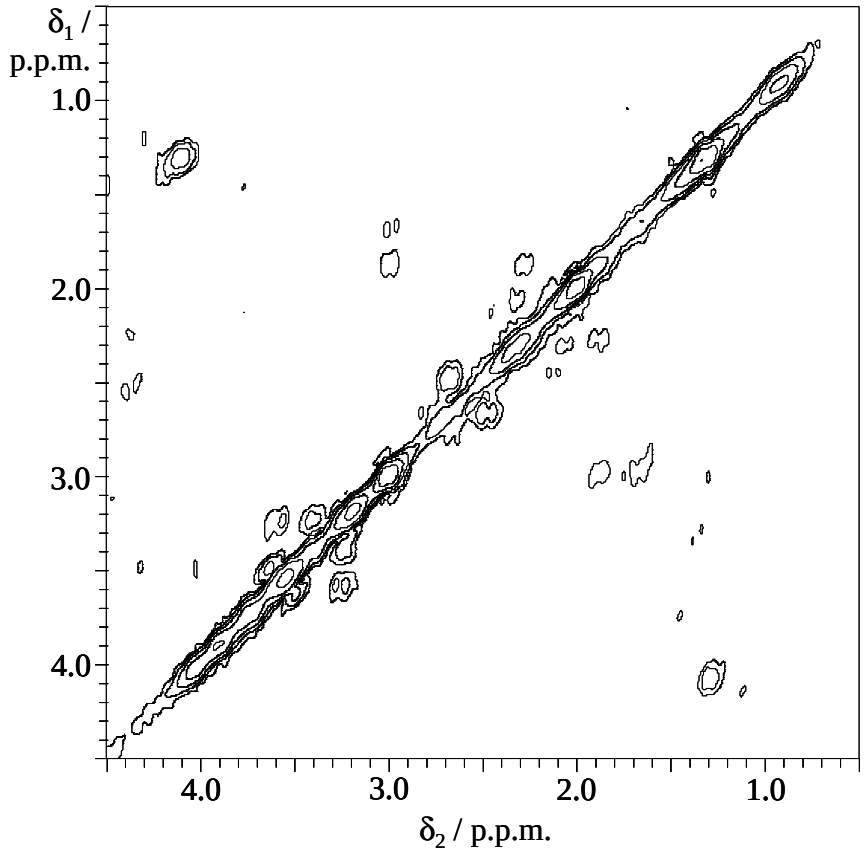
δ1 /
p.p.m.
1.0
2.0
3.0
4.0
4.0
3.0
2.0
1.0
δ2 / p.p.m.

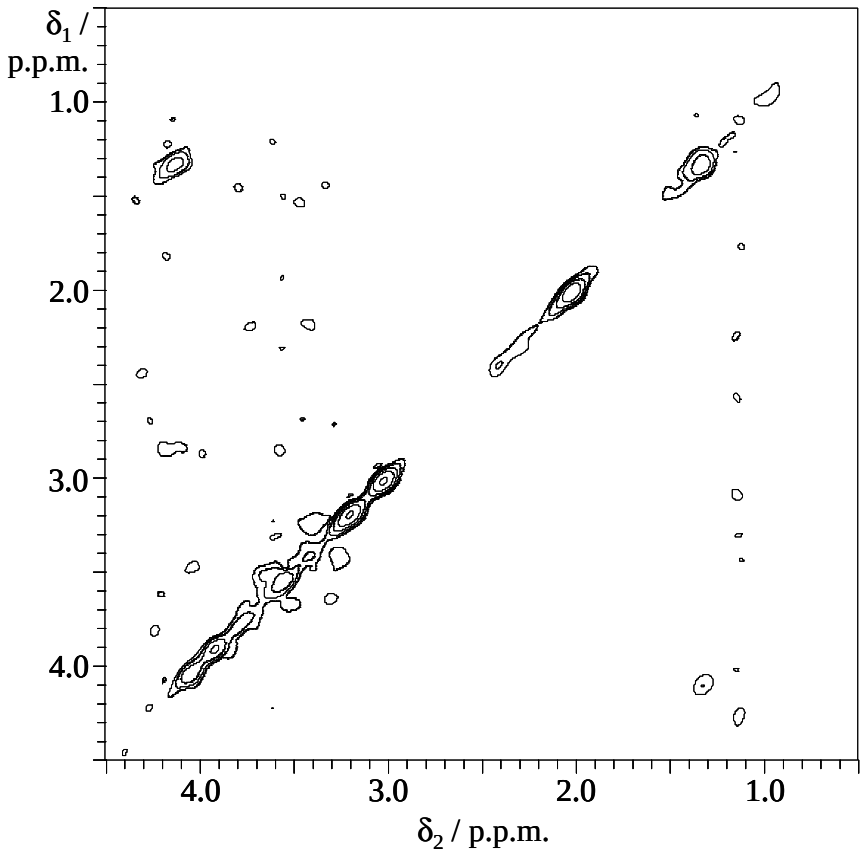
δ1 /
p.p.m.
1.0
2.0
3.0
4.0
4.0
3.0
2.0
1.0
δ2 / p.p.m.

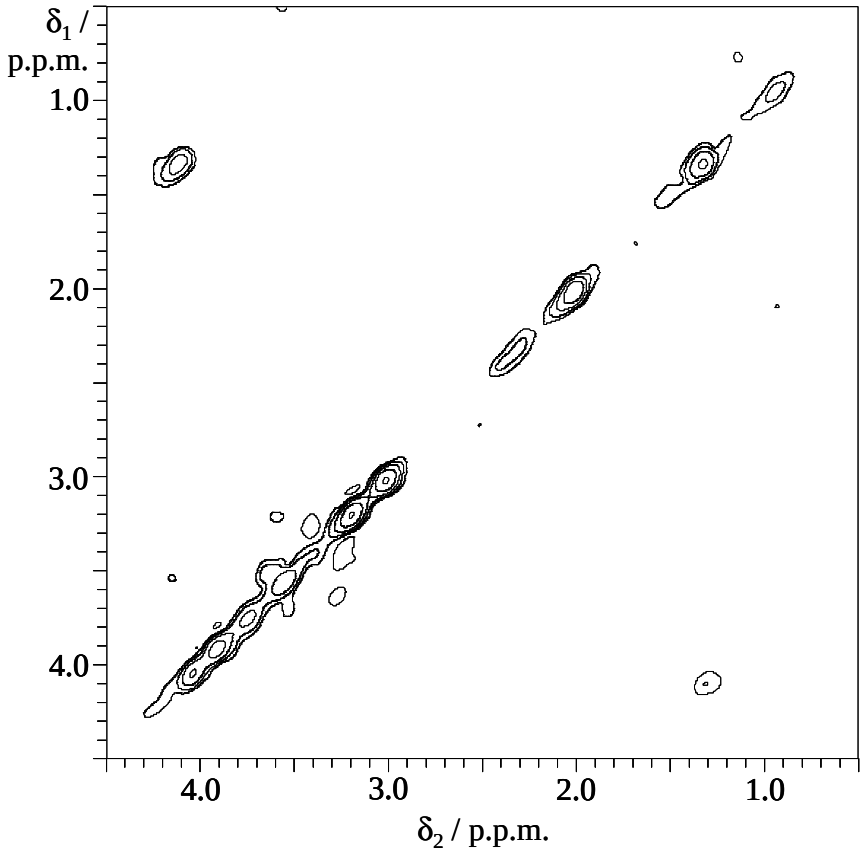
δ1 /
p.p.m.
1.0
2.0
3.0
4.0
4.0
3.0
2.0
1.0
δ2 / p.p.m.

Appendix C: Peak Assignments

The table below contains the resonances from selected molecules found in the brain and observable in ^{1}H NMR spectra either *in vivo* or in PCA extracts. The labelling of protons is as per Table 2.3. For a more exhaustive list, see Govindaraju *et al.*[57].

δ p.p.m.	Multiplicity†	*J* Hz	Coupled to δ p.p.m.	Proton
0.93	t	7.4, 7.6	1.26, 1.47	Isoleucine 5-CH_3
0.98	d	7.0	2.26	Valine 4-CH_3
0.98	d	7.0	1.72	Leucine [5,6]-CH_3
1.01	d	7.0	1.97	Isoleucine 6-CH_3
1.03	d	7.0	2.26	Valine 5-CH_3
1.26	m	7.4, 13.4, 9.3	0.93, 1.47, 1.97	Isoleucine 4-CH
1.33	d	7.3	4.10	Lactate CH_3
1.47	m	7.6, 13.4, 4.8	0.93, 1.26, 1.97	Isoleucine 4'-CH
1.47	d	7.3	3.76	Alanine CH_3
1.47	m	7.5, 7.1	1.72, 1.89	Lysine 4-CH_2
1.72	m	7.5, 7.6	1.47, 3.02	Lysine 5-CH_2
1.72	m	7.0	0.98	Leucine 3-CH_2
1.72	m	7.0	3.72	Leucine 4-CH
1.89	m	7.1, 6.1	1.47, 3.74	Lysine 3-CH_2
1.89	m	7.7, 7.7	2.29, 3.00	GABA β-CH_2
1.97	m	7.0, 9.3, 4.8, 4.0	1.01, 1.26, 1.47, 3.66	Isoleucine 3-CH
2.02	s			NAA CH_3
2.10	m	8.5, 7.2	2.35, 3.74	Glutamate β-CH_2
2.13	m	8.0, 6.5	2.44, 3.76	Glutamine β-CH_2
2.26	m	7.0, 7.0, 4.4	0.98, 1.03, 3.60	Valine 3-CH
2.29	t	7.7	1.89	GABA α-CH_2
2.35	t	8.5	2.29	Glutamate γ-CH_2
2.44	m	8.0	2.13	Glutamine γ-CH_2
2.48	dd	15.8, 10.2	2.68, 4.38	NAA β-CH
2.68	dd	15.7, 4.0	2.48, 4.38	NAA β'-CH

3.00	t	7.7	1.89	GABA γ-CH_2
3.02	t	7.6	1.72	Lysine 6-CH_2
3.03	s			Creatine CH_3
3.20	s			Choline CH_3
3.25	t	6.7	3.42	Taurine N-CH_2
3.26	t	9.3	3.61	*myo*-inositol 5-CH
3.42	t	6.7	3.25	Taurine S-CH_2
3.52	dd	9.9, 2.8	3.61, 4.04	*myo*-inositol [1,3]-CH
3.52	t	5.3	4.06	Choline 1-CH_2
3.60	d	4.3	2.26	Valine 2-CH
3.61	dd	9.7, 9.7	3.26, 3.52	*myo*-inositol [4,6]-CH
3.66	d	4.0	1.97	Isoleucine 2-CH
3.72	t	7.0	1.72	Leucine 2-CH
3.74	t	6.1	1.89	Lysine 2-CH
3.74	dd	7.2	2.10	Glutamate α-CH_2
3.76	t	6.5	2.13	Glutamine α-CH_2
3.76	q	7.3	1.47	Alanine CH
3.92	s			Creatine CH_2
4.04	t	2.3	3.52	*myo*-inositol 2-CH
4.06	t	5.3	3.52	Choline 2-CH_2
4.10	q	7.5	1.33	Lactate CH
4.38	dd	10.2, 4.1	2.48, 2.68	NAA α-CH

[†] Apparent multiplicities: s, singlet; d, doublet; t, triplet; q, quartet, m, multiplet; dd, doublet of doublets.

Appendix D: Correction Factors

The following table lists the correction factors to multiply experimentally determined peak volumes by to correct for multiplicity, *J*-coupling and processing effects, assuming the following parameters: spectrometer proton frequency, 300 MHz; line width, 14 Hz; sine bell centred at t_1, t_2 = 27.5, 40 ms (see section 3.3.3).

Metabolite	δ_1 (p.p.m.)	δ_2 (p.p.m.)	Correction Factor
Creatine	3.03	3.03	0.33
Creatine	3.91	3.91	0.50
Choline	3.19	3.19	0.11
NAA	2.70	2.70	3.31
NAA	2.52	2.52	6.56
NAA	4.40	4.40	1.92
NAA	2.02	2.02	0.33
NAA	2.70	2.52	1.91
NAA	4.40	2.70	8.86
NAA	4.40	2.52	3.96
Glutamate	3.74	3.74	1.60
Glutamate	2.04	2.04	3.08
Glutamate	2.12	2.12	2.52
Glutamate	2.34	2.34	1.01
Glutamate	2.35	2.35	1.06
Glutamate	3.74	2.04	10.63
Glutamate	3.74	2.12	11.92
Glutamate	2.12	2.04	2.73
Glutamate	2.34	2.04	5.47
Glutamate	2.34	2.12	4.62
Glutamate	2.35	2.04	5.74
Glutamate	2.35	2.12	4.85
Glutamate	2.35	2.34	1.03
Glutamine	3.75	3.75	1.62
Glutamine	2.13	2.13	1.28
Glutamine	2.11	2.11	1.30
Glutamine	2.43	2.43	1.20
Glutamine	2.45	2.45	1.13
Glutamine	3.75	2.13	4.07
Glutamine	3.75	2.11	4.12
Glutamine	2.13	2.11	1.29
Glutamine	2.43	2.13	1.55
Glutamine	2.43	2.11	1.57
Glutamine	2.43	2.45	1.16
Glutamine	2.45	2.13	1.54
Glutamine	2.45	2.11	1.55
Glutamine	2.45	2.43	1.17
Lactate	4.10	4.10	2.29
Lactate	1.33	1.33	0.46

Metabolite	δ_1 (p.p.m.)	δ_2 (p.p.m.)	Correction Factor
Lactate	4.10	1.33	1.72
Taurine	3.20	3.20	0.90
Taurine	3.40	3.40	0.93
Taurine	3.40	3.20	1.18
GABA	2.31	2.31	0.94
GABA	1.91	1.91	1.48
GABA	3.02	3.02	0.94
GABA	2.31	1.91	1.79
GABA	3.02	1.91	1.81
Inositol	3.54	3.54	1.01
Inositol	4.06	4.06	1.10
Inositol	3.62	3.62	0.90
Inositol	3.28	3.28	2.49
Inositol	4.06	3.54	11.94
Inositol	3.62	3.54	1.08
Inositol	3.62	3.28	2.61

References

1. P. B. Garlick, G. K. Radda, P. J. Seeley, and B. Chance, Phosphorus NMR studies on perfused heart, *Biochem. Biophys. Res. Commun.* **74,** 1256-1262 (1977).

2. D. I. Hoult, S. J. W. Busby, D. G. Gadian, G. K. Radda, R. E. Richards, and P. J. Seeley, Observation of Tissue Metabolites using ^{31}P Nuclear Magnetic Resonance, *Nature* **252,** 285-287 (1974).

3. G. K. Radda, Of mice and men: From early NMR studies of the heart to physiological genomics, *Biochem. Biophys. Res. Commun.* **266,** 723-728 (1999).

4. R. Ross, B. Goodpaster, D. Kelley, and F. Boada, Magnetic resonance imaging in human body composition research. From quantitative to qualitative tissue measurement, *Ann. N. Y. Acad. Sci.* **904,** 12-7 (2000).

5. H. Monoi, Nuclear magnetic resonance of tissue ^{23}Na. I. ^{23}Na signal and Na^+ activity in homogenate, *Biophys. J.* **14,** 645-51 (1974).

6. H. Monoi, Nuclear magnetic resonance of tissue ^{23}Na. II. Theoretical line shape, *Biophys. J.* **14,** 653-9 (1974).

7. P. D. Syme, R. M. Dixon, J. L. Allis, J. K. Aronson, D. G. Grahame Smith, and G. K. Radda, A non-invasive method of measuring concentrations of rubidium in rat skeletal muscle *in vivo* by ^{87}Rb nuclear magnetic resonance spectroscopy: implications for the measurement of cation transport activity *in vivo, Clin. Sci. (Colch)* **78,** 303-9 (1990).

8. J. L. Allis, C. D. Snaith, A. M. Seymour, and G. K. Radda, ^{87}Rb NMR studies of the perfused rat heart, *FEBS Lett.* **242,** 215-7 (1989).

9. J. Shen, K. F. Petersen, K. L. Behar, P. Brown, T. W. Nixon, G. F. Mason, O. A. Petroff, G. I. Shulman, R. G. Shulman, and D. L. Rothman, Determination of the rate of the glutamate/glutamine cycle in the human brain by *in vivo* ^{13}C NMR, *Proc. Natl. Acad. Sci. USA* **96,** 8235-40 (1999).

10. R. G. Shulman, T. R. Brown, K. Ugurbil, S. Ogawa, S. M. Cohen, and J. A. den Hollander, Cellular Applications of ^{31}P and ^{13}C Nuclear Magnetic Resonance, *Science* **205,** 160-166 (1979).

11. D. L. Rothman, N. R. Sibson, F. Hyder, J. Shen, K. L. Behar, and R. G. Shulman, *In vivo* nuclear magnetic resonance spectroscopy studies of the relationship between the glutamate-glutamine neurotransmitter cycle and functional neuroenergetics, *Philos. Trans. R. Soc. Lond. B Biol.Sci.* **354,** 1165-77 (1999).

12. O. A. Petroff, Biological ^{1}H NMR spectroscopy, *Comp. Biochem. Physiol. B* **90,** 249-60 (1988).

13. A. Bertolino and D. R. Weinberger, Proton magnetic resonance spectroscopy in schizophrenia, *Eur. J. Radiol.* **30,** 132-41 (1999).

14. K. L. Malisza, P. Kozlowski, and J. Peeling, A review of *in vivo* ^{1}H magnetic resonance spectroscopy of cerebral ischemia in rats, *Biochem. Cell. Biol.* **76,** 487-96 (1998).

15. N. De Stefano, A. Federico, and D. L. Arnold, Proton magnetic resonance spectroscopy in brain white matter disorders, *Ital. J. Neurol. Sci* **18,** 331-9 (1997).

16. D. L. Arnold and N. De Stefano, Magnetic resonance spectroscopy *in vivo*: applications in neurological disorders, *Ital. J. Neurol. Sci* **18,** 321-9 (1997).

17. J. C. Soares, K. R. Krishnan, and M. S. Keshavan, Nuclear magnetic resonance spectroscopy: new insights into the pathophysiology of mood disorders, *Depression* **4,** 14-30 (1996).

18. F. A. Howe, R. J. Maxwell, D. E. Saunders, M. M. Brown, and J. R. Griffiths, Proton spectroscopy *in vivo*, *Magn. Reson. Q* **9,** 31-59 (1993).

19. W. Negendank, Studies of human tumors by MRS: a review, *NMR Biomed.* **5,** 303-24 (1992).

20. J. J. H. Ackerman, T. H. Grove, G. G. Wong, D. G. Gadian, and G. K. Radda, Mapping of metabolites in whole animals by ^{31}P NMR using surface coils., *Nature* **283,** 167-170 (1980).

21. T. R. Brown, B. M. Kincaid, and K. Ugurbil, NMR chemical shift imaging in three dimensions, *Proc. Natl. Acad. Sci. USA* **79,** 3523-6 (1982).

22. R. J. Ordidge, A. Connelly, and J. A. B. Lohman, Image-selected *in vivo* spectroscopy (ISIS) – a new technique for spatially selective NMR spectroscopy, *J. Magn. Reson.* **66,** 283-294 (1986).

23. P. A. Bottomley, Spatial Localization in NMR-Spectroscopy *In Vivo*, *Ann. N. Y. Acad. Sci.* **508,** 333-348 (1987).

24. R. Kimmich and D. Hoepfel, Volume-Selective Multipulse Spin-Echo Spectroscopy, *J. Magn. Reson.* **72,** 379-384 (1987).

25. J. Frahm, K. D. Merboldt, and W. Hänicke, Localized Proton Spectroscopy Using Stimulated Echoes, *J. Magn. Reson.* **72,** 502-508 (1987).

26. W. P. Aue, E. Bartholdi, and R. R. Ernst, Two-dimensional spectroscopy. Application to nuclear Magnetic Resonance, *J. Chem. Phys.* **64,** 2229-2246 (1976).

27. J. Jeener, in *Ampère International Summer School* (Basko Polje, Yugoslavia, 1971).

28. A. E. Derome, *Modern NMR Techniques for Chemistry Research* (Pergamon Press, Oxford, 1987), pp. 183-227.

29. A. E. Derome, *Modern NMR Techniques for Chemistry Research* (Pergamon Press, Oxford, 1987), pp. 270-274.

30. W. P. Aue, J. Karhan, and R. R. Ernst, Homonuclear Broad Band and Two-dimensional *J*-resolved NMR Spectroscopy, *J. Chem. Phys.* **64,** 4226-7 (1976).

31. S. Macura and R. R. Ernst, Elucidation of Cross-correlation in Liquids by Two-dimensional NMR Spectroscopy, *Mol. Phys.* **41,** 95-117 (1980).

32. A. E. Derome, *Modern NMR Techniques for Chemistry Research* (Pergamon Press, Oxford, 1987), pp. 239-243.

33. J. Jeener, B. H. Meier, P. Bachmann, and R. R. Ernst, Investigation of Exchange Processes by Two-dimensional NMR Spectroscopy, *J. Chem. Phys.* **71,** 4546-53 (1979).

34. L. Braunschweiler and R. R. Ernst, Coherence Transfer by Isotropic Mixing: Application to Proton Correlation Spectroscopy, *J. Magn. Reson.* **53,** 521-8 (1983).

35. W. I. Jung and O. Lutz, Localized Single-Shot Double-Quantum Filter For Spectral Editing of Human *In Vivo* Proton Spectra, *J. Magn. Reson.* **94,** 587-595 (1991).

36. D. L. Hardy and T. J. Norwood, Spectral Editing Technique for the *in vitro* and *in vivo* Detection of Taurine, *J. Magn. Reson.* **133,** 70-8 (1998).

37. D. L. Rothman, O. A. Petroff, K. L. Behar, and R. H. Mattson, Localized ^{1}H NMR measurements of gamma-aminobutyric acid in human brain *in vivo*, *Proc. Natl. Acad. Sci. USA* **90,** 5662-6 (1993).

38. I. M. Brereton, G. J. Galloway, S. E. Rose, and D. M. Doddrell, Localized 2-Dimensional Shift Correlated Spectroscopy in Humans At 2 Tesla, *Magn. Reson. Med.* **32,** 251-257 (1994).

39. F. Desmoulin and J. Seelig, A Homonuclear Shift Correlated and Spatially Localized Spectroscopy Using Stimulated Echoes, *Magn. Reson. Med.* **14,** 160-168 (1990).

40. S. J. Blackband, K. A. McGovern, and I. J. McLennan, Spatially Localized Two-Dimensional Spectroscopy - SLO-COSY and SLO-NOESY, *J. Magn. Reson.* **79,** 184-189 (1988).

41. L. N. Ryner, J. A. Sorenson, and M. A. Thomas, 3D localized 2D NMR spectroscopy on an MRI scanner, *J. Magn. Reson. Series B* **107,** 126-137 (1995).

42. G. C. McKinnon and P. Bosiger, Localized Double-Quantum Filter and Correlation Spectroscopy Experiments, *Magn. Reson. Med.* **6,** 334-343 (1988).

43. W. Dreher and D. Leibfritz, Parametric multiecho proton spectroscopic imaging: application to the rat brain *in vivo*, *Magn. Reson. Imag.* **13,** 753-61 (1995).

44. O. W. Sørensen, G. W. Eich, M. H. Levitt, G. Bodenhausen, and R. R. Ernst, Product Operator Formalism for the Description of NMR Pulse Experiments, *Prog. Nucl. Magn. Reson. Spectrosc.* **16,** 163-192 (1983).

45. S. C. Wimperis and P. J. Hore, Eight Lectures on NMR Spectroscopy (Oxford, 1996), p. 33.

46. S. C. Wimperis and P. J. Hore, Eight Lectures on NMR Spectroscopy (Oxford, 1996), p. 34.

47. J. Keeler and D. Neuhaus, Comparison and evaluation of methods for two-dimensional NMR spectra with absorption-mode lineshapes, *J. Magn. Reson.* **63,** 454-472 (1985).

48. D. Marion and K. Wüthrich, Application of phase sensitive two-dimensional correlated spectroscopy (COSY) for measurements of ^{1}H-^{1}H spin-spin coupling constants in proteins, *Biochem. Biophys. Res. Commun.* **113,** 967-74 (1983).

49. D. J. States, R. A. Haberkorn, and D. J. Ruben, A Two-Dimensional Nuclear Overhauser Experiment With Pure Absorption Phase in 4 Quadrants, *J. Magn. Reson.* **48,** 286-292 (1982).

50. H. Y. Carr and E. M. Purcell, Effects of Diffusion on Free Precession in Nuclear Magentic Resonance Experiments, *Phys. Rev.* **94,** 630-8 (1954).

51. E. L. Hahn, Spin Echoes, *Phys. Rev.* **80,** 580-94 (1950).

52. S. C. Wimperis and P. J. Hore, Eight Lectures on NMR Spectroscopy (Oxford, 1996), p. 22.

53. G. Bodenhausen, R. Freeman, and D. L. Turner, Suppression of Artefacts in Two-dimensional *J* Spectroscopy, *J. Magn. Reson.* **27,** 511-514 (1977).

54. D. W. Alderman and D. M. Grant, An Efficient Decoupler Coil Design which Reduces Heating in Conductive Samples in Superconducting Spectrometers, *J. Magn. Reson.* **36,** 447-451 (1979).

55. R. J. Ogg, R. B. Kingsley, and J. S. Taylor, WET, a T_1-Insensitive and B_1-Insensitive Water-Suppression Method For *In Vivo* Localized ^{1}H-NMR Spectroscopy, *J. Magn. Reson. Series B* **104,** 1-10 (1994).

56. K. L. Behar and T. Ogino, Assignment of Resonances in the ^{1}H Spectrum of Rat Brain By 2-Dimensional Shift Correlated and *J*-Resolved NMR-Spectroscopy, *Magn. Reson. Med.* **17,** 285-303 (1991).

57. V. Govindaraju, K. Young, and A. A. Maudsley, Proton NMR Chemical Shifts and Coupling Constants for Brain Metabolites, *NMR Biomed.* **13,** 129-153 (2000).

58. W. H. Press, S. A. Teukolsky, W. T. Vetterling, and B. P. Flannery, *Numerical Recipes in Fortran: the Art of Scientific Computing* (Cambridge University Press, 1992), pp. 460-461.

59. R. R. Ernst, G. Bodenhausen, and A. Wokaun, *Principles of Nuclear Magnetic Resonance in One and Two Dimensions* (Oxford University Press, Oxford, 1987), pp. 9-12.

60. R. C. Ferguson and D. W. Marquadt, Computer Analysis of NMR Spectra: Magnetic Equivalence Factoring, *J. Chem. Phys.* **41,** 2087-2095 (1964).

61. S. Wolfram, *Mathematica*, v. 4.0 (Wolfram Research, Champaign, IL, 1999).

62. A. van der Toorn, R. M. Dijkhuizen, C. A. F. Tulleken, and K. Nicolay, T_1 and T_2 Relaxation-Times of the Major ^{1}H-Containing Metabolites in Rat-Brain After Focal Ischemia, *NMR Biomed.* **8,** 245-252 (1995).

63. C. Burger, R. Buchli, G. McKinnon, D. Meier, and P. Boesiger, The Impact of the ISIS Experiment Order On Spatial Contamination, *Magn. Reson. Med.* **26,** 218-230 (1992).

64. M. S. Silver, R. I. Joseph, and D. I. Hoult, Selective Pulse Creation By Inverse Solution of the Bloch-Riccati Equation, *Magn. Reson. Med.* **1,** 294-294 (1984).

65. M. S. Silver, R. I. Joseph, C. N. Chen, V. J. Sank, and D. I. Hoult, Selective-Population Inversion in Nmr, *Nature* **310,** 681-683 (1984).

66. M. S. Silver, R. I. Joseph, and D. I. Hoult, Highly Selective Pi/2 and Pi-Pulse Generation, *J. Magn. Reson.* **59,** 347-351 (1984).

67. M. S. Silver, R. I. Joseph, and D. I. Hoult, Selective Spin Inversion in Nuclear Magnetic-Resonance and Coherent Optics Through an Exact Solution of the Bloch-Riccati Equation, *Phys. Rev. A* **31,** 2753-2755 (1985).

68. A. Connelly, C. Counsell, J. A. B. Lohman, and R. J. Ordidge, Outer Volume Suppressed Image Related *In Vivo* Spectroscopy (OSIRIS), a High-Sensitivity Localization Technique, *J. Magn. Reson.* **78,** 519-525 (1988).

69. R. J. Ordidge, Random noise selective excitation pulses, *Magn. Reson. Med.* **5,** 93-8 (1987).

70. M. Deriche and X. P. Hu, Elimination of Water Signal By Postprocessing, *J. Magn. Reson. Series A* **101,** 229-232 (1993).

71. G. L. Ding, H. B. Hu, L. Y. Li, X. A. Mao, and C. H. Ye, Progress of water-suppression in nuclear magnetic resonance localized spectroscopy, *Prog. Nat. Sci.* **7,** 41-45 (1997).

72. J. Frahm, T. Michaelis, K. D. Merboldt, H. Bruhn, M. L. Gyngell, and W. Hänicke, Improvements in Localized Proton NMR-Spectroscopy of Human

Brain – Water Suppression, Short Echo Times, and 1-ml Resolution, *J. Magn. Reson.* **90,** 464-473 (1990).

73. M. Gueron, P. Plateau, and M. Decorps, Solvent Signal Suppression in NMR, *Prog. Nucl. Magn. Reson. Spectrosc.* **23,** 135-209 (1991).

74. M. McCoy and W. S. Warren, Pulse Shaping to Improve Performance of NMR Multiple-Pulse Sequences – 2D Solvent-Suppressed COSY of Vitamin B_1 in Water, *Chem. Phys. Lett.* **133,** 165-170 (1987).

75. P. Mutzenhardt, J. Brondeau, and D. Canet, COSY Experiments and Solvent Suppression With $\mathbf{B_1}$ Gradients, *J. Magn. Reson. Series A* **108,** 110-115 (1994).

76. J. Star-Lack, S. J. Nelson, J. Kurhanewicz, L. R. Huang, and V. D. B., Improved water and lipid suppression for 3D PRESS CSI using RF band selective inversion with gradient dephasing (BASING), *Magn. Reson. Med.* **38,** 311-321 (1997).

77. S. L. Patt and B. D. Sykes, Water Eliminated Fourier Transform NMR Spectroscopy, *J. Chem. Phys.* **56,** 3182-3183 (1972).

78. R. K. Gupta, Dynamic Range Problem in Fourier Transform NMR. Modified WEFT Pulse Sequence, *J. Magn. Reson.* **24,** 461-465 (1976).

79. C. T. W. Moonen and P. C. M. van Zijl, Highly Effective Water Suppression For *In Vivo* Proton NMR- Spectroscopy (DRYSTEAM), *J. Magn. Reson.* **88,** 28-41 (1990).

80. A. Haase, J. Frahm, W. Hänicke, and D. Matthaei, ^{1}H-NMR Chemical-Shift Selective (Chess) Imaging, *Phys. Med. Biol.* **30,** 341-344 (1985).

81. T. Ernst and J. Hennig, Improved Water Suppression For Localized *In Vivo* ^{1}H Spectroscopy, *J. Magn. Reson. Series B* **106,** 181-186 (1995).

82. D. I. Hoult, Solvent Peak Saturation with Single Phase and Quadrature Fourier Transformation, *J. Magn. Reson.* **21,** 337-347 (1976).

83. J. Schaefer, Selective Saturation of Carbon-13 Lines in Carbon-13 Fourier Transform NMR Experiments, *J. Magn. Reson.* **6,** 670-671 (1972).

84. I. D. Campbell, C. M. Dobson, G. Jeminet, and R. J. Williams, Pulsed NMR methods for the observation and assignment of exchangeable hydrogens: application to bacitracin, *FEBS Lett.* **49,** 115-9 (1974).

85. A. Bax, R. Freeman, and G. Morris, Correlation of Proton Chemical Shifts by Two-dimensional Fourier Transform NMR, *J. Magn. Reson.* **42,** 164-8 (1981).

86. K. Nagayama, K. Wuthrich, and R. R. Ernst, Two-dimensional spin echo correlated spectroscopy (SECSY) for ^{1}H NMR studies of biological macromolecules, *Biochem. Biophys. Res. Commun.* **90,** 305-11 (1979).

87. J. Pfeuffer, I. Tkác, S. W. Provencher, and R. Gruetter, Toward an *in vivo* neurochemical profile: quantification of 18 metabolites in short-echo-time ^{1}H NMR spectra of the rat brain, *J. Magn. Reson.* **141,** 104-20 (1999).

88. D. D. Clarke, A. L. Lajtha, and H. S. Maher, Intermediary Metabolism, in *Basic Neurochemistry*, edited by G. J. Siegel (Raven, New York, 1989), pp. 541-564.

89. C. L. Florian, S. R. Williams, K. K. Bhakoo, and M. D. Noble, Regional and developmental variations in metabolite concentration in the rat brain and eye: a study using ^{1}H NMR spectroscopy and high performance liquid chromatography, *Neurochem. Res.* **21,** 1065-74 (1996).

90. A. M. Mans, M. R. DeJoseph, and R. A. Hawkins, Metabolic abnormalities and grade of encephalopathy in acute hepatic failure, *J. Neurochem.* **63,** 1829-38 (1994).

91. O. A. Petroff, T. Ogino, and J. R. Alger, High-resolution proton magnetic resonance spectroscopy of rabbit brain: regional metabolite levels and *post mortem* changes, *J. Neurochem.* **51,** 163-71 (1988).

92. R. L. Veech, R. L. Harris, D. Veloso, and E. H. Veech, Freeze-blowing: a new technique for the study of brain *in vivo*, *J. Neurochem.* **20,** 183-8 (1973).

93. H. McIlwain and H. S. Bachelard, *Biochemistry and the Central Nervous System*, 5th ed. (Churchill Livingstone, Edinburgh, 1985).

94. T. L. Perry, Cerebral Amino Acid Pools, in *Handbook of Neurochemistry*, Vol. 1, 2nd ed., edited by A. Lajtha (Plenum Press, New York, 1982), pp. 151-180.

95. R. Tycko and A. Pines, Iterative Schemes for Broad-band and Narrow-band Population Inversion in NMR, *Chem. Phys. Lett.* **111,** 462-467 (1984).

96. S. Wimperis, Broad-Band, Narrow-Band, and Passband Composite Pulses For Use in Advanced NMR Experiments, *J. Magn. Reson. Series A* **109,** 221-231 (1994).

97. M. H. Levitt, Composite Pulses, in *Encyclopaedia of Magnetic Resonance*, edited by D. M. Grant and R. K. Harries (Wiley, Chichester, 1996), pp. 1396-1411.

98. C. Piérard, M. Pérès, P. Sabatin, and C. Y. Guzennec, Effects of GABA-transaminase inhibition on brain metabolism and amino-acid compartmentation: an *in vivo* study by 2D ^{1}H NMR spectroscopy coupled with microdialysis, *Exp. Brain Res.* **127,** 321-327 (1999).

99. D. A. McCormick, GABA as an inhibitory neurotransmitter in human cerebral cortex, *J. Neurophysiol.* **62,** 1018-27 (1989).

100. K. Krnjevic, GABAergic Inhibition in the Neocortex, *J. Mind Behav.* **8,** 537-547 (1987).

101. M. J. Jung, B. Lappet, B. W. Metcalf, P. Böhlen, and P. J. Schechter, Gamma-vinyl GABA (4-amino-hex-5-enoic acid): a New Selective Irreversible Inhibitor of GABA-T: Effects on Brain GABA Metabolism in Mice, *J. Neurochem.* **29,** 787-812 (1977).

102. B. W. Metcalf, Inhibitors of GABA Metabolism, *Biochem. Pharmacol.* **28,** 1705-1712 (1979).

103. T. L. Perry, S. J. Kish, and S. Hansen, gamma-Vinyl GABA: effects of chronic administration on the metabolism of GABA and other amino compounds in rat brain, *J. Neurochem.* **32,** 1641-5 (1979).

104. E. Valdizan, A. Garcia, and J. Armijo, Effects of increasing doses of vigabatrin on platelet gamma-aminobutyric acid-transaminase and brain gamma-aminobutyric acid in rats, *Eur. J. Pharmacol.* **369,** 169-73 (1999).

105. N. Preece, G. Jackson, J. Houseman, J. Duncan, and S. Williams, Nuclear magnetic resonance detection of increased cortical GABA in vigabatrin-treated rats *in vivo*, *Epilepsia* **35,** 431-6 (1994).

106. D. Manor, D. Rothman, G. Mason, F. Hyder, O. Petroff, and K. Behar, The rate of turnover of cortical GABA from [1-^{13}C]glucose is reduced in rats treated with the GABA-transaminase inhibitor vigabatrin (gamma-vinyl GABA), *Neurochemical Research* **21,** 1031-41 (1996).

107. G. Jackson, S. Williams, R. Weller, B. N. van, N. Preece, S. Williams, W. Butler, and J. Duncan, Vigabatrin-induced lesions in the rat brain demonstrated by quantitative magnetic resonance imaging., *Epilepsy Res.* **18,** 57-66 (1994).

108. O. Petroff and D. Rothman, Measuring human brain GABA *in vivo*: effects of GABA-transaminase inhibition with vigabatrin, *Mol. Neurobiol.* **16,** 97-121 (1998).

109. R. A. de Graaf, K. F. Petersen, G. F. Mason, J. Shen, K. L. Behar, G. I. Shulman, R. H. Mattson, D. L. Rothman, and O. A. C. Petroff, GABA Synthesis and Cycling in Human Brain as studied by ^{1}H and ^{13}C NMR Spectroscopy, in *Proceedings of the International Society for Magnetic Resonance In Medicine* (Denver, 2000), p. 13.

110. O. A. C. Petroff, F. Hyder, T. L. Collins, R. H. Mattson, and D. L. Rothman, Gabapentin raises Human Brain GABA within Thirty Minutes, in *Proceedings of the International Society for Magnetic Resonance In Medicine* (Denver, 2000), p. 14.

111. N. P. Verhoeff, O. A. Petroff, F. Hyder, S. S. Zoghbi, M. Fujita, N. Rajeevan, D. L. Rothman, J. P. Seibyl, R. H. Mattson, and R. B. Innis, Effects of vigabatrin on the GABAergic system as determined by ^{123}I-iomazenil SPECT and GABA MRS, *Epilepsia* **40,** 1433-8 (1999).

112. O. A. Petroff, F. Hyder, T. Collins, R. H. Mattson, and D. L. Rothman, Acute effects of vigabatrin on brain GABA and homocarnosine in patients with complex partial seizures, *Epilepsia* **40,** 958-64 (1999).

113. F. Hyder, O. A. Petroff, R. H. Mattson, and D. L. Rothman, Localized ^{1}H NMR measurements of 2-pyrrolidinone in human brain *in vivo*, *Magn. Reson. Med.* **41,** 889-96 (1999).

114. *Inflammatory Cells and Mediators in CNS Diseases*, edited by R. R. Ruffolo Jr., G. Z. Feuerstein, A. J. Hunter, G. Poste, and B. W. Metcalfe (Harwood Academic Publishers, Amsterdam, 1999).

115. L.-J. Eales, *Immunology for Life Scientists: a Basic Introduction* (Wiley, Chichester, 1997), p. 4.

116. L.-J. Eales, *Immunology for Life Scientists: a Basic Introduction* (Wiley, Chichester, 1997), pp. 90-92.

117. L.-J. Eales, *Immunology for Life Scientists: a Basic Introduction* (Wiley, Chichester, 1997), p. 91.

118. E. L. Thomas, M. B. Grisham, and M. M. Jefferson, Preparation and characterization of chloramines, *Meth. Enzymol.* **132,** 570-585 (1986).

119. Y. H. Atkinson, A. W. Murray, S. Krilis, M. A. Vadas, and A. F. Lopez, Human tumour necrosis factor-alpha (TNF-α) directly stimulates arachidonic acid release in human neutrophils, *Immunology* **70,** 82-7 (1990).

120. G. L. May, K. Sztelma, T. C. Sorrell, and C. E. Mountford, Comparison of human polymorphonuclear leukocytes from peripheral blood and purulent exudates by high resolution ^{1}H MRS, *Magn. Reson. Med.* **19,** 191-8 (1991).

121. G. L. May, K. Sztelma, M. L. Paul, and T. C. Sorrell, Proton magnetic resonance spectroscopy of polymorphonuclear leukocytes from patients with serious bacterial infections, *J. Infect. Dis.* **168,** 386-92 (1993).

122. N. R. Sibson and M. Palm, unpublished observations.

123. D. Anthony, unpublished observations.

124. O. Gonen, I. Catalaa, J. S. Babb, Y. Ge, L. J. Mannon, D. L. Kolson, and R. I. Grossman, Total brain *N*-acetylaspartate: a new measure of disease load in MS, *Neurology* **54,** 15-9 (2000).

125. J. Urenjak, S. R. Williams, D. G. Gadian, and M. Noble, Specific expression of N-acetylaspartate in neurons, oligodendrocyte-type-2 astrocyte progenitors, and immature oligodendrocytes *in vitro*, *J. Neurochem.* **59,** 55-61 (1992).

126. J. Urenjak, S. R. Williams, D. G. Gadian, and M. Noble, Proton nuclear magnetic resonance spectroscopy unambiguously identifies different neural cell types, *J. Neurosci.* **13,** 981-9 (1993).

127. K. K. Bhakoo and D. Pearce, *In vitro* expression of *N*-acetyl aspartate by oligodendrocytes: implications for proton magnetic resonance spectroscopy signal *in vivo*, *J. Neurochem.* **74,** 254-62 (2000).

128. S. Bluml, K. J. Seymour, and B. D. Ross, Developmental changes in choline- and ethanolamine-containing compounds measured with proton-decoupled ^{31}P MRS in *in vivo* human brain, *Magn. Reson. Med.* **42,** 643-54 (1999).

129. C. G. Choi and J. Frahm, Localized proton MRS of the human hippocampus: metabolite concentrations and relaxation times, *Magn. Reson. Med.* **41,** 204-7 (1999).

130. J. Frahm, H. Bruhn, M. L. Gyngell, K. D. Merboldt, W. Hanicke, and R. Sauter, Localized proton NMR spectroscopy in different regions of the human brain *in vivo*. Relaxation times and concentrations of cerebral metabolites, *Magn. Reson. Med.* **11,** 47-63 (1989).

131. P. Gideon and O. Henriksen, *In vivo* relaxation of *N*-acetyl aspartate, creatine plus phosphocreatine, and choline containing compounds during the course of brain infarction: a proton MRS study, *Magn. Reson. Imag.* **10,** 983-8 (1992).

132. P. A. Narayana, J. S. Wolinsky, E. F. Jackson, and M. McCarthy, Proton MR spectroscopy of gadolinium-enhanced multiple sclerosis plaques, *J. Magn. Reson. Imaging* **2,** 263-70 (1992).

133. A. M. Blamire, G. D. Graham, D. L. Rothman, and J. W. Prichard, Proton spectroscopy of human stroke: assessment of transverse relaxation times and partial volume effects in single volume steam MRS, *Magn. Reson. Imag.* **12,** 1227-35 (1994).

134. *Guidance for the submission of pre-market notifications for magnetic resonance diagnostic devices* (Food and Drug Administration, Rockville, USA, 1998).

135. N. R. P. Board, Revised guidance on acceptable limits of exposure during nuclear magnetic resonance clinical imaging, *Br. J. Radiol.* **56,** 974-7 (1983).

136. A. Kumar, R. V. Hosur, and K. Chandrasekhar, A Superior Pulse Scheme for Homonuclear Two-Dimensional Correlated Spectroscopy, *J. Magn. Reson.* **60,** 143-148 (1984).

137. T. Michaelis, G. Helms, and J. Frahm, Metabolic alterations in brain autopsies: proton NMR identification of free glycerol. *NMR Biomed.* **9**, 121-124 (1996).